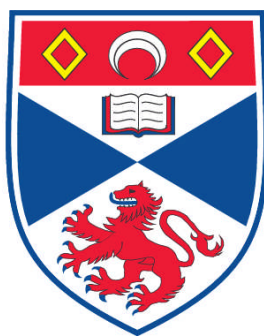


**ITINERANT METAMAGNETISM AND MAGNETIC
INHOMOGENEITY : A MAGNETIC ANALOGUE OF THE
SUPERCONDUCTING FULDE-FERRELL-LARKIN-OVCHINNIKOV
PHASE IN $\text{Sr}_3\text{Ru}_2\text{O}_7$**

Andrew McConnell Berridge

**A Thesis Submitted for the Degree of PhD
at the
University of St. Andrews**



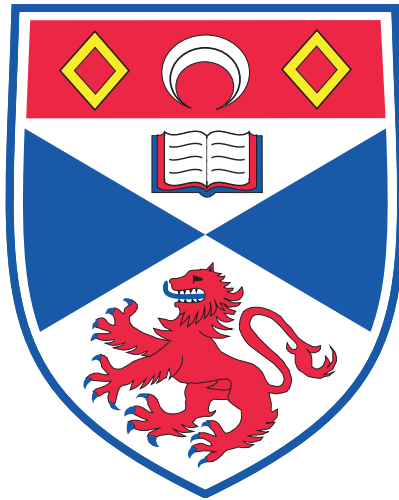
2009

**Full metadata for this item is available in the St Andrews
Digital Research Repository
at:
<https://research-repository.st-andrews.ac.uk/>**

**Please use this identifier to cite or link to this item:
<http://hdl.handle.net/10023/821>**

This item is protected by original copyright

Itinerant metamagnetism and magnetic
inhomogeneity:
a magnetic analogue of the superconducting
Fulde-Ferrell-Larkin-Ovchinnikov phase in
 $\text{Sr}_3\text{Ru}_2\text{O}_7$



A thesis presented by
Andrew McConnell Berridge
to the
University of St Andrews
in application for the degree of
Doctor of Philosophy
September 24, 2009

order to allow such access and migration, or have requested the appropriate embargo below.

The following is an agreed request by candidate and supervisor regarding the electronic publication of this thesis:

Access to Printed copy and electronic publication of thesis through the University of St Andrews.

date *signature of candidate*

date *signature of supervisor*

ABSTRACT

The formation of magnetic order in solids is a complex and subtle issue. There are a wide range of different types of magnetisation, all of which may be favoured under different circumstances. In this thesis we consider a novel combination of ideas where the formation of spatially modulated magnetisation is linked to a metamagnetic transition. In this we are inspired by a general principle of modulated phases intervening as intermediate states in phase transitions. In particular we draw analogies with the Fulde-Ferrell-Larkin-Ovchinnikov state of spatially modulated superconductivity.

We study a mean-field theory for itinerant magnetism where the crystal lattice drives the formation of a rich phase diagram. A peak in the electronic density of states due to a van Hove singularity creates ferromagnetism and a metamagnetic transition. Furthermore we find that a modulated magnetic phase - a spin-spiral, becomes favoured along the metamagnetic transition line. The appearance of this phase causes the metamagnetic transition to bifurcate to enclose the modulated region.

The topology of this reconstructed phase diagram shows remarkable similarity to that observed in experiments on $\text{Sr}_3\text{Ru}_2\text{O}_7$. This material shows a metamagnetic transition which can be tuned by field angle towards zero temperature. Before this point is reached a new phase with high and anisotropic resistivity appears.

We believe that this anomalous phase can be explained by the formation of a phase of modulated magnetisation caused by a peak in the electronic density of states. This mechanism may also apply in a range of other materials as it is driven by rather generic features of the bandstructure.

ACKNOWLEDGEMENTS

Firstly I would like to thank my supervisor Andrew Green for all of his guidance and support over the course of my Ph.D. Also my collaborators in much of this work, Santiago Grigera and Ben Simons, whose insights and assistance were invaluable. Thanks to the staff at St Andrews for sharing their knowledge with me over the years, especially Chris Hooley who has been an inexhaustible fount of knowledge.

I'd like to thank my friends and fellow students, both those engaged in the experimental side of the 327 adventure, Andreas, Jean-François, Alex, Jan and Demian, who repeatedly explained reality to me. And those who have other interests, Steve, Gary, Dave, Jill and Una, for making the last few years more enjoyable and connecting me to the rest of physics. Thanks also to Andreas and Alex for their hospitality during my homeless period. Also thanks to my all-too-brief colleagues Anne-Christine and Patrick.

Finally, I'd like to thank the staff of Taste, who fed and housed me throughout much of the final months of writing.

FREQUENTLY USED ABBREVIATIONS AND UNITS

Abbreviations

vHs	van Hove singularity
DoS	density of states
dHvA	de Haas-van Alphen
ARPES	angle resolved photoemission spectroscopy
FFLO/LOFF	Fulde-Ferrell-Larkin-Ovchinnikov

Units

h will be the external magnetic field multiplied by $g\mu_B$.

All momenta and wavevectors are multiplied by the lattice spacing $k \rightarrow ka$

ORIGINAL WORK

The majority of chapters 4, 5 and 6 of this thesis is the original work of the author, in collaboration with Dr. A. G. Green, Dr. S. A. Grigera and Prof. B. D. Simons. Chapter 4 forms the basis for the following publications:

Inhomogeneous Magnetic Phases: A Fulde-Ferrell-Larkin-Ovchinnikov-Like Phase in $\text{Sr}_3\text{Ru}_2\text{O}_7$, A. M. Berridge, A. G. Green, S. A. Grigera and B. D. Simons, *Physical Review Letters* **102**, 136404 (2009),

Inhomogeneous Magnetic Phases: A Fulde-Ferrell-Larkin-Ovchinnikov-Like Phase in $\text{Sr}_3\text{Ru}_2\text{O}_7$, A. M. Berridge, A. G. Green, S. A. Grigera and B. D. Simons, to be submitted to *Physical Review B*.

Material in Chapters 5 and 6 is work currently in progress.

Dedicated to Elizabeth McConnell Berridge

CONTENTS

<i>Part I Introduction to magnetism and the reasons for current interest</i>	1
1. <i>Introduction</i>	2
1.1 Strong correlation	2
1.2 Magnetism	4
1.2.1 The historical study of magnetism	4
1.2.2 The modern study of magnetism	8
1.2.3 Recent developments	11
2. <i>Itinerant magnetism - important developments and recent interest</i>	14
2.1 Itinerant magnetism	14
2.1.1 Magnetic phases	14
2.1.2 Metamagnetism	16
2.1.3 The generic phase diagram of itinerant magnets	17
2.1.4 Quantum criticality	19
2.2 A simple approach: the Stoner model	21
2.2.1 Mean-field theory	21
2.2.2 Metamagnetism due to peaks in the density of states	22
2.2.3 Spatially modulated magnetisation	23
2.3 Analogy with superconductivity	24
2.3.1 Analogy with homogeneous BCS superconductivity	24
2.3.2 Analogy with modulated FFLO superconductivity	27
3. <i>A topical example: $Sr_3Ru_2O_7$</i>	29
3.1 Main experimental results: magnetic phase diagram	29
3.2 Properties of the anomalous phase	32
3.2.1 Resistivity	32
3.2.2 Quantum oscillations in the anomalous phase	34
3.2.3 Thermodynamics	34
3.3 Crystal structure	35

3.4	Fermi surface	37
3.4.1	Construction of Fermi surface from simple arguments	37
3.4.2	Measured Fermi surface	39
3.4.3	Correspondence of quantum oscillation results	39
3.4.4	Reconciling the phase diagram and the Fermi surface	41
3.5	Summary	42
3.6	Our model and motivation	43

Part II Calculation of phase diagrams and properties, and comparison with experiment 45

4.	<i>Calculation of phase diagram</i>	46
4.1	Homogeneous phase diagram	46
4.1.1	Cartoon for homogeneous phase diagram	47
4.1.2	Calculation from mean-field free energy	49
4.1.3	Landau expansions	52
4.1.4	Landau phenomenology	56
4.1.5	Explicit Landau expansion of Stoner Hamiltonian	59
4.1.6	Phase separation	65
4.2	Inhomogeneous phase diagram	66
4.2.1	Cartoon for inhomogeneous phase formation	66
4.2.2	Free energy with inhomogeneity	71
4.2.3	Gradient expansion	71
4.2.4	Relation to FFLO	74
4.2.5	Ginzburg-Landau phenomenology	75
4.2.6	Full phase diagram from Ginzburg-Landau phenomenology	77
4.2.7	Building up the Ginzburg-Landau expansion	80
4.3	Summary	93
5.	<i>Thermodynamics</i>	94
5.1	Derivation of expressions for entropy and specific heat	94
5.2	Density of states with peak	96
5.2.1	Factors contributing to the entropy and specific heat	97
5.2.2	Results	101
5.3	Specific heat and entropy for inhomogeneous phase	103

6.	<i>Comparison with experiments on $Sr_3Ru_2O_7$</i>	105
6.1	Summary of experimental results	105
6.2	Topology of phase diagram	106
6.3	Properties of the phase	107
6.3.1	Thermodynamic signatures of the transition	108
6.4	Outstanding issues	108
6.4.1	Tuning the phase diagram with field angle	108
6.4.2	The possibility of observation by neutron scattering	118
6.5	Summary	119
 <i>Part III Related theories, future directions and conclusions</i>		120
7.	<i>Electron nematics</i>	121
7.1	Electron nematics	121
7.1.1	Liquid-crystal analogy	121
7.1.2	Pomeranchuk instability	122
7.1.3	d -wave distortions	123
7.1.4	Orbital ordering	125
7.1.5	Melted stripe order	126
7.2	The link between nematic and spiral order	126
8.	<i>Future research directions</i>	127
8.1	Extensions of current research	127
8.1.1	How does field angle tune the phase diagram?	127
8.1.2	More realistic dispersions	127
8.1.3	Multiple wavevectors	128
8.1.4	Transport	128
8.1.5	Entropy	128
8.2	New directions	129
8.2.1	Interplay of lattice and fluctuation effects	129
8.2.2	Electron nematics	129
9.	<i>Conclusion</i>	130

<i>Appendix</i>	133
<i>A. Partition functions and the imaginary-time coherent-state path integral</i>	134
A.1 Coherent State Path Integrals and the Partition Function	134
A.2 Hubbard-Stratonovich Transformation	135
A.3 Gaussian Integral	136
A.4 Landau Expansion	137
A.5 Matsubara Frequencies	137
<i>B. Terms in the expansion of the Stoner action</i>	139
B.1 Action and critical endpoint conditions	139
B.2 Landau expansion	140
B.3 Gradient expansion	144
B.4 Calculating the phase diagram	146
<i>C. Thermodynamic derivations</i>	148
C.1 Free energy and self-consistency	148
C.2 Useful derivatives	149
C.3 Entropy	150
C.4 Specific Heat	150
C.5 Derivatives of the chemical potential	151

LIST OF FIGURES

1.1	Lodestone and early compass	5
1.2	Exchange interaction	8
1.3	Types of magnetic order	9
1.4	Non-Fermi liquid behaviour	12
2.1	Phase diagram of water	15
2.2	Metamagnetic transition	17
2.3	Generic itinerant electron phase diagram	18
2.4	Phase formation near quantum critical points	20
2.5	Spin textures	23
2.6	Perfect nesting of the tight-binding model	25
2.7	Fermi surface nesting in chromium	25
2.8	Pairing analogy between superconductivity and magnetism	26
2.9	Phase diagram of the FFLO state	27
3.1	Phase diagram of $\text{Sr}_3\text{Ru}_2\text{O}_7$ with quantum critical endpoint	30
3.2	Resistivity exponent in $\text{Sr}_3\text{Ru}_2\text{O}_7$	31
3.3	Magnetic phase diagram of ultra-pure $\text{Sr}_3\text{Ru}_2\text{O}_7$	32
3.4	Resistivity anisotropy in the anomalous phase of $\text{Sr}_3\text{Ru}_2\text{O}_7$	33
3.5	Experimental measurements of entropy and specific heat of $\text{Sr}_3\text{Ru}_2\text{O}_7$	36
3.6	Crystal structure	37
3.7	Orbital composition of $\text{Sr}_3\text{Ru}_2\text{O}_7$	38
3.8	Construction of the Fermi surface	40
3.9	Fermi surface from ARPES	41
3.10	Density of states from ARPES	41
4.1	Electronic dispersion and van Hove singularity	48
4.2	Cartoon for the formation of metamagnetism	49
4.3	Phase diagram for the Stoner model	52
4.4	Order parameter as minimum of the Landau free energy	54

4.5	Phase transitions in the Landau expansion	54
4.6	Generic phase diagram for sixth-order Landau expansion	55
4.7	Phase diagram for symmetry-broken Landau theory	57
4.8	Homogeneous phase diagram from phenomenology	59
4.9	Homogeneous phase diagram from microscopics	64
4.10	Phase separation and Maxwell construction	65
4.11	Fermi surface reconstruction due to formation of spiral magnetism . .	67
4.12	Anticrossing of bands	68
4.13	Density of states for the spiral state	68
4.14	Transverse susceptibility and nesting vectors	70
4.15	Evaluation of K_{\perp}	74
4.16	Phase diagram for a free electron dispersion	75
4.17	Free energy for finite \mathbf{q} state	77
4.18	Phase diagram for the Ginzburg-Landau theory	78
4.19	Phase diagram in the context of the parent transition	79
4.20	Phase diagram for reduced theory with no cross terms	81
4.21	Phase diagram for reduced theory with a $U_1\phi^2\phi_{\perp}^2$ cross-term	82
4.22	Phase diagram for reduced theory with $U_1\phi^2\phi_{\perp}^2$ and $V_2\phi^2\phi_{\perp}^4$ cross-terms	85
4.23	Phase diagram for reduced theory with all symmetric terms	87
4.24	Phase diagram for full theory	92
5.1	Effect of spin-splitting on the entropy	96
5.2	Dependence of chemical potential on magnetic field	98
5.3	Effect of first order transition on entropy	99
5.4	Effect of temperature on the entropy and specific heat	100
5.5	Magnetisation, entropy and specific heat at a metamagnetic transition	102
5.6	Density of states in spiral phase	104
5.7	Entropy including inhomogeneous phase	104
6.1	Comparison of experimental and theoretical phase diagrams	106
6.2	Experimental measurements of entropy and specific heat of $\text{Sr}_3\text{Ru}_2\text{O}_7$	109
6.3	Experimental phase diagram of $\text{Sr}_3\text{Ru}_2\text{O}_7$ as a function of field com- ponents	110
6.4	Transitions with an anisotropic g factor	111
6.5	Schematic representation of the bilayer model	112
6.6	Anticrossing of bilayer dispersions	113

6.7	Peaks in the density of states	113
6.8	Effect of spin-orbit coupling on the Fermi Surface	116
6.9	Effect of orbital Zeeman coupling on the Fermi Surface	117
6.10	Comparison of full Fermi surface and orbital model	118
7.1	Smectic and nematic ordering	122
7.2	Pomeranchuk distortions	123
7.3	d -wave Fermi surface distortion	124
7.4	Orbital ordering	125
B.1	Calculation of phase diagram	147

Part I

INTRODUCTION TO MAGNETISM AND THE
REASONS FOR CURRENT INTEREST

1. INTRODUCTION

1.1 *Strong correlation*

There is a popular conception that ‘fundamental physics’ means only the study of ever more elementary components of matter. That our progress in physics relies on smashing apart particles at higher and higher energies. Theorists write equations to eventually discover a ‘theory of everything’ which unifies all that we know under one banner.

Yet some of the most difficult and long-standing problems of physics come not from probing the behaviour of more fundamental particles, but in the behaviour of *more* particles. When we take particles which we understand perfectly well on their own and allow them to interact with each other we suddenly find our traditional methods and intuitions failing. The physics of collective behaviour is just as challenging and fundamental as that found in high energy colliders, and perhaps more relevant.

We in fact already have an effective ‘theory of everything’ for everyday objects. The Schrödinger equation describes perfectly well the electrons and ions in solids, liquids and gases. In principle we only have to solve one equation: $\hat{H}\psi = i\hbar\partial_t\psi$. Here of course the ‘hat’ hides a multitude of sins. To completely describe the system the Hamiltonian must describe not only each particle, but their interactions. Including only the dominant interactions the Hamiltonian then takes the form:

$$\begin{aligned}\hat{H} = & -\sum_{j=1}^{N_e} \frac{\hbar^2}{2m_j} \nabla_j^2 + \sum_{j<k} V_{ee}(\mathbf{r}_j - \mathbf{r}_k) \\ & -\sum_{\alpha=1}^{N_i} \frac{\hbar^2}{2m_\alpha} \nabla_\alpha^2 + \sum_{\alpha<\beta} V_{ii}(\mathbf{r}_\alpha - \mathbf{r}_\beta) \\ & + \sum_{i,\alpha} V_{ei}(\mathbf{r}_i - \mathbf{r}_\alpha),\end{aligned}\tag{1.1}$$

where m_n is the mass of the n th particle, V_{ee} , V_{ii} and V_{ei} are the electron-electron, ion-ion interaction and electron-ion interactions respectively, \mathbf{r}_n is the position of the

nth particle. Roman subscripts label the electrons and Greek subscripts the ions. The problem is that it becomes impossible to solve this equation, even numerically, for more than a few particles, and in a typical macroscopic object there are $\sim 10^{23}$ particles. It is impossible to predict the properties of many-body systems from the fundamental equations.

We see however, that nature obeys beautiful organisational principles on all scales that we choose to examine it. Although these principles cannot be deduced from the microscopic description of their constituents they are nevertheless powerful and fundamental. Often these principles are blind to the underlying microscopics and are universal across many different systems. Such behaviour is said to be *emergent*. The study of these emergent principles is often more fruitful than that of reductionist principles.

Given the impossibility of solving the Schrödinger equation for a large number of particles, how are we to proceed to understand the properties of real systems? It is a remarkable and fortunate fact that the properties of most systems of interacting particles actually behave almost exactly like those of non-interacting particles, but with alterations to basic properties like the mass and charge of the particles. This principle is embodied in Landau's Fermi liquid theory [1–3]. This is the cornerstone of our understanding of metals and is one of the great triumphs of physics. The underlying principle is that of adiabatic continuity. If we took a non-interacting gas of particles and then slowly turned on the interactions then the eigenfunctions of the system would evolve continuously. The elementary excitations would no longer be single electrons, they would be quasiparticles, but they will be electron-like in that they will be characterised by the same quantum numbers with a one-to-one correspondence between the original electrons and the new quasiparticles. In this way the system behaves qualitatively the same as a non-interacting system, but with renormalized coefficients. For example the mass of the quasiparticles is greater than the bare electrons, often by many times. An extreme example of this are the so called heavy fermion materials where complex many-body effects conspire to increase the mass of the quasiparticles to hundreds of times higher than the bare electron mass [4].

Because the Fermi liquid description is so successful the situations where it fails are especially interesting. In some materials the quasiparticle picture breaks down and the behaviour becomes qualitatively new, such situations are referred to as strongly correlated. One of the most exciting areas in which non-Fermi liquids

have been observed is quantum criticality. A quantum critical point occurs when a second-order phase transition is driven by a non-thermal control parameter at zero temperature. Near such points quantum and thermal fluctuations become entwined and dominate the properties of the system over a wide range of phase space. These quantum critical properties are universal, depending only on the dimensionality of the system and the type of ordering present, and not on the microscopic details. The system has new and unusual dependencies of its properties on external parameters, as well as the possibility of novel phases being stabilized by the quantum fluctuations. Such quantum critical points occur in a wide range of materials, being important in heavy fermion materials [5] and possibly in the high temperature superconductors [6].

Less exotic states, where the Fermi liquid paradigm is still valid, are also interesting. One of the most important and common collective phenomena is magnetism. Despite having a long history of research and being of great technological and fundamental importance, there are still many unanswered questions due to the subtlety of the various competing effects and orders. Theories of magnetism range from relatively simple mean-field models to complex field-theoretic approaches. Whilst it is quite straightforward to obtain the gross results, the details are very complex correlated effects which prove elusive. To understand the status of the theory of magnetism and to put this work in context I will now briefly discuss the history of the study of magnetism and how it has led to some of the areas just mentioned.

1.2 Magnetism

1.2.1 The historical study of magnetism

Magnetism is one of the oldest known physical phenomena. The fact that certain stones attract iron was known in ancient Greece, and almost certainly before. Yet thousands of years after its discovery magnetism is still an object of intense study. Despite the easy observation and reproduction of magnetic phenomena, and their great importance for navigation and our understanding of the natural world, we have yet to fully understand magnetism in solids. Indeed, until the beginning of the twentieth century we had no chance of understanding the origin of magnets, for the phenomena is an intrinsically quantum mechanical one. We now believe that we understand the fundamental interactions that produce magnetism in materials, but the calculation of the exact properties of magnetic systems is subtle and still



Fig. 1.1: Lodestone and early compass: Leftpanel: Lodestone showing strong ferromagnetism. This phenomena of a chain of metal objects being attracted to the lodestone had been noted in Roman times [7]. Image from [8]. Right panel: an early Chinese compass, though the historical accuracy of this is disputed. Image from [9].

controversial.

Ferromagnetism was known to the Greeks at least as long ago as 800 BC. They wrote of the properties of lodestone, which is powerfully magnetic even in its natural state. Indeed the word ‘magnet’ most probably derives from the Magnesia province where lodestone was mined [7].

We now know that lodestone is the iron ore Fe_3O_4 , known as magnetite. Magnetite is an extremely common material, but lodestone is comparably rare. It has recently been suggested that the magnetisation of lodestone occurs when magnetite is struck by lightning, briefly exposing it to large magnetic fields [10].

To the ancient Greeks these facts were of course completely unknown and they linked the properties of lodestone to divine origin, even believing that lodestone itself had a soul. Slightly more recognizable to us is the subsequent idea that magnetism is due to effluvia, emanations that flowed from lodestone and displaced air, causing metal to be drawn into the empty space [7]. Regardless of the obvious shortcomings of such a theory it is remarkable to note that already there was the very loose idea of a ‘field’ being emitted by the magnet.

One of the first truly ‘scientific’ texts on magnetism, indeed on any subject¹, was written by William Gilbert of Colchester in 1600 [11]. In his remarkable book *De Magnete* Gilbert systematically investigates many of the properties of the magnet, debunking many long held superstitions, such as the assertion that garlic or dia-

¹ Gilbert was a contemporary of Galileo, who published several books on mechanics just prior to 1600.

monds weakened magnets. One of the important experiments that Gilbert carried out was the construction of a magnetic sphere, called a ‘terrella’ or ‘little earth’ and placing a compass at various points on its surface. Based on this he concluded that the earth itself was magnetic. As well as his studies of magnetism Gilbert was an early proponent of the ‘scientific method’, strongly attacking those who simply repeated the fallacies of ancient thinkers rather than conducting even simple experiments themselves. In *De Magnete* he says:

There are many modern authors who have written and copied from others about amber and jet attracting chaff... but they treat the subject in words alone, without finding any reasons or proofs from experiments, their very statements obscuring the thing in a greater fog, forsooth in a cryptic, marvellous, abstruse, secret, occult way. Wherefore also such philosophy produces no fruit, because very many philosophers, making no investigation themselves, unsupported by any practical experience, idle and inert, make no progress by their records, and do not see what light they can bring to their theories; but their philosophy rests simply on the use of certain Greek words, or uncommon ones; after the manner of our gossips and barbers nowadays, who make show of certain Latin words to an ignorant populace as the insignia of their craft, and snatch at the popular favour. [11]

Based on the empirical investigations which followed Gilbert a mathematical understanding of magnetism was founded in the work of Poisson, who introduced the concepts of magnetic potential and the equations which describe the contributions to magnetism from a body. Whilst being an elegant mathematical description of the phenomena, and of great practical use, this perspective completely ignores the physical origin of magnetism. Nowhere in this work is it necessary, or even desirable, to state the source of the magnetism.

Ideas for the nature of the magnetic sources in solids had to wait for the study of ‘magnetism’ to change into the study of ‘electromagnetism’. In 1820 Oersted realized that a current passing through a wire would deflect a nearby magnetic needle. The same year it was suggested by Ampère and Arago that magnetism was caused by electrical current loops inside magnets. Fresnel suggested that such currents should be molecular, rather than macroscopic, citing reasons such as the lack of Joule heating. A picture emerged in which microscopic circulating currents cause each molecule of a magnetic substance to act like a tiny bar magnet. In unmagnetised

samples these are randomly arranged, but magnetising causes them all to line up together. Such ideas lead ultimately to experiments such as those performed by Ewing, who arranged geometric arrays of small magnets which were free to pivot. The magnetic forces between these magnets cause them to rotate into the most favourable orientation. If this is a good model of the origin of magnetism in solids, then the behaviour of the array should provide information on ferromagnetism.

This picture fails in the respect that the interactions between our microscopic magnets are *not* classical dipole-dipole interactions, but are of a fundamentally quantum-mechanical nature. The failure of this model became manifest in two ways. Firstly it turns out that the magnetic interactions are far too weak. In 1907 Weiss proposed a theory of magnetism which, ignoring the microscopic origin of the forces between magnetic moments, described their interactions empirically via a ‘molecular field’ acting like an external magnetic field. However, the experimentally determined values of this field are some 10^4 times higher than can be explained by the magnetic dipole interactions. We now understand that the size of this constant is due to the quantum nature of the forces and the fact that it is electrostatic, rather than magnetic in origin.

The second aspect in which the classical theory fails is more dramatic. According to classical theory there can not actually be any magnetism at all. This result is known as the Bohr-van Leeuwen theorem [12, 13] and it shows that the thermal average of the internal magnetic field is zero at any temperature and for any external field. There can therefore be no magnetic response to any stimulus. The solution to this problem can only be found in quantum mechanics.

What are the fundamental, quantum, magnetic elements? The discovery of the electron and the structure of atoms gave us the necessary information. Compton, Goudsmit and Uhlenbeck [14, 15] showed empirically that as well as orbital angular momentum the electron possessed an intrinsic spin and a magnetic moment. In a beautiful example of different ‘fields’ of physics meshing together Dirac showed that this spin arises naturally from relativistic quantum mechanics [16].

With electrons (and nucleons) established as the sources of the magnetic fields we must consider how they interact. The most fundamental and far-reaching aspect of this lies in their statistics. One of the most important principles in condensed matter physics is the Pauli exclusion principle, which states that no two fermions may occupy the same quantum state. Since the electrons cannot all pile into the lowest energy state they are forced to occupy higher and higher energy states. Thus

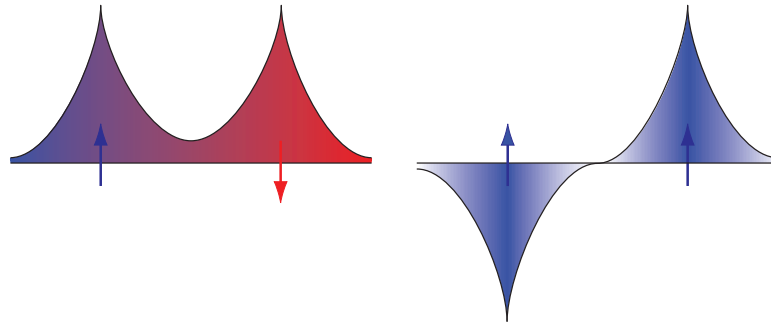


Fig. 1.2: Exchange: The quantum-mechanical origin of exchange energy. The symmetry of the spin wavefunction determines the symmetry of the spatial wavefunction. This determines the kinetic and Coulomb energies of the arrangement, thereby favouring ferro- or antiferro-magnetism.

the concept of the Fermi surface, a line dividing the full and empty momentum states is born. This completely changes the nature of the system. The energetics are now determined only by states at the Fermi surface. To excite the lower energy states requires a large energy, they are therefore considered inert.

Another consequence of the exclusion principle is the nature of the interaction between electrons, this turns out to depend on the electrostatic force between electrons which is far larger than the magnetic dipole-dipole interactions. When two electrons are brought together there are two possible alignments - the spins can be parallel or antiparallel. The two arrangements have a different energy, the difference being known as the exchange energy. The heart of Fermi-Dirac statistics is that electrons must have an antisymmetric wavefunction. The wavefunction consists of a spin part, and a spatial part. If the two spins are antiparallel then the spatial part of the wavefunction has to be symmetric. Should the spins be parallel then the spatial part of the wavefunction must be antisymmetric. This has two energetic consequences. Firstly the kinetic energy is higher in the antisymmetric case. But there is now less electronic density in the region where the Coulomb repulsion is highest. Exchange therefore captures the energetic competition at the heart of magnetism, the balance between interaction and kinetic energy. If the exchange constant is positive then the parallel spin alignment has a lower energy and a state where all electron spins align, the ferromagnetic state, is favourable.

1.2.2 The modern study of magnetism

We now believe that we understand the fundamental constituents and mechanisms of magnetism, yet predicting the details of realistic systems is a formidable task.

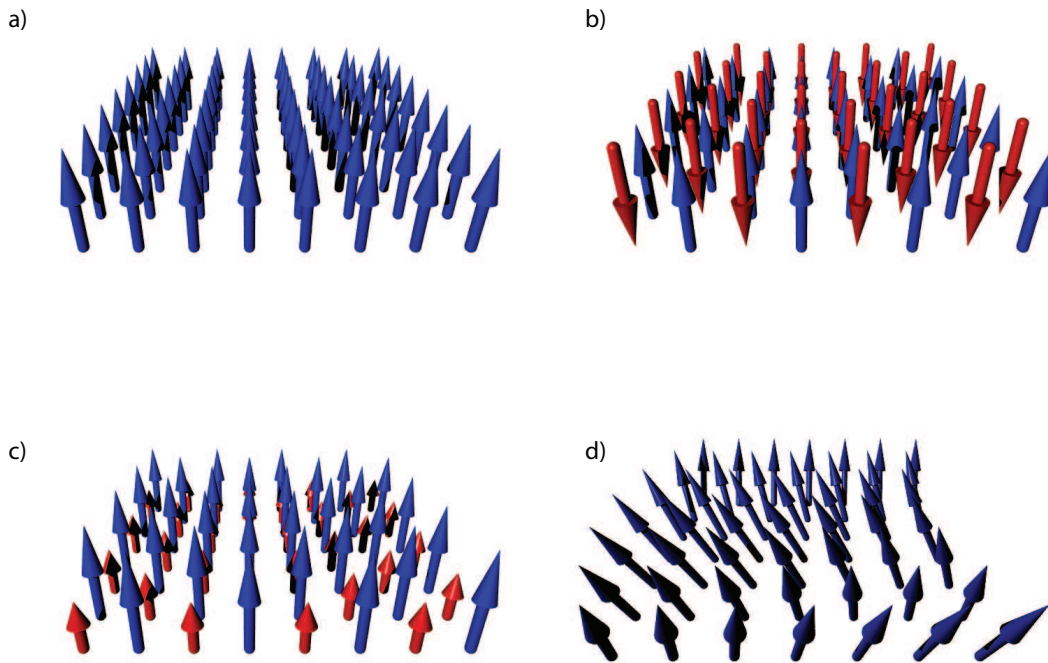


Fig. 1.3: Types of magnetic order: a) Ferromagnetism, the majority of magnetic moments are aligned in the same direction with a uniform distribution. b) Antiferromagnetism, the sign of the moment varies from site to site. c) Ferrimagnetism, the magnitude of the moment varies. d) Helimagnetism, the direction of the moment rotates about an axis.

Being unable to solve the full problem we must develop simplified models which illuminate particular aspects of magnetic behaviour and are valid within particular regimes.

The first division to be made is between insulating and metallic behaviour, between the cases where the magnetic moments are localised onto particular sites and and the case when they are delocalised over the sample. Real materials of course lie somewhere in-between and our choice is made based on the dominant character of the electrons involved. In complex cases both regimes may be involved, the interaction of localised magnetic moments with a conduction electron sea is the heart of the Kondo effect [17] and heavy fermion materials [4].

Until the 1930s only two types magnetic states were known - non-magnetic states (para- and dia-magnetism) and a uniformly magnetised state, ferromagnetism. However it was predicted by Néel in 1936 that there could be other types of magnetic

order [18]. In work that would later be awarded the Nobel prize he proposed that a form of magnetism in which the magnetic moments align anti-parallel with their neighbours could occur, a state called antiferromagnetism. This is illustrated in Fig.1.3b). It took thirteen years for this proposal to be confirmed [19].

Having realised that more complex forms of magnetic order can occur it is not hard to think of more examples. Another state predicted by Néel was ferrimagnetism, where the magnetic moment changes magnitude from site to site [20]. Indeed magnetite, long thought to be ferromagnetic, turns out to be a ferrimagnet. A further possibility is that rather than aligning along a single axis the magnetisation precesses about an axis as a function of position. This is called helimagnetism and a form of this order will be the subject of this thesis. It is generally caused by spin-orbit coupling in systems without inversion symmetry - where the singling out of one direction in the lattice is allowed by symmetry [21], but can also appear spontaneously in symmetric systems. These types of order are shown in Fig.1.3 c) and d).

The pictures presented for these forms of order have been in a localised model. In itinerant systems the modulation of the magnetisation is continuous in space. Such variations of the magnetisation are variations in the spin density, and are therefore called spin density waves. Linear spin density waves can be antiferromagnetic when their period matches the crystalline periodicity, but can also be incommensurate with the lattice.

The Stoner treatment of itinerant ferromagnetism was developed to study the fully delocalised electron case. It treats the magnetism of the system as an average field which all of the electrons feel equally. In this way it reduces the many-body problem of electron interaction to an effective single-particle picture. Here the electron moves in a field derived from the average interaction with all of the other electrons - a mean-field.

The mean-field approach of the Stoner treatment does not correctly reproduce all of the behaviour of metals, although it is a good starting point. We need to use models that go beyond the effective single-particle picture and treat correlations between the particles. The prime model for this task is the Hubbard model [22].

$$\hat{H} = - \sum_{ij\sigma} t_{ij} \hat{c}_{i\sigma}^\dagger \hat{c}_{j\sigma} + g \sum_i \hat{n}_{i\uparrow} \hat{n}_{i\downarrow}, \quad (1.2)$$

where $\hat{c}_{i\sigma}^\dagger/\hat{c}_{i\sigma}$ are the creation/annihilation operators for electrons on site i with spin

$\sigma = \uparrow / \downarrow$, t_{ij} are the hopping matrix elements, g is an interaction energy and $n_{i\uparrow/\downarrow}$ is the number operator for site i and spin up/down. The first term is the tight-binding description of single electrons moving on a discrete lattice. The second term reduces the interactions between electrons to an onsite interaction with strength g . This is an approximation which is somewhat justified by the existence of screening, where the long-range nature of the Coulomb interaction is masked in an electronic fluid.

Despite that vast simplification between the full Hamiltonian Eq.1.1 and the Hubbard Hamiltonian Eq.1.2 we are far from having a complete solution for the problem. One of the problems is the immense range of possible states that are admitted. Various magnetic and charge orderings, superconductivity, quantum Hall states, the possibilities are endless. With no way of extracting the groundstate directly from the Hamiltonian we are forced to postulate the state which is realised and then justify its stability. This task is extremely difficult given the subtlety of the problem. It is therefore not surprising that experiment generally leads theory in this field. Aside from antiferromagnetism there have only been a few states which were predicted theoretically before their observation. Relevant to the work in this thesis is the electron nematic state [23]. This is postulated to occur between the electronic liquid and crystal, breaking rotational but not translational symmetry. It has been proposed that it is present in the high-temperature superconductors [24], two dimensional electron systems [25] and more recently in the compound $\text{Sr}_3\text{Ru}_2\text{O}_7$ [26], but has not been unambiguously observed. The spatially modulated superconducting Fulde-Ferrell-Larkin-Ovchinnikov state [27, 28], with which we will draw analogies, was predicted in 1964 but has still to be conclusively observed.

1.2.3 Recent developments

On the timescales over which mankind has been aware of magnetism our growing awareness of the vast panopticon of magnetic order in the mid twentieth century may seem shockingly recent. There are however related topics of even more recent excitement. Many of these are centered around the realisation of non-Fermi liquid states.

Fermi liquid theory has been so successful that there is tremendous excitement over materials which do not follow the paradigm. These systems do not have electron-like quasiparticles and their properties can depart completely from the basic behaviour that we have come to expect. Signals of this non-Fermi liquid behaviour can be found in unexpected power-law dependencies of quantities like specific heat,

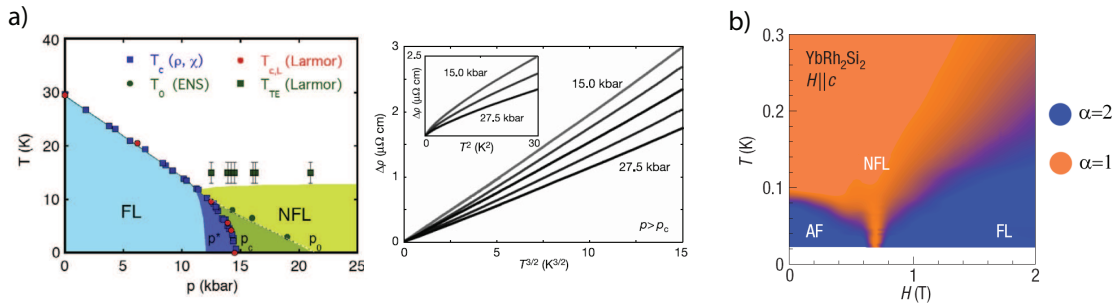


Fig. 1.4: Non-Fermi liquid behaviour: a) Non-Fermi liquid behaviour in MnSi. Phase diagram showing non-Fermi liquid regime and resistivity curves showing $T^{\frac{3}{2}}$ behaviour. Figures from [29, 30]. b) Non-Fermi liquid behaviour in YbRh₂Si₂. Resistivity exponent $\rho \propto T^\alpha$, as derived from the logarithmic derivative of resistivity with respect to temperature. $\alpha = 2$ is the standard Fermi liquid prediction. A large region of $\alpha = 1$ shows non-Fermi liquid behaviour. Figure from [5].

susceptibility and resistivity. Fermi liquid theory predicts certain temperature dependencies. For example, specific heat goes as T and resistivity as T^2 . These are generic properties depending only on the presence of electron-like quasiparticles and a Fermi surface. Finding deviations from these relations is a common indicator of non-Fermi liquid behaviour, as seen for example in MnSi (Fig.1.4a)).

The situation in which non-Fermi liquid behaviour is observed that bears most directly on this thesis is quantum criticality. Quantum critical points occur when a continuous phase transition takes place at zero temperature, driven by some non-thermal control parameter. At this point it is the quantum, and not thermal fluctuations that cause the phase transition. Although the quantum critical point is a single point at the inaccessible zero of temperature these quantum fluctuations affect a large region of the phase diagram, with a quantum critical ‘cone’ extending from the quantum critical point. In this region quantum and thermal properties become inextricably mixed. This region can be seen in Fig.1.4.

One of the interesting features of quantum criticality is that theoretically the quantum critical properties of the system are completely independent of microscopic details. They fall into universality classes which depend only on the dimensionality of the system and the type of ordered phase that is present. Quantum criticality therefore provides a unifying principle for understanding the behaviour of a wide set of systems.

The fact that quantum critical behaviour extends over a range of temperature and tuning parameter means that the presence of a putative quantum critical point can be detected even if the point itself is obscured. In many systems it seems that

the quantum critical point is avoided. Either the phase transition turns first-order as the temperature is lowered or a new phase appears to mask the quantum critical point. The search for new quantum phases is therefore often guided by the search for avoided quantum criticality.

Indeed, it may be the case that it is theoretically impossible to have a quantum critical point in itinerant ferromagnets due to interaction effects which have so far been neglected. It was recently (re-)discovered ² that the standard Hertz-Millis theory of quantum criticality [37,38] breaks down near to the critical point [39,40]. This breakdown manifests itself as non-analytic terms in the action, which cause a reconstruction of the phase diagram. These corrections cause the continuous transition to turn first-order, and stabilize the formation of modulated magnetic phases. These corrections are currently the subject of much research [32,39,40].

In this thesis we will discuss the formation of spatially modulated magnetisation, but driven by the crystal lattice, not quantum criticality.

² The fact that the susceptibility is non-analytic was discovered by Geldart and Rasolt in 1977 [31]. The non-analyticities in Hertz-Millis theory have recently [32] been shown to be connected to second-order perturbation theory results [33–36].

2. ITINERANT MAGNETISM - IMPORTANT DEVELOPMENTS AND RECENT INTEREST

2.1 *Itinerant magnetism*

2.1.1 *Magnetic phases*

Phase transitions come in a number of forms, some very familiar, some more esoteric. Most commonly known are transitions between the solid, liquid and gaseous phases of matter. For example, water may be ice, liquid water or water vapour depending on temperature and pressure, as shown in Fig.2.1. The boundaries between these phases are phase transitions.

These are extreme examples of structural transitions where the microscopic structure of the material changes. These can occur within the solid phase, with different arrangements of the nuclei favourable under different conditions. For example there are over a dozen solid phases of water [41].

Other sorts of phases are possible, such as electronic transitions between insulating, conducting and superconducting phases. There may also be more subtle types of electronic order such as charge density waves, nematic phases [23, 42, 43] or Pomeranchuk distortions [44] where it is the geometry of the Fermi surface which changes.

The transitions which we will be concerned with are between different magnetic states such as paramagnetism, ferromagnetism and antiferromagnetism. We will consider situations where the magnetic moment is due to electrons which are best described as being fully itinerant. This includes elemental metals as well as many complex compounds such as the one we will focus on, $\text{Sr}_3\text{Ru}_2\text{O}_7$ [45]. The favourability of different phases and the ability to tune through them by varying external parameters is due to the competition between the ordering tendencies of the electron-electron interactions and the disordering effect of temperature. For example, pressure slightly alters the interatomic spacing, effectively tuning the interactions between electrons. The role of the conjugate field to the order is also

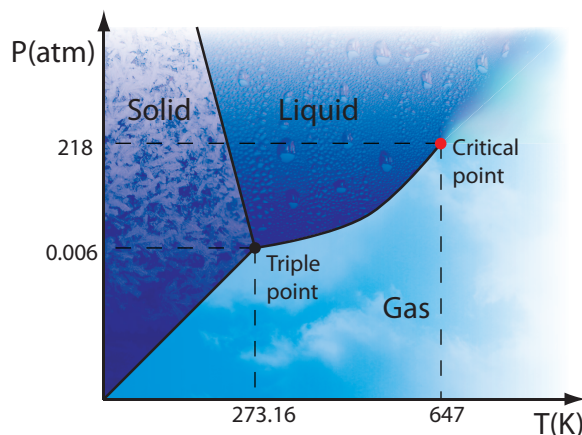


Fig. 2.1: Phase diagram of water: Sketch of the phase diagram of water. The triple point is the point at which solid, liquid and gaseous phases can co-exist. The critical point is the point at which the discontinuous change between liquid and gas stops. By moving around this point we may pass from liquid to gaseous without any non-analyticities in the free energy. There is no critical point on the solid-liquid transition line. We note that there are many different solid phases and this region of the phase diagram may be subdivided by transitions between them [41].

important. In this thesis we will be concerned with how applying a magnetic field alters the ferromagnetic phase diagram.

Phase transitions are characterised by introducing a quantity known as the order parameter. This is chosen separately for each system to be zero in the disordered phase and non-zero in the ordered phase. In the case of a ferromagnet the order parameter is the uniform magnetisation, in the case of the antiferromagnet it is the sublattice magnetisation.

Phase transitions can be split into categories depending on the behaviour of the order parameter as the transition is crossed. The phase transition is a non-analyticity in the free energy. The Ehrenfest classification scheme categorises transitions depending on the order of the derivative of the free energy which is discontinuous, a discontinuity in the first derivative is called a first-order transition, in the second derivative a second-order transition. Normally transitions of second-order and higher are called continuous transitions because of the behaviour of the order parameter. In a first-order transition the order parameter jumps suddenly, in a second-order transition it appears continuously from zero. The two types of transition are usually associated with different thermodynamic signatures - the first-order transition with a latent heat and the second-order with a diverging susceptibility.

The theory of phase transitions can proceed on two levels, one based on the

microscopic physics of the system, and one a phenomenological approach. In dealing with itinerant electronic systems most microscopic approaches are based on the Hubbard model or one of its descendants. The Hubbard model captures the basic competition between kinetic and Coulomb energies which is the driving force behind magnetic transitions. This work will use the Stoner model, this pre-dates the Hubbard model, but can be considered a mean-field version of it.

The phenomenological approach to phase transitions is the Ginzburg-Landau expansion [46]. This does not depend on microscopic details of the system, only the existence of an order parameter and the fact that it is small near to a continuous transition. Close to the transition we may therefore expand the free energy in powers of the order parameter. The form of this expansion is determined by symmetry and can be used to derive generic properties of the phase transition. As a transition becomes more strongly first-order this description becomes less accurate, but it is still applicable close to a tricritical point.

In this thesis both approaches will be used, microscopics based on the Stoner model and Ginzburg-Landau theory based on the phenomenology of the metamagnetic system. The two approaches can be linked, as the coefficients of the Ginzburg-Landau expansion may be determined explicitly from the microscopics, allowing the mapping of general properties onto a specific system. In this way we may use whichever approach is more suitable for a given task.

2.1.2 *Metamagnetism*

Metamagnetism describes a superlinear rise in magnetisation as a magnetic field is applied. In a paramagnetic material the magnetisation rises linearly with the field but in a metamagnet the magnetisation rises much more sharply at a certain critical field. We will define metamagnetism as a discontinuous jump in the magnetisation as a function of the applied field. This is not a symmetry breaking phase transition as the field has already broken the symmetry. The size of this jump decreases as temperature is increased until the magnetisation becomes continuous at a critical endpoint. Above this endpoint is a cross-over, not a true transition as there are no non-analyticities in the free energy. As we can move around this point without going through a phase transition the metamagnetism cannot occur between phases with different symmetries, since we cannot continuously break a symmetry. Returning to the example of the phases of water, metamagnetism is similar to the liquid-gas transition which ends at a critical point. In the water case the order parameter

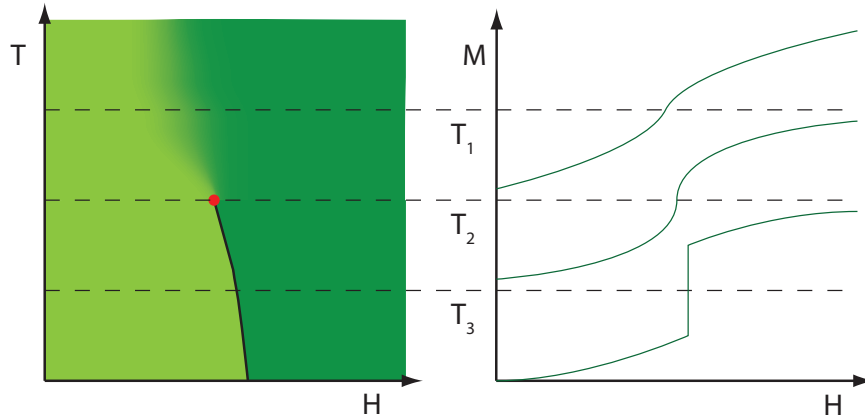


Fig. 2.2: Metamagnetic transition: Sketch of the metamagnetic transition in the magnetic field and temperature plane with critical endpoint shown in red. Green shading represent the value of magnetisation, light low and dark high. Also shown are sketches of magnetisation against field for three temperatures around the critical endpoint, the zero of magnetisation is offset for clarity.

is defined as the difference in density between the phases, this goes to zero at the critical point and varies continuously above the point.

2.1.3 The generic phase diagram of itinerant magnets

Itinerant magnets share a common form of phase diagram as a function of some tuning parameter, usually pressure, magnetic field and temperature. At zero field and low temperature the system is in its ordered phase, which could be any of the discussed magnetic phases. As temperature is increased the system goes through a continuous phase transition to the disordered phase. The critical temperature of this transition can be tuned by varying some external parameter. The critical temperature decreases, but before it reaches zero temperature the transition becomes first order. As the conjugate field is applied the first order transition extends as a metamagnetic ‘wing’, the critical endpoint of which can be tuned to lower temperature by the control parameter. This critical endpoint may be able to be depressed completely to zero temperature, in which case it becomes a quantum critical endpoint.

Such a phase diagram is realised in many systems such as MnSi [29] (where the ordered phase is a helimagnet), ZrZn₂ [47], NbFe₂ [48], UGe₂ [49], CoS₂ [50], and the material of most interest to this work, Sr₃Ru₂O₇ which at ambient pressure only has the metamagnetic wing [51].

The form of this phase diagram is captured by a very simple theory. The Landau

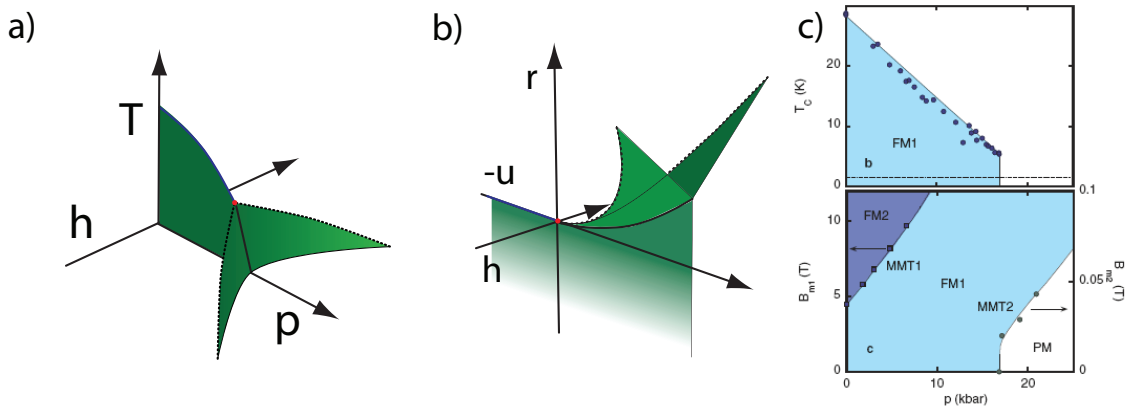


Fig. 2.3: Generic itinerant electron phase diagram: a) Sketch of the generic itinerant electron phase diagram as a function of temperature, field and another tuning parameter. b) The phase diagram for the Landau theory of the ferromagnet. The topology of the two diagrams is the same, one may be mapped onto the other by finding the expressions for r, u, v as a function of h, T and p . This can be compared with the experimental phase diagram for ZrZn_2 , shown in c). ZrZn_2 shows two metamagnetic transitions, labelled MMT1 and MMT2 in the bottom panel. These transitions are between paramagnetic (PM) and ferromagnetic (FM1) and then into a second ferromagnetic phase (FM2). At zero field only FM1 is present and the critical temperature of the continuous transition from PM to FM1 is shown in the top panel, this transition becomes first order at high pressure. This first-order transition extends at finite field as the metamagnetic transition MMT2. MMT1 occurs at far higher field and is present even at zero pressure. The transitions between paramagnet and M1 can be seen to have the same form as the generic phase diagram. Figure from [47].

theory for the ferromagnet is an expansion up to sixth order in the magnetisation. Since the energy cannot depend on the sign of the magnetisation due to time reversal symmetry only even terms are allowed in the expansion. The free energy therefore has the form

$$F = \frac{r}{2}\phi^2 + \frac{u}{4}\phi^4 + \frac{v}{6}\phi^6 - h\phi, \quad (2.1)$$

where ϕ is the order parameter, here magnetisation. This captures both the continuous and first-order transitions, reproducing the topology of the generic phase diagram. The expansion is valid around the continuous transition and at the tricritical point, but its accuracy decreases as the first order transition gets stronger. This theory will be discussed in more detail in section 4.1.3. We will also show how a particular microscopic theory can be used to map this phase diagram onto the microscopic parameters of the system, reproducing the generic phase diagram Fig.2.3a).

2.1.4 Quantum criticality

Quantum criticality occurs when a second-order phase transition takes place at zero temperature, driven by some non-thermal control parameter. The transition is not then due to thermal fluctuations as in the classical transition, but may be said to be due to ‘quantum fluctuations’. So called due to the analogy between quantum superposition and fluctuations in time, these quantum fluctuations actually measure how far the true quantum state of the system is from the classical groundstate which we expand about in calculations. At a finite-temperature critical point these quantum effects are overwhelmed by thermal effects, but as we approach zero temperature the quantum mechanics become increasingly important. Order parameter fluctuations have a characteristic frequency ω_c , when $\hbar\omega_c \gg k_B T$ the system behaves quantum mechanically. At the classical critical point the correlation time diverges, so the characteristic frequency goes to zero and the only temperature at which quantum mechanics is important is zero temperature. However near a quantum critical point, the only non-zero energy scale is provided by temperature so that $\omega_c \sim T$ (all other energy scales renormalise to zero). Near the quantum critical point then both quantum and classical effects have equal footing, statics and dynamics become intertwined and the properties of the system are radically altered. This region of novel behaviour extends over a surprisingly wide range of parameters and temperatures, as illustrated in figures 1.4 and 2.4. The identification of non-Fermi liquid behaviour in such regions has become the signature of quantum criticality.

The search for quantum critical points in itinerant systems has revealed that new phases are stabilized in their vicinity. This could be due to an existing instability being favoured as the energy scales of the system tend to zero at the quantum critical point, or quantum fluctuations mediating an entirely new phase. Superconductivity is commonly discovered around the quantum critical points of heavy fermion materials [5] and a new phase appears around the putative quantum critical endpoint of $\text{Sr}_3\text{Ru}_2\text{O}_7$ [52]. This thesis is concerned with the phase which appears in $\text{Sr}_3\text{Ru}_2\text{O}_7$. We do not invoke the quantum properties of the critical point, instead the reduction of energy scales allows the formation of a new phase of the normal Fermi liquid.

The question of how quantum criticality relates to the formation of phases is complicated. Bare itinerant ferromagnetic quantum critical points are never observed, there always seems to be a new phase intervening to mask the quantum critical point, or the continuous transition becomes first-order before reaching zero temperature. Recent developments to the theory of itinerant quantum criticality are

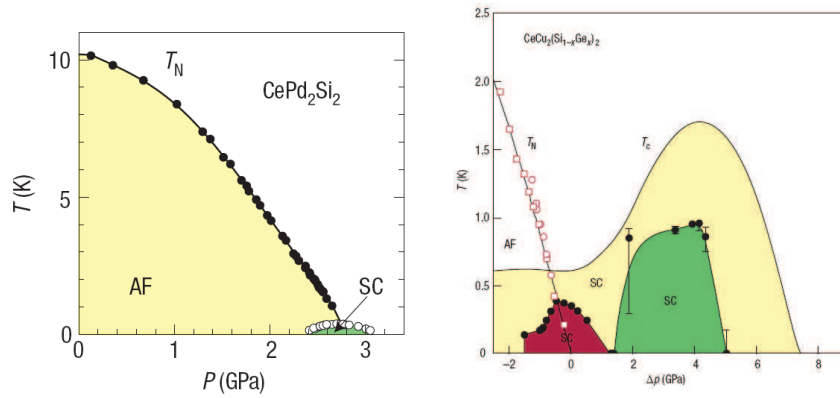


Fig. 2.4: Dome of superconductivity over quantum critical point: Dome of superconductivity over quantum critical point in CePd_2Si_2 (left) and $\text{CeCu}_2(\text{Si}_{1-x}\text{Ge}_x)_2$ (right). For the Néel temperature T_n the open circles (squares) of the right panel correspond to $x = 0.1$ ($x = 0.25$). For the superconducting transition temperature T_c the thin solid line (full circles) of the right panel corresponds to $x = 0$ ($x = 0.1$). Figures from [5].

putting this on firmer theoretical ground. The standard theory of itinerant quantum critical points, known as Hertz-Millis theory [37, 38], has recently been shown to be incomplete [39, 40]. The theory breaks down close to the quantum critical point that it was intended to describe. Extra terms have been shown to appear in the Hertz-Millis action which drive the continuous transition first-order and stabilize the presence of modulated phases [32, 39, 40].

Hertz-Millis theory is the standard description of itinerant quantum critical points. The Hertz-Millis action is typically studied in a Renormalisation Group analysis [53], as is classical criticality, or in a self-consistent renormalisation scheme [54]. It leads to the prediction of scaling laws relating the various parameters of the system in the critical region. These laws give critical exponents different from their classical counterparts, and depend on the dimension and nature of the ordering, not on the microscopic details of the system (see for example [55]).

Hertz-Millis theory is an extension of Ginzburg-Landau theory to include quantum dynamics. Underlying this is the assumption that the action can be expanded in powers of the order parameter and its gradients. This assumption turns out to be incorrect. Analysis of higher-order correction terms to the electron self-energy reveal that non-analytic terms in \mathbf{q} and T enter the action. These can alter the low-temperature phase diagram. By renormalising the quadratic and quartic coefficients of the free energy these can induce the transition to become first-order or for a modulated phase to appear as an intermediate phase in the transition.

We will not consider quantum fluctuations in the work that follows, adopting a

purely mean-field approach. The effects which we predict, although similar to those which may occur due to quantum fluctuations, are entirely due to the effect of the lattice. We will discuss the possible connection between these effects and those due to band effects which are considered in this thesis in section 8.2.1.

2.2 A simple approach: the Stoner model

The study of magnetism is complex. After a century of research employing advanced techniques and models we are left with many open questions. The problem of itinerant metamagnetism can however be addressed with some success in a simple approach. We will study a mean-field Stoner model that captures the metamagnetic phase diagram well when coupled with basic electronic band effects.

2.2.1 Mean-field theory

The simplest way to treat electron-electron interactions is to imagine that each electron moves in a field which is produced by the combined effect of all the other electrons. Thus the many-body problem is reduced to that of a single particle moving in a field, this field being the average effect of all the other electrons. This is known as mean-field theory and can be described by a Hamiltonian of the form

$$\begin{aligned} H &= \sum_{\mathbf{k},\sigma} \epsilon_{\mathbf{k}} n_{\mathbf{k},\sigma} - gm^2 - hm \\ &= \sum_{\mathbf{k},\sigma} (\epsilon_{\mathbf{k}} - \sigma(h + gm)) n_{\mathbf{k},\sigma}, \end{aligned} \quad (2.2)$$

where $\epsilon_{\mathbf{k}}$ is the electronic dispersion, $\sigma = \pm 1$ labels the different spins, $n_{\mathbf{k},\sigma}$ is the number of electrons with momentum \mathbf{k} and spin σ , g is the interaction energy, m the magnetisation and h the magnetic field. The first term of the first line is the non-interacting single-particle energy, the second term is the mean-field interaction and the final term is the Zeeman coupling. In the second line this has been re-written to emphasise how this interaction appears as an additional field. We have assumed the interaction energy is proportional to the magnetisation, which we will later justify.

The magnetism in this theory arises from the balance of the single particle kinetic energy with the interaction energy. It can be shown that this balance causes the system to magnetise when the electronic density of states is high enough. The condition for spontaneous magnetisation is known as the Stoner criterion and is $g\rho_{\text{F}} = 1$ where ρ_{F} is the density of states at the Fermi surface. The system therefore

magnetises if the density of states at the Fermi surface is high enough. If the Fermi energy can be tuned by some external parameter such that it moves through the peak in the density of states then the system will show a ferromagnetic phase when the Fermi surface is near to the peak.

2.2.2 Metamagnetism due to peaks in the density of states

Peaks in the density of states may give magnetism, but is there a generic reason for there being any peaks at all? The density of states is given by the integral over the Fermi surface of the inverse gradient of the dispersion.

$$\rho(\epsilon_{\mathbf{k}}) \propto \int_S dS \frac{1}{|\nabla \epsilon_{\mathbf{k}}|} \quad (2.3)$$

Therefore if the gradient is zero then there will be a singularity in the integrand. The feature that this produces in the density of states depends on the nature of the stationary point and the dimensionality of the system [56]. In one dimension maxima and minima in the dispersion produce an $\epsilon^{-\frac{1}{2}}$ divergence. In two dimensions a saddle-point in the dispersion leads to a logarithmic divergence of the density of states. In three dimensions saddle points produce a cusp rather than a divergence. We will consider the two dimensional case and note that all two dimensional dispersions must have saddle points due to the requirement that they be periodic ¹.

We now consider how the presence of these peaks can cause metamagnetism and not just ferromagnetism. If the Fermi surface begins slightly away from the peak, such that the Stoner criterion is not satisfied, then the system will be paramagnetic. If a magnetic field is applied then the spin-up and spin-down Fermi surfaces will be split, one of these being brought closer to the peak. It can be shown that there is a generalized form of the Stoner criterion for when the spin-species are split which is given by $1 = g(\rho_{\uparrow} + \rho_{\downarrow})$ where $\rho_{\uparrow(\downarrow)}$ is the density of states at the Fermi surface for up (down) spins. When one of the spin-species' Fermi surface gets close enough to the peak it is favourable for the system to increase its magnetisation. In other words, applying a field gives a metamagnetic transition.

The Stoner criterion predicts a second-order transition between the paramagnetic and ferromagnetic phase. If the peak in the density of states is sharp enough then it becomes energetically favourable for the Fermi surface to jump over the peak

¹ We can also have the situation where there is a maximum in the dispersion along one direction and a constant in the other - in this case the stationary point is quasi-1D and has the $\epsilon^{-\frac{1}{2}}$ form. This is the case when two quasi-1D dispersions are hybridised.

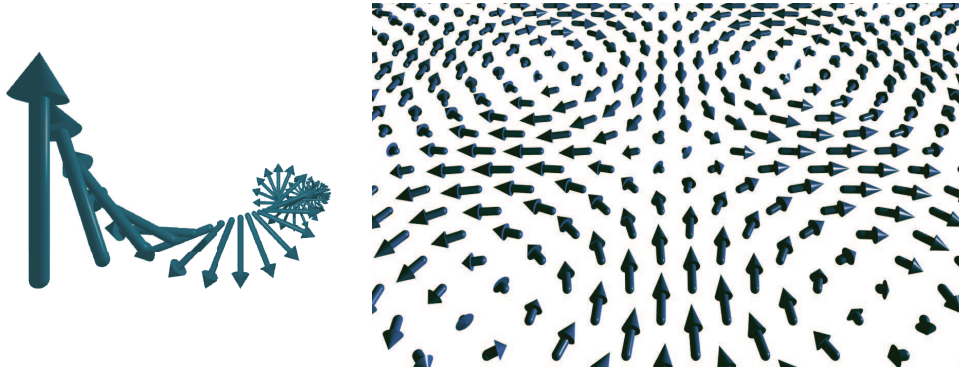


Fig. 2.5: **Spin texture:** Representation of a spin-spiral and a more complex spin-texture made by superimposing four such spirals.

discontinuously. This produces a first-order transition in the magnetisation. The condition for this to occur was derived by Wohlfarth and Rhodes [57] and is given by $\rho_F \rho_F'' > 3(\rho_F')^2$, where ρ_F' (ρ_F'') is the first (second) energy derivative of the density of states at the Fermi surface. This gives a first-order transition at low temperature. This extends as a metamagnetic wing when a magnetic field is applied.

The position of the Fermi surface, or equivalently the electron density, is the tuning parameter in this scheme. This reproduces the generic itinerant ferromagnet phase diagram (Fig.2.3a)). There is a region of ferromagnetism at zero field where the Fermi surface lies close to the peak in the density of states. Outside of this region there are metamagnetic transitions where the field tunes one Fermi surface to the peak. The phase diagram for this model will be calculated in chapter 4.

2.2.3 Spatially modulated magnetisation

It is not necessary for magnetisation to be spatially homogeneous. Both the magnitude and direction of the magnetic moment can vary in space. The formation of continuous modulations of the magnetism, so called spin-density waves, was first considered by Overhauser [58]. The simplest form of distortion is a spiral, but more complex forms may be made by superimposing several spirals. Adding two spirals travelling in opposite directions is a natural thing to do as in centrosymmetric systems both directions are degenerate. In this arrangement one component of the magnetisation cancels out and the spin-density wave becomes linear - a modulation of the magnitude, but not direction of the magnetisation. Superimposing more spirals leads to a 'spin crystal' as shown in Fig.2.5.

The spiral magnetic state is made by hybridising spin-up and -down electrons

with different momenta. This hybridisation is reflected in the Fermi surface of the spiral state which is distorted in a way which depends on the wavevector \mathbf{q} . The spin-up and -down Fermi surfaces are displaced by \mathbf{q} relative to each other and then hybridised to prevent crossings of the Fermi surfaces. This results in new quasiparticle dispersions in the spiral state. These dispersions will be examined in more detail in section 4.2.1. This anticrossing lowers the energy of states near the Fermi surface, or equivalently, produces a peak in the density of states below the Fermi surface. This peak favours magnetism in the same way as for homogeneous magnetisation by reducing the kinetic energy cost for a given magnetisation. Following the formation of the modulation the symmetry of the Fermi surface can be reduced. Should the modulation wavevector occur along one possible direction in the crystal lattice then the resulting Fermi surface will break the crystalline symmetry.

It was noticed that the geometry of the Fermi surface is important for the formation of modulation. If the Fermi surface after shifting by \mathbf{q} overlaps with the original Fermi surface then the distortion is more favourable. Fermi surfaces which have straight parallel sections are therefore highly susceptible to forming spin density waves. They are referred to as being ‘nested’.

A particular example of this is the nearest-neighbour tight-binding model. At half filling the Fermi surface is a square. By forming a modulation with $\mathbf{q} = (\pi, \pi)$ this becomes perfectly nested, the entire Fermi surface overlaps with itself. The whole Fermi surface is therefore gapped away and the system becomes a spin-density wave insulator.

One of the early successes of the Fermi surface nesting picture was the explanation of the properties of chromium [59]. The Fermi surface of chromium has electron and hole pockets which can overlap to form a nearly antiferromagnetic spin-density wave as shown in Fig.2.7.

2.3 Analogy with superconductivity

2.3.1 Analogy with homogeneous BCS superconductivity

There is an analogy to be drawn between magnetism and superconductivity. Because it is instructive to see the links between subjects, and because superconductivity is so well studied, this analogy will be elaborated here.

BCS superconductivity arises when electrons at the Fermi surface with opposite spin and momentum (\uparrow, \mathbf{k}_F and $\downarrow, -\mathbf{k}_F$) form Cooper pairs with zero total

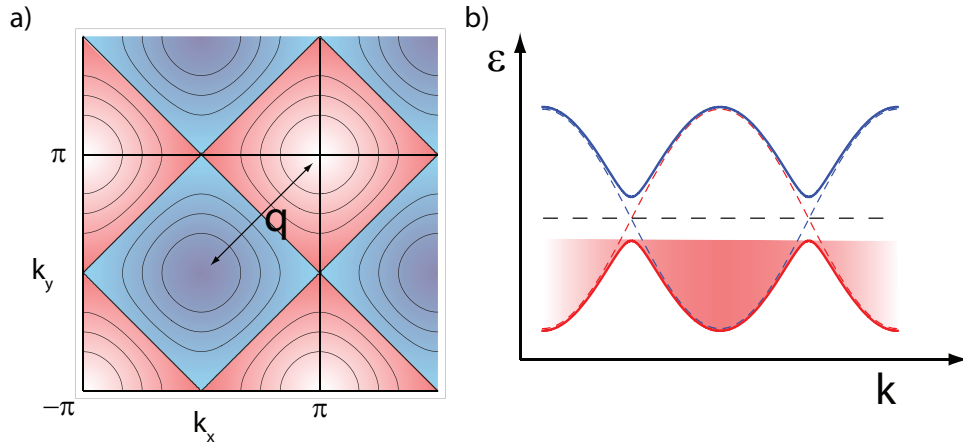


Fig. 2.6: Perfect nesting of the tight-binding model: a) At half filling the nearest-neighbour tight binding model has a square Fermi surface, shown here in blue. Shifting this by $\mathbf{q} = (\pi, \pi)$, shown in red, overlaps the original Fermi surface perfectly and fills the Brillouin zone. b) The distortion opens a gap at the Fermi surface. This is energetically favourable as the energy of states near the Fermi surface is lowered.

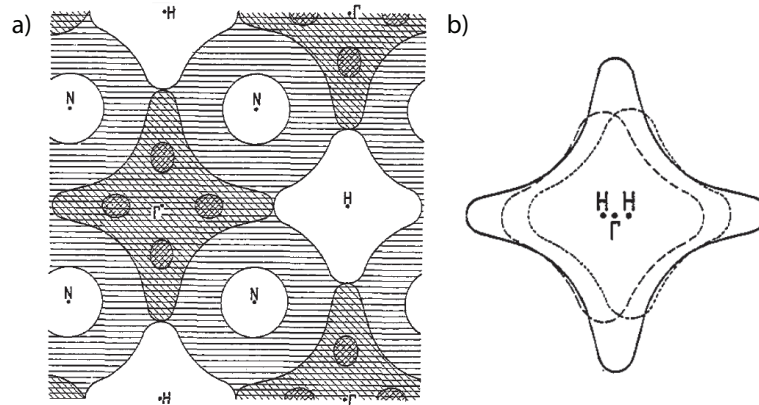


Fig. 2.7: Fermi surface nesting in chromium: a) A cut through the Fermi surface of chromium. There are similarly shaped electron and hole pockets at Γ and H which can nest to form a spin density wave. b) Fermi surface nesting forming almost antiferromagnetic spin density wave. Figures from [59].

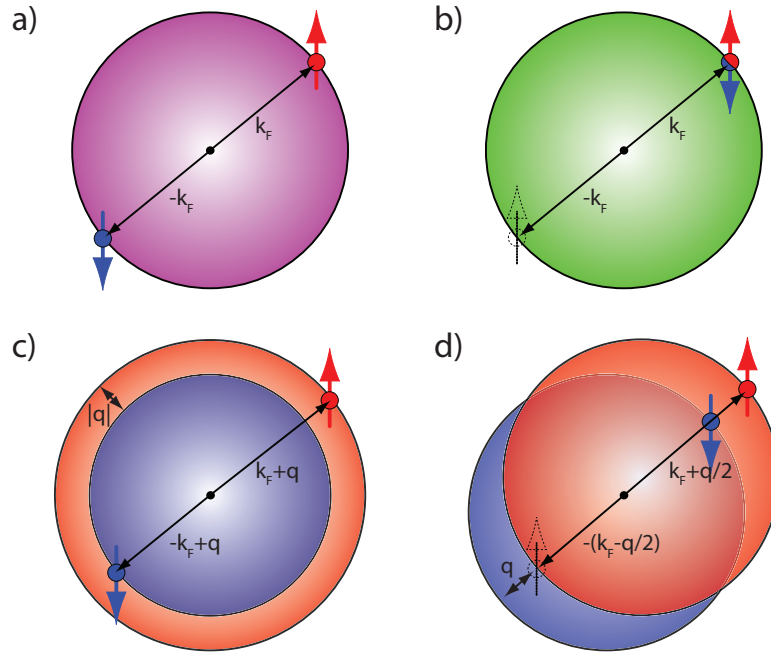


Fig. 2.8: Pairing analogy between superconductivity and magnetism: a) BCS superconductivity is the pairing of electrons across the Fermi surface. b) Stoner magnetism is the pairing of electrons and holes. c) FFLO superconductivity is the pairing of electrons with non-zero total momentum between spin-split Fermi surfaces. d) Modulated magnetism occurs when the up and down Fermi surfaces are displaced by q .

momentum(Fig.2.8a)). These Cooper pairs then condense. In doing this they take advantage of a condensation energy. This is revealed in the superconducting gap - the energy required to take electrons out of this condensed state. When magnetic field is applied the Zeeman energy favours splitting the Fermi surface so that the spin-up and -down electrons have different Fermi momenta. It is no longer possible to pair electrons with $\pm\mathbf{k}_F$. When the Zeeman energy gained by splitting matches the condensation energy which is lost then the pairing is destroyed and the system enters a magnetised normal state.

Cooper pairs form by pairing electrons with \uparrow, \mathbf{k}_F and $\downarrow, -\mathbf{k}_F$ to form a boson with zero total momentum. In the BCS mean-field theory this corresponds to the particle-particle correlator $\langle c_{\mathbf{k}_F, \uparrow}^\dagger c_{-\mathbf{k}_F, \downarrow}^\dagger \rangle$ acquiring a non-zero value. Itinerant magnetism can be thought of as pairing between electrons with \mathbf{k}_F and holes with the same momentum and spin - by promoting an electron from the Fermi surface and flipping its spin. This is encoded in the correlator which acquires non-zero value in the magnetic state, $\langle c_{\mathbf{k}, \uparrow}^\dagger c_{\mathbf{k}, \uparrow} \rangle - \langle c_{\mathbf{k}, \downarrow}^\dagger c_{\mathbf{k}, \downarrow} \rangle$.

This is nothing but the magnetisation - the order parameter in the ferromagnet.

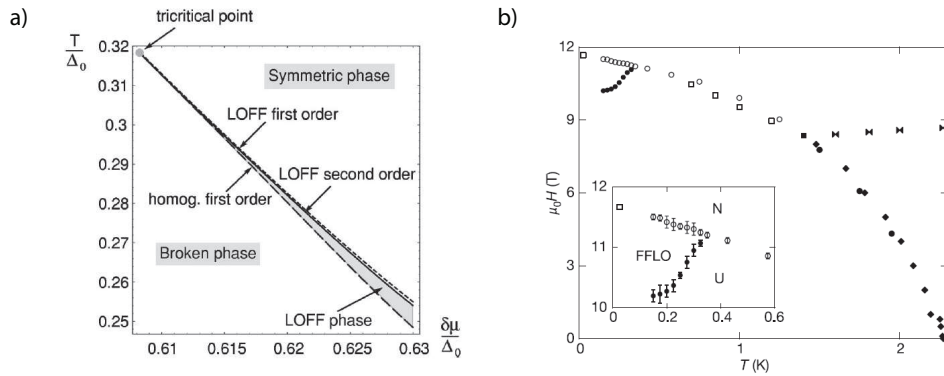


Fig. 2.9: **Phase diagram of the FFLO state:** a) Theoretical. Figure from [60]. b) Possible experimental realization in CeCoIn₅. Figure from [61].

This is defined as the difference between the number of up-spin and down-spin electrons.

$$m = \sum_{\sigma, \mathbf{k}} \sigma n_{\text{F}}(\epsilon_{\mathbf{k}} - \mu_{\sigma}) = \sum_{\sigma, \mathbf{k}} \sigma n_{\text{F}}(\epsilon_{\mathbf{k}} - \sigma(h + gm) - \mu), \quad (2.4)$$

where $n_{\text{F}}(\epsilon - \mu)$ is the Fermi-Dirac distribution, μ_{σ} is the effective chemical potential for the two spin species and $\sigma = \pm 1$, h is the magnetic field and μ is the chemical potential in the absence of magnetism or field. This equation has been written in two different ways, to emphasise the idea of each spin-species having a different effective chemical potential, and the fact that this is a self-consistent equation for m , since the magnetisation determines the mean-field.

Likewise there is a self-consistency equation for the superconducting order parameter Δ . It is called the gap equation and has the form

$$\Delta_{\mathbf{k}} = \sum_{\mathbf{k}'} (1 - 2f_{\mathbf{k}'}) \frac{\Delta_{\mathbf{k}'}}{2E_{\mathbf{k}'}} V_{\mathbf{k}'\mathbf{k}}, \quad (2.5)$$

where $V_{\mathbf{k}'\mathbf{k}}$ is the interaction and $E_{\mathbf{k}'}$ is the energy of particles in the superconductor.

Thus magnetism can be thought of as the analogue of superconductivity in the particle-hole rather than particle-particle channel.

2.3.2 Analogy with modulated FFLO superconductivity

Just as Stoner magnetism is analogous to BCS superconductivity, so the spin-density wave is analogous to spatially modulated superconductivity. In 1964 Fulde and Ferrell [27], and independently Larkin and Ovchinnikov [28], considered a case where modulated superconductivity appears due to the application of a magnetic field.

Fulde, Ferrell, Larkin and Ovchinnikov realised that in a window of magnetic field before the condensate is destroyed by Zeeman splitting it is energetically favourable to form a spatially modulated superconductivity. Electrons from the spin-split Fermi surfaces can be paired resulting in an object with non-zero total momentum, taking advantage both of Zeeman energy and some condensation energy. This is illustrated in figure 2.8, with the phase diagram for the FFLO state shown in Fig. 2.9. The transition from superconducting to normal state is split, with the system entering a spatially modulated superconducting phase as an intermediate state. The superconducting gap becomes spatially varying, $\Delta(\mathbf{r}) = \sum_n \Delta_n e^{i\mathbf{q}_n \cdot \mathbf{r}}$, the simplest analysis is to assume a single wavevector $\Delta(\mathbf{r}) = \Delta e^{i\mathbf{q} \cdot \mathbf{r}}$, which is the approach of Fulde and Ferrell. We will follow in this spirit by considering a magnetisation with a single wavevector - a spin spiral $\mathbf{m}(\mathbf{r}) = (m_\perp \cos \mathbf{q} \cdot \mathbf{r}, m_\perp \sin \mathbf{q} \cdot \mathbf{r}, m_\parallel)$.

Although it has yet to be unambiguously observed, the FFLO state has been the focus of much interest, both in the superconductors where it was postulated and in other situations such as cold atomic gases [62] and colour superconductivity in quark physics [60]. The most likely evidence for the existence of FFLO is in CeCoIn₅ [63], although this is still disputed.

3. A TOPICAL EXAMPLE: $\text{Sr}_3\text{Ru}_2\text{O}_7$

There has been a great deal of recent interest in the material $\text{Sr}_3\text{Ru}_2\text{O}_7$. A large number of experiments [26, 45, 51, 52, 64–68] have revealed extremely interesting physical phenomena. These have in turn motivated a wide range of theoretical investigations [69–73]. Research into the material was originally focussed on quantum criticality, but studies into ultra-pure samples revealed a new and unusual phase where the electronic liquid breaks the symmetry of the lattice [26, 52]. Recent studies have concentrated on this phase and a number of proposals have been made for its nature [42, 52, 72, 73]. In this thesis it is proposed that the anomalous phase is a spatially modulated magnetic phase and we extend a Stoner description of metamagnetism to include this phase. We will briefly discuss the alternative proposals in chapter 7.

In this chapter the experimental results which are relevant to this proposal are presented. Since our approach is to address broad issues before focussing on details we will begin by describing the discussion of the phase diagram and properties of the anomalous phase. We will then go on to discuss the crystal structure and Fermi surface details.

3.1 *Main experimental results: magnetic phase diagram*

The magnetic phase diagram of $\text{Sr}_3\text{Ru}_2\text{O}_7$ is dominated by a metamagnetic transition (Fig.3.1). A peak in the imaginary part of the susceptibility shows that the transition is first order below a critical point. The critical field and temperature of the transition can be tuned by varying the angle of the applied field with respect to the crystalline axes (the material is layered with planes labelled ab and the perpendicular axis c , details of the crystal structure will be considered shortly). With the field in the ab plane the critical field of this transition is at 5.1T ¹ with a critical

¹ The critical field also depends on the angle *within* the ab plane, it is 5.1T with the field along [100] and 5.4T with the field along [110] [74]. These details are not fully explored but will be briefly considered in section 6.4.1.

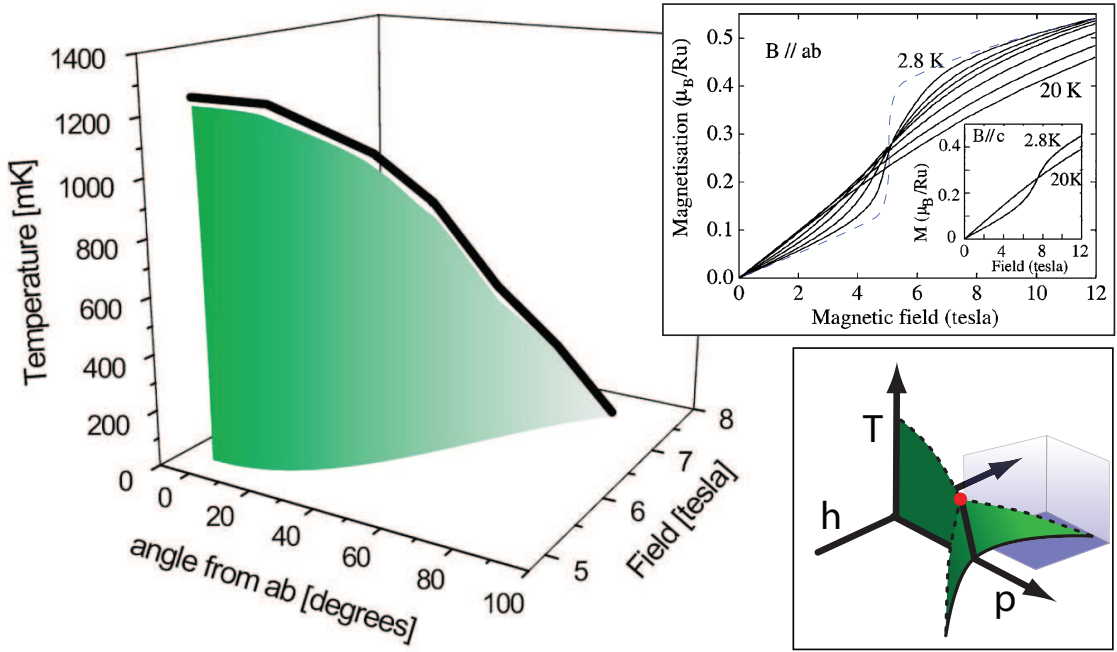


Fig. 3.1: Phase diagram of $\text{Sr}_3\text{Ru}_2\text{O}_7$ with quantum critical endpoint: Initial studies of $\text{Sr}_3\text{Ru}_2\text{O}_7$ revealed a metamagnetic transition, the critical endpoint of which could be tuned by varying the angle of the applied magnetic field with respect to the crystalline c -axis. This could be suppressed to a quantum critical endpoint with the field along the c -axis. Figure from [66]. The inset shows magnetisation curves approaching the metamagnetic transition. In blue we have superimposed schematically the ideal metamagnetic transition. Figure from [65]. Also shown is the generic itinerant electron phase diagram. The phase diagram of $\text{Sr}_3\text{Ru}_2\text{O}_7$ is considered to be section from this, indicated by the shaded region.

temperature of 1.25K. With the field rotated into the c direction the critical field is 7.8T and the critical temperature is reduced below the experimental limit of 50mK. This metamagnetic wing can be considered to be a segment of the generic itinerant electron phase diagram shown in Fig.2.3, where the tricritical point lies outside of the region accessible at ambient pressure.

In early samples the critical endpoint can be suppressed all the way to zero temperature. Since the critical endpoint is a second order phase transition then this forms a quantum critical endpoint. This was the first example of such a critical point and an example of an apparently ‘bare’ quantum critical point. The resistivity in the region of the phase diagram above the quantum critical endpoint shows the non-Fermi liquid behaviour expected from quantum criticality. This is shown in Fig.3.2 where the resistivity goes as T rather than the T^2 over much of the phase diagram.

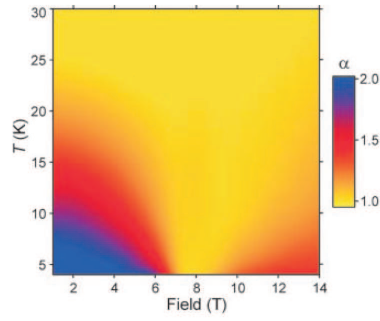


Fig. 3.2: Resistivity exponent: The exponent α from the expression for resistivity $\rho = \rho_{res} + AT^\alpha$, as derived from the logarithmic derivative of resistivity with respect to temperature. Blue indicates the quadratic dependence expected from Fermi liquid theory. Magnetic field along c -axis. Figure from [51].

The development of ultra-pure samples revealed that there was even more complexity in the physics of $Sr_3Ru_2O_7$. In these samples it was discovered that the system never actually reaches the quantum critical endpoint. Instead, upon approaching the c -axis the metamagnetic transition bifurcates to enclose an unusual phase as shown in Fig.3.3. The critical temperature of the transition begins to increase again as the field is aligned with the c -axis. In addition a second, smaller wing appears above the critical field of the main transition. As the field angle is tuned away from c -axis this wing approaches the main transition and disappears. In between these metamagnetic transitions there is a region which appears to be a new phase. The majority of theories proposed for this phase do not involve the properties of the quantum critical endpoint and this work will not consider the effect of quantum fluctuations.

A cut through the phase diagram with the field along the c -axis is shown in Fig.3.3. The first order transitions form ‘horns’ which curve away from each other slightly. Each corresponds to a jump in magnetisation. These transitions end at critical endpoints. Connecting the two critical endpoints is a ‘roof’ which is seen in a variety of experimental probes, though its exact nature is hard to identify. This is consistent with there being a distinct thermodynamic phase between the first-order horns with a second-order phase transition, the roof, bounding it for high temperatures ($\sim 1K$).

The distinguishing feature of this phase is the resistivity. This is unusually high - a factor of two greater than outside the phase, and more remarkably, it is anisotropic. The value of the resistivity is different when measured along the axis most nearly parallel or perpendicular to the in-plane field component. Furthermore,

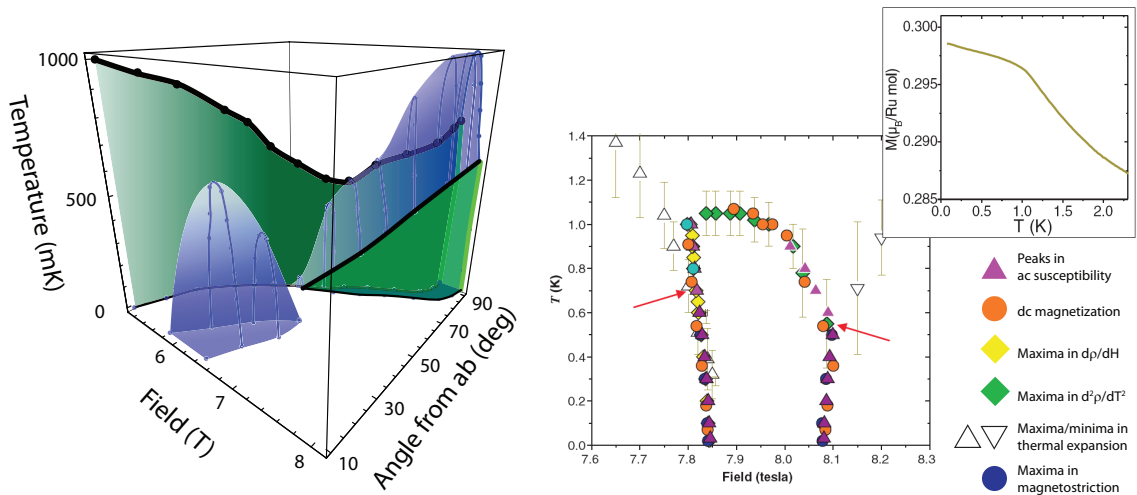


Fig. 3.3: Magnetic phase diagram of ultra-pure $\text{Sr}_3\text{Ru}_2\text{O}_7$: The phase diagram of ultra-pure $\text{Sr}_3\text{Ru}_2\text{O}_7$ shows a bifurcation of the metamagnetic transition with the wings corraling an anomalous phase. On the left is the phase diagram as a function of field strength, field angle and temperature. The metamagnetic transitions are shown in green while the anomalous phase is in blue. This phase diagram is extracted from resistivity and susceptibility data. Figure from [72]. On the right is a cut through the phase diagram at c -axis derived from a variety of experimental probes as indicated. The arrows indicate the critical endpoints of the two metamagnetic transitions. The region enclosed by these two transitions and the curved ‘roof’ is the anomalous phase. The inset shows magnetization as a function of temperature at 7.9T. Figures from [52].

the temperature dependence of the resistivity in this phase is anomalous. The properties of this phase will be discussed in more detail in the following section.

There is a second region in the phase diagram which shows the same anomalous properties. This appears when the field is aligned with the ab -plane at $\sim 6T$. This can be seen in Fig.3.3. It is associated with a second metamagnetic transition which is not shown in the figure. This phase will probably be explained by the same mechanism as the first transition and phase, but we will not consider it explicitly.

3.2 Properties of the anomalous phase

3.2.1 Resistivity

The primary indicator of the anomalous phase is the magnetoresistivity. With the field along c the resistivity in the phase is approximately twice that outside the phase. In this orientation the resistivity components along the a and b axis are the same. As soon as the field is tilted away from the c -axis the two components become inequivalent. One of these axes becomes ‘easy’ and the resistivity quickly

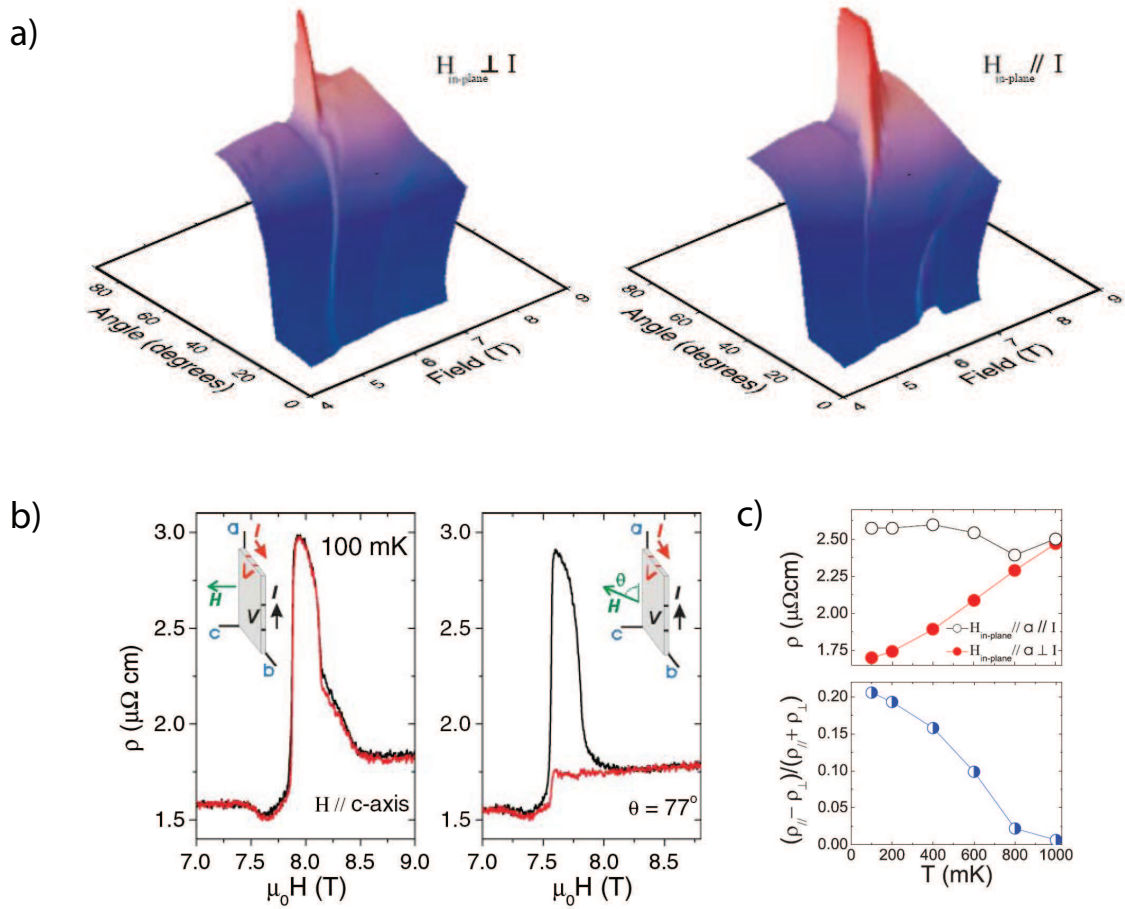


Fig. 3.4: Resistivity anisotropy in the anomalous phase of $\text{Sr}_3\text{Ru}_2\text{O}_7$: a) The magnetoresistivity of $\text{Sr}_3\text{Ru}_2\text{O}_7$ as a function of field strength and angle at a temperature of 100mK. On the left is ρ_{aa} and on the right ρ_{bb} , the components of resistivity along the in-plane crystal axes. b) The difference between the resistivity components with the field parallel to the c -axis and at 13° from c (black line ρ_{aa} , red line ρ_{bb}). c) The temperature dependence of the resistivity and the anisotropy. Figures from [26].

drops to the surrounding level with angle, the other component continues to be anomalously large. The choice of which axis remains the ‘hard’ axis is determined by the in-plane orientation of the field. The axis that is most nearly parallel to the field becomes hard and the one most nearly perpendicular becomes easy. This anisotropy is confined to the anomalous phase, transport outside of this region is the same along each in-plane crystal axis. This is shown in Fig.3.4

As well as being anisotropic the temperature dependence of resistivity in the phase is anomalous. Along the easy direction it shows standard metallic behaviour but along the hard direction it is non-metallic. Plotting the size of the anisotropy shows that it behaves like the order parameter in a second-order transition, going

continuously to zero at the roof of the phase.

Neutron scattering reveals that there is no distortion of the crystal lattice inside the phase, within an accuracy of $4 \times 10^{-5} \text{ \AA}$ [26]. This means that the anisotropy is not caused by a structural transition.

Experimental evidence therefore points to a phase in which the electronic fluid spontaneously breaks the symmetry of the lattice, resulting in the bifurcation of the metamagnetic transition.

3.2.2 Quantum oscillations in the anomalous phase

Having considered the magnetic phase diagram of $Sr_3Ru_2O_7$ and the striking transport properties of its anomalous phase we turn to recent experimental studies which attempt to reveal the nature of the phase.

An extensive dHvA study of $Sr_3Ru_2O_7$ has been performed [75], yielding important information about the metamagnetism and anomalous phase. dHvA oscillations have been observed in the anomalous phase [68]. These follow the standard Lifshitz-Kosevich temperature dependence. This strongly suggests that at least a component of the anomalous phase is a normal Fermi liquid, though additional non-Fermi liquid degrees of freedom cannot be ruled out. The frequency of the dHvA oscillations seen in the anomalous phase can be related to that of some of the sheets observed outside of the phase. This shows that at least some of the normal state Fermi surface remains inside the anomalous phase.

One of the possible phenomena in the anomalous phase is the formation of domains of some sort. Since dHvA is dependent on real-space cyclotron orbits, scattering from impurities or domain walls reduces the amplitude of the signal. Analysis of the oscillations in the anomalous phase indicates an estimated average domain size of order 500nm.

3.2.3 Thermodynamics

Magnetocaloric measurements [74] reveal that the entropy inside the phase is higher than that outside, Fig.3.5. This is consistent with the first-order boundaries of the phase, which curve outwards. The Clausius-Clapeyron relation links the curvature of the transition in the H, T plane with the change in entropy and magnetisation across the transition

$$\mu_0 \frac{dH_c}{dT} = - \frac{\Delta S}{\Delta M}. \quad (3.1)$$

Thus since the low field transition has $\frac{dH_c}{dT} < 0$ and $\Delta M > 0$ then the entropy change must be positive. At the high field transition the sign of curvature is reversed and the magnetisation once again increases, so the entropy drops upon leaving the phase. This result is counter-intuitive as the expectation from an ordered phase would be a lower entropy. This is one of the major experimental facts which theories of the anomalous phase have yet to successfully address.

Measurements within the phase show that the specific heat has a $-T^2$ correction to Fermi liquid behaviour at low temperatures. In addition signatures of the ‘roof’ in the phase diagram at c -axis show that it is consistent with a second order phase transition. There is no latent heat associated with this transition, but there is a change in the field derivative of the entropy, indicating that there is a non-analyticity in the second derivative of the free energy.

3.3 Crystal structure

Having examined the magnetic phase diagram of $\text{Sr}_3\text{Ru}_2\text{O}_7$ and the evidence regarding the nature of its anomalous phase we will consider the crystal structure of the material.

$\text{Sr}_3\text{Ru}_2\text{O}_7$ is a member of the Ruddlesden-Popper series of layered perovskite ruthenates. These have the chemical formula $\text{Sr}_{n+1}\text{Ru}_n\text{O}_{3n+1}$ and are distinguished by the systematic addition of ruthenium oxide layers. Each layer consists of oxygen octahedra arranged around ruthenium sites. These groups of layers are separated by strontium. This structure is shown in Fig.3.6.

$\text{Sr}_3\text{Ru}_2\text{O}_7$ is the bilayer member of the family. It is quasi-two dimensional, with electron hopping between the layers much less than within the layers. This can be seen in transport measurements where the out of plane resistivity is ~ 300 times greater than the in-plane resistivity at 0.3K [45]. This two dimensionality is supported by the distinctive angular dependence of dHvA measurements in both Sr_2RuO_4 and $\text{Sr}_3\text{Ru}_2\text{O}_7$ [75, 76]². This quasi-two dimensional nature will be important for the theoretical analysis presented here, as we will conduct all calculations with 2D band structures and associated density of states features.

The structure of $\text{Sr}_3\text{Ru}_2\text{O}_7$ is further complicated by a structural distortion in the planes. The ruthenium oxide octahedra are found to rotate by $\sim 7^\circ$ as shown

² In $\text{Sr}_3\text{Ru}_2\text{O}_7$ the angular dependence of dHvA only reflects two dimensionality on the low-field side of the metamagnetic transition. On the high-field side of the transition the angular dependence is complex and not fully understood [75].

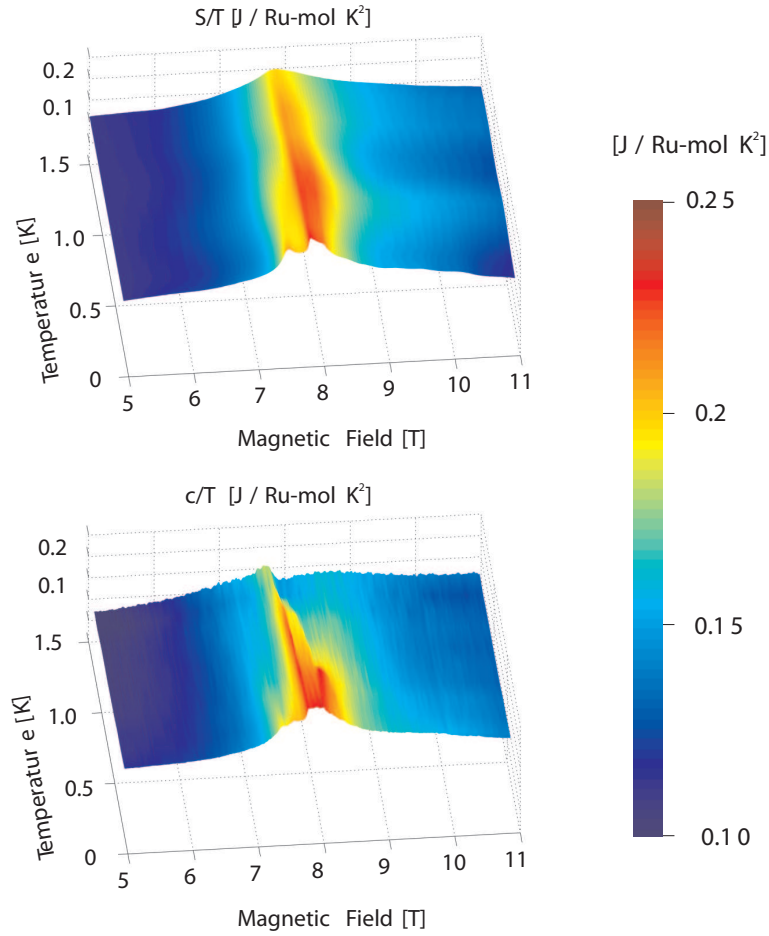


Fig. 3.5: Experimental measurements of entropy and specific heat of $\text{Sr}_3\text{Ru}_2\text{O}_7$: Experimental measurements of the entropy and specific heat for a cut through the phase diagram with field along the c -axis. This shows the anomalous phase and surrounding normal phase. In chapter 6 we will compare this to calculations of the thermodynamic properties of the Stoner model with a peak in the density of states. Figure from [74].

in Fig.3.6 [64]. This doubles the size of the unit cell, resulting in a reconstruction of the Brillouin zone which has profound consequences on the band structure. This rotation means that the crystal structure no longer strictly has fourfold rotational symmetry. The a and b parameters remain approximately, but not exactly, equal after this rotation [77]. Strictly the two in-plane axes are inequivalent. However, properties in the normal phase do not distinguish between the axes, and the ability to pin the anisotropy of the phase by field, rather than it being locked along one particular axis, means that the anomalous phase can not simply be explained by this distortion. From now on we will assume that the electronic structure of $\text{Sr}_3\text{Ru}_2\text{O}_7$ has fourfold rotational symmetry which is a reasonable simplification in this case.

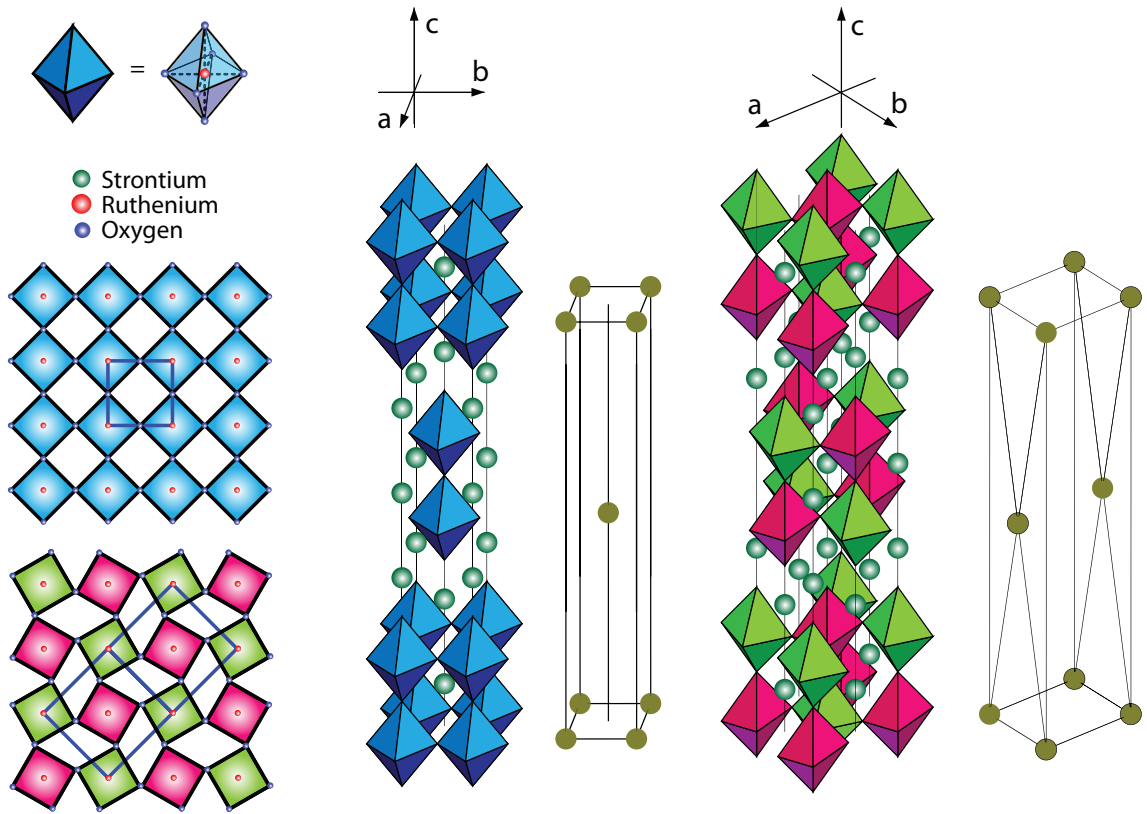


Fig. 3.6: Crystal structure: The left hand figure shows the rotation of ruthenium oxide octahedra in the ab plane. Neighbouring octahedra counter-rotate by $\sim 7^\circ$ resulting in a rotation of the unit cell with a side $\sqrt{2}$ larger than the original, as shown by the dark blue squares (the rotation is exaggerated for clarity in the diagram). On the right the three dimensional structure is shown before and after rotation. Figure adapted from [75].

3.4 Fermi surface

Understanding the properties of $\text{Sr}_3\text{Ru}_2\text{O}_7$ depends on a knowledge of the Fermi surface. The Fermi surface of $\text{Sr}_3\text{Ru}_2\text{O}_7$ may be obtained by simple arguments based on the crystal structure. Such arguments become important when trying to devise a simple, but still realistic band-structure for calculations. Here these arguments will be explained and the results compared with density functional theory (DFT) and angle-resolved photoemission spectroscopy (ARPES) results.

3.4.1 Construction of Fermi surface from simple arguments

The Fermi surface of $\text{Sr}_3\text{Ru}_2\text{O}_7$ may be built up by considering the structure one layer of complexity at a time. First the single RuO layer is considered. The effects of bringing two of these layers together into a bilayer is then incorporated. Finally the

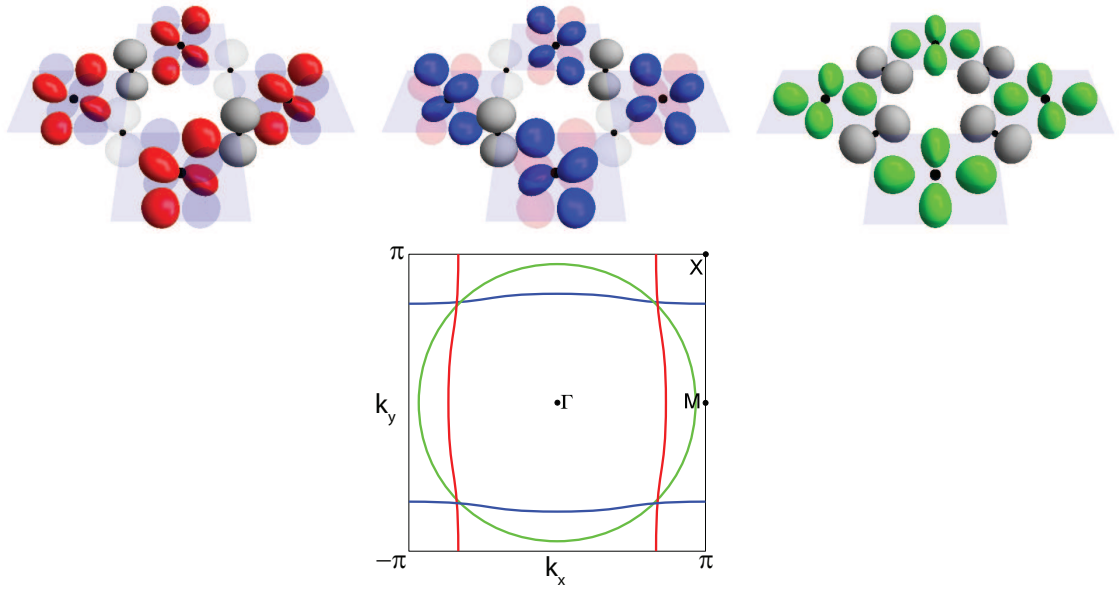


Fig. 3.7: Orbitals in a single RuO layer: Ruthenium d_{zx} (d_{yz}) orbitals, shown in red (blue), form bonds via the oxygen p_z orbitals shown in grey. This strongly directional hybridization forms quasi one-dimensional bands, shown in red (blue) in the lower panel. The ruthenium d_{xy} orbitals (green) hybridise equally in both directions via the oxygen p_x and p_y orbitals (grey) to form a quasi two-dimensional band, shown in green. Light blue shading indicates the RuO octahedra. The resulting Fermi surface is shown.

effect of the rotation of octahedra is taken into account by backfolding the Fermi surface. By these hand-waving arguments an understanding of the structure and orbital nature of this complex Fermi surface is built up.

The electronic states at the Fermi surface are made up from ruthenium d -orbitals. Considering a single layer the d_{zx} orbitals hybridize strongly via the oxygen p orbitals along the x direction, and only weakly in y . The d_{yz} orbitals do the same along the opposite directions. This results in two quasi one-dimensional bands running along the two axes of the Brillouin zone. The d_{xy} orbitals hybridize in all directions equally, resulting in a quasi two-dimensional band giving an almost circular Fermi surface as shown in Fig.3.7 and Fig.3.8a).

These one-dimensional bands then hybridise with each other. The anticrossing where the bands are degenerate causes the Fermi surface to reconstruct. The resulting Fermi surface is that of the monolayer member of the family, Sr_2RuO_4 . It consists of three bands, labelled α , β and γ as shown in Fig.3.8 b). Next the effects of the bilayer are taken into account. Interactions between the layers break their degeneracy resulting in bilayer splitting of the Fermi surface seen in panel c) of 3.8. Finally the rotation of the RuO octahedra is accounted for. This causes the

Brillouin zone to halve and rotate by 45° , the bands are then ‘backfolded’ into the reduced zone as shown in panel e) of Fig.3.8. The Fermi surface for this bilayer with rotation is obtained by anticrossing these bands. In this complex arrangement there are many possible outcomes and it is not *a priori* clear which will occur. Based upon the experimental evidence discussed in the next section the reconnection which occurs is shown in panel f). This argument, though by no means rigorous, gives good agreement with ARPES and DFT results. It will form the basis of later attempts to produce a realistic band structure for calculations in section 6.4.1.

3.4.2 Measured Fermi surface

Angle resolved photoemission spectroscopy (ARPES) allows the direct measurement of the zero-field Fermi surface through measurement of the momentum of photoelectrons emitted from the surface [67]. ARPES measurements of $\text{Sr}_3\text{Ru}_2\text{O}_7$ identified six bands as shown in Fig.3.9, these are named, based on their origin in the Fermi surface of Sr_2RuO_4 , α_1 , α_2 , β , γ_1 , γ_2 and δ . Within the resolution of ARPES it is impossible to tell if the γ_2 band crosses Fermi surface or not. Comparison with magnetocaloric measurements [74] and comparison of the measured total specific heat with that derived from dHvA quasiparticle masses [67, 75] suggest that this band does cross the Fermi surface. Density functional theory calculations including spin-orbit coupling give a reasonable match to the ARPES results. The δ pocket does not appear in our previous discussion of the Fermi surface. DFT indicates that this originates from the ruthenium $d_{x^2-y^2}$ orbitals which are unoccupied in the single-layer case.

3.4.3 Correspondence of quantum oscillation results

Quantum oscillation experiments provide a measurement of the Fermi surface in the bulk of the material. De Haas-van Alphen has confirmed the quasi two-dimensional nature of the Fermi surface and can identify the area of the Fermi surface pockets and the effective masses of the electrons at the Fermi surface [67, 68, 75]. These are generally in good agreement with the ARPES results though dHvA has difficulty seeing the γ_2 pocket due to its extremely small area. Quantum oscillations are however visible in other physical quantities, and magnetothermal oscillations have been observed [74]. The sensitivity of this technique is complementary to dHvA and in fact best identifies the small pockets. The γ_2 pocket was definitely observed in these magnetothermal measurements [74].

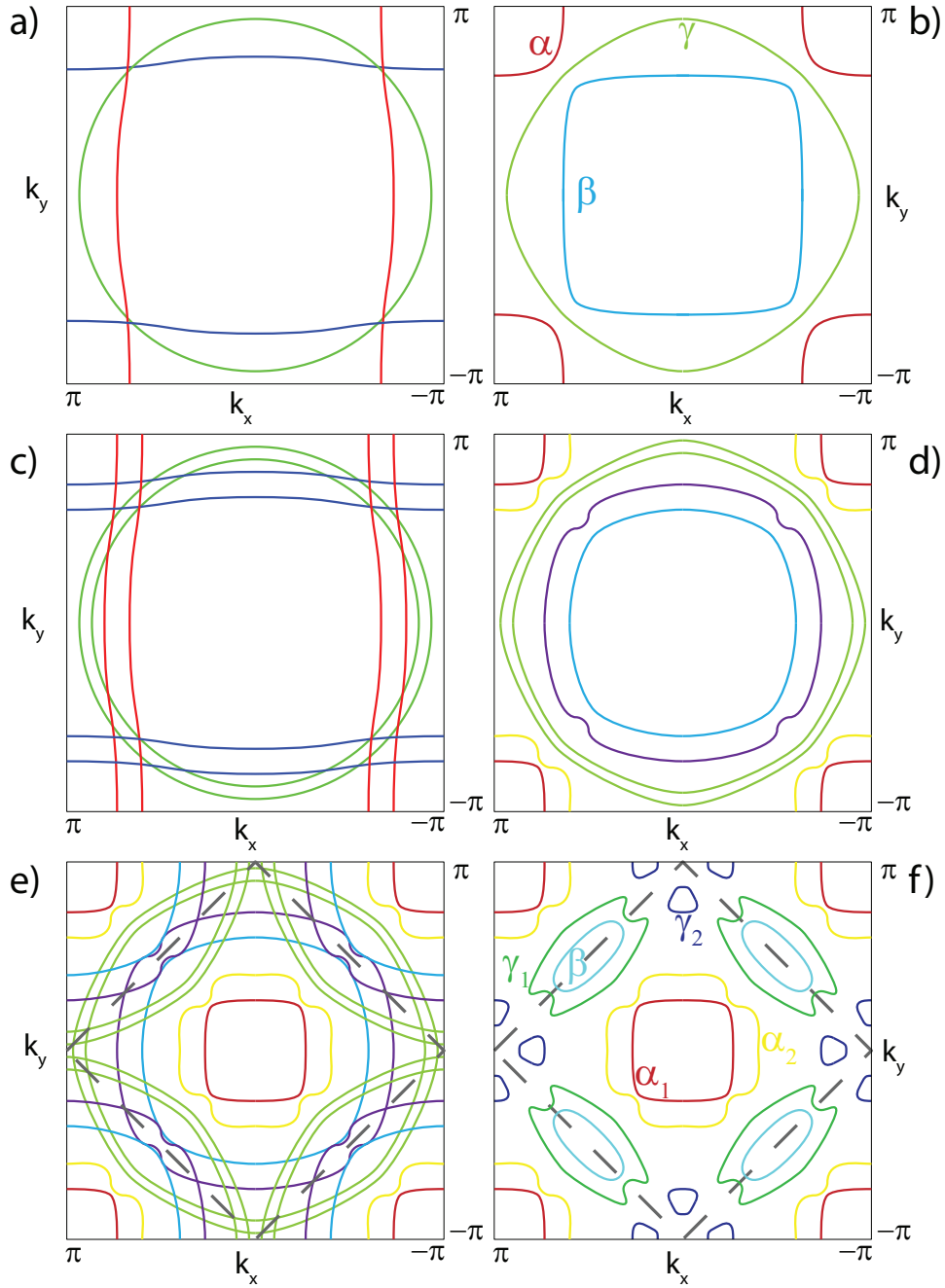


Fig. 3.8: Construction of the Fermi surface via basic arguments: The Fermi surface of $\text{Sr}_3\text{Ru}_2\text{O}_7$ is shown to be built up from the Fermi surface of the single-layer compound Sr_2RuO_4 . a) Unhybridised bands from the single-layer compound. b) Hybridised single-layer bands form the Fermi surface of Sr_2RuO_4 . c) Bilayer splitting of the single-layer bands. d) Hybridization of bilayer bands. This would be the Fermi surface of $\text{Sr}_3\text{Ru}_2\text{O}_7$ if there were no rotation of the RuO octahedra. e) Backfolding the bilayer Fermi surface into the reduced zone, to account for the rotation. The dashed line represents the reduced Brillouin zone. f) The Fermi surface of $\text{Sr}_3\text{Ru}_2\text{O}_7$ with anticrossings chosen to reproduce the experimentally determined Fermi surface. Figure from [75].

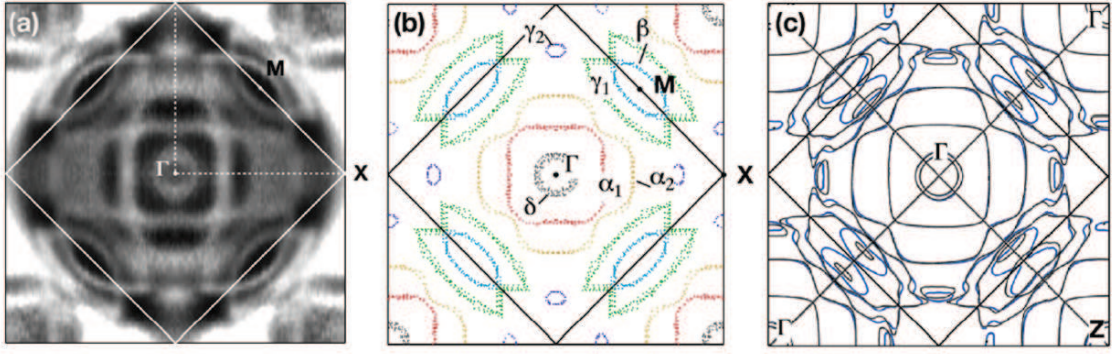


Fig. 3.9: Fermi surface from ARPES: a) Experimental data. b) Fermi surface contours extracted from data shown in a). c) Fermi surface from DFT calculation. Figure from [67].

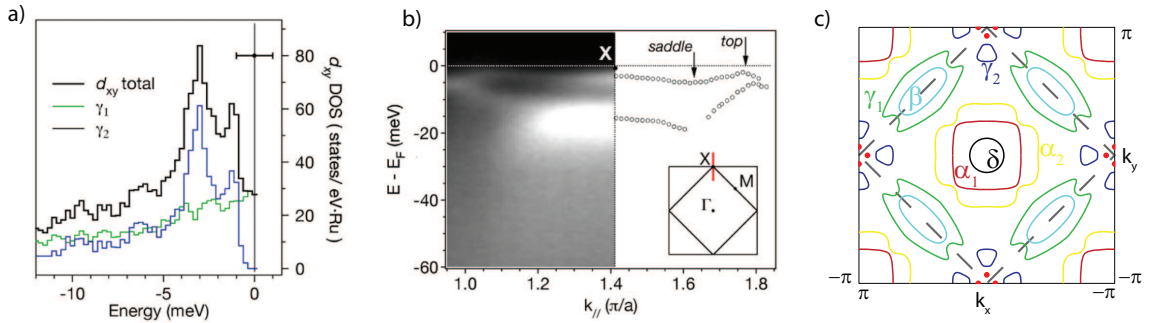


Fig. 3.10: Density of States: a) Histogram of states near the Fermi surface from ARPES measurements. In blue is the γ_2 band which shows two peaks. Also shown is the γ_1 band which has no such features. The vertical line represents the Fermi surface with an error bar representing the uncertainty in its position. Quantum oscillation experiments show that the γ_2 band must in fact cross the Fermi surface. Figure from [67]. b) Dispersion of the γ_2 band showing the saddle point and band top. Figure from [67]. c) Red dots indicate the location of the saddle points in the band structure. Figure adapted from [75]

3.4.4 Reconciling the phase diagram and the Fermi surface

In an itinerant system the simplest mechanism which produces metamagnetism is a peak in the electronic density of states. As previously discussed in section 2.2.2 this makes it favourable for a magnetic transition to occur when the Fermi surface is Zeeman split such that one spin-species' Fermi surface approaches the peak. This model gives a qualitative fit to the phase diagram of $\text{Sr}_3\text{Ru}_2\text{O}_7$. The natural cause of a peak in the density of states is a saddle-point in the electronic dispersion [56].

ARPES measurements do indeed show a peak in the density of states just below the Fermi surface, shown in Fig.3.10. The γ_2 band shows two peaks in its density of states. A large peak corresponding to a saddle point and a smaller peak corresponding to the top of the band. This large peak is $\sim 3\text{meV}$ below the Fermi surface.

This puts it slightly far from the Fermi surface to correspond to the metamagnetic transition at 8T, but we must bear in mind the uncertainty in the position of the Fermi surface in ARPES and uncertainty in the relation of field to energy in such a complex material where the coupling of the field to the Fermi surface depends on microscopic details which are not fully understood.

None of the bands visible in dHvA can be seen to have an enhancement of the quasiparticle mass near to the metamagnetic transition compared to the zero field value [75]. This indicates that the metamagnetism is due to the γ_2 band in which the mass enhancement is irresolvable. This supports a picture where one band goes through a metamagnetic transition as a result of a peak in the density of states and suggests that a single-band approach will be sufficient to explain the main features of $Sr_3Ru_2O_7$ despite its complex band structure.

Specific heat measurements have been made as a function of field strength and temperature with field aligned along the c -axis [74]. These show the onset of a divergence of the specific heat as the critical field is approached, which is cut off by the appearance of the anomalous phase. How closely this matches the prediction for a single peak in the electronic density of states will be discussed in section 5. Here we note that as the Fermi liquid prediction for the low temperature electronic specific heat goes like the density of states at the Fermi surface a divergence would be expected at a van Hove singularity.

3.5 Summary

Having discussed in some detail the experimental situation regarding $Sr_3Ru_2O_7$ we now summarize the results most relevant to the work presented here. $Sr_3Ru_2O_7$ shows a metamagnetic transition the critical field and temperature of which can be tuned by the angle of applied magnetic field relative to the crystalline c -axis. With the field along c -axis the transition is split into two. Between the two transitions is an anomalous phase with a high, anisotropic resistivity which can be oriented by the component of the field in the ab -plane. This phase is enclosed by first-order transitions at low temperature and a second-order roof at higher temperatures. The metamagnetic transition appears to be driven by a peak in the density of states of one electronic band. The other bands appear inert throughout the transition. The anomalous phase has some Fermi liquid characteristics, although it has unusual temperature dependences of the resistivity and specific heat.

3.6 Our model and motivation

We will now introduce the model that we propose to explain these features of $\text{Sr}_3\text{Ru}_2\text{O}_7$ and the motivations that drive us to take this approach.

The feature which dominates the phase diagram of $\text{Sr}_3\text{Ru}_2\text{O}_7$ is the metamagnetic transition. This occurs in both the ultra-pure samples and the less pure samples, unlike the anomalous phase which is more fragile. Furthermore, the metamagnetic transition exists for all angles whereas the anomalous phase is restricted to certain regions. We therefore reason that the metamagnetic transition has a higher energy scale than the other effects and any theory should first explain its properties before turning to the anomalous phase. The obvious place to start in describing this transition is the simple model of a peak in the density of states driving the transition via a Stoner-type mean-field interaction.

Rather than become mired in details at an early stage, and also to retain generality, we will not begin by studying the Fermi surface of $\text{Sr}_3\text{Ru}_2\text{O}_7$, but will choose the simplest example which reproduces the key feature - the peak in the density of states. We will therefore study a model using the next-nearest-neighbour tight-binding dispersion, which possesses both the peak and the observed symmetry of the normal phase.

We are interested in a reconstruction of the metamagnetic transition to form the anomalous phase. We will therefore construct a Ginzburg-Landau expansion about the metamagnetic transition and study its consequences.

Our proposal for the nature of the anomalous phase is based on the general idea of modulated phases acting as intermediate states between two phases. By forming a spatially modulated state the system can take advantage of ordering locally whilst retaining an average zero order parameter.

Spatially modulated superconductivity is the most commonly studied case. Here the modulated phase is called the Fulde-Ferrell-Larkin-Ovchinnikov [27, 28] phase and it appears in a narrow range of magnetic fields in between the normal and superconducting states. We postulate that a similar phase of spatially modulated magnetization may occur as an intermediate state in a metamagnetic transition.

Motivated by this we will study the favourability of the spatially modulated phase in a Ginzburg-Landau expansion. We will find that in certain circumstances it is a favourable state and that it causes the bifurcation of a metamagnetic transition in a way which reproduces the topology of the phase diagram of $\text{Sr}_3\text{Ru}_2\text{O}_7$.

We will calculate the phase diagram for the inhomogeneous phase based on both

microscopic and phenomenological arguments. Starting from the Stoner Hamiltonian we perform an expansion to obtain the Ginzburg-Landau theory in terms of the microscopic parameters of the theory. This will also be derived from general phenomenological principles. Using this Ginzburg-Landau expansion we will calculate the phase diagram. The thermodynamic properties of the metamagnetic transition will be calculated to obtain the specific heat and entropy as we tune with field through the transition.

Part II

CALCULATION OF PHASE DIAGRAMS AND PROPERTIES, AND COMPARISON WITH EXPERIMENT

4. CALCULATION OF PHASE DIAGRAM

This chapter is concerned with calculating the phase diagram for an itinerant metamagnetic system with spiral magnetic order. Following our top-down approach we begin by considering the homogeneous case and then calculate how this phase diagram reconstructs when modulated magnetisation is allowed. We consider both microscopic and phenomenological approaches to the problem. We will find a complex phase diagram which reproduces the topology of the experimental phase diagram of $\text{Sr}_3\text{Ru}_2\text{O}_7$.

We will begin with a cartoon picture of why peaks in the density of states favour metamagnetism. We then consider how the mean-field phase diagram for this model may be calculated. Next the framework of the Ginzburg-Landau expansion will be introduced and we will show how it can be adapted to an expansion about the line of metamagnetic critical endpoints. We will consider this phenomenologically before performing an explicit microscopic expansion. We then examine how inhomogeneous phases appear. We motivate this study by considering how modulated magnetisation may become energetically favourable. A gradient expansion of the Stoner action is then performed to show that modulation becomes favourable on the line of critical endpoints. Finally we construct the phase diagram including modulation from a Ginzburg-Landau theory. This theory is rather complicated, therefore to elucidate the role of the various terms in the expansion we conduct a term-by-term study of the phase diagram.

4.1 *Homogeneous phase diagram*

To begin the phase diagram for the case of purely homogeneous magnetisation will be calculated. We will consider the physical arguments as to why metamagnetism should occur when there is a peak in the density of states. We will then calculate the phase diagram of the Stoner model with a peak in the density of states. A Landau expansion will be developed for this case from an expansion of the Hamiltonian and the phenomenology of the situation will be investigated.

4.1.1 Cartoon for homogeneous phase diagram

We present a cartoon explaining the energetic reasons for the metamagnetic transition occurring, giving a simple physical picture for the transition. We begin from the idea that the full phase diagram, including the anomalous phase, is found by restructuring this metamagnetic transition. Based on this idea we study the simplest model which reproduces the metamagnetic transition, the Stoner model with a peak in the electronic density of states. This gives the correct topology for the metamagnetic transition with a generic 2D electronic band dispersion [69].

The Stoner model includes electron-electron interactions in a mean-field manner. The Hamiltonian \hat{H}_S is therefore easy to understand:

$$\hat{H}_S = \sum_{\mathbf{k}, \sigma=\uparrow, \downarrow} \epsilon_{\mathbf{k}} \hat{n}_{\mathbf{k}, \sigma} + g \hat{n}_{\uparrow} \hat{n}_{\downarrow} - h (\hat{n}_{\uparrow} - \hat{n}_{\downarrow}), \quad (4.1)$$

where $\epsilon_{\mathbf{k}}$ is the electronic dispersion, $\hat{n}_{\mathbf{k}, \sigma}$ is the number operator for electrons with momentum \mathbf{k} and spin σ and \hat{n}_{σ} is the total number operator for spin σ , g is the Coulomb interaction strength and h is the applied magnetic field. The first term is the single-particle energy, the second term is the interaction energy and the final term is the Zeeman energy. The interaction term can be rewritten as $n_{\uparrow} n_{\downarrow} = (n - m)(n + m) = n^2 - m^2$, so we see that magnetisation leads to a lowering of the energy. However, magnetising also raises the single particle energy. The balance between these terms will determine the magnetic properties of the system. Information about the system enters through magnitude of g and the electronic dispersion. We are interested in systems with a peak in the density of states and so will choose simple dispersions or model densities of states which show this feature. Van Hove showed that in 2D saddle points in the dispersion produce logarithmically divergent peaks in the density of states [56]. The simplest dispersion which reproduces this is the nearest-neighbour tight-binding model on a square lattice. This dispersion is however perfectly nested at half-filling and so is unstable to forming a spin-density wave, as discussed in section 2.2.3. We are interested in systems which are uniform ferromagnets at zero field and so remove the perfect nesting by adding a next-nearest-neighbour contribution to give the dispersion

$$\epsilon_{\mathbf{k}} = -(\cos k_x + \cos k_y) + t \cos k_x \cos k_y. \quad (4.2)$$

Here t measures the next-nearest-neighbour contribution. This has saddle points at

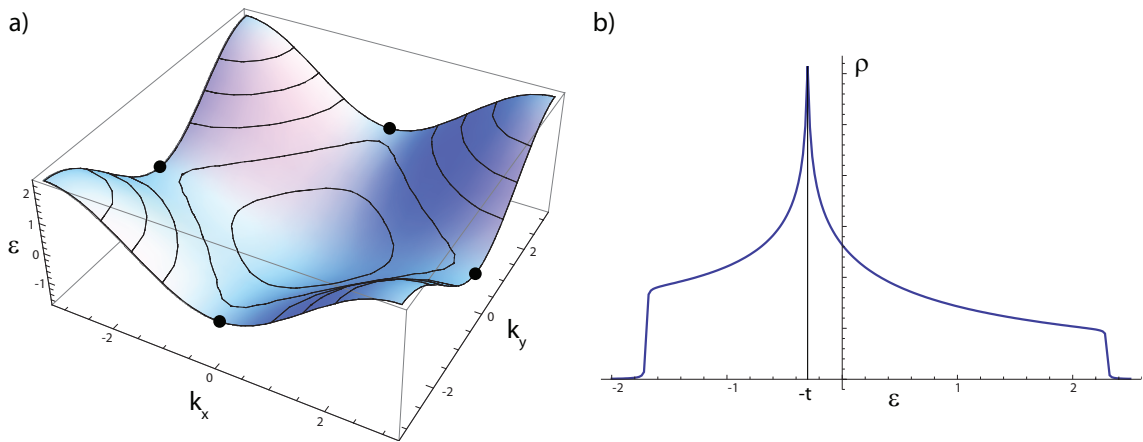


Fig. 4.1: Electronic dispersion and density of states: a) The next-nearest-neighbour tight-binding dispersion. This has saddle-points at $\mathbf{k} = (0, \pm\pi)$ and $\mathbf{k} = (\pm\pi, 0)$, indicated by dots. b) The density of states corresponding to this dispersion. There is a peak at the energy of the saddle-point.

$\mathbf{k} = (0, \pm\pi)$ and $\mathbf{k} = (\pm\pi, 0)$. These points are degenerate and so the density of states has a single peak at $\epsilon = -t$. This dispersion and its density of states are shown in Fig.4.1.

A simple picture of when magnetisation becomes favourable is as follows. Consider what happens when an itinerant system spontaneously magnetises. The Fermi surfaces of the two spin-species split to create a population imbalance. This is effectively taking some electrons from below the Fermi surface and flipping their spins, due to the Pauli exclusion principle these electrons must then be added to the other spin band *above* the Fermi-surface. This results in an energy cost to splitting the Fermi-surface as encoded in the first term of Eq.4.1. However, the magnetic field which results from this imbalance lowers the energy of the majority spin-species. This gives an energetic advantage to magnetizing due to interactions which is the second term in Eq.4.1. The final term is the Zeeman coupling to the external field.

The single particle energy cost is proportional to the energetic difference between the spin-species' Fermi surfaces, whereas the interaction energy is proportional to the magnetisation squared. The number of electrons whose energy is changed by applying a field is approximately $\rho_F \delta E$ as shown in Fig.4.2b). We therefore see that the magnetic gain is proportional to $\rho_F^2 \delta E^2$, whereas the kinetic cost is proportional to $\rho_F \delta E^2$. The magnetic term is favoured by a high density of states. When the Fermi surface is close to a peak in the density of states it will be energetically favourable for the system to become ferromagnetic.

This cartoon explains why the system should be ferromagnetic if the Fermi sur-

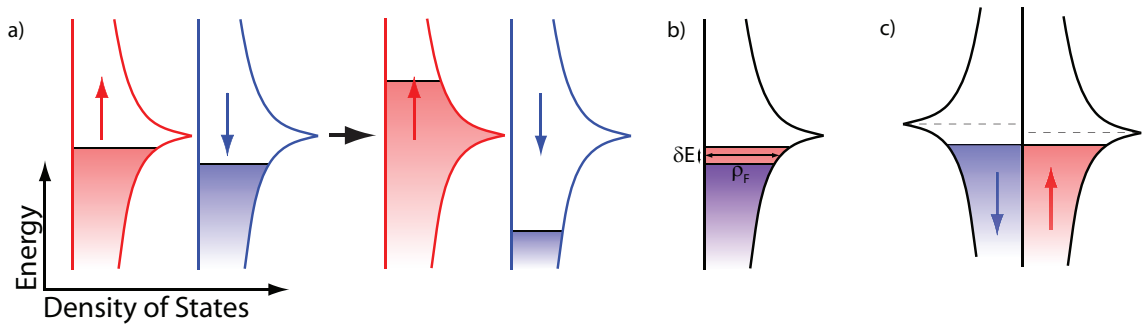


Fig. 4.2: Cartoon for the formation of metamagnetism: a) At the metamagnetic transition the majority band increases its filling through the van Hove singularity. b) The presence of this singularity leads to a reduced cost in single-particle energy allowing the gain in interaction energy to win out. The single particle energy is proportional to $\rho_F \delta E^2$ whereas the magnetisation energy is proportional to $(\rho_F \delta E)^2$. In a region of high density of states it becomes energetically favourable to magnetise. c) The picture of two Fermi surfaces is equivalent to a single Fermi surface with different densities of states for the spin-species.

face lies close enough to the peak in the density of states. It also results in metamagnetism as we now explain. If the zero-field Fermi surface lies far enough away from the peak then the system is paramagnetic. By applying a magnetic field the Fermi surfaces are split, if one of them approaches the peak in the density of states then the above arguments come into play and it is favourable for the Fermi surface to split further, resulting in a jump in the magnetisation.

This discussion has been presented in terms of there being two different Fermi surfaces for the spin-species. It is more physical to think of a single Fermi energy and the densities of states of the two species being shifted relative to each other. The two pictures are however equivalent. Throughout this thesis both will be employed depending upon the situation.

The phase diagram for the Stoner model can be calculated exactly from the free energy. We first consider this method and then go on to develop a Ginzburg-Landau expansion for the model.

4.1.2 Calculation from mean-field free energy

Based on the Hamiltonian 4.1 the free energy of the Stoner model can be written

$$F = \sum_{\sigma} \left[-k_B T \int d\epsilon \rho(\epsilon) \log \left(1 + e^{-\beta(\epsilon - \mu_{\sigma})} \right) + \mu_{\sigma} n_{\sigma} \right] + g(n^2 - m^2), \quad (4.3)$$

where n is the total number of electrons, m is the magnetisation, h is the magnetic field and T is the temperature. The term in square brackets is the single-particle contribution, the final term is the interaction energy. Here we choose to work in the canonical ensemble where electron number is conserved (note that the first term in Eq.4.3 is the Grand Potential). The Free Energy is therefore a function of n , m and T . μ_σ are the effective chemical potentials for the spin-up and -down electrons. These are determined implicitly by the equations for electron number

$$n_\sigma = \frac{n}{2} + \sigma m = \int d\epsilon \rho(\epsilon) n_{\text{F}}(\epsilon - \mu_\sigma), \quad (4.4)$$

where $n_{\text{F}}(\epsilon - \mu_\sigma)$ is the Fermi-Dirac distribution $(1 + e^{\beta(\epsilon - \mu_\sigma)})^{-1}$ and $\sigma = \pm 1$. With this definition for n_σ we have $n = n_\uparrow + n_\downarrow$ and $m = n_\uparrow - n_\downarrow$, as used in the rewriting of the interaction energy.

Writing the free energy in terms of the density of states rather than the dispersion is convenient but requires an explicit form for the density of states, which is in general hard to obtain. It is known that saddle points in the dispersion produce logarithmic divergences in the density of states in two dimensions [56]. Investigation into the form of the phase diagram with a density of states

$$\rho(\epsilon) = \log|\epsilon^{-1}| \quad (4.5)$$

which diverges at $\epsilon = 0$, has been carried out by Binz and Sigrist [69], the results are shown in Fig.4.3.

From the free energy an equation for the magnetic field as a function of n , m and T is obtained by minimizing the Gibb's free energy $G = F - hm$.

$$h = \partial_m F = \sum_\sigma \sigma \mu_\sigma - 2Um. \quad (4.6)$$

This may be numerically inverted to find m for any n , h and T . The resulting magnetisation is shown in Fig.4.3. There are some complications involving phase separation which we will address in section 4.1.6.

The second derivative of the free energy with respect to magnetisation gives the inverse of the magnetic susceptibility. The susceptibility diverges at a second order transition, giving a condition for a continuous transition, $\partial_m^2 F = 0$.

$$\partial_m^2 F = \frac{1}{\chi} = \sum_\sigma \frac{1}{\int d\epsilon \rho^{(1)}(\epsilon) n_{\text{F}}(\epsilon - \mu_\sigma)} - 2U, \quad (4.7)$$

where $\rho^{(n)}(\epsilon) = \partial_\epsilon^n \rho(\epsilon)$. Note that in the paramagnetic phase at zero field $\mu_\uparrow = \mu_\downarrow$ and this condition reduces to $1 = U \int d\epsilon \rho^{(1)}(\epsilon) n_F(\epsilon - \mu_\sigma)$. This is the finite-temperature version of the Stoner criterion as can be seen by integrating by parts $-U \int d\epsilon \rho(\epsilon) n_F^{(1)}(\epsilon - \mu_\sigma) = 1$. At zero temperature the Fermi-Dirac distribution becomes a step function and its derivative is the negative of a delta function at the Fermi surface $1 = U \int d\epsilon \rho(\epsilon) \delta(\epsilon - \epsilon_F) = U\rho(\epsilon_F)$.

The line of metamagnetic critical endpoints is determined by the third derivative of the free energy being zero:

$$\partial_m^3 F = \sum_\sigma \frac{-\sigma \int d\epsilon \rho^{(2)}(\epsilon) n_F(\epsilon - \mu_\sigma)}{(\int d\epsilon \rho^{(1)}(\epsilon) n_F(\epsilon - \mu_\sigma))^3}. \quad (4.8)$$

By symmetry this derivative must be zero when there is no field. The position of the tricritical point in the zero field plane is determined by the fourth derivative vanishing. These derivatives are the coefficients of a Landau expansion of the free energy, which we will derive shortly. These conditions may be solved numerically to give the transition lines as a function of n , h and T . With the logarithmic form of the density of states Eq.4.5 these conditions give the phase diagram shown in Fig.4.3.

The phase diagram resulting from this model displays a dome-shaped region of ferromagnetism at zero field around the divergence in the density of states. This is bounded by continuous transitions at high temperature. These transitions become first order at a tricritical point as temperature is decreased. A line of metamagnetic critical endpoints emerges from the tricritical point and extends to higher filling as field is increased. This line bounds a sheet of discontinuous jumps in the magnetisation. Above the critical temperature this transition becomes a smooth cross-over. Fig.4.3 shows this phase diagram for greater than half filling, but for a density of states with a symmetric peak the phase diagram is also symmetric about the peak.

In $\text{Sr}_3\text{Ru}_2\text{O}_7$ the angle of the applied field tunes through the metamagnetic wing (Fig.3.3), effectively taking the role of filling in Fig.4.3. The reasons for this relationship are not fully understood, but it is likely to be due to orbital effects which we will discuss in section 6.4.1.

The parent tricritical point does not appear in the phase diagram of $\text{Sr}_3\text{Ru}_2\text{O}_7$ as a function of the angle of applied field. However the application of moderate uniaxial pressure can drive the material ferromagnetic [78] suggesting that the tricritical point is not far away. $\text{Sr}_3\text{Ru}_2\text{O}_7$ can therefore be thought of as having a segment of this

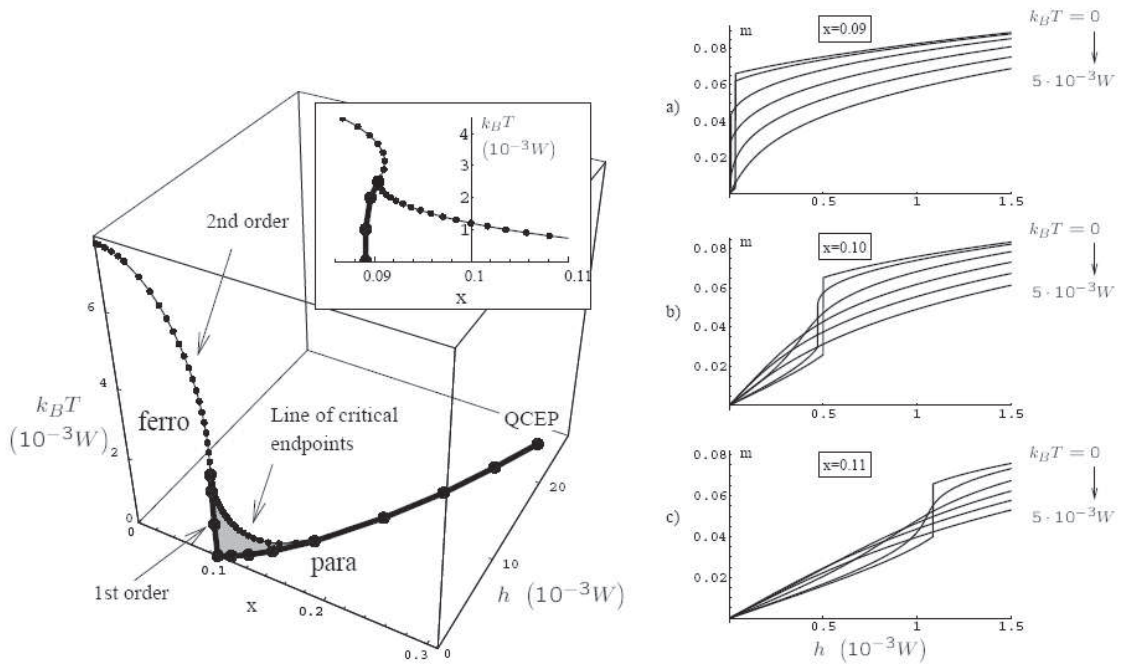


Fig. 4.3: The phase diagram for the Stoner model: The phase diagram of the Stoner model, calculated by Binz and Sigrist, as a function of filling x , magnetic field h and temperature T for a logarithmically divergent density of states. The line of second order transitions is given by $\partial_m^2 F = 0$, the line of metamagnetic critical endpoints by $\partial_m^3 F = \partial_m^2 F = 0$ and the tricritical point by $\partial_m^4 F = \partial_m^2 F = 0$. The inset shows the projection of the phase diagram onto the x, T plane. On the right are the magnetisation curves passing through the metamagnetic wing. Magnetisation is plotted as a function of field for a variety of temperatures. The first-order jump at low temperature is shown, this becomes a smooth cross-over at high temperature. The three panels are for different values of the filling x , a) is closest in filling to the zero-field first-order transition and shows the largest metamagnetic jump. c) is furthest from the zero-field transition and shows continuous behaviour setting in at lower temperature than panels a) or b). Figure from [69].

phase diagram. The phase diagrams of the neighbouring members of the ruthenate family can be thought of as covering different areas of the phase diagram, Sr_2RuO_4 being a paramagnet and $\text{Sr}_4\text{Ru}_3\text{O}_{10}$ being a ferromagnet. The full phase diagram is reproduced in a variety of itinerant magnets such as MnSi [29] and ZrZn_2 [47].

4.1.3 Landau expansions

In preparation for the development of a Ginzburg-Landau description of inhomogeneous phases we consider the Landau approach to the ferro- and meta-magnetic transitions.

The concept of a Landau expansion [46] gives an informative and tractable approach to phase transitions, incorporating both phenomenological and microscopic viewpoints. It also provides an easy-to-understand visual representation of phase transitions. The central idea of a Landau expansion is that near to a continuous phase transition the order parameter is small. The free energy may therefore be Taylor expanded in this order parameter. Truncating this expansion at sixth order is sufficient to capture both first- and second-order transitions, including metamagnetism. Certain terms in the expansion will automatically be zero due to symmetry. For example, in the case of a ferromagnet in zero external field all orientations of the magnetisation must be energetically equivalent. The Landau expansion cannot depend on the sign of the magnetisation and must contain only even powers of magnetisation. The external field then couples linearly to the magnetisation, breaking the symmetry. The Landau description of a ferromagnet therefore has the form

$$F = \frac{r}{2}m^2 + \frac{u}{4}m^4 + \frac{v}{6}m^6 - hm \quad (4.9)$$

where m is the magnitude of the magnetisation and h is the external magnetic field. r , u and v are coefficients which are varied to produce the phenomenology of different phases, or which can be calculated from microscopics.

The order parameter takes the value which minimises the Landau free energy. In order for the free energy function to be bounded from below as $m \rightarrow \infty$ it is necessary for the highest order coefficient, v , to be positive. In this case the value of magnetisation \bar{m} which minimises the free energy is given by $\bar{m}^2 = (-u \pm \sqrt{u^2 - 4rv})/2v$.

At this point we note that although the Landau free energy is by definition an analytic function it can still describe the non-analytic point of a phase transition. This is because the Landau free energy is not actually the free energy of the system - the *minimum* of the Landau free energy is the physical free energy of the system. The co-ordinates of the minimum of a function can be discontinuous even though the function is perfectly smooth, as indicated in Fig.4.4. The expansion in terms of the order parameter can be thought of as introducing an additional variable in order to transform a non-analytic function into an analytic one.

Within the Landau scheme phase transitions occur when the global minimum of the free energy changes between different values of the order parameter. This can occur in two ways which are illustrated in Fig.4.5. The $m = 0$ minima of the free energy can move smoothly to non-zero m as the quadratic Landau coefficient r becomes negative - a continuous transition. The second way is for a separate

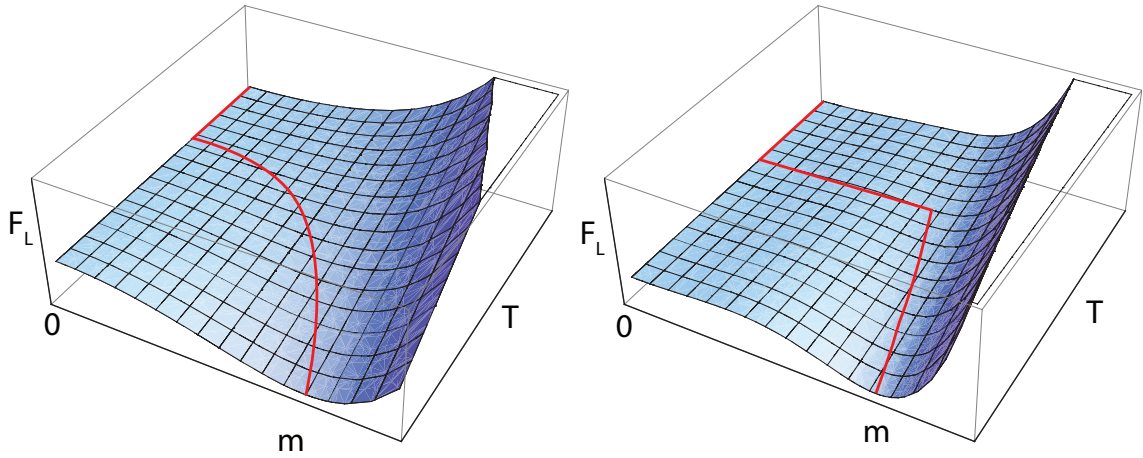


Fig. 4.4: The order parameter is the minimum of the Landau free energy: Shown are the Landau free energy curves as a function of order parameter and an external parameter (here represented by T , as this parameter is often temperature) which changes the values of the Landau coefficients. The value of the order parameter which the system adopts is the one which minimizes the Landau free energy, shown by the red line. This may have discontinuities and kinks despite the smoothness of the free energy function. Illustrated are, left, a continuous transition and right, a first-order transition.

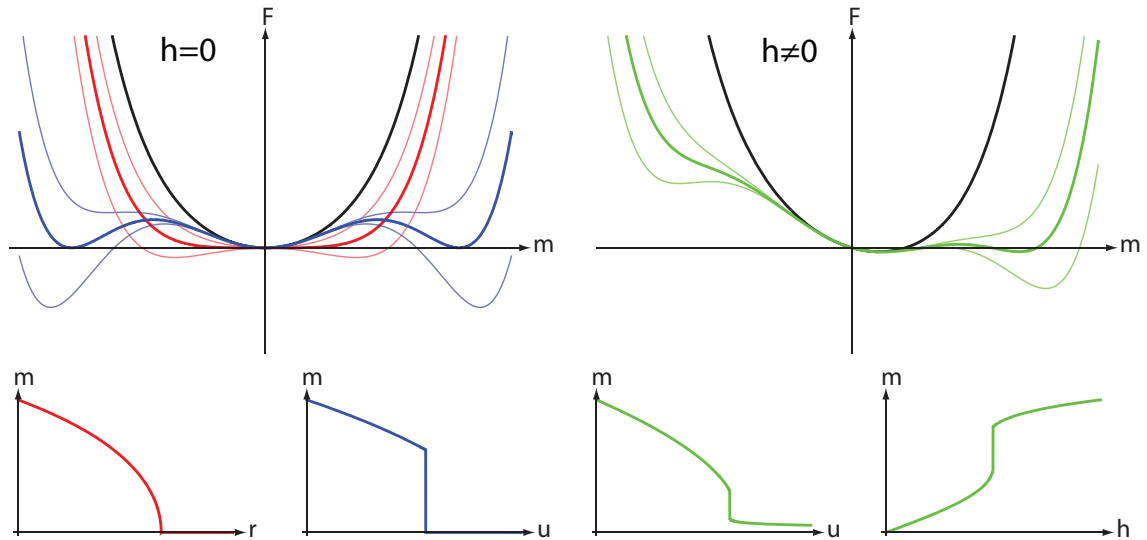


Fig. 4.5: Free energy curves for the Landau expansion: In black is the Landau free energy when r , u and v are positive. In red are Landau free energy functions showing a second-order phase transition when $r = 0$. In blue is the free energy for a first-order transition, which occurs when $u = -\sqrt{\frac{16}{3}rv}$. In green is the free energy for the metamagnetic transition, the field acts to ‘tilt’ the free energy so that it is asymmetric. On the bottom line are plots of the magnetisation for a second-order transition (red), first-order transition (blue) and metamagnetic transitions (green) as functions of u and h .

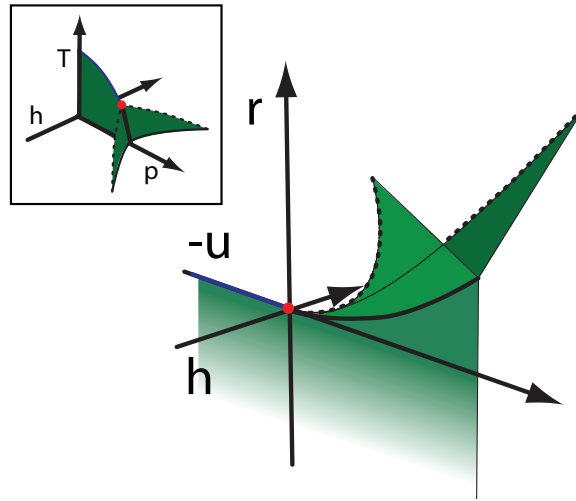


Fig. 4.6: Generic Landau phase diagram: Phase diagram for the Landau expansion $F = \frac{r}{2}m^2 + \frac{u}{4}m^4 + \frac{v}{6}m^6$. The blue line is the continuous transition, the red point is the tricritical point and the green sheets are first-order transitions. This generic diagram can be mapped onto any theory which can be described by a Landau expansion. The inset shows the generic form of this diagram for the case of itinerant magnets, where r and u are functions of temperature T and some tuning parameter p .

local minimum to form and then cross the original minimum to become the global minimum. This results in a jump of the order parameter between the two minima - a first-order transition. This is caused by the quartic term u becoming sufficiently negative while r remains positive. It is simple to calculate the conditions for these different transitions. The second order transition occurs when

$$\partial_m F|_{m=0} = r = 0, \quad (4.10)$$

the first order transition when $F(\bar{m}) = F(m)$, leading to

$$u = -\sqrt{\frac{16}{3}rv}. \quad (4.11)$$

The metamagnetic transitions are first-order transitions between two minima, both at non-zero magnetisation because of the applied field. They occur along lines given by

$$h = \pm \frac{6u^2}{25} \sqrt{\frac{3|u|}{10v^3}}, \quad r = \frac{9u^2}{20v}. \quad (4.12)$$

As calculated from the conditions for the degeneracy of two minima with a non-zero field h [70].

These equations define a phase diagram for the Landau expansion Eq.4.9 as a function of the coefficients of the expansion. This is shown in Fig.4.6. It consists of a sheet of first-order transitions for $u > 0$, $r < 0$, $h = 0$ with a continuous transition along the line $u > 0$, $r = 0$, $h = 0$. This transition terminates in a tricritical point at $r = u = h = 0$ where it becomes a first-order transition for $u < 0$, $r = \frac{3u^2}{16v}$, the sheet of first order transitions continuing below this first-order line. Two metamagnetic wings extend from the tricritical point for $h \neq 0$, the critical endpoints determined by the equations 4.12.

This is the standard description of the ferromagnet, where the terms in the expansion reflect the inversion symmetry of the system. The effects which we will consider do not occur on this zero-field phase transition but on the metamagnetic wing. The metamagnetic critical endpoint is a continuous phase transition, and therefore we may construct a Landau expansion about this line in the same way as about the zero-field continuous transition. Instead of expanding in the magnetisation we expand in the deviation of the magnetisation from its value on the line of critical endpoints. We will consider this issue in detail in later sections. Here we note that since the expansion is about a symmetry-broken state the expansion Eq.4.9 should contain odd terms in m , now representing the deviation from the magnetisation on the line of critical endpoints. This situation was considered by Green *et al.* [70]. They found that the tricritical point becomes ‘dislocated’ in the presence of asymmetric terms as shown in Fig.4.7. This result is in agreement with the topology of the metamagnetic transitions in $\text{Sr}_3\text{Ru}_2\text{O}_7$. When we consider the effect of inhomogeneity we will find a similar phase diagram with some important differences.

4.1.4 Landau phenomenology

We wish to investigate the potential for inhomogeneous order leading to a reconstruction of the metamagnetic wings. To this end, we develop a Landau expansion about the magnetisation along the line of metamagnetic critical end-points, rather than about zero magnetisation. The presence of the field singles out a particular direction in space and components of the magnetisation parallel and perpendicular to this direction may have different properties. We therefore expand in the two components separately. We will label the longitudinal magnetisation $M\hat{e}_{\parallel}$ where \hat{e}_{\parallel} is a unit vector in the direction of the applied field, and the perpendicular magnetisation $M_{\perp}\hat{e}_{\perp}$, where \hat{e}_{\perp} is a unit vector perpendicular to the applied field, so that

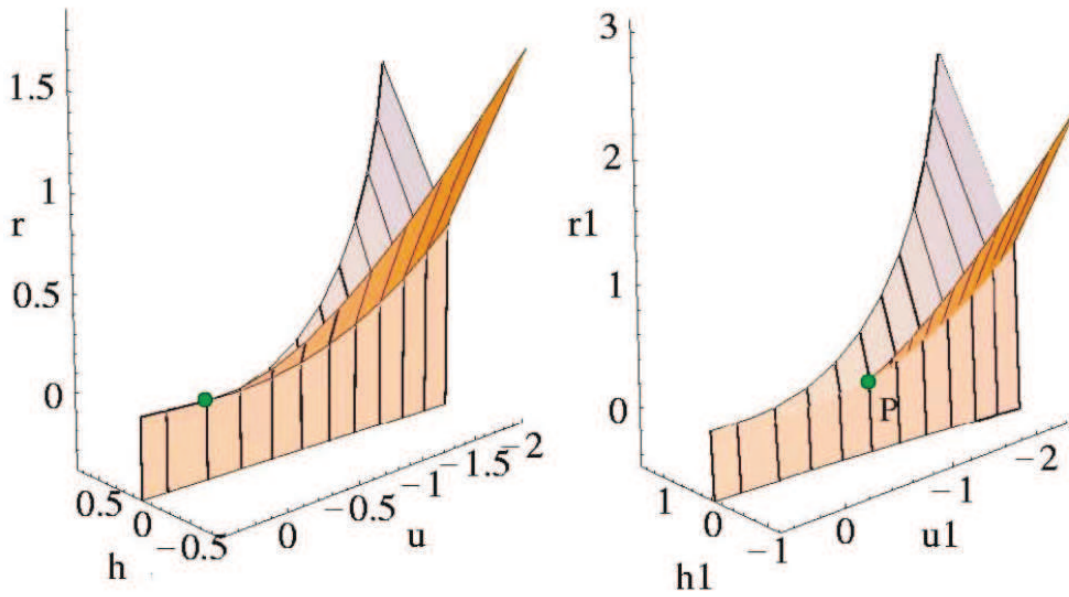


Fig. 4.7: **Phase diagram showing dislocated tricritical point:** Left, the phase diagram with only symmetric terms, right, the phase diagram with asymmetric terms. In the presence of symmetry-breaking terms the tricritical point becomes dislocated. This is similar to the bifurcation observed in ultra-pure $\text{Sr}_3\text{Ru}_2\text{O}_7$. Figure from [70].

$$\mathbf{M} = M\hat{\mathbf{e}}_{\parallel} + M_{\perp}\hat{\mathbf{e}}_{\perp}.$$

We denote the longitudinal magnetisation in the vicinity of the line of metamagnetic critical end-points by $M = m + \bar{M}$, where \bar{M} is the magnetisation on the line and m is the deviation from it. By making this shift we study small deviations of the magnetisation from the value on the line of critical endpoints, just as the standard Landau description of the ferromagnet studies deviations from zero magnetisation. Substituting this shift of order parameter into the Landau free energy

$$F = r\mathbf{M}^2 + u\mathbf{M}^4 + v\mathbf{M}^6 - \mathbf{h} \cdot \mathbf{M} \quad (4.13)$$

results in a theory with terms up to sixth order in m , \bar{M} and M_{\perp} . This unwieldy number of terms is reduced considerably by explicitly constraining our expansion to be about the line of critical end-points. The conditions that \bar{M} be the magnetisation along the line of critical end-points are that the first three derivatives of the Landau free energy Eq.4.13 with respect to \mathbf{M} are zero. This gives

$$\begin{aligned} \partial_{\mathbf{M}}F &= 0 = 2r\mathbf{M} + 4u\mathbf{M}^3 + 6v\mathbf{M}^5 - \mathbf{h}, \\ \partial_{\mathbf{M}}^2F &= 0 = 2r + 12u\mathbf{M}^2 + 30v\mathbf{M}^4, \end{aligned}$$

$$\partial_{\mathbf{M}}^3 F = 0 = 24u\mathbf{M} + 120v\mathbf{M}^3, \quad (4.14)$$

which imply the relationships $r = 15v\bar{M}^4$, $u = -5v\bar{M}^2$ and $h = 16v\bar{M}^5$ when on the line of critical endpoints.

A further simplification is afforded by normalizing the deviations in longitudinal and transverse magnetisations to the longitudinal magnetisation along the line of metamagnetic critical end points. Defining $\phi = m/\bar{M}$ and $\phi_{\perp} = M_{\perp}/\bar{M}$ and substituting into Eq.4.13 with the coefficients of the expansion constrained to lie along the line of critical end points by equations 4.14, we find

$$\begin{aligned} F = F(\bar{M}) + h\bar{M}[& R\phi^2 + S\phi^3 + U\phi^4 + T\phi^5 + V\phi^6 - H\phi \\ & + R_{\perp}\phi_{\perp}^2 + U_{\perp}\phi_{\perp}^4 + V_{\perp}\phi_{\perp}^6 \\ & + S_1\phi\phi_{\perp}^2 + U_1\phi^2\phi_{\perp}^2 + T_1\phi^3\phi_{\perp}^2 \\ & + V_1\phi^4\phi_{\perp}^2 + T_2\phi\phi_{\perp}^4 + V_2\phi^2\phi_{\perp}^4], \end{aligned} \quad (4.15)$$

where

$$\begin{aligned} S = 0, \quad U = 5/8, \quad T = 3/8, \quad V = 1/16, \\ R_{\perp} = 1/2, \quad U_{\perp} = -1/8, \quad V_{\perp} = 1/16, \\ S_1 = -1/2, \quad U_1 = 1/2, \quad T_1 = 3/4, \\ V_1 = 3/16, \quad T_2 = 3/8, \quad V_2 = 3/16. \end{aligned} \quad (4.16)$$

The condition that the point we expand about lies on the line of metamagnetic critical endpoints is sufficient to constrain the free energy. The coefficients are reduced to constants, the majority of which will be confirmed by microscopic analysis. These are therefore universal properties of the metamagnetic transition and do not depend on the microscopic details.

Exactly on the line of critical end points, $R = 0$ and $H = 0$. We allow non-zero values in order to parametrize deviations from the line of critical end points. The Landau theory of Eq.4.15 leads to a line of first order transitions at $R < 0$ terminating at a second order end point at $H = 0$, $R = 0$ as shown in Fig.4.8, corresponding to a cut through the metamagnetic wing of Fig.4.6.

These phase diagrams are generic, describing the topology of the phase diagram for any system in which the Landau expansion is valid. Mapping this phase diagram onto a particular case involves finding explicit expressions for the Landau coefficients in terms of the parameters of the system, such as temperature, pressure, or in the

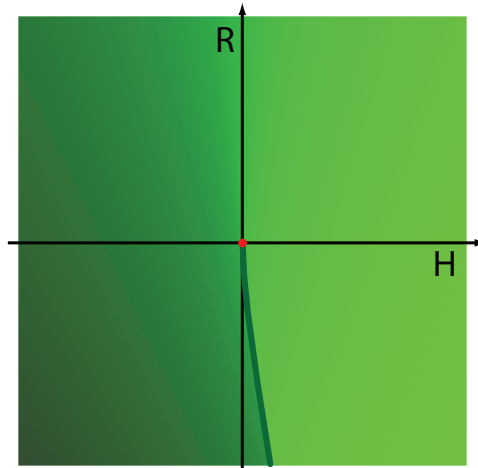


Fig. 4.8: Phase diagram for homogeneous magnetisation: The green line is the metamagnetic transition, the red point is the tricritical point. Green shading represents the magnitude of magnetisation, dark green is low magnetisation, light green is high magnetisation. Note the sharp jump at the first order transition and the gradual change above the tricritical point.

case of $\text{Sr}_3\text{Ru}_2\text{O}_7$ the angle of the applied field. We will now develop such a mapping for the Stoner model.

4.1.5 Explicit Landau expansion of Stoner Hamiltonian

We now turn to detailed calculation to obtain the Ginzburg-Landau expansion from the Stoner Hamiltonian. This will give us expressions for the coefficients of the Ginzburg-Landau expansion in terms of the microscopic parameters of the theory, allowing the mapping of the generic phase diagram Fig.4.6 onto the specific case considered. This process follows several standard steps (see for example [79]). The partition function is written as a path integral and the interaction terms decoupled. The action is then expanded in powers of \mathbf{M} to obtain the terms of the Landau expansion. Details of this process are contained in appendix A and B. We are no longer working in a number-conserving scheme, but instead fix the chemical potential μ .

We begin from the Hamiltonian

$$\hat{\mathcal{H}} - \mu\hat{\mathcal{N}} = \sum_{\mathbf{k}} \psi_{\mathbf{k}}^\dagger (\epsilon_{\mathbf{k}} - \mu) \psi_{\mathbf{k}} - \frac{g}{4} \int d\mathbf{x} (\psi_{\mathbf{x}}^\dagger \bar{\sigma} \psi_{\mathbf{x}})^2 - h \int d\mathbf{x} \psi_{\mathbf{x}}^\dagger \sigma_z \psi_{\mathbf{x}}, \quad (4.17)$$

where $\psi_{\mathbf{k}/\mathbf{x}}^\dagger = (c_{\mathbf{k}/\mathbf{x},\uparrow}^\dagger, c_{\mathbf{k}/\mathbf{x},\downarrow}^\dagger)$ represents the electron creation operators in the momentum and position representations respectively, $\bar{\sigma} = (\sigma_x, \sigma_y, \sigma_z)$ is the vector of

Pauli matrices, g is the Coulomb interaction strength and h is the applied magnetic field. Here we have explicitly expressed the interaction in terms of the magnetisation. Note that the field couples only to the longitudinal magnetisation component whereas the interaction term includes both components.

The partition function is written as a path integral over Grassman fields,

$$\mathcal{Z} = \int \mathcal{D}(\psi^\dagger, \psi) e^{-\int_0^\beta d\tau [\psi^\dagger \partial_\tau \psi + \hat{\mathcal{H}} - \mu \hat{N}]}. \quad (4.18)$$

The interaction terms are decoupled by a Hubbard-Stratonovich transformation with coupling $\mathbf{M}(\mathbf{x}) \cdot (\psi_{\mathbf{x}}^\dagger \boldsymbol{\sigma} \psi_{\mathbf{x}})$. Integrating over the fermionic fields the partition function can be expressed as a field integral, $\mathcal{Z} = \int \mathcal{D}\mathbf{M} e^{-\mathcal{S}[\mathbf{M}]}$ where the Euclidean time action takes the form

$$\begin{aligned} \mathcal{S}[\mathbf{M}] &= \frac{g}{4} \int dx \mathbf{M}^2 - \text{tr} \ln \left[\hat{G}_0^{-1} + \frac{g}{2} \boldsymbol{\sigma} \cdot \mathbf{M} \right] \\ &= \frac{g}{4} \int dx \mathbf{M}^2 - \text{tr} \ln [\hat{G}_0^{-1}] + \sum_{n=1}^{\infty} \frac{(-1)^n}{n} \left(\frac{g}{2} \right)^n \text{tr} [\hat{G}_0 \boldsymbol{\sigma} \cdot \mathbf{M}]^n, \end{aligned} \quad (4.19)$$

where $\int dx \equiv \int_0^\beta d\tau \int d^d r$. Here $\hat{G}_0^{-1} = -\partial_\tau - \xi_{\mathbf{p}} + h\sigma_z$, denotes the inverse Green's function of the non-interacting electron, where $\xi_{\mathbf{p}} = \epsilon_{\mathbf{p}} - \mu$. In the second line of this expression we have introduced the expansion of the action in powers of \mathbf{M} .

The Landau theory is developed as an expansion around the saddle point of this action along the line of critical end-points. Varying the action with respect to \mathbf{M} and applying the ansatz $\mathbf{M} = \bar{M} \hat{\mathbf{e}}_{\parallel}$ constant, where \bar{M} is a shifted magnetisation which includes the external field $\bar{M} \mapsto \bar{M}' = \bar{M} + \frac{2}{g}h$, gives the equation for the uniform saddle-point:

$$\bar{M} - \frac{2}{g}h = \frac{1}{\beta L^d} \sum_{k\sigma} \sigma G_\sigma(k) = \frac{1}{L^d} \sum_{k\sigma} \sigma n_{\text{F}} \left[\epsilon_{\mathbf{k}} - g\bar{M}\sigma/2 \right], \quad (4.20)$$

where $G_\sigma(k) = (i\omega_n - \xi_{\mathbf{k}} + \frac{g}{2}\bar{M}\sigma)^{-1}$ and $n_{\text{F}}(\epsilon) = (e^{\beta(\epsilon-\mu)} + 1)^{-1}$ denotes the Fermi distribution function. For a given interaction g , this gives the value of the saddle-point magnetisation \bar{M} as a function of chemical potential μ , magnetic field h and temperature T . As previously we must address the issue of phase separation, which is considered in section 4.1.6

The coordinates of the metamagnetic critical endpoint are found by the requirement that the second and third derivatives of the free energy with respect to mag-

netisation are zero. This gives the conditions

$$\begin{aligned}\frac{2}{g} &= -\frac{1}{L^d} \sum_{\mathbf{k}\sigma} n_{\mathbf{F}}^{(1)} \left[\epsilon_{\mathbf{k}} - (g\bar{M}/2 + h)\sigma \right], \\ 0 &= \frac{1}{L^d} \sum_{\mathbf{k}\sigma} \sigma n_{\mathbf{F}}^{(2)} \left[\epsilon_{\mathbf{k}} - (g\bar{M}/2 + h)\sigma \right],\end{aligned}\quad (4.21)$$

where $n_{\mathbf{F}}^{(n)}(\epsilon) = \partial_{\epsilon}^n n_{\mathbf{F}}(\epsilon)$. These equations will be used to simplify the expressions for the coefficients of the Landau expansion.

The Ginzburg-Landau expansion is constructed by evaluation of the terms in the expansion of the action (4.19). As the expansion is centered on the line of critical endpoints we expand about the saddle-point value \bar{M} and not zero. We set $\mathbf{M} = (\bar{M} + m)\hat{\mathbf{e}}_{\parallel} + \mathbf{m}_{\perp}$ where $\hat{\mathbf{e}}_{\parallel}$ is a unit vector in the direction of the applied field, with the deviation from the saddle-point solution \bar{M} presumed small. Discarding the constant contribution to the action, the saddle-point solution ensures that most of the terms at first order in \mathbf{M} must vanish, leaving only the field-dependent contribution,

$$\mathcal{S}^{(1)} = - \int dx hm. \quad (4.22)$$

At second order the action can be split into longitudinal and transverse components,

$$\mathcal{S}^{(2)} = \frac{g}{4} \int dx \mathbf{m}^2 + \left(\frac{g}{2}\right)^2 \text{tr} \left[\hat{G}_{\uparrow} \mathbf{m}_{\perp} \cdot \hat{G}_{\downarrow} \mathbf{m}_{\perp} + \frac{1}{2} \left((\hat{G}_{\uparrow} m)^2 + (\hat{G}_{\downarrow} m)^2 \right) \right]. \quad (4.23)$$

Defining the longitudinal and transverse susceptibilities

$$\begin{aligned}\Pi_{\parallel\sigma}(\mathbf{q}) &= \frac{1}{\beta L^d} \sum_{\mathbf{k}} G_{\sigma}(\mathbf{k}) G_{\sigma}(\mathbf{k} + \mathbf{q}), \\ \Pi_{\perp}(\mathbf{q}) &= \frac{1}{\beta L^d} \sum_{\mathbf{k}} G_{\uparrow}(\mathbf{k}) G_{\downarrow}(\mathbf{k} + \mathbf{q}),\end{aligned}\quad (4.24)$$

we have

$$\begin{aligned}\mathcal{S}^{(2)} &= \mathcal{S}_{\parallel}^{(2)} + \mathcal{S}_{\perp}^{(2)}, \\ \mathcal{S}_{\parallel}^{(2)} &= \frac{g}{4} \int dx m^2 + \frac{g^2}{8} \beta \sum_{\mathbf{q}\sigma} \Pi_{\parallel\sigma}(\mathbf{q}) m_{\mathbf{q}} m_{-\mathbf{q}}, \\ \mathcal{S}_{\perp}^{(2)} &= \frac{g}{4} \int dx m_{\perp}^2 + \frac{g^2}{4} \beta \sum_{\mathbf{q}} \Pi_{\perp}(\mathbf{q}) \mathbf{m}_{\perp\mathbf{q}} \mathbf{m}_{\perp-\mathbf{q}}.\end{aligned}\quad (4.25)$$

Expanding in powers of \mathbf{q} will lead to the gradient terms in the expansion. These terms will indicate the favourability of inhomogeneity and will be considered shortly. Initially we will consider the $\mathbf{q} = 0$ homogeneous case. Evaluating the susceptibilities we find

$$\begin{aligned}\mathcal{S}_{\parallel}^{(2)} &= \beta \int d^d r r m^2, \\ \mathcal{S}_{\perp}^{(2)} &= \beta \int d^d r r_{\perp} \mathbf{m}_{\perp}^2,\end{aligned}\tag{4.26}$$

where

$$\begin{aligned}r &= \frac{g}{4} + \frac{g^2}{8} \frac{1}{L^d} \sum_{\mathbf{k}\sigma} n_{\text{F}}^{(1)}(\epsilon_{\mathbf{k}} - g\bar{M}\sigma/2), \\ r_{\perp} &= \frac{g}{4} - \frac{g^2}{4} \frac{1}{g\bar{M}} \frac{1}{L^d} \sum_{\mathbf{k},\sigma} \sigma n_{\text{F}}(\epsilon_{\mathbf{k}} - g\bar{M}\sigma/2).\end{aligned}\tag{4.27}$$

In the case of zero field, $\bar{M} \rightarrow 0$. Then r_{\perp} tends to a constant and r tends to $\frac{g}{4} \left(1 + \frac{g}{L^d} \sum_{\mathbf{k}} n_{\text{F}}^{(1)}(\epsilon_{\mathbf{k}})\right)$. $r = 0$ corresponds to a second-order transition, this is the standard Stoner criterion, $1 = g\rho(\epsilon_{\text{F}})$ at zero temperature as $1 + \frac{g}{L^d} \sum_{\mathbf{k}} n_{\text{F}}^{(1)}\Big|_{T=0} = 1 + g \int d\epsilon \rho(\epsilon) n_{\text{F}}^{(1)}\Big|_{T=0} = 1 - g\rho(\epsilon_{\text{F}})$. If the Fermi level is tuned such that it moves to a region of high density of states then the system will undergo a second order transition to a ferromagnet.

At third order, the longitudinal and transverse magnetisations become coupled. It is this coupling which allows inhomogeneity in the transverse component to affect the phase diagram of the longitudinal magnetisation as we will later find.

$$\begin{aligned}\mathcal{S}^{(3)} &= -\frac{g^3}{24} \text{tr} [(\hat{G}_{\uparrow} m)^3 - (\hat{G}_{\downarrow} m)^3] - \frac{g^3}{8} \text{tr} [\hat{G}_{\uparrow}^2 \hat{G}_{\downarrow} m \mathbf{m}_{\perp}^2 - \hat{G}_{\downarrow} \hat{G}_{\uparrow}^2 m \mathbf{m}_{\perp}^2] \\ &= \beta \int d^d r [s m^3 + s_1 m \mathbf{m}_{\perp}^2],\end{aligned}\tag{4.28}$$

where

$$\begin{aligned}s &= -\frac{g^3}{48} \frac{1}{L^d} \sum_{\mathbf{k}\sigma} \sigma n_{\text{F}}^{(2)}(\epsilon_{\mathbf{k}} - g\bar{M}\sigma/2), \\ s_1 &= -\frac{2}{(g\bar{M})^2} \frac{1}{L^d} \sum_{\mathbf{k}\sigma} \left[\sigma n_{\text{F}}(\epsilon_{\mathbf{k}} - g\bar{M}\sigma/2) + \frac{g\bar{M}}{2} n_{\text{F}}^{(1)}(\epsilon_{\mathbf{k}} - g\bar{M}\sigma/2) \right].\end{aligned}\tag{4.29}$$

s vanishes in the absence of an external field, as expected from symmetry. $r = s = 0$

is the condition for the line of critical endpoints. There is no term in \mathbf{m}_\perp^3 as the external field does not couple to this component, so the $m_\perp \rightarrow -m_\perp$ symmetry is retained.

This process can be repeated at each order to obtain the coefficients of the Landau expansion. There is little to be gained by a detailed description of this process and we simply present the results here, more details can be found in appendix B. On the line of critical endpoints many simplifications occur. Applying the conditions Eq.4.21 to the expressions for the coefficients and adopting dimensionless magnetisations $\phi = m/\bar{M}$ and $\phi_\perp^2 = (\mathbf{M}_\perp \cdot \mathbf{M}_\perp)/\bar{M}^2$, we find a Landau expansion of the form

$$\begin{aligned}
F_L = & h\bar{M}[R\phi^2 + S\phi^3 + U\phi^4 + T\phi^5 + V\phi^6 - H\phi \\
& + R_\perp\phi_\perp^2 + U_\perp\phi_\perp^4 + V_\perp\phi_\perp^6 \\
& + S_1\phi\phi_\perp^2 + U_1\phi^2\phi_\perp^2 + T_1\phi^3\phi_\perp^2 \\
& + V_1\phi^4\phi_\perp^2 + T_2\phi\phi_\perp^4 + V_2\phi^2\phi_\perp^4]
\end{aligned} \tag{4.30}$$

where

$$\begin{aligned}
R &= 0, & S &= 0, \\
U &= \frac{1}{4!} \left(\frac{\bar{M}^3}{h}\right) \left(\frac{g}{2}\right)^4 \frac{1}{L^d} \sum_{\mathbf{k}\sigma} n_{\mathbf{F}}^{(3)}(\epsilon_{\mathbf{k}} - g\bar{M}\sigma/2), \\
T &= \frac{1}{5!} \left(\frac{\bar{M}^4}{h}\right) \left(\frac{g}{2}\right)^5 \frac{1}{L^d} \sum_{\mathbf{k}\sigma} \sigma n_{\mathbf{F}}^{(4)}(\epsilon_{\mathbf{k}} - g\bar{M}\sigma/2), \\
V &= \frac{1}{6!} \left(\frac{\bar{M}^5}{h}\right) \left(\frac{g}{2}\right)^6 \frac{1}{L^d} \sum_{\mathbf{k}\sigma} n_{\mathbf{F}}^{(5)}(\epsilon_{\mathbf{k}} - g\bar{M}\sigma/2), \\
R_\perp &= \frac{1}{2}, & U_\perp &= -\frac{1}{8}, & V_\perp &= \frac{1}{16}, \\
S_1 &= -\frac{1}{2}, & U_1 &= -4U_\perp = \frac{1}{2}, \\
T_1 &= -\frac{1}{2} + 2U, & T_2 &= \frac{3}{8}, \\
V_1 &= 1 - 2U - \frac{5}{2}T, & V_2 &= -\frac{3}{4} + \frac{3}{2}U.
\end{aligned} \tag{4.31}$$

The conditions for the line of critical end-points are sufficient to reduce many of the coefficients of the expansion to constants. This independence of the coefficients from the details of the dispersion and filling shows that we are able to deduce them from general principles as done in the previous section. The values for the transverse

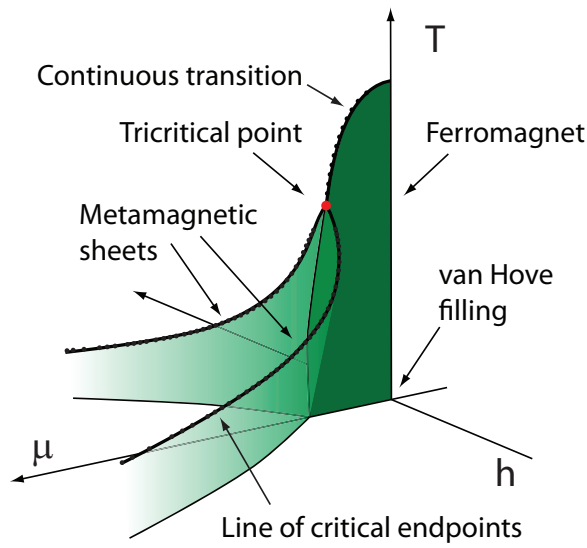


Fig. 4.9: Phase diagram for homogeneous magnetisation: Phase diagram for the Stoner model with a next-nearest-neighbour tight-binding dispersion, as determined by the coefficients Eq.4.27 and Eq.4.29. The dark green plane at $h = 0$ is the ferromagnetic region close to the van Hove singularity. The lines of metamagnetic critical endpoints emerge from the tricritical point and bound a first order transition, indicated schematically.

coefficients, and some of the coupling coefficients, are identical to that found from the phenomenological analysis Eq.4.16. The longitudinal coefficients depend on the microscopics and vary along the line of critical endpoints, so would not be expected to be reproduced by the phenomenological analysis. The same applies to those coupling coefficients which depend on the values of the longitudinal coefficients. If the values for the longitudinal coefficients from Eq.4.16 are substituted into Eq.4.31 then the values are consistent.

These coefficients are sufficient to determine the phase diagram for homogeneous magnetisation. Taking a next-nearest-neighbour tight-binding dispersion $\epsilon_{\mathbf{k}} = -(\cos k_x + \cos k_y) + t \cos k_x \cos k_y$ we obtain the phase diagram shown in Fig.4.9. There is a metamagnetic transition in the longitudinal magnetisation for fillings just outside of the ferromagnetic region around the van Hove singularity. The critical endpoint of this transition moves to higher field and lower temperature as filling gets further from the van Hove singularity. It is not favourable to form transverse magnetisation in the homogeneous case as it is always favourable to align with the external field.

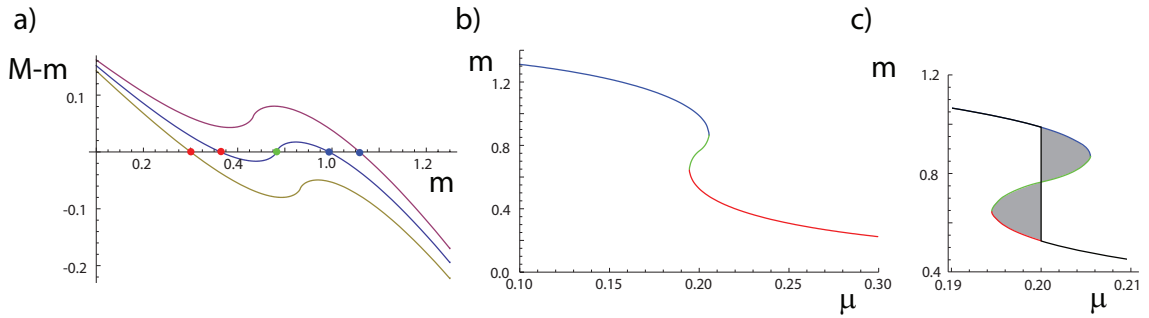


Fig. 4.10: Phase separation and Maxwell construction: a) Self-consistent determination of m . The intercept with the axis is a solution for m . The three curves correspond to different values of μ . We see that for some values there are multiple solutions. b) m as a function of μ . This is multivalued in the region of the transition. c) The Maxwell construction restores the single-valuedness of m by bridging the curve such that the shaded areas are equal.

4.1.6 Phase separation

It has been noted that there is a region of phase separation around the metamagnetic transition [80]. Here the system breaks up into regions of different electron densities. We note that this phenomena also appears in the magnetisation.

Previously we have assumed that Eq.4.20 defines the magnetisation uniquely. This is not actually the case. If we plot $M(m) - m$, where $M(m) = \sum_{\mathbf{k},\sigma} \sigma n_{\mathbf{F}}(\epsilon + \sigma \left(\frac{gm}{2} + h\right))$ against m then the intercept with zero is the self-consistent value of m . This is shown in Fig.4.10a), we see that there is a range of μ where there are multiple solutions. If we plot these solutions as a function of μ then we obtain Fig.4.10b) where the magnetisation has an ‘S’ shape. The first order transition is a jump between the upper and lower branches of this function. To determine exactly where it occurs we use the Maxwell construction, which states that the transition occurs such that the two shaded areas in Fig.4.10c) are equal.

The first order transition being a jump in the magnetisation means that as a function of n the transition becomes a region of phase separation where regions of both high and low m co-exist. The volume of these regions changes so that the average magnetisation interpolates between the high and low values. This also occurs when considering the phase diagram as a function of m rather than h . The effects considered here are related to the first-order transition and disappear when the transition becomes continuous. Thus the line of critical endpoints, which we are primarily concerned with, is unaffected.

4.2 Inhomogeneous phase diagram

Having discussed how features in the density of states can lead to metamagnetism, we show that they can also lead to spatial modulation of the magnetism. We begin with a discussion of the transverse susceptibility and the energetic reasons for forming modulation. We then discuss the explicit gradient expansion of the Stoner action. Motivated by this we construct a phase diagram from the Ginzburg-Landau phenomenology.

4.2.1 Cartoon for inhomogeneous phase formation

In order to get a physical picture of why inhomogeneous magnetisation is favourable we will consider the way in which the energy dispersions are altered by inhomogeneity and how this appears in terms of peaks in the density of states. The formation of a spiral magnetisation state involves hybridizing spin-up and -down electrons. The dispersion of the hybridised state is given by

$$2E_{\mathbf{k},\mathbf{q}}^{\pm} = \left(\epsilon_{\mathbf{k}+\mathbf{q}/2} + \epsilon_{\mathbf{k}-\mathbf{q}/2} \right) \pm \sqrt{\left(\epsilon_{\mathbf{k}+\mathbf{q}/2} - \epsilon_{\mathbf{k}-\mathbf{q}/2} + gm_{\parallel} + h \right)^2 + (gm_{\perp})^2}, \quad (4.32)$$

where m_{\parallel} and m_{\perp} are the components of magnetisation parallel and perpendicular to the applied field h and \mathbf{q} is the wavevector of the modulation. The prescription for constructing the hybridised Fermi surfaces can be seen from this form. The spin-split Fermi surfaces of the homogeneous state are displaced by $\pm\mathbf{q}/2$. The transverse magnetisation then acts as an interaction hybridising the two bands Fig.4.11a) shows the Fermi surfaces of the homogeneous state. Fig.4.11b) shows the undistorted Fermi surfaces shifted by $\pm\mathbf{q}$. The development of transverse magnetisation then hybridises the bands, leading to the dispersion shown in Fig.4.11c).

The anti-crossing where the undistorted bands are degenerate results in the appearance of additional saddle-points in the dispersion, as is illustrated in Fig.4.12. These saddle points produce additional peaks in the density of states, shown in Fig.4.13. We see that while the original Fermi surface lies just below a peak in the density of states, the Fermi surface in the new dispersion lies between the old and new peaks. By occupying the states under this new peak the formation of spiral magnetisation reduces the energy cost in forming the transverse magnetisation, the same mechanism as in the homogeneous Stoner magnetism.

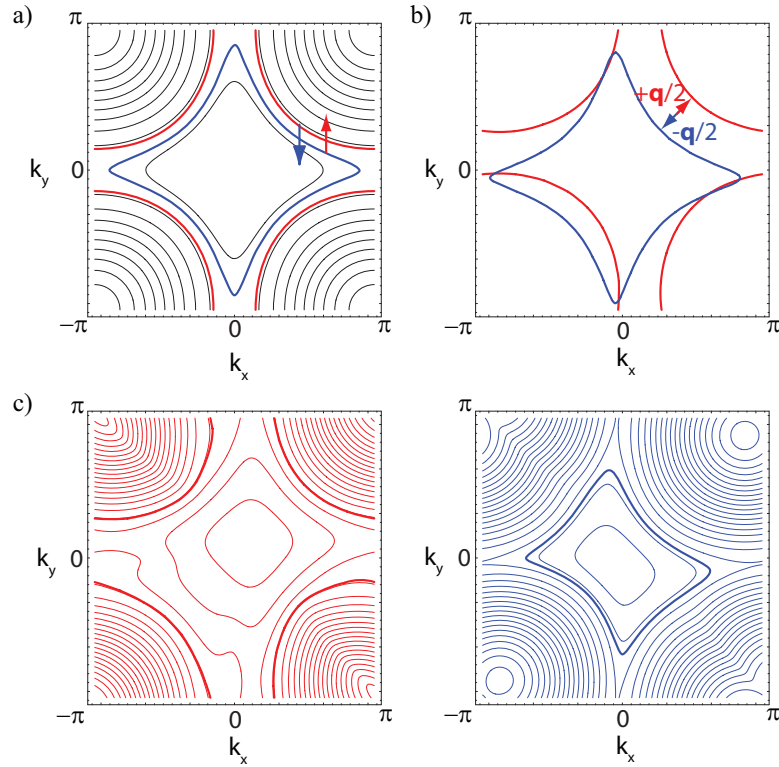


Fig. 4.11: Fermi surface reconstruction due to formation of spiral magnetism: a) Spin-up and -down Fermi surfaces for homogeneous magnetisation. b) Displacement of Fermi surface by $\pm\mathbf{q}/2$ illustrating nesting. c) Fermi surfaces after hybridisation. Contours of the energy dispersion are also shown.

The tendency of the system to form order at any wavevector is encoded in the \mathbf{q} -dependent susceptibility. We consider modulation in the component of the magnetisation transverse to the applied field. The susceptibility for transverse magnetisation is

$$\begin{aligned}
 \Pi_{\perp}(\mathbf{q}) &= \frac{1}{\beta L^d} \sum_{\mathbf{k}} G_{\uparrow}(\mathbf{k}) G_{\downarrow}(\mathbf{k} + \mathbf{q}) \\
 &= \sum_{\mathbf{k}} \frac{n_{\text{F}}\left(\epsilon_{\mathbf{k}+\mathbf{q}} - \mu - \frac{g\bar{M}}{2}\right) - n_{\text{F}}\left(\epsilon_{\mathbf{k}} - \mu + \frac{g\bar{M}}{2}\right)}{\epsilon_{\mathbf{k}} - \epsilon_{\mathbf{k}+\mathbf{q}} + g\bar{M}}
 \end{aligned} \tag{4.33}$$

from Eq.4.24 including the full \mathbf{q} -dependence, where $n_{\text{F}}(\epsilon - \mu) = \left(1 + e^{\beta(\epsilon - \mu)}\right)^{-1}$ is the Fermi-Dirac distribution, \mathbf{q} is the wavevector of modulation and \bar{M} is a shifted magnetisation which includes the external field $\bar{M} \mapsto \bar{M}' = \bar{M} + \frac{2}{g}h$. This may be evaluated for all \mathbf{q} at any point (μ, \bar{M}, T) in the phase diagram [81]. Within this

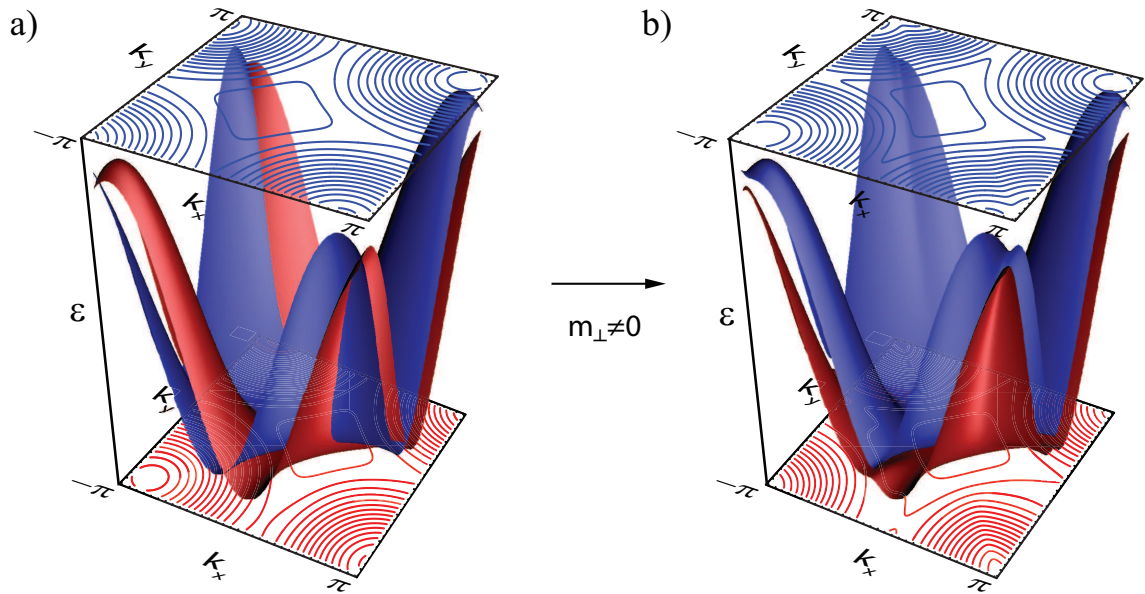


Fig. 4.12: Anticrossing of bands: a) Energy dispersions for the spin-up (red) and spin-down (blue) Fermi surfaces shifted by $\pm\mathbf{q}/2$. b) Energy dispersions including a transverse magnetisation. This hybridises the bands, causing anticrossing and the formation of new saddle points.

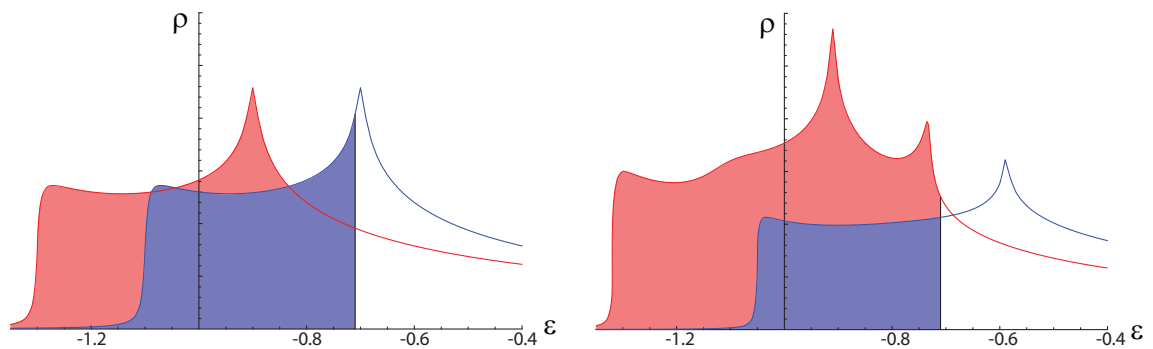


Fig. 4.13: Density of states for the spiral state: Density of states for original (left) and hybridised (right) dispersions. The formation of the spiral state produces a new peak in the density of states. The Fermi surface lies between this and the original peak.

model we find plenty of scope for the formation of modulated states at a variety of different wavevectors. Fig.4.14 shows the transverse susceptibility evaluated for several points on the metamagnetic transition. This plot shows that the susceptibility has peaks both at high and low wavevector. These peaks are related to the partial nesting wavevectors of the Fermi surface. We see from 4.33 that when a displacement of the Fermi surface by \mathbf{q} overlaps significantly with the original Fermi surface then the denominator is minimised and the distortion is favoured. Nesting vectors corresponding to the peaks in the susceptibility and the Fermi surfaces after hybridisation are shown in Fig.4.14.

We note that the wavevector of the distortion in this picture may be a substantial fraction of the Brillouin zone. These cartoons also allow us to deduce how the wavevector of the modulation depends on the position within the phase diagram. Wavevectors such as \mathbf{q}_1 and \mathbf{q}_3 in Fig.4.14 correspond to nesting the same side of the Fermi surface on each spin species. This wavevector increases as the magnetization, and therefore the splitting of the Fermi surfaces, increases. The further from van Hove filling the larger the magnetization required to reach the metamagnetic transition and therefore the larger the wavevector at the transition. Vectors corresponding to nesting opposite sides of the Fermi surfaces will not change with magnetization, as while one Fermi surface expands, the other contracts, leaving a constant distance between opposite edges. Vectors such as \mathbf{q}_4 correspond to the distance from one Fermi surface to the van Hove singularity. These are linked to the size of the metamagnetic transition, which is related to how far the Fermi surface has to move to jump over the peak in the density of states.

The nesting vectors of course depend on the Fermi surface shape and those considered in this simple picture may not correspond to those found in a real material like $\text{Sr}_3\text{Ru}_2\text{O}_7$. Nevertheless this shows that such tendencies to modulation exist, even in simple models ¹.

¹ The simplest model - the half-filled nearest-neighbour tight-binding dispersion - is in fact *perfectly* nested. Its Fermi surface overlaps itself perfectly at half filling and is completely gapped away when hybridisation occurs. This model is therefore unstable to being an antiferromagnetic band insulator. The addition of next-nearest-neighbour interactions suppresses this tendency.

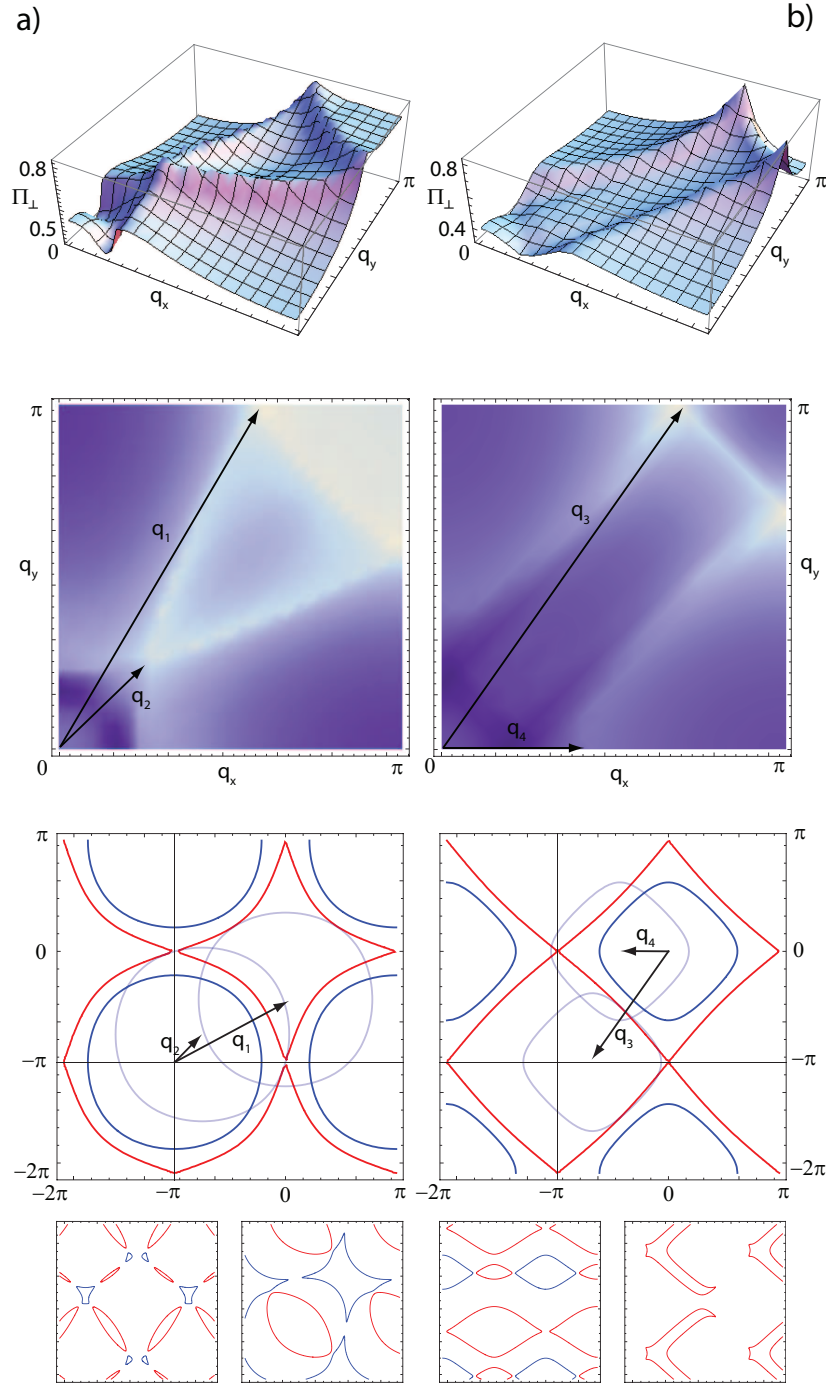


Fig. 4.14: Transverse susceptibility and nesting vectors: The transverse susceptibility evaluated for a) $t = 0.8$, $\mu = -0.6$, $\bar{M} = 0.235$ and b) $t = 0.2$, $\mu = -0.45$, $\bar{M} = 0.294$. This shows peaks at large and small \mathbf{q} . Note that the jagged ridges in a) are an artifact of the numerical calculation. Also shown are the nesting vectors which these peaks correspond to in the Fermi surface and the Fermi surface of the modulated state which is produced.

4.2.2 Free energy with inhomogeneity

It should be possible to calculate the phase diagram for the mean-field free energy in a similar way as for the homogeneous case. Taking the Grand Potential

$$\Omega = \int d\epsilon \ln \left(1 + e^{-\beta(\epsilon - \mu)} \right), \quad (4.34)$$

we substitute in the energy for the spiral state (Eq.4.32) to obtain $\Omega(\mathbf{q}, m, m_{\perp})$. We should then be able to calculate self-consistency equations for m , m_{\perp} and \mathbf{q} .

$$\begin{aligned} m &= \partial_h \Omega, \\ m_{\perp} &= \partial_{h_{\perp}} \Omega, \end{aligned} \quad (4.35)$$

where we have artificially introduced a conjugate field to the transverse magnetisation, h_{\perp} , which we take to zero. The calculation for \mathbf{q} may be simplified by expanding the free energy in \mathbf{q} and finding the minimum of this expansion, before substituting back in to the free energy.

$$\begin{aligned} \Omega(m, m_{\perp}, q) &\approx \Omega(0) + \frac{1}{2} \partial_q^2 \Omega(m, m_{\perp}, 0) q^2 + \frac{1}{4!} \partial_q^4 \Omega(m, m_{\perp}, 0) q^4 \\ \bar{q}^2 &= -6 \frac{\partial_q^2 \Omega(m, m_{\perp}, 0)}{\partial_q^4 \Omega(m, m_{\perp}, 0)} \end{aligned} \quad (4.36)$$

Calculating the phase diagram this way is however complex and numerically hard. We will proceed to analyze the favourability of spiral magnetisation in a Ginzburg-Landau expansion.

4.2.3 Gradient expansion

Having found the phase diagram for homogeneous magnetisation and motivated the possibility of inhomogeneous states, we calculate the phase diagram including such phases. We wish to consider whether inhomogeneous magnetic states are more favourable over any region of the phase diagram than the homogeneous ferromagnetic or paramagnetic states. Such inhomogeneous states will produce extra contributions to the free energy dependent on the magnetisation gradient which we now calculate.

We consider a situation where the transverse component of magnetisation is inhomogeneous. Whilst spatial modulation of the longitudinal magnetisation is possible, it does not lead to the type of phase reconstruction studied here. We will neglect terms in the free energy corresponding to gradients of the longitudinal magnetisation

for simplicity. We further restrict our study to systems with inversion symmetry. In this case, terms linear in the gradient are forbidden by symmetry— inhomogeneity in this model is not the result of a Dzyaloshinskii-Moriya interaction [21, 82, 83].

Transforming to the momentum representation spatial gradients become wavevectors \mathbf{q} . Continuing in the spirit of a Ginzburg-Landau theory we may expand the coefficients of the Landau expansion in powers of these wavevectors. This approach is valid when considering small wavevector features. As we will later argue it is not necessary for the structure of the phase diagram that the inhomogeneity is at small \mathbf{q} . However, we will restrict our explicit analysis to cases where this expansion is valid and carry our conclusions across to the more general case with appropriate modifications.

In order to simplify our analysis, we study a simple form of inhomogeneity, namely a spiral $\phi_{\perp}(\mathbf{r}) = \phi_{\perp}(\cos \mathbf{q} \cdot \mathbf{r}, \sin \mathbf{q} \cdot \mathbf{r})$, where \mathbf{q} is the wavevector of the spiral. This is the magnetic analogue of the Fulde-Ferrell ansatz [27] where only one wavevector is considered. As in the superconducting LOFF state the most stable inhomogeneous phase may consist of spirals with several different \mathbf{q} -vectors superposed, creating a ‘crystalline’ structure [60, 84]. The competition between such states is complex and will not be considered here. With this simplifying ansatz, the free energy has the form

$$\begin{aligned}
 F = h\bar{M} & \left[(R\phi^2 + U\phi^4 + T\phi^5 + V\phi^6 - H\phi) \right. \\
 & + (U_{\perp} + K_{\perp}\mathbf{q}^2 + L_{\perp}\mathbf{q}^4 + \{S_1 + K_1\mathbf{q}^2\}\phi \\
 & \quad \left. + \{U_1 + K_2\mathbf{q}^2\}\phi^2 + T_1\phi^3 + V_1\phi^4) \phi_{\perp}^2 \right. \\
 & \left. + (K_3\mathbf{q}^2 + U_{\perp} + T_2\phi + V_2\phi^2) \phi_{\perp}^4 + V_{\perp}\phi_{\perp}^6 \right], \quad (4.37)
 \end{aligned}$$

where the terms L_{\perp} , K_1 , K_2 and K_3 are required to bound the free energy for the case of non-zero \mathbf{q} . In order to calculate the expressions for the gradient terms, we return to the transverse susceptibility equation (4.24) and allow for the previously neglected momentum dependence. Expanding the Green’s function gives

$$\begin{aligned}
 G_{\sigma}(\mathbf{k} + \mathbf{q}) = G_{\sigma}(\mathbf{k}) & + [G_{\sigma}(\mathbf{k})]^2 \partial_{k_i} \epsilon_{\mathbf{k}} q_i \\
 & + \left([G_{\sigma}(\mathbf{k})]^3 \partial_{k_i} \epsilon_{\mathbf{k}} \partial_{k_j} \epsilon_{\mathbf{k}} + \frac{1}{2} [G_{\sigma}(\mathbf{k})]^2 \partial_{k_i, k_j}^2 \epsilon_{\mathbf{k}} \right) q_i q_j + O(q^3). \quad (4.38)
 \end{aligned}$$

The first term in this expansion gives the homogeneous term already considered.

Terms of first order in \mathbf{q} cannot contribute to the action due to the symmetry of the electronic dispersion. In other words, the energy cannot depend on the *sign* of the gradient. Otherwise one particular direction, and not just axis, would be picked out. In a system with inversion symmetry this is impossible, though in non-centrosymmetric systems such terms exist. Mathematically, odd derivatives of the dispersion are antisymmetric in \mathbf{k} and so give zero on integration.

Expanding the second order term of the Stoner action 4.25 to second order in \mathbf{q} we find

$$\mathcal{S}_{\perp}^{(2)} = \beta \int d^d r \left[r_{\perp} \mathbf{m}_{\perp}^2 + K_{\perp} \mathbf{q}^2 \right], \quad (4.39)$$

where r_{\perp} is as before and

$$K_{\perp} = -\frac{1}{4g\bar{M}^3} \frac{1}{L^d} \sum_{\mathbf{k}\sigma} \left[\sigma n_{\text{F}}(\epsilon_{\mathbf{k}} - g\bar{M}\sigma/2) + \frac{g\bar{M}}{2} n_{\text{F}}^{(1)}(\epsilon_{\mathbf{k}} - g\bar{M}\sigma/2) \right] (\partial_{\mathbf{k}} \epsilon_{\mathbf{k}})^2. \quad (4.40)$$

Although the coefficient K_{\perp} is independent of the direction of \mathbf{q} this is not true for all coefficients. Higher order terms such as L_{\perp} (which is 4th order in \mathbf{q}) are anisotropic and pin the wavevectors to specific directions in the lattice. In the square lattice, the isotropic component, $(\partial^2 \phi_{\perp})^2$, is augmented by a term proportional to $(\partial_x^2 \phi_{\perp}) \cdot (\partial_y^2 \phi_{\perp})$. Since we are considering a lattice with square symmetry, there will be at least four degenerate directions along which \mathbf{q} -vectors could lie. The K_1 , K_2 and K_3 terms may also be calculated by gradient expansions of the appropriate terms, although for simplicity we will not consider their explicit forms.

K_{\perp} is the leading order tendency to formation of spiral magnetisation. We may numerically evaluate this coefficient at every point along the line of metamagnetic critical endpoints. We find that it varies smoothly as we move along the transition and in fact becomes negative as we move to μ further from the van Hove singularity, as shown in Fig.4.15. This shows an instability to the formation of spatially modulated magnetisation along the metamagnetic transition. We will use this fact to build a phase diagram for the formation of inhomogeneous magnetisation along the metamagnetic transition.

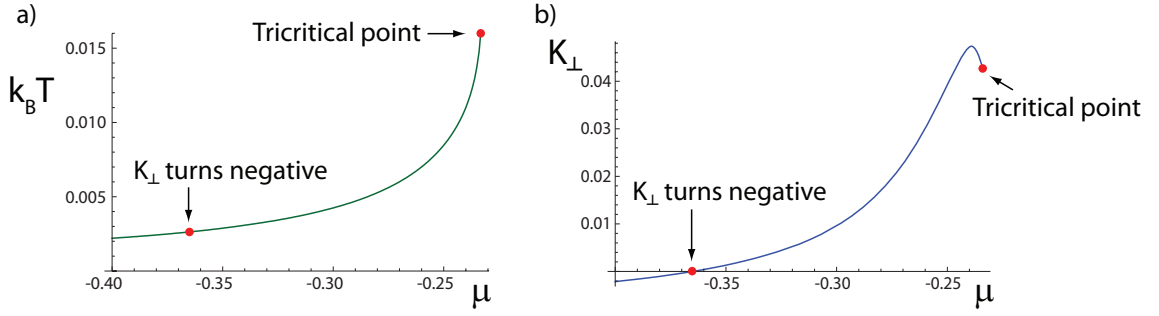


Fig. 4.15: **Evaluation of K_{\perp}** : a) The line of metamagnetic critical endpoints in the μ , T plane. Shown are the tricritical point and the point at which K_{\perp} turns negative. b) K_{\perp} evaluated along the line of critical endpoints. This varies smoothly and turns negative at a certain distance from the tricritical point. Calculations performed for the dispersion $\epsilon_{\mathbf{k}} = -(\cos k_x + \cos k_y) + t \cos k_x \cos k_y$, parameters $t = 0.2$, $g = 1.7$.

4.2.4 Relation to FFLO

We now consider how this relates to the analysis in the LOFF case. We consider an isotropic dispersion and linearise about the Fermi surface, assuming that all contributions to the integrals come from the Fermi surface, where derivatives of the Fermi-Dirac distribution are non-zero. In this case the expansion of the longitudinal magnetisation to quadratic order in \mathbf{q} gives a coefficient $K \propto U$. In the case of zero external field we have

$$\begin{aligned}
 U &= \frac{1}{4!} \left(\frac{g}{2}\right)^4 \frac{1}{L^d} \sum_{\mathbf{k}\sigma} n_{\mathbf{F}}^{(3)}(\epsilon), \\
 K &= -\frac{1}{4!} \left(\frac{g}{2}\right)^2 \frac{1}{L^d} \sum_{\mathbf{k}\sigma} n_{\mathbf{F}}^{(3)}(\epsilon_{\mathbf{k}}) (\partial_{\mathbf{k}} \epsilon_{\mathbf{k}})^2 \\
 &\approx -\frac{1}{4!} \left(\frac{g}{2}\right)^2 \frac{1}{L^d} \sum_{\mathbf{k}\sigma} n_{\mathbf{F}}^{(3)}(\epsilon_{\mathbf{k}}) v_{\mathbf{F}}^2 \\
 &= \left(\frac{2}{g}\right)^2 v_{\mathbf{F}}^2 U,
 \end{aligned} \tag{4.41}$$

where $v_{\mathbf{F}}$ is the Fermi velocity. Since U becomes negative at the tricritical point this indicates that modulated states become favourable at the tricritical point and rather than simply turning first-order the transition occurs via an inhomogeneous phase as shown in Fig.4.16. There is in fact a series of relationships between the higher-order coefficients, which is necessary for the exact calculation of the phase diagram.

In the zero magnetisation limit the equations for spatially modulated magneti-

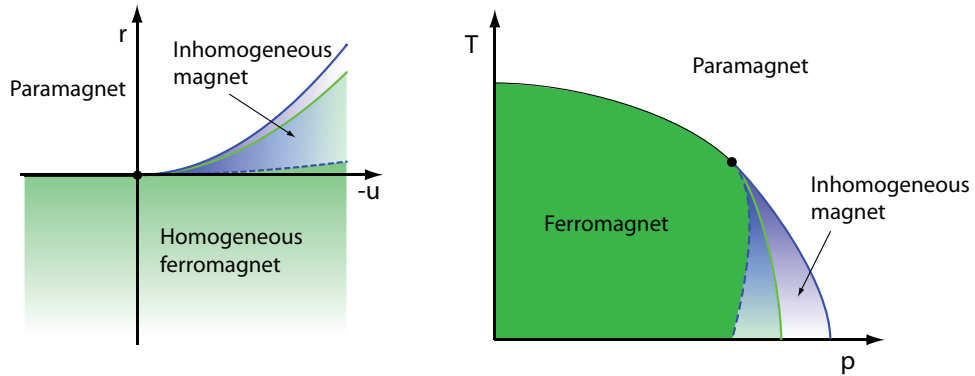


Fig. 4.16: Zero field phase diagram for a free electron dispersion: The first-order transition to the homogeneous ferromagnet is pre-empted by a transition to a modulated magnetic state because $K \propto u$, this then undergoes a transition into the homogeneous state. Blue lines are transitions into and out-of the inhomogeneous phase, the order of these transitions depends on the details of the Ginzburg-Landau theory, which we will not consider for this case. The green line shows where the first-order transition into the homogeneous magnetic state would occur if inhomogeneity did not intervene. On the right is this phase diagram mapped onto temperature and tuning parameter. We do not consider how the metamagnetic wing of Fig.4.6 would reconstruct. This situation is not realised in the realistic dispersion which we use and is included to make the comparison with LOFF (see for example [60]).

sation and superconductivity become equivalent [60, 85]. The Ginzburg-Landau expansion for the LOFF state shows the same relationships between Landau coefficients as just discussed. The appearance of the spatially modulated superconducting state is associated with the tricritical point, as shown in Fig.2.9. This form of relationship also arises in the study of quantum fluctuation corrections, leading to the formation of modulated states around the putative quantum critical point [32].

In the case which we are presently considering the metamagnetic transition is caused by proximity to van Hove singularities. In this situation the dispersion cannot be linearised about the Fermi surface and the full form must be used instead. In this case there is no simple relation as in LOFF. We will go on to show how modulated states appear around the metamagnetic transition in the case with the lattice dispersion.

4.2.5 Ginzburg-Landau phenomenology

We now consider the phenomenology of the inhomogeneous phase. We begin by including the necessary gradient terms in the free energy.

First order gradient terms cannot contribute by symmetry, so the first term that

must be added to the free energy density is $K_{\perp} (\nabla\phi_{\perp}(\mathbf{r}))^2$. Should the transverse magnetisation stiffness, K_{\perp} , become negative then there is an energetic gain in forming an inhomogeneous state. When $K_{\perp} < 0$ additional, higher order gradient terms are required in the free energy density: $L(\nabla^2\phi_{\perp})^2$, $K_2\phi^2(\nabla\phi_{\perp})^2$ and $K_3(\nabla\phi_{\perp})^2\phi_{\perp}$. Such a Ginzburg-Landau free energy is used, *mutatis mutandis*, to describe superconductors, where the LOFF state is signalled by a vanishing stiffness. We may, therefore, anticipate that a similar effect occurs in magnetisation, where the transition between low and high magnetisation states on the metamagnetic wing is split by the formation of an inhomogeneous magnetic phase.

In order to simplify our analysis, we study the simplest form of inhomogeneity, namely a spiral $\phi_{\perp}(\mathbf{r}) = \phi_{\perp}(\cos \mathbf{q} \cdot \mathbf{r}, \sin \mathbf{q} \cdot \mathbf{r})$, where \mathbf{q} is the wavevector of the spiral. With this simplifying ansatz, the free energy 4.15 including the effects of spatial modulation reduces to

$$\begin{aligned}
F = h\bar{M} & \left[\left(R\phi^2 + \frac{5}{8}\phi^4 + \frac{3}{8}\phi^5 + \frac{1}{16}\phi^6 - H\phi \right) \right. \\
& + \left(\frac{1}{2} + K_{\perp}\mathbf{q}^2 + L_{\perp}\mathbf{q}^4 + \{K_1\mathbf{q}^2 - \frac{1}{2}\} \phi \right. \\
& \quad \left. + \{K_2\mathbf{q}^2 + \frac{1}{2}\} \phi^2 + \frac{3}{4}\phi^3 + \frac{3}{16}\phi^4 \right) \phi_{\perp}^2 \\
& \left. + \left(K_3\mathbf{q}^2 - \frac{1}{8} + \frac{3}{8}\phi + \frac{3}{16}\phi^2 \right) \phi_{\perp}^4 + \frac{1}{16}\phi_{\perp}^6 \right]. \quad (4.42)
\end{aligned}$$

As we have shown from our microscopic calculation of K_{\perp} (equation 4.40 and figure 4.15) this coefficient varies smoothly along the line of metamagnetic critical endpoints and eventually turns negative. We will therefore use K_{\perp} as a parameter which represents movement along the metamagnetic wing. When this parameter turns negative it will be energetically favourable to form inhomogeneous transverse magnetisation. The formation of this inhomogeneity will reconstruct the metamagnetic transition, as we will shortly show. We will determine the phase diagram of the Ginzburg-Landau free energy (4.42) as a function of R , H and K_{\perp} . These coefficients parametrize directions within the metamagnetic wing, perpendicular to it and along the line of critical end points, respectively.

Finally, we note that such a model has a fundamental anisotropy due to the influence of the lattice and, strictly, this is reflected in the higher order gradient terms in Eq.(4.42). This anisotropy will determine the direction of \mathbf{q} , but does not affect the topology of the phase diagram and we do not treat it explicitly. We will now calculate the phase diagram for this free energy.

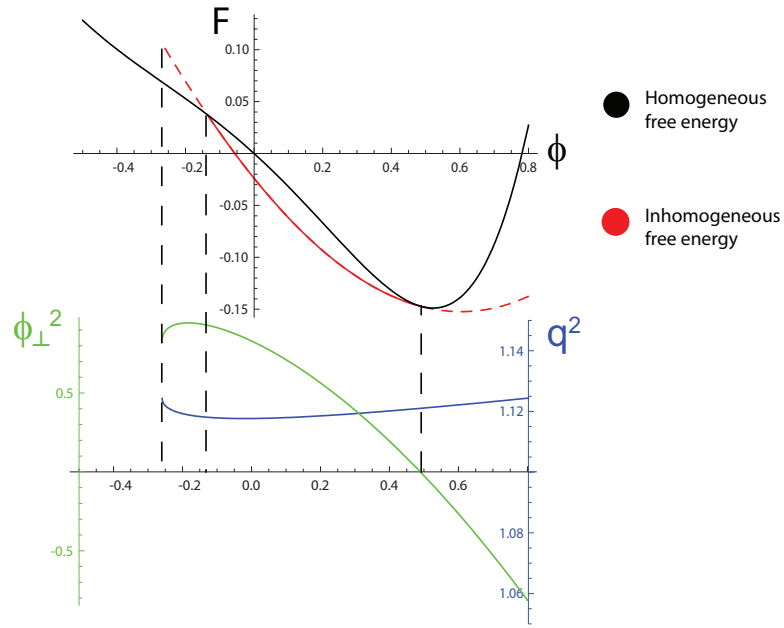


Fig. 4.17: Free energy for finite \mathbf{q} state: An example free energy curve. The black line is the homogeneous free energy, the red line is the free energy for the inhomogeneous state, the solid section is the physically realised region, the dotted sections are unphysical. Also shown are the optimum wavevector (blue) and the square of the transverse magnetisation (green). The point where the transverse magnetisation becomes imaginary is one of the boundaries of the physical homogeneous region. All quantities are obtained by minimisation of the free energy Eq.4.42 for an illustrative choice of R , H , K_{\perp} , L_{\perp} , K_1 , K_2 and K_3 .

4.2.6 Full phase diagram from Ginzburg-Landau phenomenology

Determining the phase diagram for Eq.4.42 involves locating the minima of the free energy as a function of ϕ , ϕ_{\perp} and \mathbf{q} . The broad scheme is as follows: Minimizing the free energy with respect to \mathbf{q} gives the optimum wavevector $\bar{\mathbf{q}}(\phi, \phi_{\perp})$. Focusing on this wavevector, minimization of the free energy with respect to ϕ_{\perp} gives the optimum inhomogeneous transverse magnetisation $\bar{\phi}_{\perp}(\phi)$. There is no real solution for $\bar{\phi}_{\perp}(\phi)$ over much of the phase diagram. This leads to a restricted region where inhomogeneity is allowed. This corresponds to the region in which the inhomogeneous terms of the free energy lower the total free energy, rather than raise it, as shown in Fig.4.17. The value of ϕ which minimizes the free energy therefore determines the longitudinal and transverse magnetisation, as well as the wavevector of the inhomogeneous magnetisation.

In general care must be taken with such a multi-component minimisation scheme. If the free energy has multiple minima as a function of one of the components then

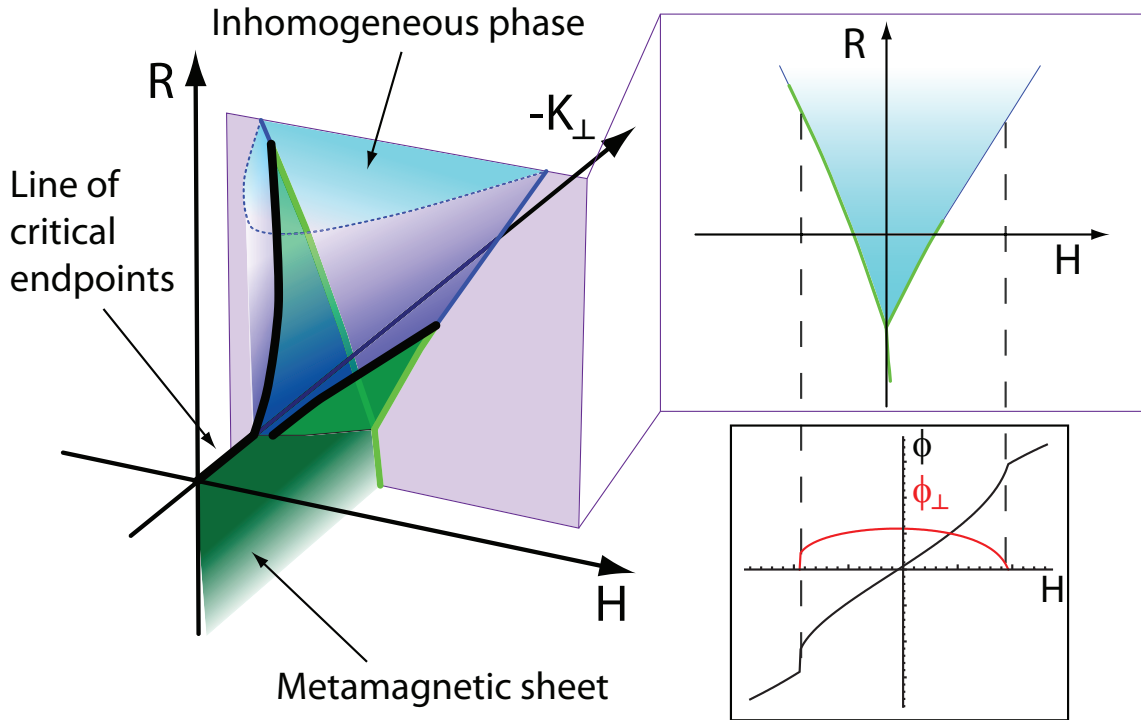


Fig. 4.18: Phase diagram for the Ginzburg-Landau theory: Green sheets represent first-order transitions in ϕ . Blue sheets represent continuous transitions into the inhomogeneous phase. A cut through the phase diagram at constant K_{\perp} is shown and the variation of ϕ and ϕ_{\perp} is plotted along a path through this cut, showing both first-order and continuous transitions.

the global minimum of the free energy may not be found if the wrong minimum is chosen early on. In the present case we are confident that we locate the global minima by this method.

There are many terms in the free energy and it is hard at first glance to understand the role of the various terms and how the phase diagram comes about. To clarify this we have performed an extensive study of the role of the various terms which we present in the next section.

Carrying out the minimization analysis results in the phase diagram indicated in Fig.4.18. In this figure, the line $R = H = 0$ is the parent line of metamagnetic critical end points. Upon moving along this line away from the tricritical point K_{\perp} reduces from a positive value, eventually becoming negative. When it becomes sufficiently negative, the metamagnetic sheet bifurcates into two wings. This structure is symmetry broken, or dislocated, in that the smaller first-order wing at higher fields does not emerge from the metamagnetic sheet at the same point as the larger wing. This phase diagram is very similar to the dislocated tricritical point of Green

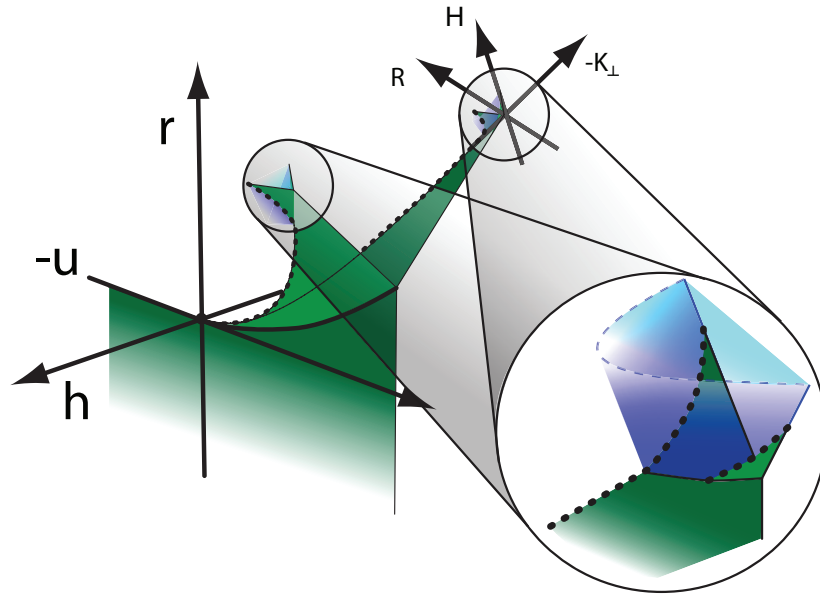


Fig. 4.19: Phase diagram in the context of the parent metamagnetic transition: Sketch showing how the phase diagram of Fig.4.18 fits into the phase diagram for the metamagnetic system. This consists of a rotated version of Fig.4.18 placed on the metamagnetic wing of Fig.4.6. The light blue region is the inhomogeneous magnetic phase, the dark green sheet is the $h = 0$ transition, the lighter green sheet is the metamagnetic transition.

et al. [70]. In the present case the bifurcation is caused by the appearance of the inhomogeneous phase which provides a ‘roof’ to the anomalous phase which is missing in the previous theory. This region of inhomogeneous magnetisation lies between the metamagnetic wings. Transitions into this inhomogeneous region occur in two different ways: In the first case, indicated by the green wings in Fig.4.18, the transition is first order in both the longitudinal and transverse magnetisation with a step change in the former and the latter appearing discontinuously from zero (and at finite \mathbf{q}). The second type of transition into the inhomogeneous region is indicated by the blue sheet in Fig.4.18. On this sheet the transverse magnetisation undergoes a second order transition, appearing continuously from zero. The longitudinal magnetisation undergoes a continuous transition with a step change in its gradient upon moving through this sheet. This kink is the ‘ghost’ of the transition in the transverse magnetisation.

Recalling that this phase diagram is constructed from an expansion about the line of critical endpoints the full phase diagram for the metamagnetic system is obtained by placing the bifurcated structure back into the context of the metamagnetic wing. The inhomogeneous phase then appears as shown in Fig.4.19.

4.2.7 Building up the Ginzburg-Landau expansion

The complexity of the Ginzburg-landau theory 4.42 makes it hard to identify the role of each term. In order to clarify this we break down the expansion and study the effect of each term one at a time. As well as having explanatory value this analysis will make explicit the process of calculating the phase diagram and reveal the fact that the smallness of \mathbf{q} is not necessary for the phase reconstruction which we find. We first consider a theory with no cross-terms between the magnetisation components. We then introduce the cross-terms until the theory has all of the symmetric terms. We then see how the remaining asymmetric terms alter the phase diagram.

No cross-terms

Initially we consider a theory without cross terms between ϕ and ϕ_{\perp} , and q -dependence in only the ϕ_{\perp}^2 term:

$$\begin{aligned} \frac{\beta}{hM} F(\phi, \phi_{\perp}, q) = & R\phi^2 + U\phi^4 + V\phi^6 \\ & + (R_{\perp} + K_{\perp}q^2 + L_{\perp}q^4) \phi_{\perp}^2 \\ & + U_{\perp}\phi_{\perp}^4 + V_{\perp}\phi_{\perp}^6. \end{aligned} \quad (4.43)$$

The longitudinal and transverse magnetisations are independent in this simple model. The combined phase diagram for both longitudinal and transverse magnetisation is shown in Fig.4.20. The main features are as follows: The longitudinal magnetisation displays a first order metamagnetic transition for $R < 0$ and $H = 0$ indicated by the dark green sheet in Fig.4.20. The line $R = 0$, $H = 0$ corresponds to the critical endpoint of this metamagnetic transition. Inhomogeneous transverse magnetisation appears beyond a certain negative value of K_{\perp} . The inhomogeneous phase extends over all R and H below this value of K_{\perp} .

Next, we apply the general procedure for determining the phase diagram, optimizing the free energy over \mathbf{q} and ϕ_{\perp} , and substituting these optimum values back into the free energy at each stage. Although the application of this procedure is straightforward in this simple case, it is useful to go through the analysis explicitly to orient us for the more complicated cases to come later. The optimum wavevector is $\bar{q} = \sqrt{-K_{\perp}/2L_{\perp}}$ (found by solving $\partial_q F = 0$). Since there are no cross terms in the simplified free energy 4.43, the optimum wavevector is independent of ϕ .

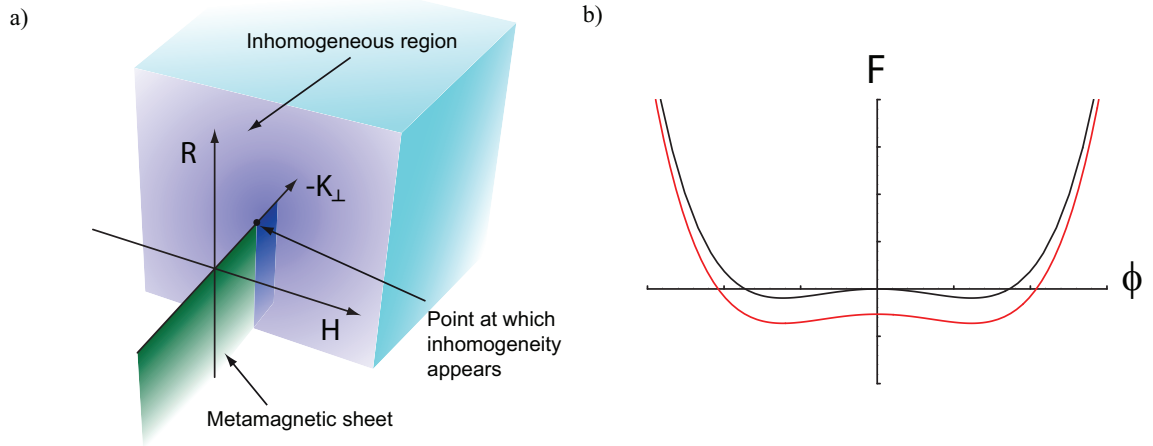


Fig. 4.20: Phase diagram for reduced theory: a) Phase diagram for a theory with no cross terms. b) free energy with homogeneous terms only (black) and inhomogeneous terms (red). L_{\perp} is taken as 0.1.

Substituting \bar{q} into Eq.4.43 we get an effective free energy

$$\begin{aligned} \frac{\beta}{hM} F_{\text{eff}}(\phi, \phi_{\perp}) &= R\phi^2 + U\phi^4 + V\phi^6 + \left(R_{\perp} - \frac{K_{\perp}^2}{4L_{\perp}}\right) \phi_{\perp}^2 \\ &\quad + U_{\perp}\phi_{\perp}^4 + V_{\perp}\phi_{\perp}^6. \end{aligned} \quad (4.44)$$

Optimizing over ϕ_{\perp}^2 gives

$$\bar{\phi}_{\perp}^2 = \frac{-2U_{\perp} + \sqrt{4U_{\perp}^2 - 12V_{\perp}R'_{\perp}}}{6V_{\perp}} \quad (4.45)$$

where $R'_{\perp} = R_{\perp} - K_{\perp}^2/(4L_{\perp})$. A real, non-zero solution of this equation for $\bar{\phi}_{\perp}$ can only be obtained for $R'_{\perp} < 0$. When $\bar{\phi}_{\perp}^2$ is real and non-zero, the inhomogeneous terms contribute a negative constant to the free energy. Therefore, as soon as K_{\perp} becomes sufficiently negative, inhomogeneous terms will lower the free energy for all ϕ as shown in Fig.4.20. Using the values for the coefficients from the phenomenological analysis Eq.4.16 the critical value is $K_{\perp} = -\sqrt{5L_{\perp}/3}$.

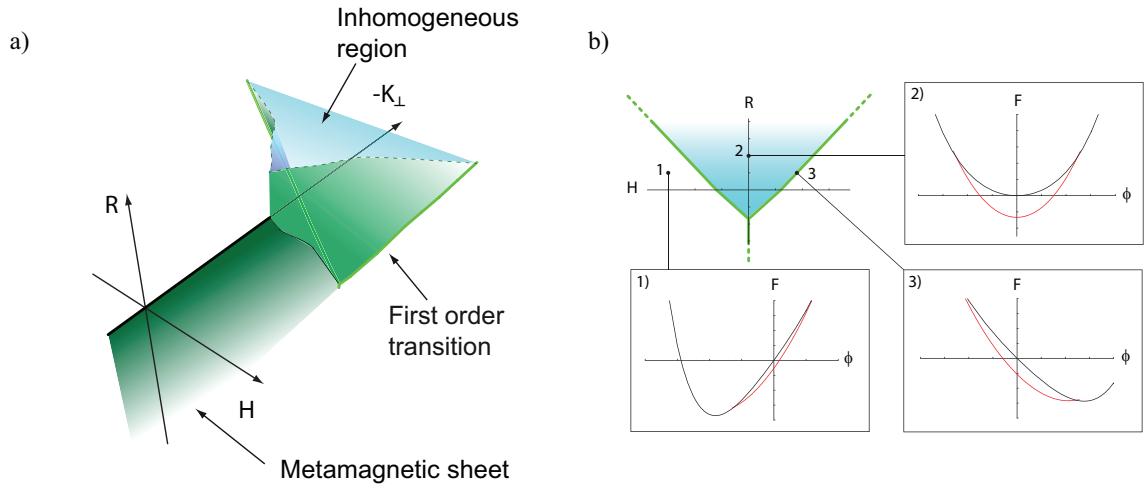


Fig. 4.21: Phase diagram for reduced theory: a) Phase diagram for a theory with a $U_1\phi^2\phi_\perp^2$ cross-term. b) A cut through the phase diagram at $K_\perp = -0.5$ with example free energy curves. Note the first order transition in panel 3 where there are two degenerate minima. [We take $L_\perp = 0.1$]

Cross-terms: adding the $U_1\phi^2\phi_\perp^2$ term

Next, we include symmetric cross-terms that couple ϕ and ϕ_\perp . Including a term $U_1\phi^2\phi_\perp^2$, the free energy becomes,

$$\begin{aligned} \frac{\beta}{hM}F(\phi, \phi_\perp, q) &= R\phi^2 + U\phi^4 + V\phi^6 \\ &+ (R_\perp + K_\perp q^2 + L_\perp q^4 + U_1\phi^2)\phi_\perp^2 \\ &+ U_\perp\phi_\perp^4 + V_\perp\phi_\perp^6. \end{aligned} \quad (4.46)$$

The phase diagram corresponding to this free energy is shown in Fig.4.21. The addition of cross terms between longitudinal and transverse magnetisation leads to interdependence between the components and additional structure in the phase diagram. Before turning to the derivation of the phase diagram, we discuss its main features. For small K_\perp the longitudinal magnetisation has a single metamagnetic transition. At sufficiently negative K_\perp , the formation of inhomogeneous transverse magnetisation becomes favourable. The metamagnetic wing splits into a Y shape, as shown in the cut through the phase diagram in Fig.4.21. The arms and leg of the Y are first order transitions in both ϕ and ϕ_\perp and extend to infinity. Between the arms of this Y the transverse magnetisation is inhomogeneous.

Now let us discuss how this phase diagram follows from the free energy given in Eq.4.46. The result of introducing cross terms between longitudinal and transverse

magnetisation is that real, non-zero solutions for the transverse magnetisation exist in a restricted range of longitudinal magnetisation and hence H . Our analysis proceeds as before by finding the optimum wavevector $\bar{\mathbf{q}}$ and optimum transverse magnetisation $\bar{\phi}_\perp$ and substituting them back into the free energy to obtain an effective free energy $F_{\text{eff}}(\phi)$. We will then present a graphical analysis of this free energy to give a feel for the main structure of the phase diagram and end by showing analytically why all of the phase transitions between homogeneous and inhomogeneous phases are first order in this simplified theory.

The optimum wavevector, $\bar{q} = \sqrt{-K_\perp/2L_\perp}$, remains the same as before. Substituting into Eq.4.46 gives

$$\begin{aligned} \frac{\beta}{hM} F_{\text{eff}}(\phi, \phi_\perp) &= R\phi^2 + U\phi^4 + V\phi^6 + \left(R_\perp - \frac{K_\perp^2}{4L_\perp} + U_1\phi^2 \right) \phi_\perp^2 \\ &\quad + U_\perp\phi_\perp^4 + V_\perp\phi_\perp^6. \end{aligned} \quad (4.47)$$

The optimum transverse magnetisation calculated from this free energy is given by

$$\bar{\phi}_\perp^2 = \frac{-2U_\perp + \sqrt{4U_\perp^2 - 12V_\perp(R'_\perp + U_1\phi^2)}}{6V_\perp}, \quad (4.48)$$

where $R'_\perp = R_\perp - K_\perp^2/(4L_\perp)$.

The effective free energy as a function of ϕ , $F_{\text{eff}}(\phi)$, is obtained by substituting $\bar{\phi}_\perp^2$ from Eq.4.48 into $F_{\text{eff}}(\phi, \phi_\perp)$ (4.47). There are two subtleties in making this substitution. Firstly, in order that the free energy $F_{\text{eff}}(\phi)$ be an expansion in powers of ϕ , we Taylor expand Eq.4.48 for $\bar{\phi}_\perp^2$ before substitution. Secondly, we must allow for the fact that $\bar{\phi}_\perp^2$ is only real and non-zero in certain regions. We account for this by introducing step functions that restrict the inhomogeneous contributions to the free energy to regions where $\bar{\phi}_\perp^2$ is real and positive. Substituting $\bar{\phi}_\perp^2$ into $F_{\text{eff}}(\phi)$ accounting for these considerations results in an effective free energy

$$\begin{aligned} \frac{\beta}{hM} F_{\text{eff}}(\phi) &= R\phi^2 + U\phi^4 + V\phi^6 - H\phi \\ &\quad + (\alpha + \beta\phi^2 + \gamma\phi^4 + \delta\phi^6) \Theta(\theta)\Theta(\bar{\phi}_\perp^2) \end{aligned} \quad (4.49)$$

where

$$\alpha = \frac{2U_\perp^3 - 9R'_\perp U_\perp V_\perp - 2U_\perp^2 A + 6R'_\perp V_\perp A}{27V_\perp^2}$$

$$\begin{aligned}
\beta &= \frac{U_{\perp}(U_{\perp}^2 - 3R'_{\perp}V_{\perp} - U_{\perp}A)}{3V_{\perp}A} \\
\gamma &= -\frac{U_{\perp}^2}{4A} \\
\delta &= -\frac{U_{\perp}^3V_{\perp}}{8A^3} \\
A &= \sqrt{U_{\perp}^2 - 3R'_{\perp}V_{\perp}} \\
\theta &= 4U_{\perp}^2 - 12V_{\perp}R'_{\perp}
\end{aligned} \tag{4.50}$$

We now turn to a more detailed look at the transitions into and out of the inhomogeneous phase. In the first instance, rather than delve into the complicated analytical details of the free energy, we present a graphical discussion. Fig.4.21b) shows the free energy plotted at various points on the phase diagram. The black curve is the free energy with no contribution from inhomogeneity in the transverse magnetisation. The red curve shows the free energy with the effect of inhomogeneity in the transverse magnetisation; *i.e* in the region where the step functions in Eq.4.49 are 1. We see that for low and high H the global minimum of the free energy lies on the homogeneous (black) curve. The free energy is minimised by a value of ϕ which corresponds to $\bar{\phi}_{\perp} = 0$ and the system is in the homogeneous state. For low H we see that the global minimum lies on the inhomogeneous (red) curve. The inhomogeneous terms in the free energy have created an additional minimum of the free energy at low ϕ . For values of H for which this is the absolute minimum of the free energy the system is in the inhomogeneous state.

The nature of the transitions from one phase to the other depend on the magnetisations corresponding to the minima of the free energy when they are degenerate. Plotting the free energy at the transition point we see that there are two distinct local minima. The global minimum jumps discontinuously between the minimum in the homogeneous region and the minimum in the inhomogeneous region as H is varied. This results in a discontinuity in the optimum value of ϕ and a sudden jump to a non-zero value of ϕ_{\perp} . This is a first order transition in both longitudinal and transverse magnetisation. In fact, we may construct a rigorous argument why transitions between the homogeneous and inhomogeneous phases are first order in ϕ and ϕ_{\perp} in the present simplified theory. For a transition between the homogeneous and inhomogeneous phases to be second order $\bar{\phi}_{\perp}^2$ must be zero at the transitions. From 4.48 we see that there is no real solution for ϕ when $\bar{\phi}_{\perp}^2 = 0$ and, therefore, that the transitions into the inhomogeneous phase are always first order.

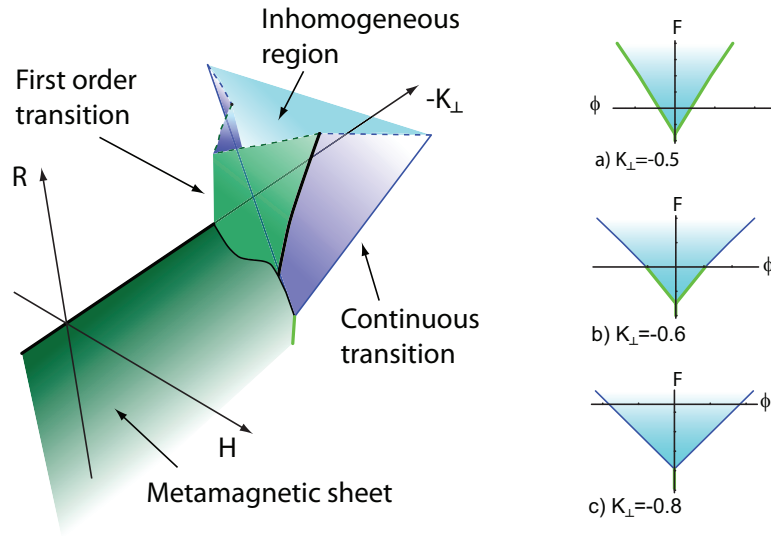


Fig. 4.22: **Phase diagram for reduced theory:** Phase diagram for a theory with $U_1\phi^2\phi_\perp^2$ and $V_2\phi^2\phi_\perp^4$ cross-terms. Cuts show a) $K_\perp = -0.5$, all transitions first order. b) $K_\perp = -0.6$, transitions change from first to second order at a critical point. c) $K_\perp = -0.8$, all transitions second order. [We take $L_\perp = 0.1$]

Cross-terms: adding the $V_2\phi^2\phi_\perp^4$ term

Adding a further cross-term $V_2\phi^2\phi_\perp^4$ the free energy becomes

$$\begin{aligned} \frac{\beta}{hM}F(\phi, \phi_\perp, q) &= R\phi^2 + U\phi^4 + V\phi^6 \\ &+ (R_\perp + K_\perp q^2 + L_\perp q^4 + U_1\phi^2)\phi_\perp^2 \\ &+ (U_\perp + V_2\phi^2)\phi_\perp^4 + V_\perp\phi_\perp^6. \end{aligned} \quad (4.51)$$

The phase diagram now takes the form shown in Fig.4.22. Many of the features of this phase diagram are the same as found in the preceding case. For a positive and weakly negative K_\perp there is a conventional metamagnetic transition. When K_\perp becomes sufficiently negative, this transition opens into a Y shape, the arms and leg of which extend to infinity. The region between the arms of the Y consists of a phase of inhomogeneous transverse magnetisation.

The main difference between the phase diagram obtained from Eq.4.51 (Fig.4.22) and that obtained from Eq.4.46 (Fig.4.21) is the order of the transitions between the homogeneous and inhomogeneous regions. In the case of Eq.4.46 these transitions were always first order in both longitudinal and transverse magnetisation. In the phase diagram of Eq.4.51 the transition may be either first order or continuous.

When the Y first appears the transition between homogeneous and inhomogeneous order is first order in both longitudinal and transverse magnetisation. At more negative values of K_{\perp} , the transition becomes continuous above a critical value of R — as indicated by the change from green to blue lines in Fig.4.22. Along these blue lines, the transition is second order in ϕ_{\perp} , with inhomogeneous transverse magnetisation appearing continuously from zero amplitude. The corresponding transition in longitudinal magnetisation is also continuous but with a discontinuity in its gradient; *i.e.* there is a kink in the longitudinal magnetisation.

The structure of this phase diagram can be understood as before by optimising the free energy over ϕ_{\perp} and q^2 and substituting back their optimum values to obtain an effective free energy for the longitudinal magnetisation ϕ . After substituting the optimum wavevector ($\bar{q}^2 = -K_{\perp}^2/2L_{\perp}$ as before) into Eq.4.51, the effective free energy is given by

$$\begin{aligned} \frac{\beta}{hM} F_{\text{eff}}(\phi, \phi_{\perp}) &= R\phi^2 + U\phi^4 + V\phi^6 \\ &+ \left(R_{\perp} - \frac{K_{\perp}^2}{4L_{\perp}} + U_1\phi^2 \right) \phi_{\perp}^2 \\ &+ (U_{\perp} + V_2\phi^2) \phi_{\perp}^4 + V_{\perp}\phi_{\perp}^6. \end{aligned} \quad (4.52)$$

The optimum value of ϕ_{\perp}^2 is

$$\bar{\phi}_{\perp}^2 = \frac{-2(U_{\perp} + V_2\phi^2)}{6V_{\perp}} + \frac{\sqrt{4(U_{\perp} + V_2\phi^2)^2 - 12V_{\perp}(R'_{\perp} + U_1\phi^2)}}{6V_{\perp}}. \quad (4.53)$$

The effective free energy $F_{\text{eff}}(\phi)$ may be obtained by substituting this expression into Eq.4.52, making the appropriate allowance for the region in which $\bar{\phi}_{\perp}^2$ is real and positive. The details of this final step are straightforward and not particularly illuminating.

Analysis of the expression for $\bar{\phi}_{\perp}^2$ allows us to deduce the order of transitions between the homogeneous and inhomogeneous regions of the phase diagram. This is determined by the value of $R'_{\perp} = R_{\perp} - K_{\perp}^2/(4L_{\perp})$. At a second order transition $\bar{\phi}_{\perp}$ must be zero. This occurs when the $U_{\perp} + V_2\phi^2$ term and the square root term of Eq.(4.53) are zero. These conditions are satisfied for real ϕ only when $R'_{\perp} < -\frac{1}{3}$. For $R'_{\perp} > -\frac{1}{3}$ all transitions must be first order. For $R'_{\perp} < -\frac{1}{3}$ transitions can be second order. This free energy gives first order transitions near to the point where

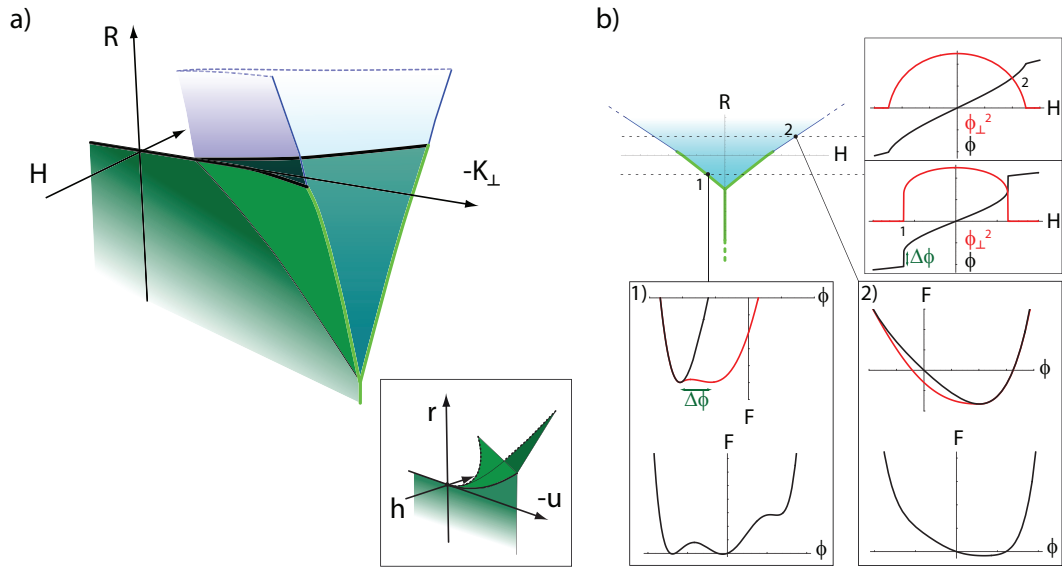


Fig. 4.23: Phase diagram for reduced theory: a) Phase diagram for the symmetric theory with particular choices for K_2 and K_3 . Inset shows the tricritical point structure of a conventional Landau theory. b) A cut through the phase diagram taken at $K_{\perp} = -1$ showing first order transitions below $R = 0.2$ and second order transitions above. Plots of the effective free energy show 1) a first order transition, and 2) a second order transition. The top free energy curve shows how this occurs for the inhomogeneous theory and the bottom for a conventional theory. Black curves are homogeneous terms only and red curves include inhomogeneous terms. Also shown are magnetisation plots as a function of H showing both longitudinal (black) and transverse (red) magnetisation. The magnitude of the jump in ϕ at the first order transition $\Delta\phi$ is related to the spacing of minima in the free energy. [We take $L_{\perp} = 0.1$, $K_2 = 0.3$ and $K_3 = 0.2$].

the inhomogeneous phase first appears, which become second order as we move to more negative K_{\perp} .

All symmetric terms

We now include the remaining symmetric terms from the free energy 4.37; $V_1\phi^4\phi_{\perp}^2$, $K_2q^2\phi^2\phi_{\perp}^2$ and $K_3q^2\phi_{\perp}^4$. The free energy with these additional terms is given by

$$\begin{aligned} \frac{\beta}{hM} F(\phi, \phi_{\perp}, q) &= R\phi^2 + U\phi^4 + V\phi^6 - H\phi \\ &+ (R_{\perp} + K_{\perp}q^2 + K_2q^2\phi^2 + L_{\perp}q^4 + U_1\phi^2 + V_1\phi^4) \phi_{\perp}^2 \\ &+ (U_{\perp} + K_3q^2 + V_2\phi^2) \phi_{\perp}^4 + V_{\perp}\phi_{\perp}^6, \end{aligned} \tag{4.54}$$

and the resulting phase diagram is shown in Fig.4.23. The phase diagram shares much the same structure as the preceding two cases shown in Figs. 4.21 and 4.22. The major modification is the location of the line of critical points where the transition between homogeneous and inhomogeneous order becomes first order. These lines now converge upon the parent line of metamagnetic critical end-points to form a tricritical point structure —although this is of a slightly unusual type due to the presence of inhomogeneity. As we will see in more detail below, the most important of the additional terms in driving this restructuring of the phase diagram is the $\mathbf{q}^2\phi_{\perp}^4$ term.

As in the preceding analysis, the phase diagram is obtained by considering an effective free energy for the longitudinal magnetisation, $\beta F_{\text{eff}}(\phi)$. The first step in deriving this effective free energy is to optimize over \mathbf{q} . Because of the additional, wavevector-dependent cross terms between ϕ and ϕ_{\perp} , $\bar{\mathbf{q}}$ is not constant, but depends upon ϕ and ϕ_{\perp} ;

$$\bar{q}^2 = -\frac{K_{\perp} + K_2\phi^2 + K_3\phi_{\perp}^2}{2L_{\perp}}. \quad (4.55)$$

Substituting this into Eq.(4.54) gives

$$\begin{aligned} \frac{\beta}{hM} F_{\text{eff}}(\phi, \phi_{\perp}) &= R\phi^2 + U\phi^4 + V\phi^6 - H\phi \\ &+ (R'_{\perp} + U'_{\perp}\phi^2)\phi_{\perp}^2 + (U'_{\perp} + V'_{\perp}\phi^2)\phi_{\perp}^4 \\ &+ V'_{\perp}\phi_{\perp}^6, \end{aligned} \quad (4.56)$$

where

$$\begin{aligned} R'_{\perp} &= R_{\perp} - \frac{K_{\perp}^2}{4L_{\perp}}, \\ U'_{\perp} &= U_{\perp} - \frac{K_3K_{\perp}}{2L_{\perp}}, \\ V'_{\perp} &= V_{\perp} - \frac{K_3^2}{4L_{\perp}}, \\ U'_1 &= U_1 - \frac{K_2K_{\perp}}{2L_{\perp}}, \\ V'_1 &= V_1 - \frac{K_2^2}{4L_{\perp}}, \\ V'_2 &= V_2 - \frac{K_2K_3}{2L_{\perp}}. \end{aligned} \quad (4.57)$$

The optimum value of ϕ_{\perp}^2 is given by

$$\bar{\phi}_{\perp}^2 = \frac{1}{6(V'_{\perp})} \left(-2(U'_{\perp} + V'_2\phi^2) + \sqrt{4(U'_{\perp} + V'_2\phi^2)^2 - 12V'_{\perp}(R'_{\perp} + U'_1\phi^2 + V'_1\phi^4)} \right). \quad (4.58)$$

The effective free energy as a function of ϕ , $F_{\text{eff}}(\phi)$ is found by substituting $\bar{\phi}_{\perp}^2$ from Eq.4.58 into Eq.4.56. As before, we Taylor expand the expression for $\bar{\phi}_{\perp}^2$ to obtain a power series in ϕ and include step functions to restrict inhomogeneous contributions to the free energy to regions where $\bar{\phi}_{\perp}^2$ is real and positive. After doing this, we obtain,

$$\frac{\beta}{hM} F_{\text{eff}}(\phi) = R\phi^2 + U\phi^4 + V\phi^6 - H\phi + (\alpha + \beta\phi^2 + \gamma\phi^4 + \delta\phi^6) \Theta(\theta)\Theta(\bar{\phi}_{\perp}^2). \quad (4.59)$$

This has exactly the same form as Eq.4.49, the only difference being the dependence of the parameters α , β and γ upon the control parameters K_{\perp} , H and R ;

$$\begin{aligned} \alpha &= \frac{2U_{\perp}^3 - 9R'_{\perp}U'_{\perp}V'_{\perp} - 2U_{\perp}^2A + 6R'_{\perp}V'_{\perp}A}{27V_{\perp}^{\prime 2}} \\ \beta &= \frac{-2U_{\perp}^3V'_2 - 3R'_{\perp}V'_{\perp}(3B + V'_2A) + U_{\perp}^2(3B + 2V'_2A) + U'_{\perp}(6R'_{\perp}V'_2V'_{\perp} - 3BA)}{9V_{\perp}^{\prime 2}A} \\ \gamma &= \frac{-8U_{\perp}^2V_2^{\prime 2} + 4U'_{\perp}V_2(3B + 2V'_2A) - 3V'_{\perp}(-4R'_{\perp}V_2^{\prime 2} + U'_{\perp}(3B + 4V'_2A))}{36V_{\perp}^{\prime 2}A} \\ \delta &= \frac{-16U_{\perp}^3V_2^{\prime 3} + 16U_{\perp}^2V_2^{\prime 3}A + 18U'_{\perp}V_2^{\prime 2}V'_{\perp}(4R'_{\perp}V_2^{\prime 2} + 3U'_{\perp}B) - 3V'_{\perp}(9B + 4V'_2A)}{216V_{\perp}^{\prime 2}A^3} \\ A &= \sqrt{U_{\perp}^2 - 3R'_{\perp}V'_{\perp}} \\ B &= U'_{\perp}V'_{\perp} \\ \theta &= 4(U'_{\perp} - V'_2\phi^2)^2 - 12V'_{\perp}(R'_{\perp} + U'_1\phi^2 + V'_1\phi^4) \end{aligned} \quad (4.60)$$

The phase diagram shown in Fig.4.23a) shows a marked similarity to that of a conventional tricritical point (inset to Fig.4.23a)). Indeed, the topology of the first order transitions in the phase diagrams — indicated by the green surfaces in Fig.4.23 — is identical. There are, however, important differences due to the phase of inhomogeneous transverse magnetisation which has produced the bifurcation. These similarities and differences are emphasized in the following discussion.

A cut through the phase diagram at negative K_{\perp} , as shown in Fig.4.23b), consists of a Y shape with arms and leg that extend to infinity. The arms begin by describing a first order transition in both longitudinal and transverse magnetisation — indicated in green. At a critical value of R , the order of the transition described by these arms changes — in a conventional tricritical point, the arm would stop here at a critical end point. Along the blue lines in Fig.4.23b) and over the entire blue surface in Fig.4.23a) a second order transition from zero to finite transverse inhomogeneous magnetisation is accompanied by a kink in the longitudinal magnetisation. This latter feature has no analogue near the conventional tricritical point. Tracking back towards positive K_{\perp} , the point at which the transition becomes continuous gets closer and closer to the junction of the Y until it coincides with it at the tricritical point.

These similarities and differences carry over to a comparison of the free energy curves. Such a comparison is made for typical points along the metamagnetic wing in Fig.4.23b). A first order transition occurs when local minima of the free energy at two different ϕ have the same free energy. As H is varied the global minimum jumps between these two minima. For the present theory one of the minima is in the inhomogeneous phase (shown in red) and the other in the homogeneous phase (shown in black). This leads to a jump in longitudinal magnetisation, $\Delta\phi$, and also a jump to non-zero inhomogeneous transverse magnetisation. For the conventional case there is no inhomogeneous phase, but the transition remains a jump between two homogeneous minima as shown in Fig.4.23b). As we move along the transition line in the direction of increasing R the size of the jump in magnetisation decreases. Along the blue line, the minimum of the free energy swaps continuously between the homogeneous (black) and inhomogeneous (red) curves. Near the conventional tricritical point there is no signature in the free energy along this line.

This structure of the bifurcated metamagnetic wings and the crucial role of the $K_3\mathbf{q}^2\phi_{\perp}^4$ term in leading to it can be appreciated from an analysis of Eq.4.58. This is simplified by restricting the analysis to the vicinity of the tricritical point so that ϕ - and ϕ_{\perp} -dependent terms can be neglected in equations 4.55 and 4.58. In this limit, the renormalized ϕ_{\perp}^4 coefficient is given by $U'_{\perp} = U_{\perp} + K_3\bar{q}^2$ in accord with Eq.4.57. In fact, the optimum wavevector is only weakly dependent upon ϕ and this is the dominant effect of the $K_3\mathbf{q}^2\phi_{\perp}^4$ term throughout the inhomogeneous regime. How does this affect the structure of the metamagnetic bifurcation? The change from first order to continuous transitions on the metamagnetic bifurcated wings follows

from the condition that at a second order transition, $\bar{\phi}_\perp$ must be zero. Near to the tricritical point this leads to the condition

$$-2U'_\perp + \sqrt{4U'^2_\perp - 12V_\perp R'_\perp} = 0. \quad (4.61)$$

If U'_\perp is negative (recall that $U_\perp = -1/8$) then this cannot be satisfied. If the renormalisation of U_\perp due to the the $K_3 \mathbf{q}^2 \phi_\perp^4$ term is large enough then U'_\perp becomes positive. The condition for a continuous transition becomes $R'_\perp < 0$, which is by definition satisfied in the inhomogeneous region, thus implying that the transition into the inhomogeneous region is continuous at the tricritical point.

Adding antisymmetric terms

When we add antisymmetric terms (such as ϕ^3 and $\phi\phi_\perp^2$), the tricritical point becomes symmetry broken or dislocated. A conventional Landau theory of a dislocated tricritical point was previously proposed by Green *et al* [70] to explain experimental data obtained from $\text{Sr}_3\text{Ru}_2\text{O}_7$. Whilst the latter theory did a good job of capturing the phase diagram obtained from longitudinal magnetic susceptibility, it could not accommodate the ‘roof’ over the region of anomalous transport found experimentally [52] (see Fig.3.3). The blue surface in Fig.4.24a) correctly reproduces the features of the roof. We may reorient the phase diagram to represent the dependence of the Landau coefficients on the experimental parameters. This is shown in Fig.4.24b). The sheet of continuous transitions becomes a roof after this transformation is made.

Finally, we comment upon the wavevector of the inhomogeneous order. So far we have assumed that this is small and performed a standard Ginzburg-Landau expansion in powers of \mathbf{q} . In fact, it is not necessary that \bar{q} be small in order to obtain the phase reconstruction discussed here. As indicated in our discussion of the role of the $K_3 \mathbf{q}^2 \phi_\perp^4$ term above, the optimum wavevector stays largely constant through the inhomogeneous phase. Its role is mainly to renormalise various homogeneous coefficients in the free energy. It is not necessary that \bar{q} be small in order to fulfil this role. The only requirement is that the inhomogeneous order become favourable at some point along the line of metamagnetic critical end-points upon moving away from the parent tricritical point. As we saw in the microscopic analysis, it is plausible that inhomogeneity occurs at either small or large wave-vectors depending upon the details of the electronic dispersion.

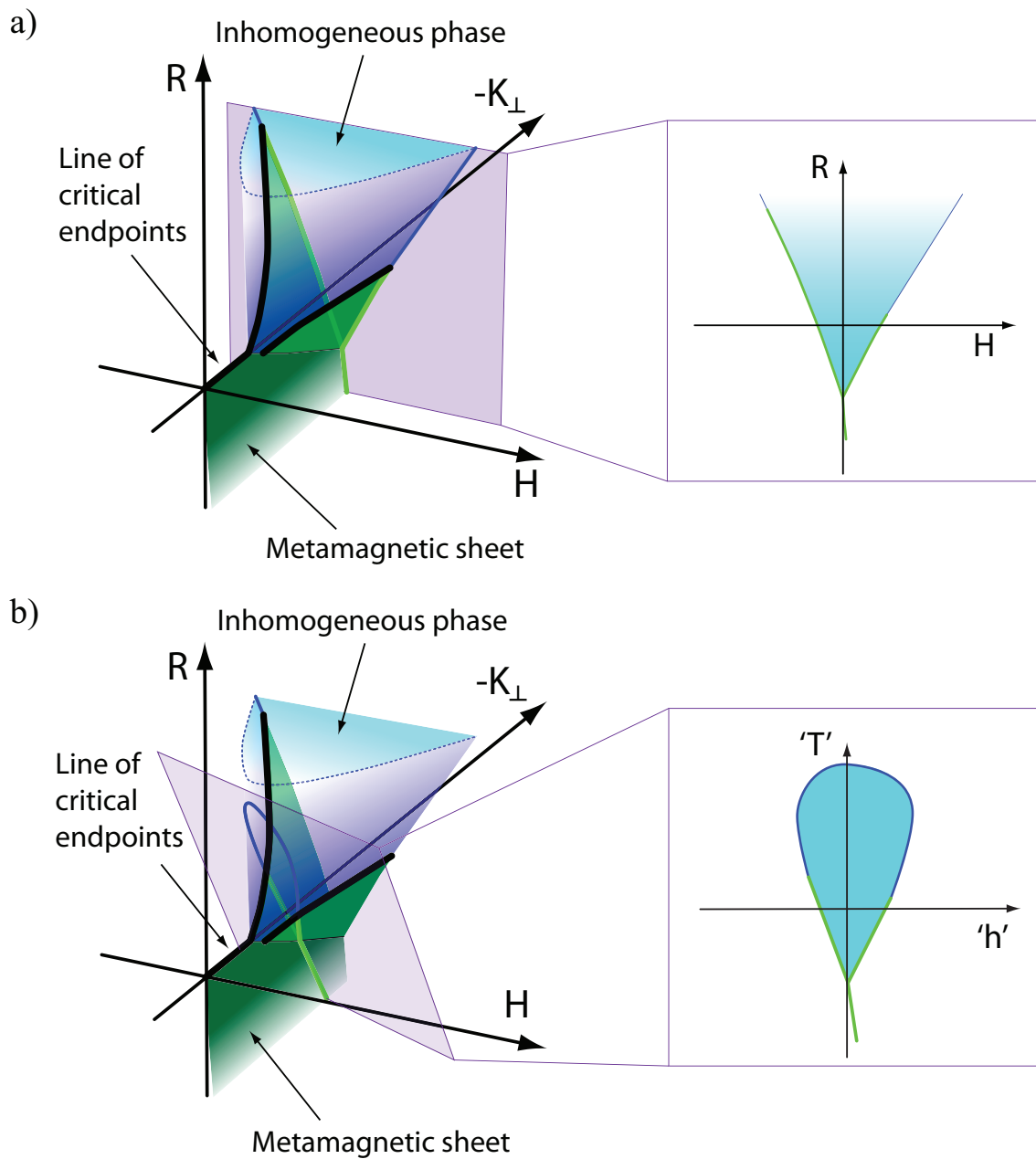


Fig. 4.24: Phase diagram for full theory: Phase diagram for the Ginzburg-Landau theory. Green sheets represent first-order transitions in ϕ . The vertical sheet is the metamagnetic sheet and the two 'wings' form the walls of the inhomogeneous phase. Blue sheets represent transitions into the inhomogeneous phase which are continuous in ϕ . K_{\perp} represents movement along the metamagnetic wing. H moves in a direction perpendicular to the wing. a) shows a vertical cut at some K_{\perp} . Solid blue lines indicate continuous transitions into the inhomogeneous phase and solid green lines indicate first order transitions. The inhomogeneous region extends to $R = \infty$. b) Taking a cut at an angle to the R -axis shows how the inhomogeneous region becomes finite.

4.3 Summary

We will now summarise what we have achieved in this chapter. We studied the Stoner model where magnetism is driven by a peak in the electronic density of states. We have shown that there is a metamagnetic transition which bifurcates to include a region of spatially modulated magnetisation. The topology of this phase diagram closely matches the experimental results on $\text{Sr}_3\text{Ru}_2\text{O}_7$ as we shall discuss in chapter 6.

Beginning from the homogeneous case we showed how a Ginzburg-Landau expansion could be constructed on the line of critical endpoints both microscopically and phenomenologically. We then showed that the favourability of modulated states increased as we moved along the line of critical endpoints through an expansion of the transverse susceptibility. The appearance of modulation reconstructs the phase diagram as calculated through the Ginzburg-Landau expansion. The parent metamagnetic transition bifurcates at a dislocated tricritical point. Between the wings of this transition is a region of inhomogeneous magnetisation. This is bounded by first order transitions near to the metamagnetic sheet and continuous transitions away from the parent transition.

We will now calculate the thermodynamic signatures of the peak in the density of states. We will then compare the predictions of our model to the experimental data on $\text{Sr}_3\text{Ru}_2\text{O}_7$.

5. THERMODYNAMICS

In the previous chapter we have shown that both the metamagnetic transition and the modulated phase can be caused by a sharp peak in the electronic density of states. This results in a number of interesting effects in the properties of the system. Here we study the thermodynamic aspects of the metamagnetic transition. We will see that the peak in the density of states alters some naive expectations about the system.

We present a calculation of the specific heat and entropy from the Stoner model for a general density of states. These results must be evaluated numerically. However the form of the results can be obtained by basic reasoning based on the density of states and the presence of metamagnetism. We examine this reasoning and predict the specific heat and entropy curves passing through the metamagnetic transition. We then present the numerical evaluation of the calculations for a cut through the metamagnetic wing of the phase diagram. These agree well with our predictions.

We will study the generic case of the logarithmic singularity in the density of states, which we have shown induces a metamagnetic transition. These results will be compared with experiment in the next chapter.

5.1 *Derivation of expressions for entropy and specific heat*

We calculate the entropy and specific heat from the free energy of the Stoner model. Number conservation is enforced by requiring $n_\sigma = n + \sigma m$ where $\sigma = \pm 1$, and $n = n_\uparrow + n_\downarrow$ constant, and determining the chemical potential μ_σ from the number n_σ ¹.

We begin from the free energy in the Stoner model

$$F = \sum_\sigma \left[-T \int d\epsilon \rho(\epsilon) \ln \left(1 + e^{-\frac{\epsilon - \mu_\sigma}{T}} \right) + \mu_\sigma n_\sigma \right] + gn_\uparrow n_\downarrow - hm, \quad (5.1)$$

¹ For calculational convenience we will return to working in a scheme where the Fermi surfaces are split, rather than the physically more realistic picture of the density of states for each spin-species changing.

where we have set $k_B = 1$. $\sigma = \{\uparrow, \downarrow\}$ labels spin and μ_σ is the effective chemical potential for the spin species. This chemical potential is defined through the equation $n_\sigma = \int d\epsilon \rho(\epsilon) n_F(\epsilon - \mu_\sigma)$, where $n_F(\epsilon - \mu_\sigma)$ is the Fermi-Dirac distribution. In section 4.1.2 it was shown that this free energy gives a self-consistent equation for the magnetisation:

$$h = \mu_\uparrow(n, m) - \mu_\downarrow(n, m) - 2gm. \quad (5.2)$$

The entropy is defined by $S = -\partial_T F|_{n, h}$ and the specific heat as $C = -T \partial_T^2 F|_{n, h}$. These are evaluated with the conditions that total number is conserved. This condition is encoded in the behaviour of the chemical potentials through the condition that $n = n_\uparrow + n_\downarrow$ is constant. This results in a non-trivial form for $\partial_T \mu_\sigma$. The evaluation of these derivatives is lengthy and is presented in appendix C. Here we give the results of these calculations:

$$\begin{aligned} S &= \sum_\sigma \left[\int d\epsilon \rho(\epsilon) \ln \left(1 + e^{-\frac{\epsilon - \mu_\sigma}{T}} \right) + T \int d\epsilon \rho(\epsilon) \partial_T \ln \left(1 + e^{-\frac{\epsilon - \mu_\sigma}{T}} \right) - \partial_T \mu_\sigma n_\sigma \right], \\ C &= \sum_\sigma \left[\int d\epsilon \epsilon \rho(\epsilon) \partial_T n_F(\epsilon - \mu_\sigma) \right] - (2gm + h) \partial_T n_\uparrow. \end{aligned} \quad (5.3)$$

The temperature derivatives of the chemical potential are given by

$$\partial_T \mu_\sigma = \frac{-T \frac{\int d\epsilon \left(\Xi_\downarrow \frac{\epsilon - \mu_\downarrow}{T^2} + \Xi_\uparrow \frac{\epsilon - \mu_\uparrow}{T^2} \right)}{\int d\epsilon \Xi_{(-\sigma)}} + 2g \int d\epsilon \Xi_\sigma \frac{\epsilon - \mu_\sigma}{T^2}}{1 - \frac{2g}{T} \int d\epsilon \Xi_\sigma + \frac{\int d\epsilon \Xi_{(-\sigma)}}{\int d\epsilon \Xi_\sigma}}, \quad (5.4)$$

where

$$\Xi_\sigma = \rho(\epsilon) \frac{e^{\frac{\epsilon - \mu_\sigma}{T}}}{\left(1 + e^{\frac{\epsilon - \mu_\sigma}{T}} \right)^2}. \quad (5.5)$$

The specific heat and entropy may be calculated for any n , h and T from equations 5.3 and 5.4. These expressions produce the magnetic transitions of the Stoner model, although they do not include the effects of phase separation which we discussed previously. We will evaluate these expressions numerically for a particular density of states in section 5.2.2.

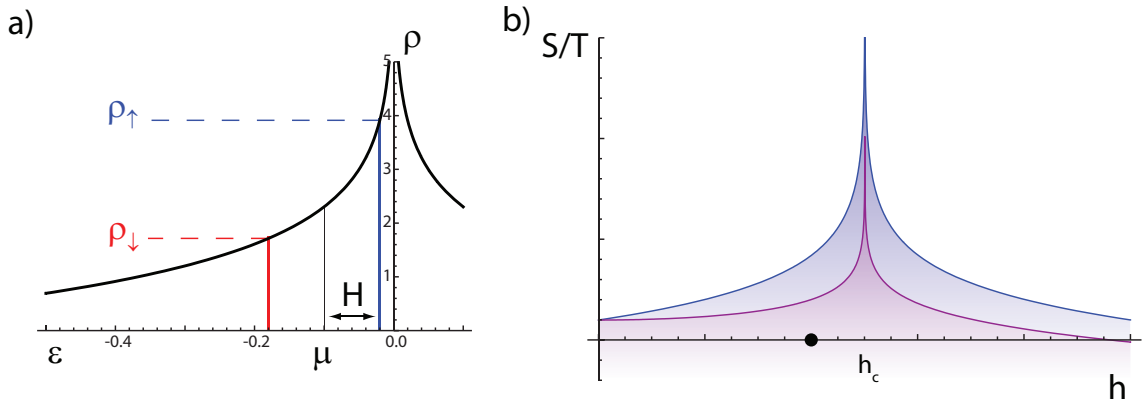


Fig. 5.1: Effect of spin-splitting on the entropy: a) A field H splits the spin-up and spin-down Fermi surfaces. If the entropy was proportional to the density of states at a single Fermi surface which field tuned through the peak then then S/T would be proportional to $2\rho_{\uparrow}$. Because the Fermi surface is split S/T is proportional to $\rho_{\uparrow} + \rho_{\downarrow}$, which is smaller as the down-spin Fermi surface is moved to lower energy. b) ‘Entropy’ curves constructed from the sum of the density of states at each Fermi surface. Blue: If field tuned a single Fermi surface through the density of states. In this case the entropy would mirror the density of states. Purple: Taking into account spin-splitting. The peak is compressed due to one spin species sampling a lower density of states. The point labels the field at which panel a) was plotted.

5.2 Density of states with peak

With these results it is possible to evaluate the magnetization, entropy and specific heat as a function of filling, magnetic field and temperature, for any given density of states and interaction strength. We will choose to look at a logarithmically divergent density of states, as produced by saddle points in the electronic dispersion. This model density of states is given by

$$\rho(\epsilon) = \frac{1}{W} \ln \left| \frac{W}{\epsilon - \epsilon_c} \right| \quad (5.6)$$

where the density of states is defined over $\epsilon = -W$ to $\epsilon = W$. The density of states diverges at $\epsilon = \epsilon_c$. In the following we will take the interaction strength to be $g = 0.3W$. We choose to look at a filling which is below the van Hove point and use field to tune the system through the metamagnetic wing. Before examining the results of Eq.5.3 let us consider what we might expect to see based on general arguments.

5.2.1 Factors contributing to the entropy and specific heat

The shape of the entropy and specific heat curves may be deduced from some basic principles. Entropy is a measure of the number of available states. It would therefore be expected to have the same shape as the density of states as a function of the Fermi energy at low temperatures. There are three effects which alter this dependence - spin-splitting due to the external field, interaction induced magnetism and temperature. The first two effects are further modified by requiring number conservation.

We will consider each of these in turn. We begin with spin-splitting, then number conservation, interaction effects and temperature. After the entropy we will examine the specific heat. We will see that the peak in the density of states produces a double peaked structure in the specific heat. This is then modified by the same effects of spin-splitting, number conservation and interactions as the entropy.

First we consider the entropy, S . S/T is proportional to the density of states at the Fermi surface. Upon application of a magnetic field the spin-species' Fermi surfaces become split. S/T is then given by the sum of the density of states at two different energies. Since one Fermi surface is moved to a lower density of states this has the effect of compressing the peak in entropy around the van Hove singularity as shown in Fig.5.1.

We now consider one of the consequences of enforcing number conservation on a system with a peak in the density of states. Applying a magnetic field splits the spin-species' Fermi surfaces by H . However, by moving a fixed energy interval the Fermi surface closest to the peak expands to include more electrons than the Fermi surface further from the peak loses by contracting (assuming the Fermi surfaces lie below the peak). This means that the overall number of electrons has increased. In order to conserve number the average, or 'zero-field' Fermi surface must move to lower filling with field so that the majority Fermi surface moves more slowly than the minority Fermi surface. This results in a slower approach to the peak than would naively be expected. This is shown in Fig.5.2.

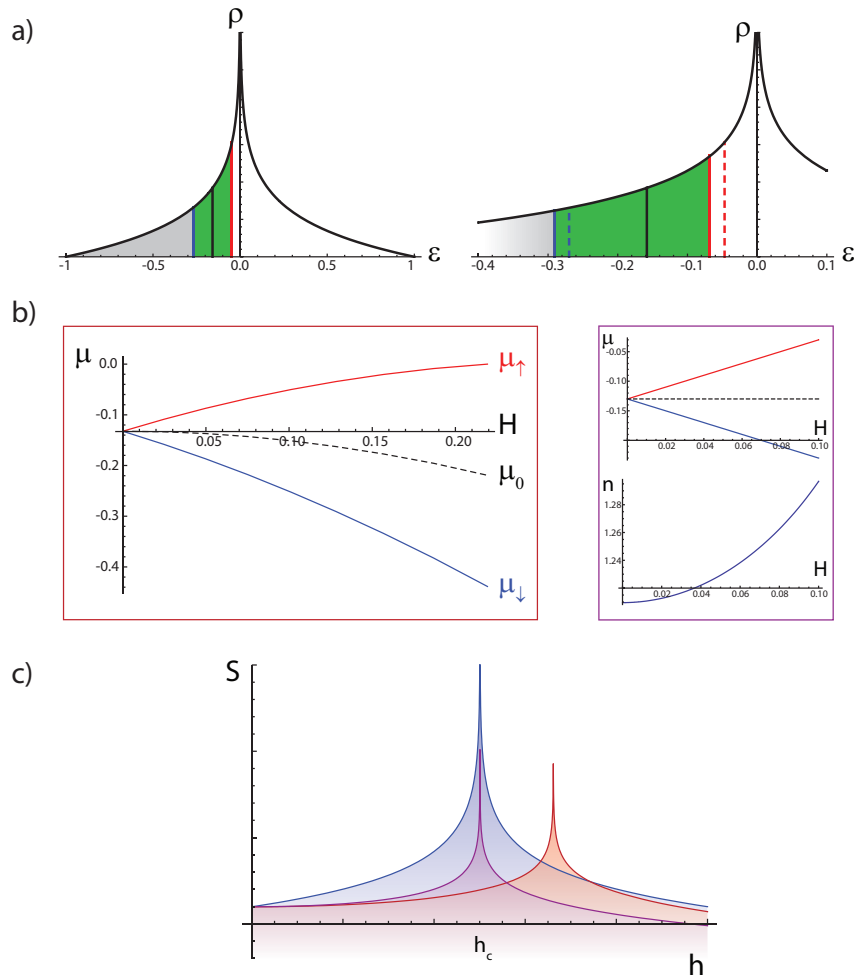


Fig. 5.2: Dependence of chemical potential on magnetic field: When splitting the spin-species' Fermi surfaces with a magnetic field, number conservation forces a non-linear dependence of the chemical potential on field. a) The density of states on the left shows the zero-field filling (black line) and the Fermi surfaces split by $2H$. The green area represents the magnetisation, note that the green area above the zero-field Fermi surface is larger than below, the number of electrons has therefore changed. On the right is the situation where number conservation has been enforced. The Fermi surfaces are still split by $2H$ but have both moved to lower energy so that there are the same number of electrons as before the splitting. For comparison the dotted lines show the Fermi surfaces without number conservation. As the splitting gets larger the amount by which the Fermi surfaces must move increases. b) The plot boxed in red shows how the chemical potentials for the up- and down-spin electrons and their average varies with field near the peak. We see that the Fermi surfaces move with field at different speeds and are slowed in their approach to the peak compared to the non-number conserving case. Boxed in purple are plots showing the splitting and total number with no number conservation in force. c) The sum of the spin-up and -down Fermi surfaces if (blue) only one was tuned through the singularity, (purple) the Fermi surfaces are split with no number conservation, and (red) the Fermi surfaces are split with number conservation. Note that in the last case it takes a higher field to tune through the singularity due to the number conservation requirement.

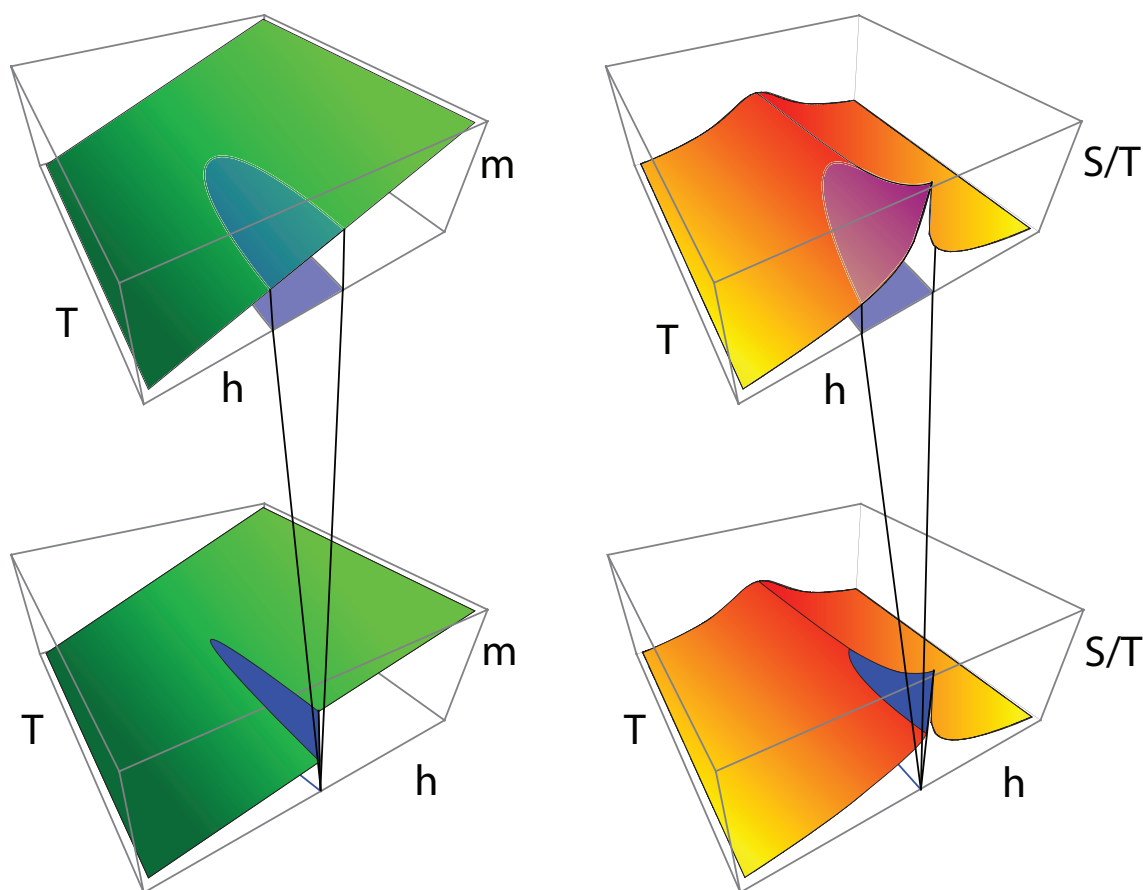


Fig. 5.3: Effect of first order transition: On the top row the magnetisation and entropy in the absence of the metamagnetic transition. The values which will be removed by the transition are shaded. On the bottom row the first order transition removes a ‘wedge’ of magnetization values, this removes a section from the entropy curve.

As well as the splitting due to the external field there is an additional splitting of the Fermi surfaces due to the metamagnetism. The effects of this magnetisation are shown in Fig.5.3. When the transition is continuous this has the effect of compressing the field scale around the transition. When the transition is discontinuous a range of magnetisation values are ‘jumped over’ by the transition. This removes a slice of the putative entropy curve beginning at the critical endpoint and getting wider as temperature is decreased and the transition gets stronger. The entropy therefore becomes discontinuous at the metamagnetic transition. Since the region removed is around the peak, it is possible for the highest value of S/T to occur at non-zero temperature, where the jump is smaller.

These effects mean that a straightforward comparison of field and temperature scales cannot be made, the interactions in the system alter the rate at which field

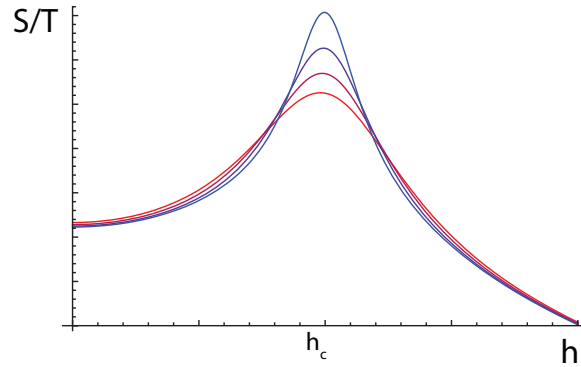


Fig. 5.4: Effect of temperature on the entropy and specific heat: Temperature broadening of S/T with spin-splitting present. Blue, low temperature, red, high temperature.

tunes into the peak in the density of states relative to temperature.

In a multi-band system the change in chemical potential, due to this effect or a metamagnetic transition, will affect all bands. Electrons are transferred between bands as some donate electrons to compensate the band with the peak. In this way all electronic bands are linked so that signals of approaching a peak in the density of states should be visible in all of them, though the effect may be small. This effect has been suggested as an explanation for features in the dHvA signals of the α_1 and α_2 bands of $\text{Sr}_3\text{Ru}_2\text{O}_7$ [75]. Upon approaching the metamagnetic transition these bands show peaks in their dHvA frequencies which can be explained through a non-linear spin splitting due to a peak in the density of states of a different band. Features above the metamagnetic transition in these data can not however be explained by this simple model. The high-field side of the transition remains poorly understood.

Finally we consider the effect of temperature. This broadens the Fermi-Dirac distribution, allowing the thermal occupation of states under the peak in the density of states as temperature is increased. The peak in entropy therefore becomes broadened. This is shown in Fig.5.4.

The low temperature specific heat of non-interacting fermions normally follows the density of states,

$$c_{\text{el}} = \frac{\pi^2}{3} k_B^2 T \rho(\epsilon_F). \quad (5.7)$$

This result relies on using the Sommerfeld expansion of the Fermi-Dirac distribution. This result is normally a good approximation, however in the present case we have a peak in the density of states near to the Fermi level and this approximation fails.

We will consider the effect of temperature, magnetic field, and the inclusion of interactions on this result.

Raising temperature has the effect of broadening the Fermi-Dirac distribution, the range of states occupied around the chemical potential is therefore increased. Starting with the chemical potential on either side of the density of states peak and raising the temperature will allow thermal occupation of the states under the peak. As shown in Fig.5.4 this increase is most rapid on either side of the peak. Specific heat is the temperature derivative of the entropy and will therefore be largest in these regions. We therefore expect a structure which is logarithmic at zero temperature with a peak which bifurcates and broadens as temperature increases.

The magnetic field and interactions have the same effect as discussed for the entropy - a compression along the field axis and the removal of a ‘wedge’ of field values due to the first order transition.

5.2.2 Results

Figure 5.5 gives the results of numerically evaluating Eq.5.2 for magnetization and Eq.5.3 for entropy and specific heat, for a cut through the metamagnetic wing in the h, T plane with the logarithmic density of states Eq.5.6. These plots are in good agreement with the anticipated results. Magnetization has the familiar first-order transition at low temperature which becomes continuous at a critical endpoint. The entropy has the temperature-broadened peak of the density of states with the position and symmetry of the peak shifting due to the effect of the metamagnetism and number conservation. Specific heat shows the expected double-peak structure as well as the other signatures of the metamagnetic transition in the field dependence. In section 6 we will compare these results to experimental data.

A striking feature of the results is that the temperature and field scales of the system are different. The effects of interactions and number conservation mean that spin-splitting by field detects the peak in the density of states at a different energy to temperature broadening of the Fermi surface. The ratio of these energies can be altered by varying the interaction strength. This means that care is needed when identifying zero field features as a function of temperature with low temperature features at a certain field.

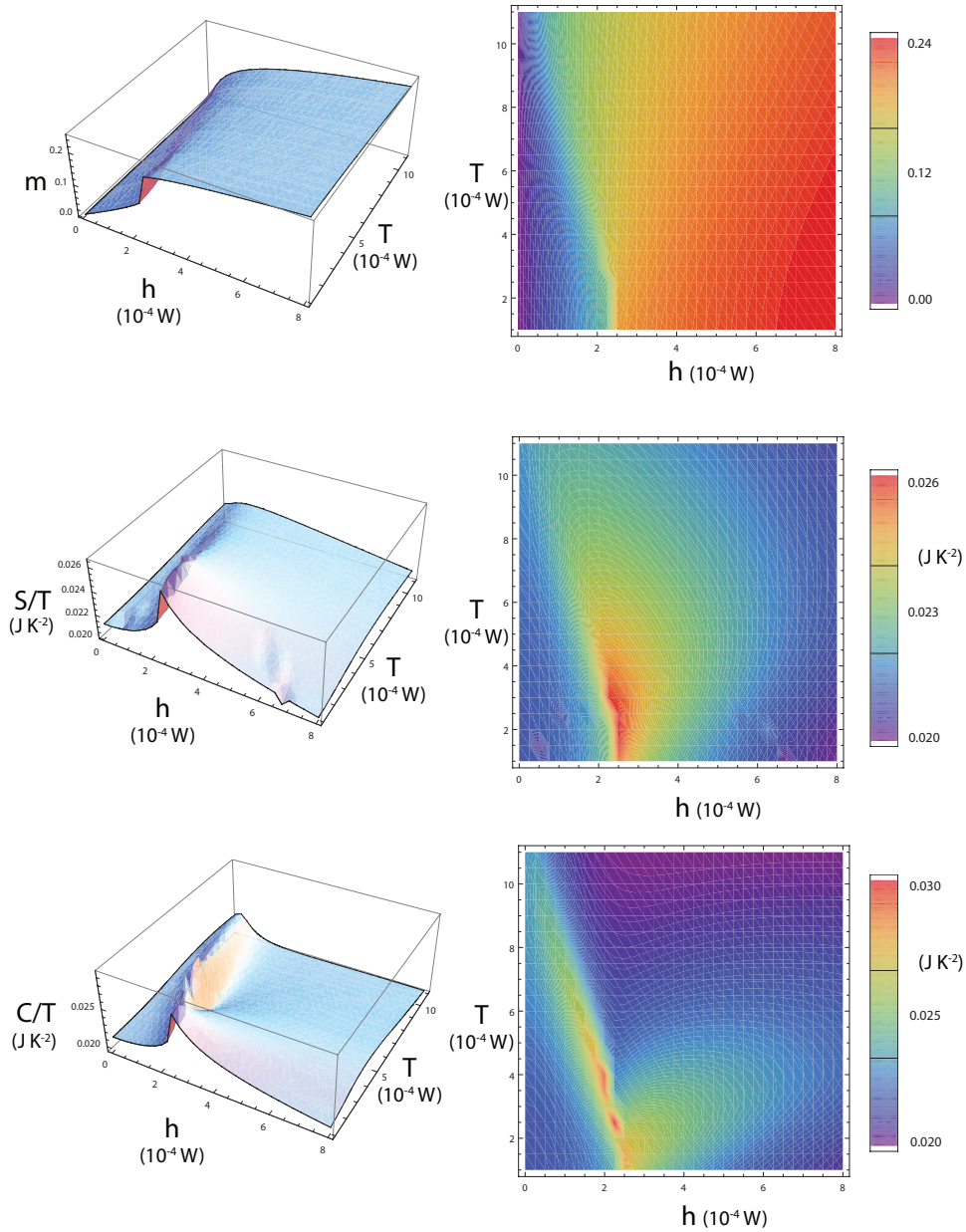


Fig. 5.5: Magnetisation, entropy and specific heat at a metamagnetic transition: From top to bottom the magnetisation, entropy and specific heat as we cross a metamagnetic transition in the Stoner model with a logarithmic peak in the density of states. $g = 0.3W$, filling fraction is 0.4. The results are shown both as 3D plots and gradient plots for clarity. The unevenness and jagged peaks in some of the plots are due to numerical error.

5.3 Specific heat and entropy for inhomogeneous phase

A full evaluation of the entropy and specific heat for the phase diagram with the modulated phase would require analysis of the free energy $F(q, m, m_{\perp}, T)$ and the temperature dependence of the modulation wavevector and transverse magnetization. As previously noted this study is numerically intractable and has not yet been completed. However, based on the arguments just presented and our previous calculation of the density of states for the spiral case we can deduce what form the entropy may take.

In the homogeneous region of the phase diagram the entropy will be the sum of the density of states at the Fermi surface for the two spin-species as before. In the region which was previously compressed or ‘chopped out’ by the metamagnetic transition there will now be the inhomogeneous phase. The entropy here will be the sum of the density of states at the Fermi surface for the spiral quasiparticle dispersions. An exact calculation of this sum would involve the full free energy calculation. An example density of states is shown in Fig.5.6, we have reverted to the scheme of a single chemical potential and two densities of states, as the spiral state has different densities of states for each species. We see that the Fermi surface jumps to a point between two peaks in the density of states. Field will then tune through this spiral density of states before jumping back to the homogeneous case. Possible plots of entropy as a function of field for the inhomogeneous case are sketched in Fig.5.7.

In this case the density of states in the spiral phase is lower than in the homogeneous phase, though it is not certain that this is always the case. This leads to a lower entropy in the anomalous phase than outside. This contradicts the experimental evidence, which shows a higher entropy in the phase. The full details of the thermodynamic calculations still remain to be performed. When these are completed it may turn out that the entropy in the phase may be higher than outside. We note that one possible explanation for a higher entropy is the presence of a Goldstone mode due to the breaking of translational symmetry by the modulation, an effect which remains to be explored along with the role of fluctuations in the wavevector of modulation at finite temperature.

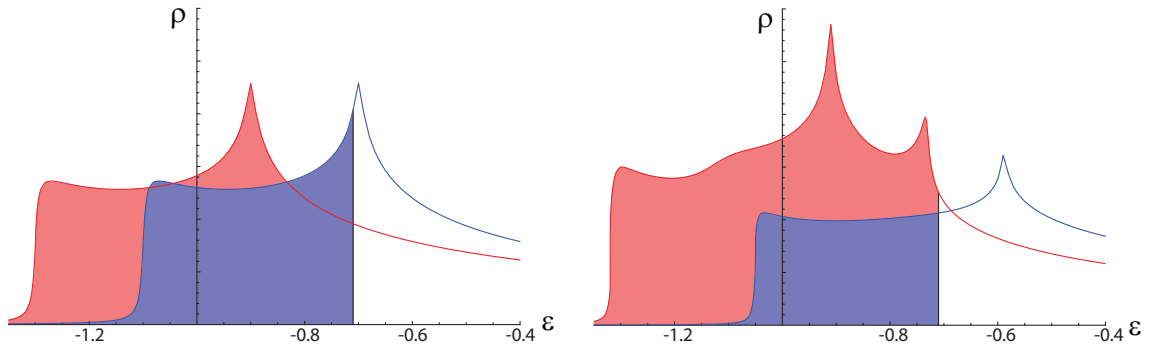


Fig. 5.6: Density of states in spiral phase: On the left is the density of states in the homogeneous phase close to the metamagnetic transition. On the right is the density of states for the spiral phase, calculated from the dispersion Eq.4.32. The Fermi surface now lies between two peaks.

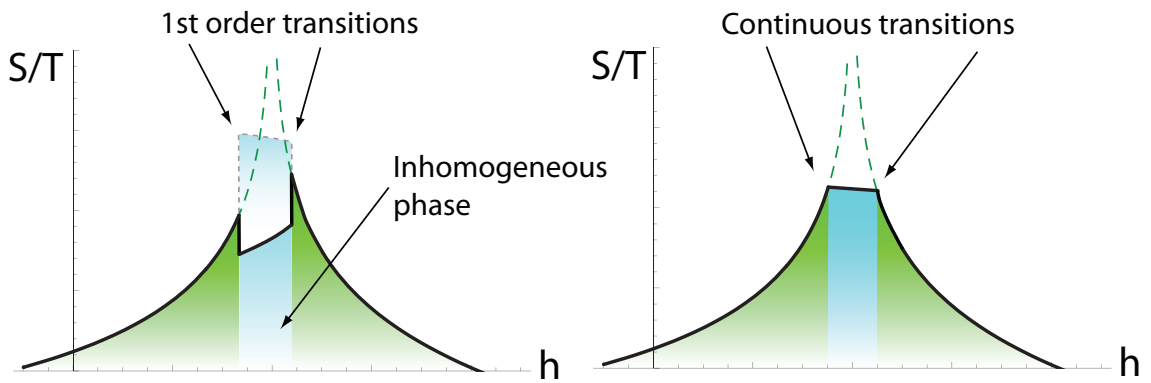


Fig. 5.7: Entropy including inhomogeneous phase: Outside the inhomogeneous phase the system has the same entropy as in the completely homogeneous case. Inside of the phase the entropy is determined by the spiral density of states. There is a first-order phase transition into the inhomogeneous phase, and one out of the phase. When the transitions are continuous this would result in a flattening of the peak in the entropy. Shown in pale is the curve if the inhomogeneous phase has a higher entropy to the homogeneous phase. We can not yet say which of these cases is realised in our model.

6. COMPARISON WITH EXPERIMENTS ON $\text{Sr}_3\text{Ru}_2\text{O}_7$

Having calculated the phase diagram for the inhomogeneous phase and the thermodynamic signatures of the metamagnetic transition, we will now compare them with experimental results on $\text{Sr}_3\text{Ru}_2\text{O}_7$. Our model readily accommodates the behaviour of $\text{Sr}_3\text{Ru}_2\text{O}_7$. We will consider how the topology of the phase diagram is reproduced by our theory and how the properties of the anomalous phase may be reproduced by the modulated magnetic state. The main aspect currently missing from the model is the dependence on field angle. We will consider three proposals for how this may be included.

6.1 *Summary of experimental results*

We first give a brief reiteration of the experimental results on $\text{Sr}_3\text{Ru}_2\text{O}_7$ before discussing the signatures of our proposed inhomogeneous state and how they compare. A more detailed discussion of the experimental data is found in section 3.

The bilayered ruthenate $\text{Sr}_3\text{Ru}_2\text{O}_7$ shows a sequence of metamagnetic transitions [66]. Early studies focussed on a line of metamagnetic critical end-points that could be tuned to a quantum critical point by adjusting the magnetic field strength and orientation [51]. Subsequently, ultra-pure samples showed a bifurcation of this metamagnetic line upon approaching the putative quantum critical point [52, 70] with a second line of critical end-points emerging from the zero-temperature plane (see Fig.6.1). This bifurcation is accompanied by a striking peak in resistivity [52] with curious, anisotropic dependence on the relative orientation of current, lattice and in-plane magnetic field [26]. When current flows in the crystallographic direction most nearly perpendicular to the in-plane field, the resistivity peak rapidly decreases as the field is moved away from the c -axis. When it is nearly parallel to the in-plane field, the peak persists.

The bifurcating metamagnetic transitions are shown by green surfaces in Fig.(6.1) with the region of resistive anisotropy further delimited by the roof shown in blue. Similar features occur elsewhere in the phase diagram [26], with further bifurcations

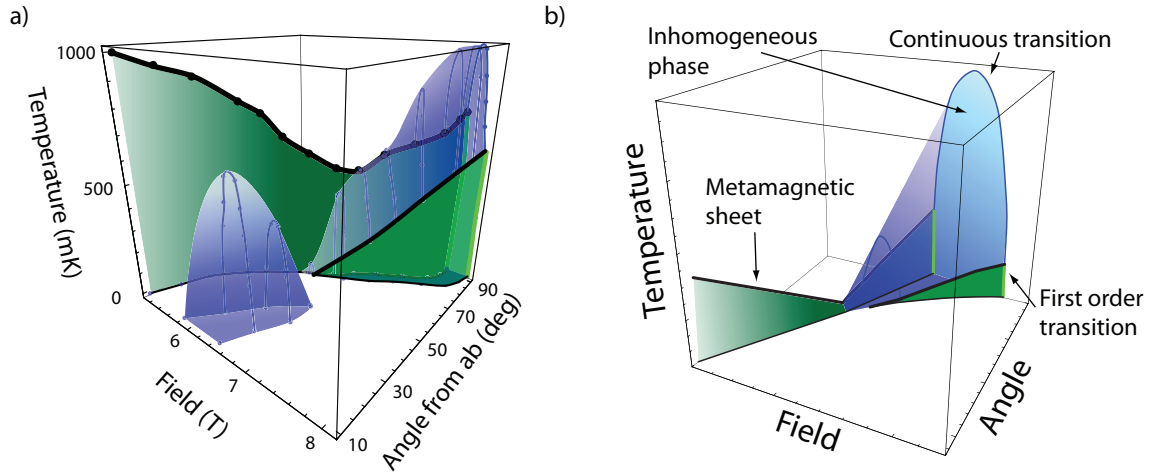


Fig. 6.1: Comparison of experimental and theoretical phase diagrams: a) The experimental phase diagram as inferred from in-plane transport properties. Green planes correspond to abrupt changes in resistivity as a function of field. Blue shading indicates regions where the in-plane resistivity is anomalously high, becomes highly anisotropic with respect to the in-plane component of the field [26] and shows an anomalous temperature dependence: for currents in the direction of maximum resistivity, the resistivity *decreases* with increasing temperature. The phase diagram obtained from magnetic susceptibility [70] shows the same first order transitions as indicated here in green, but lacks the roof shown in blue. b) Theoretical phase diagram made by a linear mapping of the Landau parameters R , H and K_{\perp} onto field, field angle and temperature. This results in a distortion of the phase diagram of Fig.4.24

apparent upon approaching the ab -plane. These show a smaller resistance anomaly, but have the same characteristic anisotropy (the blue dome-shaped region in the foreground of Fig.6.1).

6.2 Topology of phase diagram

We have previously obtained the phase diagram for our model of modulated magnetisation in terms of the Landau parameters R , H and K_{\perp} . The experimental phase diagram, Fig.6.1a), is obtained— in the spirit of Ginzburg-Landau theory— by interpreting R , H and K_{\perp} as functions of the experimental parameters T , θ and h . Near to the dislocated tricritical point these functions will be approximately linear. Although in principle these functions can be calculated, as was done in chapter 4, it becomes impractical as the number of terms increases. Since we wish to compare with the experimental results on $\text{Sr}_3\text{Ru}_2\text{O}_7$ we would also have to perform the calculations with the correct dispersion. As can be seen from the discussion of the Fermi surface in section 3.4 this dispersion is extremely complicated. We there-

fore take a possible linear mapping of the parameters which, in the spirit of our phenomenology, maps the Landau-Ginzburg theory onto the experimental results. Fig.6.1 b) shows the result of such a transformation.

The parent metamagnetic transition of the Stoner model is present. The critical temperature of this transition falls as we move away from van Hove filling, as we know is the case from microscopics. At a certain point a second first-order transition appears - the bifurcation of the transition. This is asymmetric, with the new wing being much smaller than the first and emerging at a different point in the zero-temperature plane. Between these two transitions is the inhomogeneous phase.

The sheet of continuous transitions into the inhomogeneous phase becomes a ‘roof’ stretching between the first-order transitions. This roof encloses the anomalous phase and has been detected in several experimental probes [52]. This roof is signaled by a qualitative change in the temperature dependence of resistivity and by a noticeable kink in the magnetization. We associate it with the continuous transition into the inhomogeneous phase found in the present theory. This roof previously presented a real puzzle as there is no obvious way to obtain it from a simple Landau theory for magnetization, but is nevertheless required to enclose the postulated broken symmetry phase in the bifurcated region.

6.3 Properties of the phase

The experimental signature of the anomalous phase is a high and anisotropic resistivity. We believe that our proposal will capture this property. Spatially inhomogeneous magnetic structures lead inevitably to enhanced scattering in certain directions, leading to a resistive anisotropy. In order to fully explain the anisotropy, there must be a mechanism for an in-plane magnetic field to align the magnetic inhomogeneity. Our simple model does not contain such a mechanism. We suggest that its origin lies in the in-plane magnetic field and the orbital effects to which this leads. This modifies the dispersion, breaking the symmetry between different orientations of the underlying helices. We will show how this can come about in section 6.4.1. When the sample is in the anomalous phase, there is significant magnetic inhomogeneity leading to enhanced resistivity. With a magnetic field in the c-direction, the inhomogeneity does not break the crystal symmetry (at least macroscopically) and resistivity is isotropic. As the field is rotated into the plane, the magnetic inhomogeneity no longer preserves the lattice symmetry— either through the formation of an anisotropic spin crystal or by a preponderance of domains of spin density waves

of one orientation. This anisotropy will be reflected in resistivity.

As the anomalous behaviour only appears in the cleanest samples, any mechanism that explains it must be sensitive to disorder. Our mechanism shows this sensitivity, since disorder smooths out features in the density of states and the sharpness of these features is required for the effects which we predict.

This theory relies on a peak in the density of states near to the Fermi surface. Experimental evidence seems to support these facts with ARPES showing a peak in the density of states below the Fermi surface [67]. Obviously our model uses a much simplified model of the band structure of $\text{Sr}_3\text{Ru}_2\text{O}_7$, although ongoing work is moving to a more realistic dispersion, as explained below. The higher-field features of the phase diagram may be explained by similar reasoning based on further features in the density of states.

6.3.1 Thermodynamic signatures of the transition

In Fig.6.2 we show the experimentally measured entropy and specific heat of $\text{Sr}_3\text{Ru}_2\text{O}_7$ with the field aligned along the c -axis [74]. This shows the anomalous phase, which we have not yet calculated the thermodynamic signatures of. Aside from the anomalous phase region these results resemble the theoretical predictions for a metamagnetic transition driven by a peak in the density of states. Extracting a power law dependence of specific heat on the low field side however does not give the correct dependence for approach to a logarithmic singularity. Several effects may be responsible for this, the single band logarithmic density of states is still a vast simplification, a more realistic model may produce slightly different results. The specific heat may have contributions from elsewhere - for example, quantum critical fluctuations. As well as qualitative agreement on either side of the anomalous phase the specific heat at high temperature shows the double peak structure which we predict. This is consistent with the normal phase of the material seeing only a peak in the density of states as would occur in our model outside of the modulated phase.

6.4 Outstanding issues

6.4.1 Tuning the phase diagram with field angle

The natural parameters of our microscopic theory are field, temperature and band filling. An additional mechanism is required to translate from filling to angle. This mechanism is currently absent from the theory, although we have investigated several

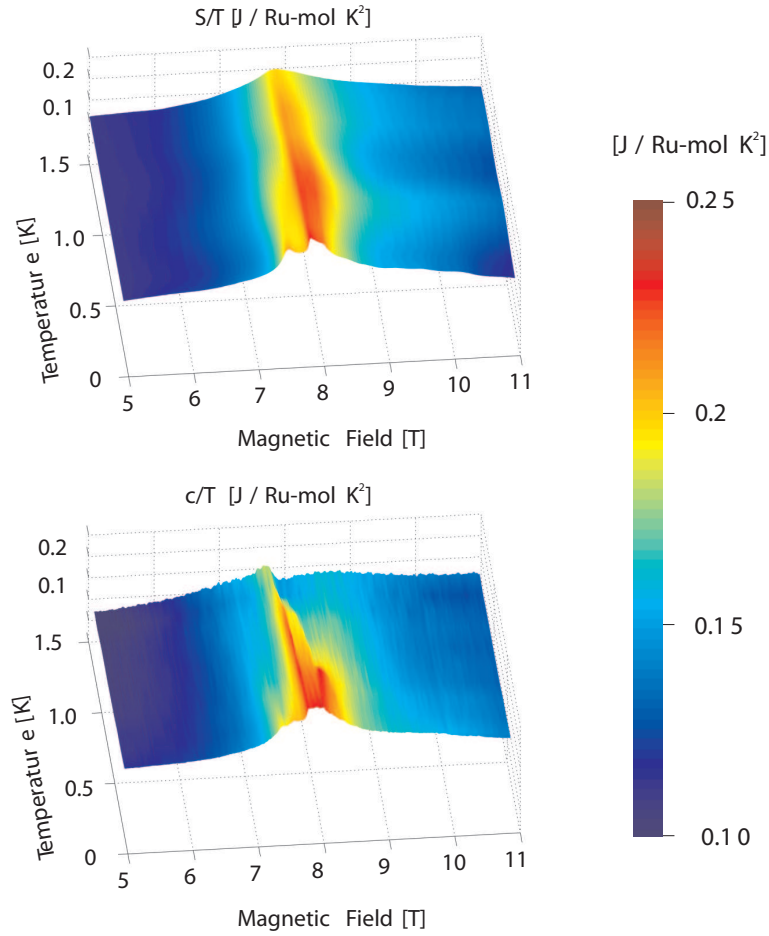


Fig. 6.2: Experimental measurements of entropy and specific heat of $\text{Sr}_3\text{Ru}_2\text{O}_7$: Experimental measurements of the entropy and specific heat for a cut through the phase diagram with field along the c -axis. This shows the anomalous phase and surrounding normal phase. The broadening and bifurcation of the peak in C/T are consistent with our analysis of a peak in the density of states (see Fig.5.5). Figure from [74].

possibilities. Of these, in-plane orbital effects are the best explanation. The three possibilities which we will now discuss are:

- An angle-dependent Zeeman coupling [75]. This may be caused by spin-orbit interactions.
- Inter-plane orbital effects. The bilayer structure allows the orientation of the field to alter the bandstructure via magnetic flux between the layers.
- In-plane orbital effects. Orbital Zeeman and spin-orbit coupling lead to an angle-dependent bandstructure [73].

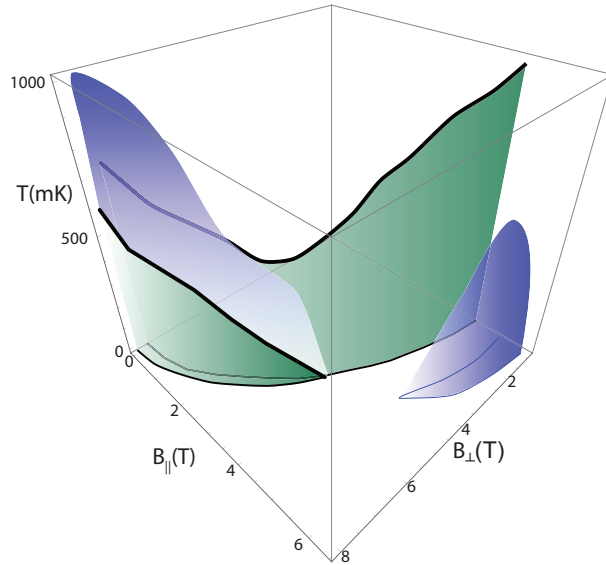


Fig. 6.3: Experimental phase diagram of $\text{Sr}_3\text{Ru}_2\text{O}_7$: The phase diagram of $\text{Sr}_3\text{Ru}_2\text{O}_7$ shown in Fig.3.3 replotted as a function of parallel and perpendicular fields. The critical field of the metamagnetic transition is anisotropic, being larger with the field along c -axis than in the ab -plane.

We will now discuss the arguments in favour and against these proposals. We conclude that the effects of orbital Zeeman and spin-orbit coupling are likely to provide the explanation to the angular dependence. These may be straightforwardly included in our model.

Angle-dependent Zeeman splitting

We will first consider the effects of an angle-dependent Zeeman coupling. Spin-orbit coupling can lead to an anisotropic Zeeman coupling. This reproduces the angular dependence of the metamagnetic critical field but does not explain the appearance of the anomalous phase.

The field splits the Fermi surfaces so that the position of the spin-up or -down Fermi surface is given by $\mu_{\uparrow/\downarrow} = \mu_0 \pm g\mu_B \sqrt{B_{\perp}^2 + B_{\parallel}^2}$. There is a metamagnetic transition when one of the Fermi surfaces gets close enough to the van Hove singularity. For simplicity we will take the transition to occur at the singularity itself. The Fermi surface lies on the van Hove singularity when $\mu_0 \pm g\mu_B \sqrt{B_{\perp}^2 + B_{\parallel}^2} = \epsilon_{vH}$. The transition occurs on a circle in the B_{\perp} , B_{\parallel} plane, defined by $B_{\perp}^2 + B_{\parallel}^2 = \left(\frac{\epsilon_{vH} \pm \mu_0}{g\mu_B}\right)^2$.

Now let us consider that g may be a function of angle $g(\theta)$ where θ is defined as $\theta = \tan^{-1}\left(\frac{B_{\perp}}{B_{\parallel}}\right)$. Assuming a form $g(\theta) = \sqrt{g_{\parallel}^2 \cos^2 \theta + g_{\perp}^2 \sin^2 \theta}$ we find that the metamagnetic transition now forms an ellipse in the B_{\perp} , B_{\parallel} plane.

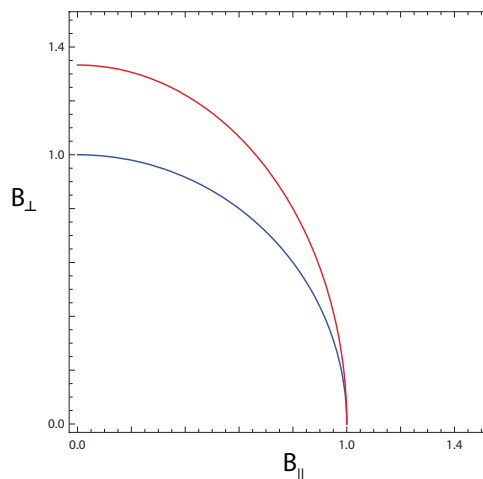


Fig. 6.4: Metamagnetic transitions with an anisotropic g factor: Shown in blue is the condition for one of the spin-split Fermi surfaces to reach the van Hove singularity assuming a constant μ_0 and an isotropic g . In red is the condition for an anisotropic g .

This provides an explanation for the differing critical fields with the field aligned along different axes, but does not seem to offer an explanation as to why the anomalous phase should form as a function of angle, or why the critical temperature of the transition should change.

Orbital effects between layers

We now consider how the spatial separation of the layers in the bilayer of $\text{Sr}_3\text{Ru}_2\text{O}_7$ allows coupling to the angle of the magnetic field. Flux between the layers of the bilayer affect the electrons which circulate from layer to layer, leading to a modified dispersion. This gives the possibility for a rich angle-dependent phase diagram. However, the fields required to observe the effects are far too large to be physically realistic.

We consider a model consisting of two layers, each with a simple tight-binding dispersion, with some inter-layer interaction. The effect of in-plane field is taken into account by minimal substitution of the vector potential into the electron momentum. Since the layers are separated each sees a slightly different potential. The difference in the vector potential between layers changes with angle. The interaction between layers allows the system's properties to depend on the field angle through this difference.

We use the following Hamiltonian to describe the bilayer system (neglecting

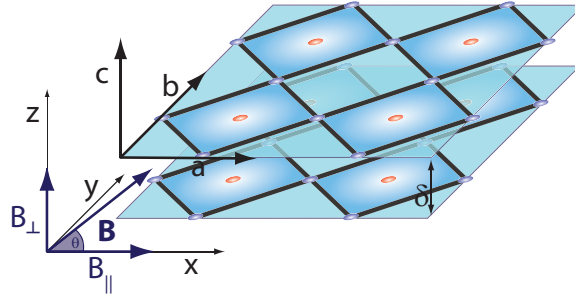


Fig. 6.5: Geometry of the bilayer scheme: The two ruthenium oxide layers are separated by a distance δ . The magnetic field is applied at an angle to the c -axis. The vector potential at the two layers is different and varies with the angle θ .

spin-up and -down for the present):

$$\hat{H} = (\psi_1^\dagger, \psi_2^\dagger) \begin{pmatrix} \epsilon_1(\mathbf{k}) & \Delta \\ \Delta & \epsilon_2(\mathbf{k}) \end{pmatrix} \begin{pmatrix} \psi_1 \\ \psi_2 \end{pmatrix}, \quad (6.1)$$

where 1 and 2 label the layers, $\epsilon(\mathbf{k})$ is the dispersion and Δ is the inter-layer interaction. For simplicity we take Δ to be a constant. This Hamiltonian has eigenvalues

$$2\epsilon_{\pm} = [\epsilon_1(\mathbf{k}) + \epsilon_2(\mathbf{k})] \pm \sqrt{[\epsilon_1(\mathbf{k}) - \epsilon_2(\mathbf{k})]^2 + 4\Delta^2}. \quad (6.2)$$

We now include a magnetic field parallel to the layers (see figure 6.5). Working in the Landau gauge this has the vector potential $\mathbf{A} = (0, B_{\parallel}z, 0)$. The minimal substitution scheme involves the replacement $\mathbf{p} \rightarrow \mathbf{p} - e\mathbf{A}$. In the presence of the field there is a difference in the magnitude of \mathbf{A} between the layers of $\Delta\mathbf{A} = \delta B_{\parallel}$ where δ is the interlayer spacing. The energies of the layers therefore become

$$2\epsilon_{\pm} = \left[\epsilon \left(\mathbf{k} - \frac{e\delta B_{\parallel}}{\hbar} \right) + \epsilon(\mathbf{k}) \right] \pm \sqrt{\left[\epsilon \left(\mathbf{k} - \frac{e\delta B_{\parallel}}{\hbar} \right) - \epsilon(\mathbf{k}) \right]^2 + 4\Delta^2}. \quad (6.3)$$

Graphically this has the effect of shifting one dispersion relative to the other and then anticrossing the two, as shown in Fig.6.6. This process can shift pre-existing saddle points, and create new ones. These saddle points will each produce a peak in the density of states and possibly a metamagnetic transition. In addition to this effect the field produces a Zeeman splitting of the Fermi surface. As this is proportional to the magnitude of the applied field and not the angle (in the isotropic g-factor case we are considering here), the field component perpendicular to the

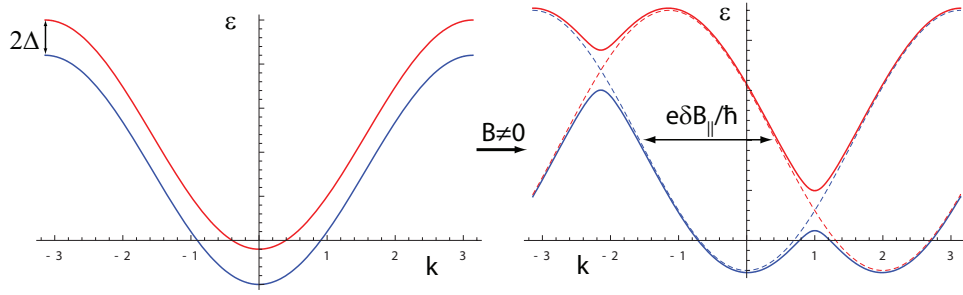


Fig. 6.6: Anticrossing of bilayer dispersion with parallel field: In the absence of a parallel field component the dispersions of the two layers are identical but split by an energy Δ . Upon applying a field the dispersions are shifted relative to each other before applying this splitting - this causes anticrossing of the dispersions and forms new stationary points in the dispersion. Some of these stationary points will be saddle points and cause peaks in the density of states.

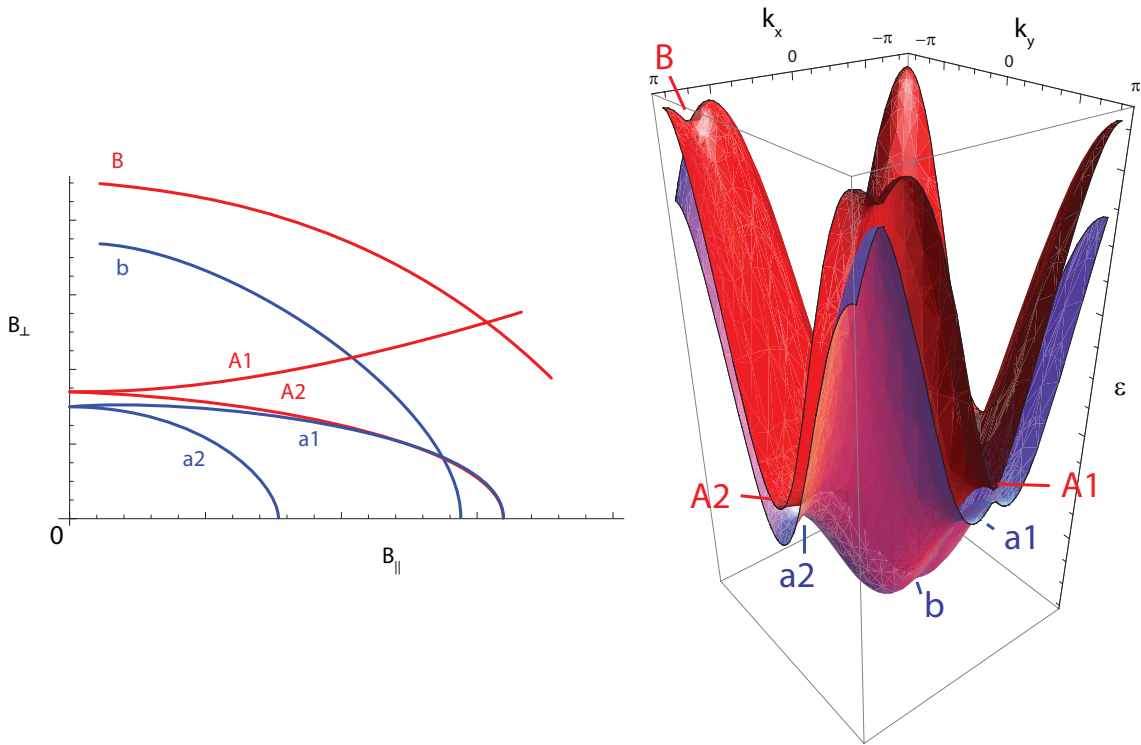


Fig. 6.7: Tracking peaks in the density of states: The lines represent the parallel and perpendicular field values which put one of the spin species' fermi surface at a peak in the density of states. Note that the upper two lines do not appear for $B_{\parallel} = 0$ and the splitting of the lower lines also occurs at non-zero B_{\parallel} . The lines are numbered to identify the saddle point which they relate to, shown in the right-hand figure. The exact position of these lines depends on the chemical potential and bilayer splitting.

planes will contribute to the Zeeman splitting but not the anticrossing phenomena.

We find that the position of the van Hove singularities moves as a function of

in-plane field B_{\parallel} . Some singularities split and others appear as the field is applied. Tracking the coincidences of one of the Fermi surfaces with these peaks gives a rough zero-temperature phase diagram, shown in Fig.6.7. This phase diagram is potentially very complex, including anisotropic critical fields and transitions which bifurcate.

The size of field required to produce these effects is however excessively large. We find an order of magnitude expression for the required size of magnetic field. The shift in layer dispersions needs to be comparable to the size of the Brillouin zone in order to see this effect. The spacing between bilayers is of the order of a lattice spacing and so the required field is.

$$B_{\parallel} = \frac{\hbar}{e\delta a} = \frac{\hbar}{ea^2} \approx \frac{10^{-15}}{10^{-19}10^{-20}} \frac{eVs}{em^2} = 10^{24}T \quad (6.4)$$

Obviously 10^{24} tesla is rather a lot - especially since the transition in $\text{Sr}_3\text{Ru}_2\text{O}_7$ occurs at about 10T. $B_{\parallel} = 10T$ gives a \mathbf{k} shift of $\sim 10^{-33}m^{-1}$. Approximating the dispersion to be that of a free electron $\epsilon = \frac{\hbar^2k^2}{2m}$ gives anticrossing of two previously degenerate dispersions at an energy of $\sim 10^{-140}meV$ - well below that of any bilayer splitting. Therefore the effects of reasonable field sizes are completely negligible. Such effects have been considered in the theory of a nematic state [71], but run into the same problems of field scales.

In-plane orbital effects

Another way of including angular dependence is to include orbital effects in the system. This requires stepping back from our simple 2D models and considering the orbital make-up of the band structure, as discussed in section 3.4. Each set of orbitals produces its own band. The role of spin-orbit coupling is to hybridise these bands in a way which depends on the magnitude and angle of the applied field. In addition we need to consider the coupling of the magnetic field to the orbital angular momentum of the electrons. This scheme was considered in the case of nematic ordering [73] (see section 7) but can be carried across straightforwardly to our analysis. Here we will follow the scheme of [73] to investigate how the Fermi surface is affected by the field angle.

Spin-orbit coupling enters the Hamiltonian as $\mathbf{L} \cdot \mathbf{S}$. The Hamiltonian for our model without electron-electron interaction can then be written as the sum of an

orbital or band part H_O and a spin-orbit part H_{SO} :

$$\begin{aligned}\hat{H} &= \hat{H}_O + \hat{H}_{SO}, \\ \hat{H}_O &= \sum_{\langle ij \rangle, \sigma, \alpha} c_{i, \sigma, \alpha}^\dagger \hat{T}_{i, j, \alpha} c_{j, \sigma, \alpha} = \sum_{\mathbf{k}, \sigma, \alpha} \epsilon_{\mathbf{k}, \sigma, \alpha} \hat{n}_{\mathbf{k}, \sigma, \alpha}, \\ \hat{H}_{SO} &= \lambda_{SO} \sum_{i, \sigma, \alpha} c_{i, \sigma, \alpha}^\dagger (\mathbf{L} \cdot \mathbf{S}) c_{i, \sigma, \alpha},\end{aligned}\quad (6.5)$$

where α labels the orbitals, i and j label the sites, σ labels the spin and $\hat{T}_{i, j, \alpha}$ is an operator which allows hopping from one site to another. The orbital part of the Hamiltonian can be recast as the standard single-particle band term where the dispersion $\epsilon_{\mathbf{k}, \sigma, \alpha}$ is obtained by considering the geometry of the orbitals. The spin-orbit term produces interactions between these various bands. \mathbf{S} is the vector of Pauli matrices $\mathbf{S} = (\sigma_x, \sigma_y, \sigma_z)$. The components of \mathbf{L} can be written

$$l_x = \begin{pmatrix} 0 & 0 & 0 \\ 0 & 0 & -1 \\ 0 & -1 & 0 \end{pmatrix}, \quad l_y = \begin{pmatrix} 0 & 0 & -1 \\ 0 & 0 & 0 \\ -1 & 0 & 0 \end{pmatrix}, \quad l_z = \begin{pmatrix} 0 & i & 0 \\ -i & 0 & 0 \\ 0 & 0 & 0 \end{pmatrix}, \quad (6.6)$$

giving

$$\mathbf{L} \cdot \mathbf{S} = \begin{pmatrix} l_z & l_x - il_y \\ l_x + il_y & -l_z \end{pmatrix}. \quad (6.7)$$

Fig.6.8 shows the bands before and after including spin-orbit coupling. Spin-orbit coupling hybridises the bands, the quasi-one-dimensional bands become quasi-two-dimensional and the anticrossing produces new peaks in the density of states. The spin-orbit term is angle dependent as the angular momentum operators are defined relative to the crystalline axis but the spin quantization axis is aligned with the field. \mathbf{S} is therefore modified as

$$\mathbf{S}(\theta) = \exp\left(-i\frac{\sigma \cdot \mathbf{n}}{2}\theta\right) \mathbf{S} \exp\left(i\frac{\sigma \cdot \mathbf{n}}{2}\theta\right), \quad (6.8)$$

where θ is the angle with the c -axis. The band structure therefore becomes angle-dependent.

An additional dependence of the band structure on field strength and angle lies in the Zeeman term. The orbital angular momentum is not completely quenched, so as well as coupling to the spin moment the field couples to the orbital moment.

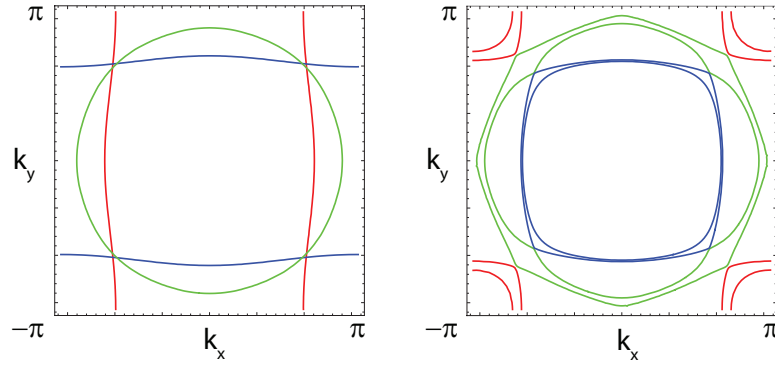


Fig. 6.8: **Effect of spin-orbit coupling on the Fermi Surface:** Electronic bands based on the Ru d -orbitals of $\text{Sr}_3\text{Ru}_2\text{O}_7$ before and after spin-orbit coupling.

The standard Zeeman term is replaced by

$$\hat{H}_Z = -\mathbf{H} \cdot \sum_{i,\sigma,\alpha} c_{i,\sigma,\alpha}^\dagger (\mathbf{L} + \mathbf{S}) c_{i,\sigma,\alpha}. \quad (6.9)$$

Neglecting for the moment the standard spin Zeeman coupling we have the orbital Zeeman term

$$\hat{H}_{OZ} = - \sum_{i,\sigma,\alpha} c_{i,\sigma,\alpha}^\dagger [H_x l_x + H_y l_y + H_z l_z] c_{i,\sigma,\alpha} \quad (6.10)$$

where l_x, l_y, l_z are as in Eq.6.6, $\psi_{i,\sigma}$ is the vector $(c_{i,\sigma,zx}, c_{i,\sigma,yz}, c_{i,\sigma,xy})$ and

$$H_x = H \sin \theta \cos \phi, \quad H_y = H \sin \theta \sin \phi, \quad H_z = H \cos \theta, \quad (6.11)$$

with θ the angle from c -axis and ϕ the angle from a in the ab -plane and H is the magnitude of the field.

This term is obviously zero in the absence of any field and so the spin-orbit term is necessary to hybridise the bands. However, in the presence of a field we expect the orbital Zeeman term to dominate over the spin-orbit term. The effect of changing field angle on the Fermi surface due to this term is shown in Fig.6.9. We see that anisotropy is produced and aligned by an in-plane field component.

Having established that orbital effects lead to an angle-dependent band structure we ask how this will affect the properties of $\text{Sr}_3\text{Ru}_2\text{O}_7$ and our model for inhomogeneous phase formation. In principle we can take the dispersions obtained by diagonalising the above Hamiltonians and calculate the magnetic phase diagram in exactly the same way as previously, except fixing the chemical potential or filling

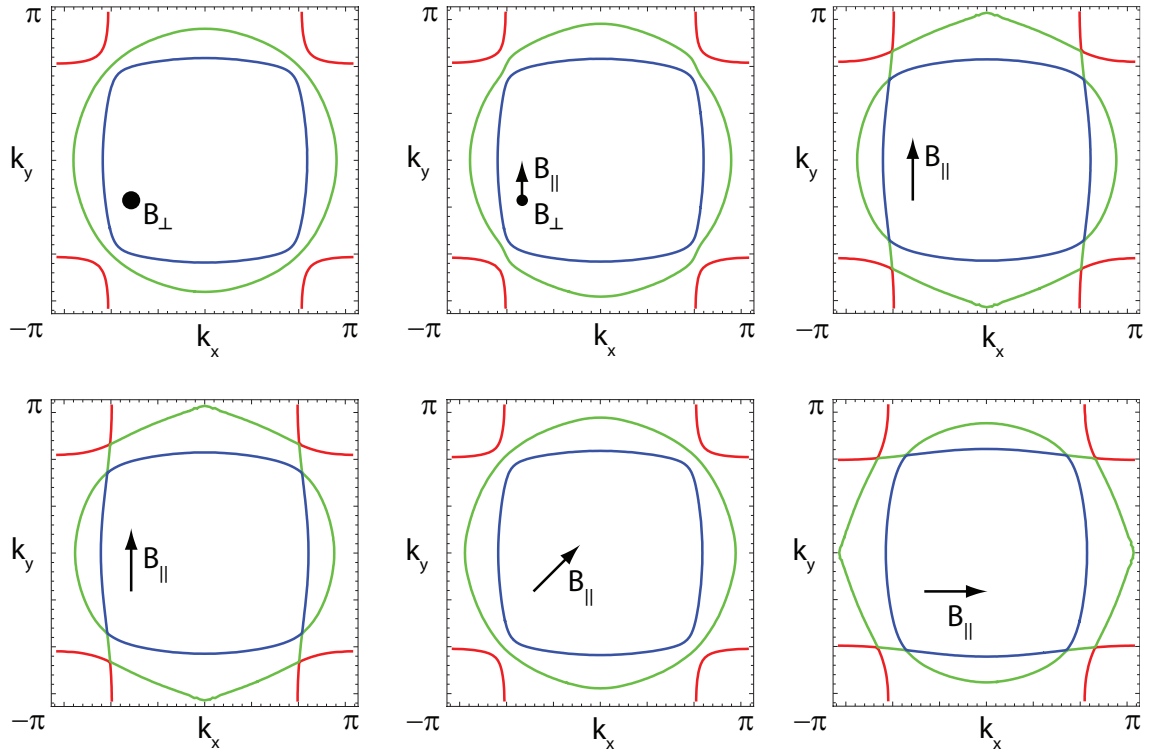


Fig. 6.9: Effect of orbital Zeeman coupling on the Fermi Surface: The top row shows the effect of rotating the field from c -axis into the ab -plane. θ is the angle from c -axis and ϕ is the angle within the ab -plane. a) $\theta = 0$, $\phi = 0$, b) $\theta = \frac{\pi}{4}$, $\phi = 0$, c) $\theta = \frac{\pi}{2}$, $\phi = 0$. The bottom row shows rotation of the field in the ab -plane. a) $\theta = \frac{\pi}{2}$, $\phi = 0$, b) $\theta = \frac{\pi}{2}$, $\phi = \frac{\pi}{4}$, c) $\theta = \frac{\pi}{2}$, $\phi = \frac{\pi}{2}$. The arrow indicates the direction of the field. Effects are exaggerated for clarity.

and varying the field angle. Varying the angle will move or broaden the peaks in the density of states which come from anticrossing of the bands. The critical field and temperature of the metamagnetic transition will therefore be tuned by field angle, as the transition is caused by the peak. These calculations are numerically more difficult than for the simple tight-binding models and the calculation of the phase diagram is currently in progress. Once a line of metamagnetic critical endpoints is established the spin-stiffness K_{\perp} can be calculated along the line in same way as we have done for the next-nearest-neighbour tight-binding model.

As well as tuning the metamagnetic transition and phase boundaries the angle of the applied field alters the properties of the anomalous phase. The degree of anisotropy is determined by the angle of the field with the c -axis. The direction of anisotropy is pinned to a crystal axis determined by the angle of field in the ab -plane. There is currently no mechanism for this dependence in our model. The orbital

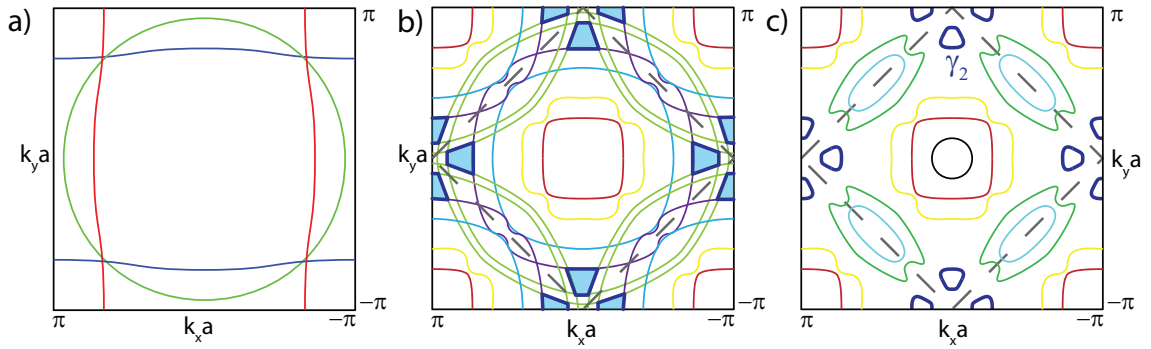


Fig. 6.10: Comparison of full Fermi surface and orbital model: a) The basic model we have used to illustrate orbital effects. b) The full 12 bands required to make up the experimentally determined Fermi surface of $\text{Sr}_3\text{Ru}_2\text{O}_7$, the regions which will become the γ_2 pockets have been indicated. c) The experimentally determined Fermi surface of $\text{Sr}_3\text{Ru}_2\text{O}_7$ with γ_2 indicated.

effects presented here however give a clear mechanism. An in-plane field component breaks the symmetry of the dispersion in a way which depends on the in-plane angle as shown in Fig.6.9. The wavevector of the spiral modulation is determined by the direction of this weak underlying anisotropy, whereupon the modulation produces the larger, observed, anisotropy. With the field along the c -axis there is no symmetry breaking and the modulation is made either by an equal superposition of spirals in different directions resulting in a spin-crystal, or by domains of alternative orientations, giving no overall anisotropy.

The Fermi surface of $\text{Sr}_3\text{Ru}_2\text{O}_7$ is extremely complex, as described in section 3 and illustrated again in Fig.6.10. Constructing a model including all of the bands plus spin-orbit and orbital Zeeman couplings is a formidable task. If, as we postulate, the phenomena observed in $\text{Sr}_3\text{Ru}_2\text{O}_7$ are single-band effects then we do not require this full model, only an effective dispersion for the band in question. Based on experimental evidence (section 3) this would seem to be the γ_2 band which produces the small pockets in the corner of the reduced Brillouin zone. The next step would therefore be the construction of a minimal model which describes this pocket, and the calculation of its properties.

6.4.2 The possibility of observation by neutron scattering

The modulated magnetic phase which we predict should be directly detectable in elastic neutron scattering. Unfortunately such data in the anomalous phase do not exist. Experiments done outside of the phase show fluctuations at $q = 0.25$ of the

tetragonal Brillouin zone (the zone before the reconstruction due to rotation of the ruthenium oxide octahedra). The strength of these fluctuations increases as the phase is approached [86, 87]. It is tempting to interpret this as the ‘freezing in’ of modulated order, although the static phase has not been observed.

The wavevector of this fluctuation corresponds to a nesting vector between the γ_2 pockets. In a fermi surface of this complexity it is not surprising that a particular nesting vector can be found, but it is suggestive that it connects the pockets which are thought to be involved in the metamagnetism.

The modulation may be hard to observe, if it is a small modulation on top of a homogeneous background, as well as due to uncertainty in the wavevector which should be examined. There is also the possibility that a spiral phase may be ‘melted’ and therefore form a nematic phase which breaks rotational but not translational symmetry, these will be considered in chapter 7. Elastic scattering in the phase will hopefully determine whether or not modulation exists.

6.5 Summary

The modulated magnetic phase is a good candidate for matching the properties of the anomalous phase of $\text{Sr}_3\text{Ru}_2\text{O}_7$. Our model reproduces the topology of the experimental phase diagram, giving the bifurcation of the metamagnetic transition and a second-order transition enclosing the phase as a ‘roof’. We expect that the modulated phase will reproduce the transport anisotropy of the anomalous phase, although we have not yet performed calculations of this. Our proposal is based on a peak in the density of states, which has been shown to exist in ARPES studies [67]. Calculations of the thermodynamic signatures associated with this peak match well with experiment, giving a specific heat which rises as we approach the phase and a double peak structure above it. It remains to calculate the thermodynamic properties of the modulated phase itself, but it is possible that these will match the experimental observation of a higher entropy in the anomalous phase than outside. The experimental phase diagram is tuned by field angle, whereas our model is tuned by band filling. The angle dependence is most likely due to orbital effects which may be included in our model. Our proposal is for a state with a spatially modulated magnetisation, which should be visible in neutron scattering experiments. These will ultimately determine if the anomalous phase has static modulated magnetic order.

Part III

RELATED THEORIES, FUTURE DIRECTIONS AND
CONCLUSIONS

7. ELECTRON NEMATICS

7.1 *Electron nematics*

In chapter 4 we showed that the crystal lattice can drive spatial modulation of magnetic order. We will now consider a proposal for a type of phase which is related to the modulated state, but where only the rotational and not the translational symmetry of the system is broken. These are known as ‘nematic’ phases [23]. They are an alternative proposal for the anomalous phase of $\text{Sr}_3\text{Ru}_2\text{O}_7$ [52, 71, 73, 88].

We will discuss the different realisations of the nematic state which have been proposed. We will show that the energetic drive for these phases is very similar to the modulated state which we study and consider how the two states are connected.

7.1.1 *Liquid-crystal analogy*

The name ‘nematic’ is borrowed from the terminology of liquid crystals. In these systems it is easy to construct orderings which are intermediate between liquid and crystalline order. Imagine a system of anisotropic particles, each one a rod for example. In the liquid phase they are arranged completely randomly, with full rotational and translational symmetry on large scales (Fig.7.1). On the other extreme, in the crystalline phase the particles are arranged in a rigid array, with their axes aligned with one another. This arrangement breaks both translational and rotational symmetries. There are two states which restore some of these symmetries. If the position of the particles is random, but they are aligned along a particular direction, then the system has translational symmetry, but the rotational symmetry is broken. This is called the nematic phase. Alternatively, as well as aligning, the particles can order positionally in one dimension, forming layers, each of which has liquid-like positioning within it. These are known as smectics.

It has been postulated that similar symmetry breaking states may exist in electronic systems [23]. In between the isotropic Fermi liquid and the Wigner crystal [89] there may be phases which break some, but not all, of the symmetries [90]. The spiral state which we have considered may be considered a smectic phase - it breaks

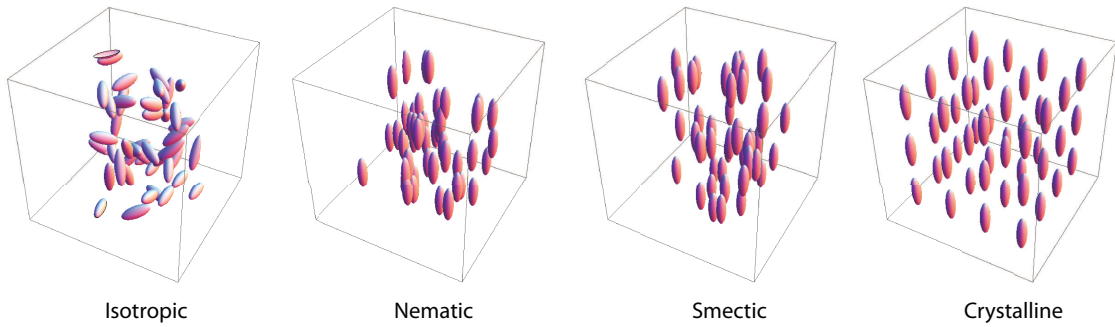


Fig. 7.1: Liquid crystal orderings: In the isotropic case the particles are arranged with random position and orientation. In the nematic case the positioning is still random, but the orientation is uniform. In the smectic case the particles are also ordered in position along one axis. In the crystalline case the particles are ordered in position and direction.

rotational symmetry, and translational symmetry along one axis. When we speak of an electron nematic state in a lattice we must bear in mind that the symmetries of free space have already been broken by the lattice. In this case the nematic breaks the symmetry of the lattice, reducing, for example, a system with fourfold rotational symmetry to twofold.

Nematics may form in several ways. A state which does break translational symmetry, such as a spin-density wave like we have considered, a charge-density wave or stripe order [91], may be ‘melted’ [90,92]. By breaking up the pattern over large distance scales the translational symmetry is restored at long range. Alternatively distortions may be made in the k -space order which break rotational symmetry, but not the real-space translational symmetry. Such distortions are called Pomeranchuk distortions [44] and may come in various forms.

7.1.2 Pomeranchuk instability

Pomeranchuk considered how interactions may drive a distortion of the Fermi surface even in the absence of a lattice [44]. Some of these distortions are illustrated in Fig.7.2.

Such distortions will result in transport anisotropy and were suggested as a candidate for the anomalous phase of $\text{Sr}_3\text{Ru}_2\text{O}_7$ [52]. Microscopic interactions which produce such distortions have been studied theoretically in the isotropic [93] and lattice cases [94,95]. When a lattice is present the Fermi surface is not initially isotropic, and the distortion will also be shaped by the symmetry of the lattice.

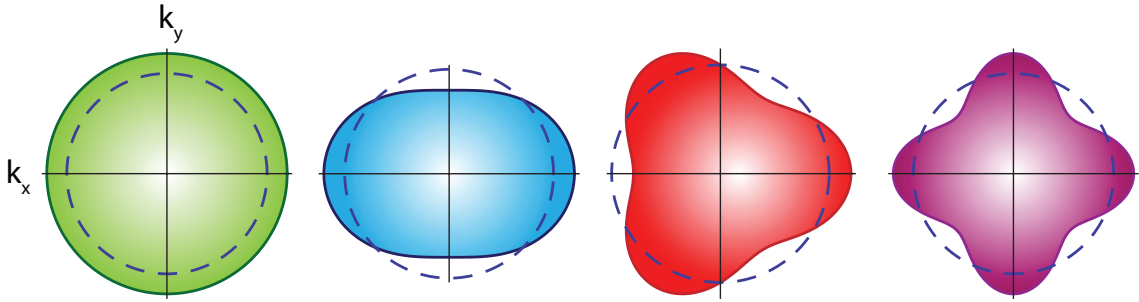


Fig. 7.2: **Pomeranchuk distortions:** Pomeranchuk distortions of the Fermi surface. The s -wave distortion (green) corresponds to a uniform magnetization.

7.1.3 d -wave distortions

When there is a lattice present distortions of the Fermi surface will reflect this symmetry. There has been much interest in so-called d -wave distortions in a two dimensional square lattice [42,43,71,88,94,95]. This has the tight-binding dispersion Eq. 4.2 and the associated van Hove singularities. In this distortion the Fermi surface elongates along one axis of the lattice, jumping over two of the van Hove points. There is some numerical renormalisation group evidence for an increased forward scattering near to the van Hove points in the Hubbard [94] and t-J models [95], although this effect is delicate [80]. The majority of calculations assume that this form of distortion occurs and calculate the mean-field phase diagram [42,43,71,88].

A Hamiltonian of the following form is assumed:

$$H = \sum_{\mathbf{k}} \epsilon_{\mathbf{k}} n_{\mathbf{k}} + \sum_{\mathbf{k}, \mathbf{k}'} (g - u d_{\mathbf{k}} d_{\mathbf{k}'}) n_{\mathbf{k}n_{\mathbf{k}'}} \quad (7.1)$$

Here $d_{\mathbf{k}}$ is a function with $d_{x^2-y^2}$ symmetry, such as $\cos k_x - \cos k_y$.

At the mean-field level this theory is identical to Stoner magnetism. The proximity to van Hove singularities favours the splitting of Fermi surfaces, except that since the interaction is now anisotropic the Fermi surface distorts in one direction preferentially. As in the Stoner case this can be first-order or second-order. The magnetic field splits the Fermi surfaces so that one approaches the van Hove singularity. It becomes favourable for the Fermi surface distortion to occur and the system breaks the fourfold symmetry. As the field increases there is a second jump as the Fermi surface returns to the lattice symmetry. In this respect the predictions are similar to the case which we consider, except that the distortion exists all along the van Hove lines rather than appearing only away from the van Hove filling. We also note that the first-order transitions in this model are associated with phase

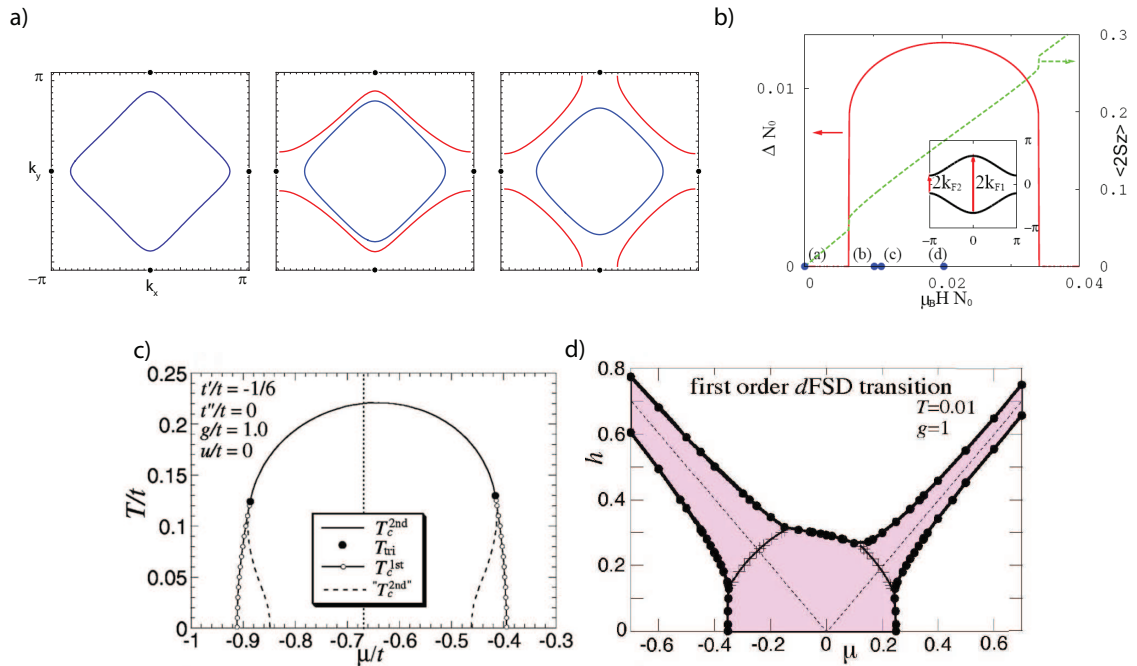


Fig. 7.3: The d -wave Fermi surface distortion: a) The Fermi surface at zero field, in the nematic region and on the high-field side of the nematic region. Black dots are the position of van Hove singularities in the dispersion. The Fermi surface distortion jumps over two of these before the others, breaking the symmetry of the lattice. b) The magnetization (dashed line) and nematic order parameter (solid line) as a function of field. Figure from [96]. c) The nematic region in the μ, T plane. Figure from [43]. d) The nematic region of the h, μ plane, the van Hove singularity is at $\mu = 0$, the dotted lines represent where one Fermi surface touches the van Hove singularity. Figure from [88].

separation in the same way as those in our model.

While the distortion of the Fermi surface will result in transport properties that break the symmetry of the lattice it must be noted that most of the change is around the van Hove points. Here the Fermi velocity is already extremely small and so the distortion will have little effect on the bulk properties. In order to explain the magnitude of the effects seen in $\text{Sr}_3\text{Ru}_2\text{O}_7$ it is necessary to invoke further effects, such as the formation of domains of different nematic orientations. Here the enhanced resistivity is due to scattering off domain walls.

An alternative perspective on these distortions is to step back and consider the orbital basis of the electronic bands making up the Fermi surface.

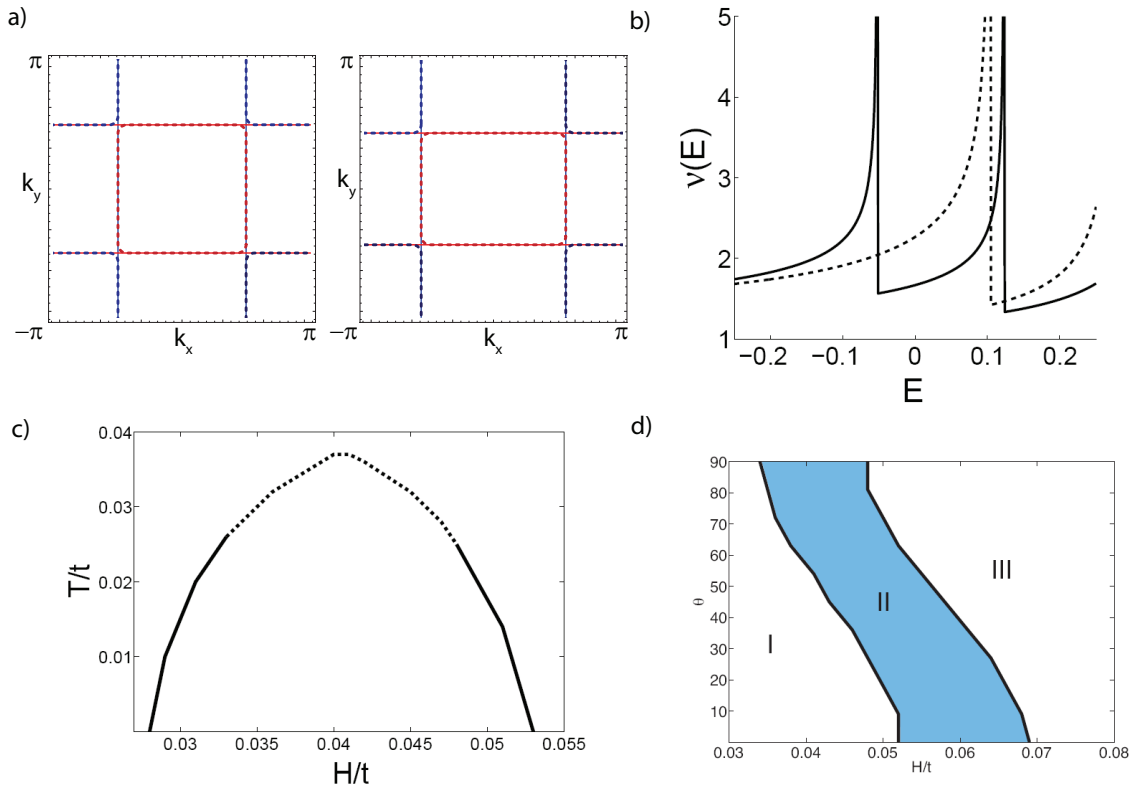


Fig. 7.4: **Orbital ordering:** a) Fermi surface before and after nematic ordering. b) Density of states in the nematic state (solid line) and normal state (dotted line). c) Cut through phase diagram in the H, T plane. d) Angular dependence of the nematic region. Figures b) c) and d) from [73].

7.1.4 Orbital ordering

The real band structure of $\text{Sr}_3\text{Ru}_2\text{O}_7$ is made up from the Ru d -orbitals as discussed in section 3. Recent work has investigated a model consisting of the orbitals forming the three basic bands of the ruthenium oxide layer [73, 97]. These quasi-1D bands have sharp van Hove singularities and so show the Stoner instability. By introducing an inter-orbital interaction it is possible to form a ‘magnetic’ interaction where instead of electron transfer between spin-up and spin-down bands the occupation of different orbitals becomes uneven. This orbital ordering is reflected in the Fermi surface as a distortion similar to the d-wave picture, this is shown in Fig.7.4.

This model captures some of the angular dependence observed in $\text{Sr}_3\text{Ru}_2\text{O}_7$ through the inclusion of orbital Zeeman and spin-orbit coupling terms. The effect of these terms on the Fermi surface was considered in section 6.4.1. This reproduces the angular dependence of the metamagnetic transition, but not the restriction of

the anomalous phase to a small range of angles, as can be seen in figure 7.4.

7.1.5 *Melted stripe order*

The environment in which electronic nematic behaviour has been most clearly seen is the two dimensional electron gas [25]. Here the nematic state is due to a ‘melting’ of charge modulated order. In semiconductor heterojunctions a two dimensional layer of conduction electrons is formed. These have extremely low electron densities and allow the study of physics associated with Landau levels, such as the quantum Hall effect. In high Landau levels it is predicted that electrons form charge modulated, or ‘stripe’ phases [98,99]. This is a smectic phase consisting of a modulation of the filling fraction in one direction. If dislocations are introduced into this ordering such that the translational symmetry is restored then the phase would become nematic [92]. This situation seems to have been realized in a number of experiments, leading to highly anisotropic transport [25]. This anisotropy can be aligned by the in-plane field. Stripe phases, and possibly nematicity, have also been observed in the cuprates [24, 91]. This provides an example of how modulated and nematic order are related which may be pursued in the case of our spiral state.

7.2 *The link between nematic and spiral order*

The spiral magnetic order which we have proposed is in many ways related to nematic order. The Fermi surface distortions related to forming the states are similar, possibly identical. The main difference is that this k -space distortion is associated with a real space modulation in the case of the spin-spiral. As we have noted this may be ‘melted’ by introducing phase-slips and dislocations to restore translational symmetry and create a nematic state.

These similarities can be seen in the energetic favourability of the states which is due both in the spiral and d-wave distortions to occupying peaks in the density of states caused by the lattice. It is possible that this similarity will carry across to the case where spiral order is stabilised by quantum fluctuations [32, 40], so that nematic order may also be stabilised near to quantum critical points.

8. FUTURE RESEARCH DIRECTIONS

There are many opportunities for future study opened up by the research reported in this thesis. Some of these are straightforward extensions of the work presented. Others move into new areas which are nevertheless connected to the ideas discussed here, such as nematic states and quantum criticality.

8.1 *Extensions of current research*

8.1.1 *How does field angle tune the phase diagram?*

The major element missing between our theory and the experimental situation of $\text{Sr}_3\text{Ru}_2\text{O}_7$ is the dependence of the transitions and anomalous phase on the angle of the applied magnetic field with respect to the crystalline axes. We have assumed that this angle effectively tuned the filling of the relevant bands relative to a peak in the density of states.

It seems that this angular dependence can be incorporated through spin-orbit and orbital Zeeman couplings, as discussed in section 6.4.1. These have the effect of slightly changing the bandstructure with field angle, moving or widening the relevant peaks. Incorporating these effects into the dispersion used for calculations will allow an inclusion of the angle into our theory.

8.1.2 *More realistic dispersions*

Associated with including orbital effects is moving towards a realistic bandstructure for $\text{Sr}_3\text{Ru}_2\text{O}_7$ in the calculations. While it seems unlikely that the full bandstructure of $\text{Sr}_3\text{Ru}_2\text{O}_7$ will be tractable, or necessary, in calculations, an effective model of the relevant Fermi surface pockets could be made.

With the relevant bands identified an accurate prediction for the magnitude and direction of the modulation wavevector \mathbf{q} could be made. Determining this would greatly assist in neutron scattering experiments to confirm the presence of magnetic modulation.

8.1.3 Multiple wavevectors

Modulation need not occur at a single wavevector. Indeed, considering the degeneracy of different directions in the lattice, it seems likely that a superposition of several wavevectors would occur. Two spirals running in opposite directions will give a linear spin-density wave, four arranged in a square will give a spin-crystal, and so on. Such a situation is found in FFLO, where the optimum combination of wavevectors is determined by external parameters and the crystal lattice. These different arrangements lead to different transitions to the homogeneous state. Calculating the phase diagram including all these possibilities has proved a complex and delicate task, nonetheless, a full picture of magnetic modulation must include these possibilities. The various spin-textures may also have different signals in the thermodynamics and the transport properties of the phase, since now translational symmetry is broken in all directions.

8.1.4 Transport

The property which identifies the anomalous phase of $\text{Sr}_3\text{Ru}_2\text{O}_7$ is the anisotropic transport. The magnetoresistance of $\text{Sr}_3\text{Ru}_2\text{O}_7$ is anomalously high in the phase and is different parallel or perpendicular to an axis which is picked out by the applied field. The variation in magnetism along the modulation wavevector would produce enhanced scattering, thereby causing this anisotropic transport. We have not yet calculated this explicitly however and such calculations would provide compelling evidence for our proposal as well as an additional way to distinguish the smectic and nematic proposals.

8.1.5 Entropy

One of the surprising experimental features of the anomalous phase is that it has a higher entropy than its surroundings. This fact has yet to be replicated by any theory of the phase. Careful calculation of the density of states in the spiral phase will reveal whether this is also the case in our proposal. We must then consider how the Goldstone mode and fluctuations about the mean-field minimum of the free energy affect the properties of the phase.

8.2 *New directions*

8.2.1 *Interplay of lattice and fluctuation effects*

Quantum fluctuations have been shown to cause the same sort of effects which have been studied here as a consequence of the lattice. Both metamagnetism and spin-spiral states have been predicted around itinerant quantum critical points [32,39,40]. Currently these calculations are carried out in the absence of a lattice. This opens up the question of how fluctuation-induced and lattice-induced effects interact. In a system close to a peak in the density of states do the effects reinforce each other, creating a higher-temperature tricritical point and larger region of inhomogeneity? Do they cancel to reinstate the continuous transition? Or does one simply dominate the phase diagram?

As well as the zero-field phase diagram the metamagnetic quantum critical endpoint must be considered. The effect of quantum fluctuations on this point, and their interplay with the modulated phase which we predict, should be calculated.

8.2.2 *Electron nematics*

The various forms of nematic order are intriguing new phases. Their relation to the melting of modulated order and presence in the phase diagram along with this order should be clarified, as well as a possible connection with quantum critical points worked out.

These are possible research directions which link the effects considered in this thesis with other topics of current interest. By combining these subjects a more complete picture of itinerant magnetism will be built up.

9. CONCLUSION

We set out to study a model for a modulated magnetic state acting as an intermediate phase in a metamagnetic transition. We were inspired in this idea by experimental results on the material $\text{Sr}_3\text{Ru}_2\text{O}_7$ and by a general principle of modulated phases appearing as intermediate states in phase transitions. This is most clearly seen in the superconducting Fulde-Ferrell-Larkin-Ovchinnikov phase, which is analogous to the magnetic system we consider. Such phases are also found in cold-atomic gases [62], excitonic insulators [100], color superconductivity in quark matter [60] and neutron stars, where they have been invoked to explain glitches in pulsar rotation [60].

We showed that generic features in the band-structure could drive not only metamagnetism, but magnetic spiral states. These states appear as an intermediate phase in the metamagnetic transition, causing the bifurcation of the parent transition to enclose the phase. We expect the same reasoning to carry across to more complex spin-textures made from superpositions of spirals. Having calculated the phase diagram for such an intermediate phase we see that it matches closely the topology of the experimentally determined phase diagram of $\text{Sr}_3\text{Ru}_2\text{O}_7$. In addition we have shown that the thermodynamic consequences of our proposal are in agreement with experiment. This suggests that the anomalous phase of $\text{Sr}_3\text{Ru}_2\text{O}_7$ may be just such a modulated phase. The same effects may occur in other systems, such as NbFe_2 and ZrZn_2 which show metamagnetism associated with resistive anomalies [47, 48]. Our analysis is not specific to one material, being based on rather generic features of the bandstructure.

Our calculation of the phase diagram proceeds from a consideration of the overall experimental phase diagram of $\text{Sr}_3\text{Ru}_2\text{O}_7$. This is dominated by a metamagnetic transition. We therefore take the simplest theory which explains this transition - a Stoner model with a peak in the electronic density of states. We calculate the phase diagram via a Ginzburg-Landau expansion based both on phenomenological arguments and an expansion of the microscopic Hamiltonian. We then show that modulated states arise naturally in this model and calculate that modulated or-

der becomes more favourable as we tune along the metamagnetic transition away from the van Hove singularity. Using the Ginzburg-Landau expansion we calculate how the parent metamagnetic transition reconstructs to accommodate this modulated magnetisation. The transition bifurcates at a dislocated tricritical point, with the modulated phase lying between the two transitions. The phase is bounded from above by a sheet of continuous transitions that form a roof which encloses the phase. This phase diagram matches the topology of the experimentally determined phase diagram for $\text{Sr}_3\text{Ru}_2\text{O}_7$ [52]. This material shows a metamagnetic transition, the critical endpoint of which can be tuned until the transition bifurcates. Between the wings is a phase with an anomalously high and anisotropic resistivity. We believe that this phase is the modulated magnetic order which we propose.

Following on from this we examined the thermodynamic properties of the parent metamagnetic transition, calculating how the specific heat and entropy evolve with applied field and temperature. We found subtlety even in this basic feature of the phase diagram, with the specific heat having a double-peak as a function of field and a non-trivial relationship of field and temperature scales. These results are a good match for the experimentally determined thermodynamic behaviour of $\text{Sr}_3\text{Ru}_2\text{O}_7$ [74] and inform the interpretation of this data. The next step is a calculation of the thermodynamic properties of the spiral phase. These calculations have not yet been completed but we note that our modulated phase provides possibilities for reconciling with experimental data on $\text{Sr}_3\text{Ru}_2\text{O}_7$ which should be examined.

As well as thermodynamic data the phase is characterised by its transport properties [26]. The formation of a modulated state would produce enhanced scattering of electrons and the wavevector dependence would result in anisotropy. We therefore believe that our proposed phase would produce the high and anisotropic resistivity of $\text{Sr}_3\text{Ru}_2\text{O}_7$. This is another subject for future calculation.

There are several extensions of our model that will allow even closer connection to the experimental data on $\text{Sr}_3\text{Ru}_2\text{O}_7$. These are the inclusion of the effect of the magnetic field angle and a more realistic picture of the electron dispersion. It seems likely that this angle dependence can be accounted for by introducing an orbital Zeeman coupling which modifies the band structure as the field angle is changed. Associated with this will be the choice of a minimal model of the band structure which will accurately reflect $\text{Sr}_3\text{Ru}_2\text{O}_7$ while remaining amenable to calculation. These effects should be straightforward to introduce into our framework.

The study of phase transitions at low temperatures is closely linked to quantum

criticality. Although we have not included the effect of quantum fluctuations in our model there are several possible areas of connection. The initial interest in $\text{Sr}_3\text{Ru}_2\text{O}_7$ lay in the presence of a quantum critical endpoint. Although models of the anomalous phase do not include its effects quantum critical points are known to stabilize new phases and so may be important. Indeed recent work on non-analytic corrections to Hertz-Millis theory shows that itinerant quantum critical points are unstable to the formation of first-order transitions and spin-spiral states [32, 39, 40] - exactly the phenomena studied here in a lattice-driven context. The interplay of the two will be important to the behaviour of real systems.

As well as the modulated states which we consider there are intriguing proposals for nematic states which retain the orientational but not translational orientation of the modulated state [23]. These may be made by melting modulated states and have very similar energetics. The connection between these two types of order is another interesting extension of the ideas contained here.

It is clear that there is much subtlety in the phases of itinerant magnets. The crystal lattice can drive a number of ordering tendencies, like the ferromagnetism and the spiral magnetism considered here. We have shown how a complex magnetic phase diagram may come about by combining several simple ideas. These ideas present a compelling explanation for the anomalous phase of $\text{Sr}_3\text{Ru}_2\text{O}_7$. The ideas may be extended further, continuing to explore the rich phenomenology of strongly correlated systems.

APPENDIX

A. PARTITION FUNCTIONS AND THE IMAGINARY-TIME COHERENT-STATE PATH INTEGRAL

A.1 Coherent State Path Integrals and the Partition Function

The formulation of many-body finite-temperature physics is based on an observation that the Boltzmann weight looks like a time-evolution operator in imaginary time:

$$e^{i\frac{\hat{H}\tau}{\hbar}} \rightarrow e^{i\frac{\hat{H}(-it)}{\hbar}} \rightarrow e^{\beta\hat{H}t}. \quad (\text{A.1})$$

So finite temperature many body physics can be neatly reformulated by using evolution in imaginary time. In this formulation the partition function \mathcal{Z} becomes a path integral in imaginary time.

In order to take account of the many-body nature of the problem we will use a coherent state path integral. Coherent states are eigenstates of the annihilation operator and formulation of the coherent state path integral proceeds as for the normal path integral. As we are dealing with fermions we must remember that our eigenvalues are now anti-commuting Grassman numbers and use the following relations:

$$1 = \int d\eta d\bar{\eta} e^{-\bar{\eta}\eta} |\eta\rangle\langle\eta| \quad (\text{A.2})$$

$$\langle\eta|\nu\rangle = e^{\bar{\eta}\nu} \quad (\text{A.3})$$

We proceed by writing the partition function,

$$\mathcal{Z} = \text{Tr} e^{-\beta(\hat{H}-\mu\hat{N})} = \sum_n \langle n| e^{-\beta(\hat{H}-\mu\hat{N})} |n\rangle, \quad (\text{A.4})$$

and inserting a resolution of the identity,

$$\mathcal{Z} = \int d\underline{\bar{\psi}} d\underline{\psi} e^{-\underline{\bar{\psi}}\cdot\underline{\psi}} \sum_n \langle n| \underline{\psi}\rangle \langle\underline{\psi}| e^{-\beta(\hat{H}-\mu\hat{N})} |n\rangle$$

$$\begin{aligned}
&= \int d\bar{\psi}d\psi e^{-\bar{\psi}\cdot\psi} \sum_n (-1)^n \langle \underline{\psi} | e^{-\beta(\hat{H}-\mu\hat{N})} | n \rangle \langle n | \underline{\psi} \rangle \\
&= \int d\bar{\psi}d\psi e^{-\bar{\psi}\cdot\psi} (-1) \langle \underline{\psi} | e^{-\beta(\hat{H}-\mu\hat{N})} | \underline{\psi} \rangle. \tag{A.5}
\end{aligned}$$

We now divide the imaginary time interval $0 \rightarrow \beta$ into N slices and insert resolutions of the identity between the slices

$$\mathcal{Z} = \int (-1) \prod_n d\bar{\psi}d\psi e^{-\bar{\psi}\cdot\psi} \langle \underline{\psi} | \dots \rangle_{n+1} | \underline{\psi}_n \rangle \langle \underline{\psi}_n | \left(e^{-\beta(\hat{H}-\mu\hat{N})} \right)_n | \underline{\psi}_{n-1} \rangle \langle \underline{\psi}_{n-1} | (\dots) \tag{A.6}$$

We now allow the operators to act on the states $\bar{\psi}, \psi$ turning them into numbers and allowing us to remove the exponential and combine the states using the previous relationship.

$$\begin{aligned}
\mathcal{Z} &= \int (-1) \prod_n d\bar{\psi}d\psi e^{-\frac{\beta}{N} [H(\bar{\psi}_n, \psi_{n-1}) - \mu N(\bar{\psi}_n, \psi_{n-1})] - \bar{\psi}_n \cdot \psi_n + \bar{\psi}_n \cdot \psi_{n-1}} \\
&= \int (-1) \prod_n d\bar{\psi}d\psi e^{-\frac{\beta}{N} [H(\bar{\psi}_n, \psi_{n-1}) - \mu N(\bar{\psi}_n, \psi_{n-1})] + \bar{\psi}_n \cdot (\psi_n - \bar{\psi}_{n-1})}. \tag{A.7}
\end{aligned}$$

In the continuum limit this becomes

$$\begin{aligned}
\mathcal{Z} &= \int \mathcal{D}\bar{\psi} \mathcal{D}\psi e^{-\int_0^{\beta\hbar} d\tau [\bar{\psi} \partial_\tau \psi + \hat{H}(\bar{\psi}, \psi) - \mu \hat{N}(\bar{\psi}, \psi)]} \\
&= \int \mathcal{D}(\bar{\psi}, \psi) e^{-\mathcal{S}[\bar{\psi}, \psi]}. \tag{A.8}
\end{aligned}$$

Inserting our Hamiltonian we have a partition function for the Stoner model

$$\mathcal{S}[\bar{\psi}, \psi] = \int_0^\beta d\tau \int d^d r \int d^d r' \left[\bar{\psi} [\sigma_0 (\partial_\tau + \epsilon(\mathbf{k})) - \sigma_z h] \psi - g (\bar{\psi} \bar{\sigma} \psi)^2 \right]. \tag{A.9}$$

We will now remove the quartic term by using a Hubbard-Stratonovich transformation.

A.2 Hubbard-Stratonovich Transformation

A Hubbard-Stratonovich transformation [101, 102] is little more than Gaussian integration and completing the square. Given a quartic term y^4 we may introduce a new variable x which we integrate out. By completing the square and shifting this new x variable we can reduce the quartic term to a squared term. Consider the

following:

$$\mathcal{A} = Ae^{\alpha y^4} = \int \mathcal{D}(x)e^{-\alpha x^2} e^{\alpha y^4}, \quad (\text{A.10})$$

we may shift the x variable such that

$$\mathcal{A} = \int \mathcal{D}(x)e^{-\alpha(x-y^2)^2} e^{\alpha y^4} = \int \mathcal{D}(x)e^{-\alpha x^2 - \alpha y^4 + 2\alpha xy^2 + \alpha y^4} = \int \mathcal{D}(x)e^{-\alpha x^2 + 2\alpha xy^2}, \quad (\text{A.11})$$

we therefore have a prescription for decoupling a fourth order term.

In our case $g(\bar{\psi}\sigma\psi)^2 \longrightarrow -\bar{\psi}\frac{g}{2}\sigma\cdot\mathbf{m}\psi - \frac{g}{4}\mathbf{m}^2$ giving for our action

$$\mathcal{S}[\mathbf{m}, \bar{\psi}, \psi] = \int_0^\beta d\tau \int d^d r \left[\bar{\psi} \left[\sigma_0(\partial_\tau + \epsilon(\mathbf{k})) - \sigma_z h - \frac{g}{2}\sigma\cdot\mathbf{m} \right] \psi - \frac{g}{4}\mathbf{m}^2 \right]. \quad (\text{A.12})$$

Here we have exchanged the quartic interaction for an additional field. Although exact, there is some choice in the Hubbard-Stratonovich transformation to be used. We choose the decoupling most suited to our problem.

A.3 Gaussian Integral

We may now perform the Gaussian integral over the Grassman variable $\psi, \bar{\psi}$ to get

$$\mathcal{Z} = \int \mathcal{D}(\mathbf{m})e^{-\mathcal{S}_m} \det \left[\sigma_0(\partial_\tau + \epsilon(\mathbf{k})) - \sigma_z h - \frac{g}{2}\sigma\cdot\mathbf{m} \right], \quad (\text{A.13})$$

where we have defined

$$\mathcal{S}_m = -\frac{g}{4} \int_0^\beta d\tau \int d^d r \mathbf{m}^2. \quad (\text{A.14})$$

Using the identity $\ln \det \hat{\mathbf{A}} = \text{tr} \ln \hat{\mathbf{A}}$, we get

$$\mathcal{Z} = \int \mathcal{D}(\mathbf{m})e^{-\mathcal{S}_m + \text{tr} \ln [\sigma_0(\partial_\tau + \epsilon(\mathbf{k})) - \sigma_z h - \frac{g}{2}\sigma\cdot\mathbf{m}]}. \quad (\text{A.15})$$

We may transform into the frequency representation where imaginary time derivatives become frequencies ω_n , known as Matsubara frequencies. We note that this can be written

$$\mathcal{Z} = \int \mathcal{D}(\mathbf{m})e^{-\mathcal{S}_m + \text{tr} \ln [G_0^{-1} + V]} = \int \mathcal{D}(\mathbf{m})e^{\text{tr} \ln [G^{-1}]}, \quad (\text{A.16})$$

where G_0 is the free-electron Green's function.

A.4 Landau Expansion

Since $\mathcal{F} = -kT \ln \mathcal{Z}$, $\mathcal{Z} = e^{-\beta\mathcal{F}}$, the exponent of our expression is the Free Energy, to find the Landau coefficients we can therefore expand it in powers of m .

We now expand the $\text{tr} \ln [G^{-1}]$ in powers of the order parameter \mathbf{m} (Note $V \propto m$).

$$G^{-1} = \begin{bmatrix} -(i\omega_n - \epsilon_k) + m_z & m_\perp \\ -m_\perp & -(i\omega_n - \epsilon_k) - m_z \end{bmatrix}. \quad (\text{A.17})$$

and

$$G_0^{-1} = \begin{bmatrix} -(i\omega_n - \epsilon_k) & 0 \\ 0 & -(i\omega_n - \epsilon_k) \end{bmatrix}, \quad V = \begin{bmatrix} m_z & m_\perp \\ -m_\perp & -m_z \end{bmatrix}. \quad (\text{A.18})$$

then

$$\text{tr} \ln [G^{-1}] = \text{tr} \ln [-G_0^{-1}] + \text{tr} \ln [1 + G_0 V]. \quad (\text{A.19})$$

Taylor expanding the \ln we get:

$$\text{tr} \ln [G^{-1}] = \text{tr} \ln [-G_0^{-1}] - \sum_{n=1}^{\infty} \frac{1}{n} \text{tr} [(G_0 V)^n]. \quad (\text{A.20})$$

A.5 Matsubara Frequencies

We require to evaluate sums of the form $\sum_{\omega_n} (i\omega_n - \epsilon_k)^{-n}$, these are known as Matsubara frequency sums and are evaluated as follows.

We note that the fermi function $n_F(z)$ has simple poles at $z = i\omega_n$, so for a general function $f(z)$ we may write

$$k_B T \sum_{\omega_n} f(i\omega_n) = - \int_C \frac{dz}{2\pi i} f(z) n_F(z), \quad (\text{A.21})$$

by contour integration. We may distort this contour to include the poles of $f(z)$ so that in the case of $f(z) = (z - \epsilon_k)^{-1}$ we have

$$k_B T \sum_{\omega_n} \frac{1}{(i\omega_n - \epsilon_k)} = - \int_{C'} \frac{dz}{2\pi i} \frac{1}{(z - \epsilon_k)} n_F(z) = n_F(\epsilon_k). \quad (\text{A.22})$$

In the case of multiple poles we must integrate by parts, recalling that for a closed

contour the boundary terms are zero.

$$\begin{aligned}
 k_B T \sum_{\omega_n} \frac{1}{(i\omega_n - \epsilon_k)^p} &= - \int_{C'} \frac{dz}{2\pi i} \frac{1}{(z - \epsilon_k)^p} n_F(z) \\
 &= - \int_{C'} \frac{dz}{2\pi i} \frac{-1}{p-1} \frac{1}{(z - \epsilon_k)^{p-1}} \partial_z n_F(z) \\
 &= - \int_{C'} \frac{dz}{2\pi i} \frac{(-1)^{p-1}}{(p-1)!} \frac{1}{(z - \epsilon_k)} \partial_z^{p-1} n_F(z) \\
 &= \frac{(-1)^p}{(p-1)!} n_F^{p-1}(\epsilon_k). \tag{A.23}
 \end{aligned}$$

We will also use the relation

$$\begin{aligned}
 I(u_\uparrow, u_\downarrow) &= \frac{1}{\beta} \sum_k \frac{1}{i\omega_n - \epsilon_k + u_\uparrow} \frac{1}{i\omega_n - \epsilon_k - u_\downarrow} \\
 &= \sum_k \frac{1}{u_\uparrow + u_\downarrow} [n_F(\epsilon_k + u_\downarrow) - n_F(\epsilon_k - u_\downarrow)] \\
 &= - \frac{1}{u_\uparrow + u_\downarrow} \sum_{k\sigma} \sigma n_F(\epsilon_k - \sigma u_\sigma) \tag{A.24}
 \end{aligned}$$

And finally the remaining terms may be calculated by manipulations following the form

$$\begin{aligned}
 -(\partial_{u_\uparrow} + \partial_{u_\downarrow}) I(u_\uparrow, u_\downarrow) &= \frac{1}{\beta} \sum_k \frac{1}{(i\omega_n - \epsilon_k + u_\uparrow)^2} \frac{1}{(i\omega_n - \epsilon_k - u_\downarrow)} \\
 &\quad - \frac{1}{\beta} \sum_k \frac{1}{(i\omega_n - \epsilon_k + u_\uparrow)} \frac{1}{(i\omega_n - \epsilon_k - u_\downarrow)^2} \\
 &= - \frac{2}{(u_\uparrow + u_\downarrow)^2} \sum_{k\sigma} \sigma n_F(\epsilon_k - \sigma u_\sigma) \\
 &\quad - \frac{1}{(u_\uparrow + u_\downarrow)} \sum_{k\sigma} n_F^{(1)}(\epsilon_k - \sigma u_\sigma) \tag{A.25}
 \end{aligned}$$

B. TERMS IN THE EXPANSION OF THE STONER ACTION

Here we consider in more detail the procedure and results of the expansion of the Stoner action 4.19.

B.1 Action and critical endpoint conditions

The action is

$$\mathcal{S}[\mathbf{m}] = \frac{g}{4} \int dx \mathbf{m}^2 - \text{tr} \ln [\hat{G}_0^{-1}] + \sum_{n=1}^{\infty} \frac{(-1)^n}{n} \left(\frac{g}{2}\right)^n \text{tr} [\hat{G} \bar{\sigma} \cdot \mathbf{m}]^n, \quad (\text{B.1})$$

where $\int dx \equiv \int_0^\beta d\tau \int d^d r$ and $\mathbf{m} = (\bar{m} + \bar{M}) \hat{\mathbf{e}}_{\parallel} + \mathbf{m}_{\perp}$. Here

$$G = \begin{pmatrix} G_{\uparrow} & 0 \\ 0 & G_{\downarrow} \end{pmatrix} \quad (\text{B.2})$$

$\hat{G}_{\sigma}^{-1} = -\partial_{\tau} - \xi_{\mathbf{k}\sigma} - \mu$, where $\xi_{\mathbf{k}\sigma} = \epsilon_{\mathbf{k}} - \sigma g \bar{M}/2$. $\bar{\sigma}$ is the vector of Pauli matrices $\bar{\sigma} = (\sigma_x, \sigma_y, \sigma_z)$

$$\sigma_x = \begin{pmatrix} 0 & 1 \\ 1 & 0 \end{pmatrix}, \quad \sigma_y = \begin{pmatrix} 0 & -i \\ i & 0 \end{pmatrix}, \quad \sigma_z = \begin{pmatrix} 1 & 0 \\ 0 & -1 \end{pmatrix}. \quad (\text{B.3})$$

On the line of critical endpoints we have the following conditions

$$\begin{aligned} \bar{M} - \frac{2}{g} h &= \frac{1}{L^d} \sum_{\mathbf{k}\sigma} \sigma n_{\text{F}}, \\ \frac{2}{g} &= -\frac{1}{L^d} \sum_{\mathbf{k}\sigma} n_{\text{F}}^{(1)}, \\ 0 &= \frac{1}{L^d} \sum_{\mathbf{k}\sigma} \sigma n_{\text{F}}^{(2)} \end{aligned} \quad (\text{B.4})$$

where $n_{\text{F}} = n_{\text{F}}(\epsilon_{\mathbf{k}} - g \bar{M} \sigma / 2)$ is the Fermi-Dirac distribution and $n_{\text{F}}^{(n)} = \partial_{\epsilon}^n n_{\text{F}}(\epsilon_{\mathbf{k}} - g \bar{M} \sigma / 2)$.

B.2 Landau expansion

We now examine the terms in the expansion of the action up to sixth order, discarding the constant contribution, $\text{tr} \ln [\hat{G}_0^{-1}]$.

1st order:

$$\begin{aligned} \mathcal{S}^{(1)} &= -\left(\frac{g}{2}\right) \frac{1}{L^d} \sum_{\mathbf{k}, \omega_n} (\hat{G}_\uparrow - \hat{G}_\downarrow) \bar{m} \\ &= \frac{\beta}{L^d} \sum_{\mathbf{k}\sigma} \sigma n_{\text{F}} \bar{m}. \end{aligned} \quad (\text{B.5})$$

Applying B.4 gives

$$\mathcal{S}^{(1)} = -\beta \int d^d r \, h \bar{m} \quad (\text{B.6})$$

on the line of critical endpoints.

2nd order:

$$\begin{aligned} \mathcal{S}^{(2)} &= \frac{g}{4} \int dx \, \mathbf{m}^2 \\ &\quad + \frac{1}{2} \left(\frac{g}{2}\right)^2 \frac{1}{L^d} \sum_{\mathbf{q}} \sum_{\mathbf{k}, \omega_n} [((\hat{G}_\uparrow \bar{m}_q)^2 + (\hat{G}_\downarrow \bar{m}_{-q})^2) + 2\hat{G}_\uparrow \mathbf{m}_{\perp, q} \cdot \hat{G}_\downarrow \mathbf{m}_{\perp, -q}]. \\ &= \beta \int d^d r \, (r \bar{m}^2 + r_\perp \mathbf{m}_\perp^2), \end{aligned} \quad (\text{B.7})$$

where

$$\begin{aligned} r &= \frac{g}{4} + \frac{1}{2} \left(\frac{g}{2}\right)^2 \frac{1}{\beta L^d} \sum_{\mathbf{k}, \omega_n} (\hat{G}_\uparrow^2 + \hat{G}_\downarrow^2) \\ &= \frac{g}{4} + \frac{1}{2} \left(\frac{g}{2}\right)^2 \frac{1}{L^d} \sum_{\mathbf{k}, \sigma} \sigma n_{\text{F}}^{(1)}, \\ r_\perp &= \frac{g}{4} \mathbf{m}_\perp^2 + \left(\frac{g}{2}\right)^2 \frac{1}{\beta L^d} \sum_{\mathbf{k}, \omega_n} \hat{G}_\uparrow \hat{G}_\downarrow \\ &= \frac{g}{4} \mathbf{m}_\perp^2 + \left(\frac{g}{2}\right)^2 \frac{1}{L^d} \frac{1}{gM} \sum_{\mathbf{k}, \sigma} \sigma n_{\text{F}} \end{aligned} \quad (\text{B.8})$$

Applying B.4 we get on the line of critical endpoints

$$\begin{aligned} r &= \frac{g}{4} - \frac{1}{2} \left(\frac{g}{2}\right)^2 \frac{2}{g} = 0, \\ r_{\perp} &= \frac{g}{4} + \left(\frac{g}{2}\right)^2 \frac{1}{g\bar{M}} \left(\bar{M} - \frac{2}{g}h\right) = \frac{h}{\bar{M}}. \end{aligned} \quad (\text{B.9})$$

3rd order:

$$\begin{aligned} \mathcal{S}^{(3)} &= -\frac{1}{3} \left(\frac{g}{2}\right)^3 \frac{1}{L^d} \sum_{\mathbf{k}, \omega_n} [(\hat{G}_{\uparrow}^3 - \hat{G}_{\downarrow}^3) \bar{m}^3 + 3(\hat{G}_{\uparrow}^2 \hat{G}_{\downarrow} - \hat{G}_{\uparrow} \hat{G}_{\downarrow}^2) \bar{m} \mathbf{m}_{\perp}^2] \\ &= \beta \int d^d r [s \bar{m}^3 + s_1 \bar{m} \mathbf{m}_{\perp}^2], \end{aligned} \quad (\text{B.10})$$

where

$$\begin{aligned} s &= -\frac{1}{3} \left(\frac{g}{2}\right)^3 \frac{1}{\beta L^d} \sum_{\mathbf{k}} (\hat{G}_{\uparrow}^3 - \hat{G}_{\downarrow}^3) \\ &= \frac{1}{6} \left(\frac{g}{2}\right)^3 \sum_{\mathbf{k}\sigma} \sigma n_{\text{F}}^{(2)} \\ s_1 &= -\left(\frac{g}{2}\right)^3 \frac{1}{\beta L^d} \sum_{\mathbf{k}} (\hat{G}_{\uparrow}^2 \hat{G}_{\downarrow} - \hat{G}_{\uparrow} \hat{G}_{\downarrow}^2) \\ &= \left(\frac{g}{2}\right)^3 \sum_{\mathbf{k}\sigma} \left(\frac{2}{(g\bar{M})^2} \sigma n_{\text{F}} + \frac{1}{g\bar{M}} n_{\text{F}}^{(1)} \right) \end{aligned} \quad (\text{B.11})$$

Applying B.4 on the line of critical endpoints gives

$$\begin{aligned} s &= 0 \\ s_1 &= \left(\frac{g}{2}\right)^3 \left(\frac{2}{(g\bar{M})^2} \left(\bar{M} - \frac{2}{g}h\right) - \frac{1}{g\bar{M}} \frac{2}{g} \right) = -\frac{h}{2\bar{M}^2} \end{aligned} \quad (\text{B.12})$$

4th order:

$$\mathcal{S}^{(4)} = \frac{1}{4} \left(\frac{g}{2}\right)^4 \text{tr} [(\hat{G}_{\uparrow} m)^4 + (\hat{G}_{\downarrow} m)^4] + \frac{1}{2} \left(\frac{g}{2}\right)^4 \text{tr} [\hat{G}_{\uparrow}^2 \hat{G}_{\downarrow}^2 \mathbf{m}_{\perp}^4]$$

$$\begin{aligned}
& + \left(\frac{g}{2}\right)^4 \text{tr} \left[(\hat{G}_\uparrow^3 \hat{G}_\downarrow + \hat{G}_\uparrow^2 \hat{G}_\downarrow^2 + \hat{G}_\uparrow \hat{G}_\downarrow^3) \bar{m}^2 \mathbf{m}_\perp^2 \right] \\
= & \beta \int d^d r \left[u \bar{m}^4 + u_\perp \mathbf{m}_\perp^4 + u_1 \bar{m}^2 \mathbf{m}_\perp^2 \right], \tag{B.13}
\end{aligned}$$

$$\begin{aligned}
u & = \frac{1}{4} \left(\frac{g}{2}\right)^4 \frac{1}{\beta L^d} \sum_{\mathbf{k}, \omega_n} [\hat{G}_\uparrow^4 + \hat{G}_\downarrow^4] \\
& = \frac{1}{4!} \left(\frac{g}{2}\right)^4 \frac{1}{L^d} \sum_{\mathbf{k}} n_{\text{F}}^{(3)} \\
u_\perp & = \frac{1}{2} \left(\frac{g}{2}\right)^4 \frac{1}{\beta L^d} \sum_{\mathbf{k}} \hat{G}_\uparrow^2 \hat{G}_\downarrow^2 \\
& = \frac{1}{2} \left(\frac{g}{2}\right)^4 \frac{1}{L^d} \sum_{\mathbf{k}, \sigma} \left(\frac{2}{(g\bar{M})^3} \sigma n_{\text{F}} + \frac{1}{(g\bar{M})^2} n_{\text{F}}^{(1)} \right) \\
u_1 & = \left(\frac{g}{2}\right)^4 \frac{1}{\beta L^d} \sum_{\mathbf{k}} [(\hat{G}_\uparrow^3 \hat{G}_\downarrow - \hat{G}_\uparrow^2 \hat{G}_\downarrow^2 + \hat{G}_\uparrow \hat{G}_\downarrow^3)] \\
& = \left(\frac{g}{2}\right)^4 \frac{1}{L^d} \sum_{\mathbf{k}, \sigma} \left(\frac{-4}{(g\bar{M})^3} \sigma n_{\text{F}} - \frac{2}{(g\bar{M})^2} n_{\text{F}}^{(1)} + \frac{1}{g\bar{M}} \sigma n_{\text{F}}^{(2)} \right) \tag{B.14}
\end{aligned}$$

$$\begin{aligned}
u_\perp & = \frac{1}{2} \left(\frac{g}{2}\right)^4 \left(\frac{2}{(g\bar{M})^3} \left(\bar{M} - \frac{2}{g} h \right) + \frac{1}{(g\bar{M})^2} \frac{-2}{g} \right) \\
& = -\frac{1}{8} \frac{h}{\bar{M}^3} \\
u_1 & = -\left(\frac{g}{2}\right)^4 \left(\frac{-4}{(g\bar{M})^3} \left(\bar{M} - \frac{2}{g} h \right) - \frac{2}{(g\bar{M})^2} \frac{-2}{g} + \frac{1}{g\bar{M}} 0 \right) \\
& = -\frac{h}{2\bar{M}^3} \tag{B.15}
\end{aligned}$$

5th order:

$$\begin{aligned}
\mathcal{S}^{(5)} & = -\frac{1}{5} \left(\frac{g}{2}\right)^5 \text{tr} [(\hat{G}_\uparrow m)^5 - (\hat{G}_\downarrow m)^5] \\
& \quad - \left(\frac{g}{2}\right)^5 \text{tr} [(\hat{G}_\uparrow^4 \hat{G}_\downarrow - \hat{G}_\uparrow^3 \hat{G}_\downarrow^2 + \hat{G}_\uparrow^2 \hat{G}_\downarrow^3 - \hat{G}_\uparrow \hat{G}_\downarrow^4) \bar{m}^3 \mathbf{m}_\perp^2]
\end{aligned}$$

$$\begin{aligned}
& - \left(\frac{g}{2}\right)^5 \text{tr} [(\hat{G}_\uparrow^3 \hat{G}_\downarrow^2 - \hat{G}_\uparrow^2 \hat{G}_\downarrow^3) \bar{m} \mathbf{m}_\perp^4] \\
& = \beta \int d^d r [t \bar{m}^5 + t_1 \bar{m}^3 \mathbf{m}_\perp^2 + t_2 \bar{m} \mathbf{m}_\perp^4], \tag{B.16}
\end{aligned}$$

$$\begin{aligned}
t & = \frac{1}{5!} \left(\frac{g}{2}\right)^5 \frac{1}{L^d} \sum_{\mathbf{k}, \sigma} \sigma n_{\mathbf{F}}^{(4)} \\
t_1 & = - \left(\frac{g}{2}\right)^5 \frac{1}{L^d} \sum_{\mathbf{k}, \sigma} \left(-\frac{8}{(g\bar{M})^4} \sigma n_{\mathbf{F}} - \frac{4}{(g\bar{M})^3} n_{\mathbf{F}}^{(1)} - \frac{3}{2} \frac{1}{(g\bar{M})^2} \sigma n_{\mathbf{F}}^{(2)} - \frac{1}{6} \frac{1}{(g\bar{M})} n_{\mathbf{F}}^{(3)} \right) \\
t_2 & = \left(\frac{g}{2}\right)^5 \frac{1}{L^d} \sum_{\mathbf{k}, \sigma} \left(\frac{6}{(g\bar{M})^4} \sigma n_{\mathbf{F}} + \frac{3}{(g\bar{M})^3} n_{\mathbf{F}}^{(1)} + \frac{1}{(g\bar{M})^2} \sigma n_{\mathbf{F}}^{(2)} \right) \tag{B.17}
\end{aligned}$$

$$\begin{aligned}
t_1 & = \left(\frac{g}{2}\right)^5 \left(\frac{-8}{(g\bar{M})^4} \left(\bar{M} - \frac{2}{g}h\right) - \frac{4}{(g\bar{M})^3} \frac{-2}{g} \right) + \frac{2}{\bar{M}} u \\
& = -\frac{1}{2} \frac{h}{\bar{M}^4} + \frac{2}{\bar{M}} u \\
t_2 & = \left(\frac{g}{2}\right)^5 \left(\frac{6}{(g\bar{M})^4} \left(\bar{M} - \frac{2}{g}h\right) + \frac{3}{(g\bar{M})^3} \frac{-2}{g} \right) \\
& = \frac{3}{8} \frac{h}{\bar{M}} \tag{B.18}
\end{aligned}$$

6th order:

$$\begin{aligned}
\mathcal{S}^{(6)} & = \frac{1}{6} \left(\frac{g}{2}\right)^6 \text{tr} [(\hat{G}_\uparrow m)^6 + (\hat{G}_\downarrow m)^6] + \frac{1}{6} \left(\frac{g}{2}\right)^6 \text{tr} [2\hat{G}_\uparrow^3 \hat{G}_\downarrow^3 \mathbf{m}_\perp^6] \\
& + \left(\frac{g}{2}\right)^6 \text{tr} [(\hat{G}_\uparrow^5 \hat{G}_\downarrow - \hat{G}_\uparrow^4 \hat{G}_\downarrow^2 + \hat{G}_\uparrow^3 \hat{G}_\downarrow^3 - \hat{G}_\uparrow^2 \hat{G}_\downarrow^4 + \hat{G}_\uparrow \hat{G}_\downarrow^5) \bar{m}^4 \mathbf{m}_\perp^2] \\
& + \frac{1}{6} \left(\frac{g}{2}\right)^6 \text{tr} [(9\hat{G}_\uparrow^4 \hat{G}_\downarrow^2 + 12\hat{G}_\uparrow^3 \hat{G}_\downarrow^3 + 9\hat{G}_\uparrow^2 \hat{G}_\downarrow^4) \bar{m}^2 \mathbf{m}_\perp^4] \\
& = \beta \int d^d r [v \bar{m}^6 + v_\perp \mathbf{m}_\perp^6 + v_1 m^4 \mathbf{m}_\perp^2 + v_2 m^2 \mathbf{m}_\perp^4] \tag{B.19}
\end{aligned}$$

$$\begin{aligned}
v & = \frac{1}{6!} \left(\frac{g}{2}\right)^6 \sum_{\mathbf{k}, \sigma} n_{\mathbf{F}} \\
v_\perp & = \frac{1}{6} \left(\frac{g}{2}\right)^6 \frac{1}{L^d} \sum_{\mathbf{k}, \sigma} \left(\frac{-12}{(g\bar{M})^5} \sigma n_{\mathbf{F}} - \frac{6}{(g\bar{M})^4} n_{\mathbf{F}}^{(1)} - \frac{1}{(g\bar{M})^3} \sigma n_{\mathbf{F}}^{(2)} \right)
\end{aligned}$$

$$\begin{aligned}
 v_1 &= \left(\frac{g}{2}\right)^6 \frac{1}{L^d} \sum_{\mathbf{k}, \sigma} \left(-\frac{16}{(g\bar{M})^5} \sigma n_{\mathbf{F}} - \frac{8}{(g\bar{M})^4} n_{\mathbf{F}}^{(1)} - \frac{3}{2} \frac{1}{(g\bar{M})^3} \sigma n_{\mathbf{F}}^{(2)} - \frac{1}{3} \frac{1}{(g\bar{M})^2} n_{\mathbf{F}}^{(3)} \right. \\
 &\quad \left. - \frac{1}{24} \frac{1}{(g\bar{M})} \sigma n_{\mathbf{F}}^{(4)} \right) \\
 v_2 &= \frac{1}{6} \left(\frac{g}{2}\right)^6 \frac{1}{L^d} \sum_{\mathbf{k}, \sigma} \left(\frac{144}{(g\bar{M})^5} \sigma n_{\mathbf{F}} + \frac{72}{(g\bar{M})^4} n_{\mathbf{F}}^{(1)} + \frac{36}{(g\bar{M})^3} \sigma n_{\mathbf{F}}^{(2)} \right. \\
 &\quad \left. + \frac{9}{6} \frac{1}{(g\bar{M})^2} n_{\mathbf{F}}^{(3)} \right) \tag{B.20}
 \end{aligned}$$

$$\begin{aligned}
 v_{\perp} &= \frac{1}{6} \left(\frac{g}{2}\right)^6 \left(\frac{-12}{(g\bar{M})^5} \left(\bar{M} - \frac{2}{g} h \right) - \frac{6}{(g\bar{M})^4} \frac{-2}{g} \right) \\
 &= \frac{1}{16} \frac{h}{\bar{M}^5} \\
 v_1 &= \left(\frac{g}{2}\right)^6 \left(-\frac{16}{(g\bar{M})^5} \left(\bar{M} - \frac{2}{g} h \right) - \frac{8}{(g\bar{M})^4} \left(\frac{-2}{g} \right) \right) - \frac{2u}{(\bar{M})^2} - \frac{5}{2} \frac{t}{(\bar{M})} \\
 &= \frac{h}{\bar{M}^5} - \frac{2u}{\bar{M}^2} - \frac{5}{2} \frac{t}{\bar{M}} \\
 v_2 &= \frac{1}{6} \left(\frac{g}{2}\right)^6 \left(\frac{144}{(g\bar{M})^5} \left(\bar{M} - \frac{2}{g} h \right) + \frac{72}{(g\bar{M})^4} \left(\frac{-2}{g} \right) \right) + \frac{9}{6} \frac{u}{\bar{M}^2} \\
 &= -\frac{3}{4} \frac{h}{\bar{M}^5} + \frac{3}{2} \frac{u}{\bar{M}^2} \tag{B.21}
 \end{aligned}$$

B.3 Gradient expansion

We now discuss how the wavevector-dependent terms of the action are obtained. A gradient expansion of the Green's function is given by

$$\begin{aligned}
 G(\mathbf{k} + \mathbf{q}) &= G(\mathbf{k}) + [G(\mathbf{k})]^2 \partial_{k_i} \epsilon_{\mathbf{k}} q_i \\
 &\quad + \left[[G(\mathbf{k})]^3 \partial_{k_i} \epsilon_{\mathbf{k}} \partial_{k_j} \epsilon_{\mathbf{k}} + [G(\mathbf{k})]^2 \partial_{k_i, k_j}^2 \epsilon_{\mathbf{k}} \right] q_i q_j + O(q^3). \tag{B.22}
 \end{aligned}$$

The longitudinal susceptibility is then

$$\Pi_{\sigma}(q) = \frac{1}{\beta L^d} \sum_{\mathbf{k}} G_{\sigma}(\mathbf{k}) G_{\sigma}(\mathbf{k} + \mathbf{q})$$

$$\begin{aligned}
 &= \frac{1}{\beta L^d} \sum_{\mathbf{k}} G_{\sigma}(\mathbf{k}) G_{\sigma}(\mathbf{k}) \\
 &+ \frac{1}{\beta L^d} \sum_{\mathbf{k}} G_{\sigma}(\mathbf{k}) \left[[G(\mathbf{k})]^3 \partial_{k_i} \epsilon_{\mathbf{k}} \partial_{k_j} \epsilon_{\mathbf{k}} + [G(\mathbf{k})]^2 \partial_{k_i, k_j}^2 \epsilon_{\mathbf{k}} \right] q_i q_j \\
 &+ O(q^3)
 \end{aligned} \tag{B.23}$$

where we have discarded the term first order in q as it makes no contribution to the action.

$$\begin{aligned}
 &\frac{1}{\beta L^d} \sum_{\mathbf{k}} G_{\sigma}(\mathbf{k}) \left[[G(\mathbf{k})]^3 \partial_{k_i} \epsilon_{\mathbf{k}} \partial_{k_j} \epsilon_{\mathbf{k}} + [G(\mathbf{k})]^2 \partial_{k_i, k_j}^2 \epsilon_{\mathbf{k}} \right] \\
 &= \frac{2}{\beta L^d} \sum_{\mathbf{k}} G_{\sigma}(\mathbf{k}) [G(\mathbf{k})]^3 \partial_{k_i} \epsilon_{\mathbf{k}} \partial_{k_j} \epsilon_{\mathbf{k}} \\
 &= -\frac{1}{L^d} \frac{1}{6} \sum_{\mathbf{k}} n_{\text{F}}^{(3)}(\epsilon_{\mathbf{k}} - \sigma \frac{g\bar{M}}{2}) \partial_{k_i} \epsilon_{\mathbf{k}} \partial_{k_j} \epsilon_{\mathbf{k}}
 \end{aligned} \tag{B.24}$$

Therefore

$$K = -\frac{1}{L^d} \frac{1}{12} \left(\frac{U}{2} \right)^2 \sum_{\mathbf{k}, \sigma} n_{\text{F}}^{(3)}(\epsilon_{\mathbf{k}} - \sigma \frac{g\bar{M}}{2}) (\partial_{\mathbf{k}} \epsilon_{\mathbf{k}})^2. \tag{B.25}$$

Likewise the transverse component

$$\begin{aligned}
 \Pi_{\perp}(q) &= \frac{1}{\beta L^d} \sum_{\mathbf{k}} G_{\uparrow}(\mathbf{k}) G_{\downarrow}(\mathbf{k} + \mathbf{q}) \\
 &= \frac{1}{\beta L^d} \sum_{\mathbf{k}} G_{\uparrow}(\mathbf{k}) G_{\downarrow}(\mathbf{k}) \\
 &+ \frac{1}{\beta L^d} \sum_{\mathbf{k}} G_{\uparrow}(\mathbf{k}) \left[[G_{\downarrow}(\mathbf{k})]^3 \partial_{k_i} \epsilon_{\mathbf{k}} \partial_{k_j} \epsilon_{\mathbf{k}} + [G_{\downarrow}(\mathbf{k})]^2 \partial_{k_i, k_j}^2 \epsilon_{\mathbf{k}} \right] q_i q_j \\
 &+ O(q^3)
 \end{aligned} \tag{B.26}$$

where we have discarded the term first order in q as it makes no contribution to the action.

$$\begin{aligned}
 &\frac{1}{\beta L^d} \sum_{\mathbf{k}} G_{\uparrow}(\mathbf{k}) \left[[G_{\downarrow}(\mathbf{k})]^3 \partial_{k_i} \epsilon_{\mathbf{k}} \partial_{k_j} \epsilon_{\mathbf{k}} + [G_{\downarrow}(\mathbf{k})]^2 \partial_{k_i, k_j}^2 \epsilon_{\mathbf{k}} \right] \\
 &= -\frac{1}{L^d} \frac{1}{(g\bar{M})^3} \sum_{\mathbf{k}, \sigma} \left[\sigma n_{\text{F}}(\epsilon_{\mathbf{k}} + \frac{g\bar{M}}{2}) + \frac{g\bar{M}}{2} n_{\text{F}}^{(1)}(\epsilon_{\mathbf{k}} - \sigma \frac{g\bar{M}}{2}) \right] \partial_{k_i} \epsilon_{\mathbf{k}} \partial_{k_j} \epsilon_{\mathbf{k}}
 \end{aligned} \tag{B.27}$$

$$K_{\perp} = -\frac{1}{4g\bar{M}^3} \frac{1}{L^d} \sum_{\mathbf{k}, \sigma} \left[\sigma n_{\text{F}}(\epsilon_{\mathbf{k}} + \frac{g\bar{M}}{2}) + \frac{g\bar{M}}{2} n_{\text{F}}^{(1)}(\epsilon_{\mathbf{k}} - \sigma \frac{g\bar{M}}{2}) \right] \partial_{k_i} \epsilon_{\mathbf{k}} \partial_{k_j} \epsilon_{\mathbf{k}}. \quad (\text{B.28})$$

Had we retained higher order terms in the gradient expansion of the Green function then we could continue to calculate terms in the action proportional to $q^4 m^2$, or even higher orders. Should we substitute the expansion into the higher order terms in m then we could obtain terms such as $q^2 m^4$. Such terms rapidly become extremely complex.

B.4 Calculating the phase diagram

The phase diagram is found by numerically solving the equation $r = 0$ for the second order transitions. The sheet of solutions is shown in blue in figure B.1. The line of metamagnetic critical endpoints is found by the intersection of this with the sheet defined by $s = 0$. This is shown in green in figure B.1. The tricritical point would be determined by $u = 0$.

The dome of second order transitions is not actually realised. Figure B.1 is calculated in terms of \bar{M} , this is the shifted magnetisation $\bar{M} = \bar{m} + \frac{2}{g}h$. The first-order transition therefore compresses all the values of \bar{M} under the blue dome into one first-order transition line.

We note that the shape of the second order transition sheet is the same as the nematic region discussed in chapter 7. This reflects the similarity of the mean-field theories when magnetisation is replaced by the nematic order.

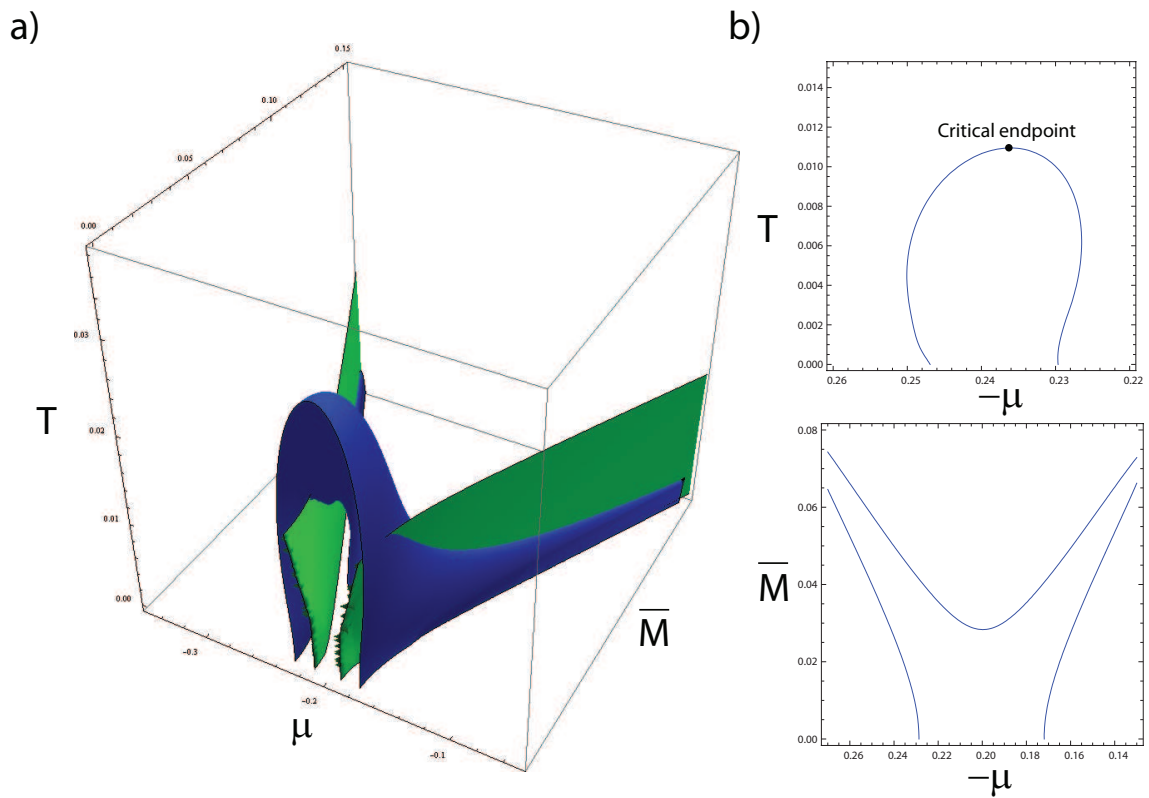


Fig. B.1: **Calculation of phase diagram:** a) Blue: the sheet defined by $r = 0$. Green: the sheet defined by $s = 0$. b) Cuts through the sheet of continuous transitions. Top: a cut at $\bar{M} = 0.04$ showing a cross-section of the ‘leg’ of the sheet. Bottom: a cut at $T = 0.005$.

C. THERMODYNAMIC DERIVATIONS

C.1 Free energy and self-consistency

The Free Energy for the Stoner model in the Canonical Potential is:

$$F = \sum_{\sigma} \left[-T \int d\epsilon \rho(\epsilon) \ln \left(1 + e^{-\frac{\epsilon - \mu_{\sigma}}{T}} \right) + \mu_{\sigma} n_{\sigma} \right] + U n_{\uparrow} n_{\downarrow} - h m, \quad (\text{C.1})$$

where $\sigma = \uparrow, \downarrow$ and μ_{σ} is the effective chemical potential for the spin species, k_B has been set to 1.

Minimizing this Free Energy with respect to magnetization allows us to find the magnetisation as a function of field, or the field as a function of magnetization:

$$h = \mu_{\uparrow} - \mu_{\downarrow} - 2U m. \quad (\text{C.2})$$

We use the definitions

$$\begin{aligned} n &= n_{\uparrow} + n_{\downarrow}, \\ m &= \frac{n_{\uparrow} - n_{\downarrow}}{2}, \\ n_{\sigma} &= \int d\epsilon \rho(\epsilon) f_{\sigma}, \end{aligned} \quad (\text{C.3})$$

where $f_{\sigma} = f(\epsilon - \mu_{\sigma}) = \left(1 + e^{\beta(\epsilon - \mu_{\sigma})} \right)^{-1}$. Working with fixed n , h and T , leads to the following relations:

$$\begin{aligned} \partial_T n &= \partial_T n_{\uparrow} + \partial_T n_{\downarrow} = 0 \\ \Rightarrow \partial_T n_{\uparrow} &= -\partial_T n_{\downarrow}, \\ \partial_T m &= \frac{1}{2} (\partial_T n_{\uparrow} - \partial_T n_{\downarrow}) \\ &= \partial_T n_{\uparrow} = -\partial_T n_{\downarrow}, \\ \partial_T h &= \partial_T \mu_{\uparrow} - \partial_T \mu_{\downarrow} - 2U \partial_T m \end{aligned}$$

$$\begin{aligned}
&= \partial_T \mu_\uparrow - \partial_T \mu_\downarrow - 2U \partial_T n_\uparrow = 0 \\
\Rightarrow \partial_T \mu_\uparrow &= \partial_T \mu_\downarrow + 2U \partial_T n_\uparrow.
\end{aligned} \tag{C.4}$$

$$\begin{aligned}
\partial_T^2 n &= \partial_T^2 n_\uparrow + \partial_T^2 n_\downarrow = 0 \\
\Rightarrow \partial_T^2 n_\uparrow &= -\partial_T^2 n_\downarrow, \\
\partial_T^2 m &= \frac{1}{2} (\partial_T^2 n_\uparrow - \partial_T^2 n_\downarrow) \\
&= \partial_T^2 n_\uparrow = -\partial_T^2 n_\downarrow, \\
\partial_T^2 h &= \partial_T^2 \mu_\uparrow - \partial_T^2 \mu_\downarrow - 2U \partial_T^2 m \\
&= \partial_T^2 \mu_\uparrow - \partial_T^2 \mu_\downarrow - 2U \partial_T^2 n_\uparrow = 0 \\
\Rightarrow \partial_T^2 \mu_\uparrow &= \partial_T^2 \mu_\downarrow + 2U \partial_T^2 n_\uparrow.
\end{aligned} \tag{C.5}$$

C.2 Useful derivatives

We now evaluate some derivatives which will prove to be useful.

$$\begin{aligned}
\partial_T f_\sigma &= \partial_T \frac{1}{1 + e^{\frac{\epsilon - \mu_\sigma}{T}}} \\
&= \frac{e^{\frac{\epsilon - \mu_\sigma}{T}}}{(1 + e^{\frac{\epsilon - \mu_\sigma}{T}})^2} \left[\frac{\epsilon - \mu_\sigma}{T^2} + \frac{\partial_T \mu_\sigma}{T} \right], \\
\partial_T \ln \left(1 + e^{-\frac{\epsilon - \mu_\sigma}{T}} \right) &= \frac{1}{1 + e^{\frac{\epsilon - \mu_\sigma}{T}}} \left[\frac{\epsilon - \mu_\sigma}{T^2} + \frac{\partial_T \mu_\sigma}{T} \right] \\
&= f_\sigma \left[\frac{\epsilon - \mu_\sigma}{T^2} + \frac{\partial_T \mu_\sigma}{T} \right], \\
\partial_T^2 \ln \left(1 + e^{-\frac{\epsilon - \mu_\sigma}{T}} \right) &= \frac{1}{1 + e^{\frac{\epsilon - \mu_\sigma}{T}}} \left[-2 \frac{\epsilon - \mu_\sigma}{T^3} - 2 \frac{\partial_T \mu_\sigma}{T^2} + \frac{\partial_T^2 \mu_\sigma}{T} \right] \\
&\quad + \frac{e^{\frac{\epsilon - \mu_\sigma}{T}}}{(1 + e^{\frac{\epsilon - \mu_\sigma}{T}})^2} \left[\frac{\epsilon - \mu_\sigma}{T^2} + \frac{\partial_T \mu_\sigma}{T} \right]^2 \\
&= f_\sigma \left[-2 \frac{\epsilon - \mu_\sigma}{T^3} - 2 \frac{\partial_T \mu_\sigma}{T^2} + \frac{\partial_T^2 \mu_\sigma}{T} \right] + \partial_T f_\sigma \left[\frac{\epsilon - \mu_\sigma}{T^2} + \frac{\partial_T \mu_\sigma}{T} \right].
\end{aligned} \tag{C.6}$$

C.3 Entropy

Entropy is the first derivative of the Free energy with respect to temperature, $S = -\partial_T F$.

$$\begin{aligned} \partial_T F &= \sum_{\sigma} \left[- \int d\epsilon \rho(\epsilon) \ln \left(1 + e^{-\frac{\epsilon - \mu_{\sigma}}{T}} \right) - T \int d\epsilon \rho(\epsilon) \partial_T \ln \left(1 + e^{-\frac{\epsilon - \mu_{\sigma}}{T}} \right) \right. \\ &\quad \left. + \partial_T \mu_{\sigma} n_{\sigma} + \mu_{\sigma} \partial_T n_{\sigma} \right] \\ &\quad + U (\partial_T n_{\uparrow} n_{\downarrow} + n_{\uparrow} \partial_T n_{\downarrow}) - h \partial_T m \end{aligned} \quad (\text{C.7})$$

Using Eq.(C.4) and Eq.(C.2)

$$\begin{aligned} \mu_{\uparrow} \partial_T n_{\uparrow} + \mu_{\downarrow} \partial_T n_{\downarrow} + U (\partial_T n_{\uparrow} n_{\downarrow} + n_{\uparrow} \partial_T n_{\downarrow}) - h \partial_T m &= (n_{\uparrow} - n_{\downarrow} + 2Um - h) \partial_T n_{\uparrow} \\ &= 0, \end{aligned} \quad (\text{C.8})$$

and so

$$\begin{aligned} \partial_T F &= \sum_{\sigma} \left[- \int d\epsilon \rho(\epsilon) \ln \left(1 + e^{-\frac{\epsilon - \mu_{\sigma}}{T}} \right) - T \int d\epsilon \rho(\epsilon) \partial_T \ln \left(1 + e^{-\frac{\epsilon - \mu_{\sigma}}{T}} \right) \right. \\ &\quad \left. + \partial_T \mu_{\sigma} n_{\sigma} \right], \\ S &= \sum_{\sigma} \left[\int d\epsilon \rho(\epsilon) \ln \left(1 + e^{-\frac{\epsilon - \mu_{\sigma}}{T}} \right) + T \int d\epsilon \rho(\epsilon) \partial_T \ln \left(1 + e^{-\frac{\epsilon - \mu_{\sigma}}{T}} \right) \right. \\ &\quad \left. - \partial_T \mu_{\sigma} n_{\sigma} \right]. \end{aligned} \quad (\text{C.9})$$

C.4 Specific Heat

$$C = - \left. \frac{\partial^2 F}{\partial T^2} \right|_{n,h} = -T \left. \frac{\partial U}{\partial T} \right|_{n,h}$$

$$\begin{aligned} U &= \sum_{\sigma} \left[\int d\epsilon (\epsilon - \sigma h) \rho(\epsilon) f_{\sigma} \right] + U n_{\uparrow} n_{\downarrow} \\ &= \sum_{\sigma} \left[\int d\epsilon \epsilon \rho(\epsilon) f_{\sigma} \right] + U n_{\uparrow} n_{\downarrow} - hm. \end{aligned} \quad (\text{C.10})$$

$$C = \partial_T U = \sum_{\sigma} \left[\int d\epsilon \epsilon \rho(\epsilon) \partial_T f_{\sigma} \right] + U (\partial_T n_{\uparrow} n_{\downarrow} + n_{\uparrow} \partial_T n_{\downarrow}) - h \partial_T m$$

$$= \sum_{\sigma} \left[\int d\epsilon \epsilon \rho(\epsilon) \partial_T f_{\sigma} \right] - (2Um + h) \partial_T n_{\uparrow}. \quad (\text{C.11})$$

C.5 Derivatives of the chemical potential

Before we can evaluate the Specific Heat or Entropy we need to calculate expressions for the temperature derivatives of the chemical potentials. The expression for the number of electrons of each spin species is

$$n_{\sigma} = \int d\epsilon \rho(\epsilon) f_{\sigma}, \quad (\text{C.12})$$

and so

$$\begin{aligned} \partial_T n_{\sigma} &= \int d\epsilon \rho(\epsilon) \partial_T f_{\sigma} \\ &= \int d\epsilon \rho(\epsilon) \frac{e^{\frac{(\epsilon - \mu_{\sigma})}{T}}}{(1 + e^{\frac{(\epsilon - \mu_{\sigma})}{T}})^2} \left[\frac{\epsilon - \mu_{\sigma}}{T^2} + \frac{\partial_T \mu_{\sigma}}{T} \right]. \end{aligned} \quad (\text{C.13})$$

From Eq.(C.4) we have

$$\begin{aligned} \partial_T n_{\uparrow} &= -\partial_T n_{\downarrow} \\ \int d\epsilon \rho(\epsilon) \Xi_{\uparrow} \left[\frac{\epsilon - \mu_{\uparrow}}{T^2} + \frac{\partial_T \mu_{\uparrow}}{T} \right] &= - \int d\epsilon \rho(\epsilon) \Xi_{\downarrow} \left[\frac{\epsilon - \mu_{\downarrow}}{T^2} + \frac{\partial_T \mu_{\downarrow}}{T} \right], \\ \partial_T \mu_{\downarrow} &= -T \frac{\int d\epsilon \rho(\epsilon) \left(\Xi_{\downarrow} \frac{\epsilon - \mu_{\downarrow}}{T^2} + \Xi_{\uparrow} \frac{\epsilon - \mu_{\uparrow}}{T^2} \right)}{\int d\epsilon \rho(\epsilon) \Xi_{\downarrow}} - \partial_T \mu_{\uparrow} \frac{\int d\epsilon \rho(\epsilon) \Xi_{\uparrow}}{\int d\epsilon \rho(\epsilon) \Xi_{\downarrow}}, \end{aligned} \quad (\text{C.14})$$

where $\Xi_{\sigma} = \frac{e^{\frac{(\epsilon - \mu_{\sigma})}{T}}}{\left(1 + e^{\frac{(\epsilon - \mu_{\sigma})}{T}}\right)^2}$. Also

$$\begin{aligned} \partial_T \mu_{\uparrow} &= \partial_T \mu_{\downarrow} - 2U \partial_T n_{\downarrow} \\ &= \partial_T \mu_{\downarrow} - 2U \int d\epsilon \rho(\epsilon) \Xi_{\downarrow} \left[\frac{\epsilon - \mu_{\downarrow}}{T^2} + \frac{\partial_T \mu_{\downarrow}}{T} \right] \\ &= \partial_T \mu_{\downarrow} \left(1 - \frac{2U}{T} \int d\epsilon \rho(\epsilon) \Xi_{\downarrow} \right) - 2U \int d\epsilon \rho(\epsilon) \Xi_{\downarrow} \frac{\epsilon - \mu_{\downarrow}}{T^2}, \end{aligned} \quad (\text{C.15})$$

resulting in

$$\partial_T \mu_{\downarrow} = \frac{-T \frac{\int d\epsilon \rho(\epsilon) \left(\Xi_{\downarrow} \frac{\epsilon - \mu_{\downarrow}}{T^2} + \Xi_{\uparrow} \frac{\epsilon - \mu_{\uparrow}}{T^2} \right) + 2U \int d\epsilon \rho(\epsilon) \Xi_{\downarrow} \frac{\epsilon - \mu_{\downarrow}}{T^2}}{\int d\epsilon \rho(\epsilon) \Xi_{\uparrow}}}{1 - \frac{2U}{T} \int d\epsilon \rho(\epsilon) \Xi_{\downarrow} + \frac{\int d\epsilon \rho(\epsilon) \Xi_{\downarrow}}{\int d\epsilon \rho(\epsilon) \Xi_{\uparrow}}}. \quad (\text{C.16})$$

BIBLIOGRAPHY

- [1] L. Landau, Sov. Phys. JETP **3**, 920 (1956).
- [2] L. Landau, Sov. Phys. JETP **5**, 101 (1957).
- [3] L. Landau, Sov. Phys. JETP **8**, 70 (1958).
- [4] *The Kondo Problem to Heavy Fermions*, edited by A. C. Hewson (Cambridge University Press, The Pitt Building, Trumpington Street, Cambridge CB2 1RP, 1993).
- [5] P. Gegenwart, Q. Si, and F. Steglich, Nature Physics **4**, 186 (2008).
- [6] D. van der Marel, H. J. A. Molegraaf, J. Zaanen, Z. Nussinov, F. Carbone, A. Damascelli, H. Eisaki, M. Greven, P. H. Kes, and M. Li, Nature **425**, 271 (2003).
- [7] Lucretius Carus, De Rerum Natura, 1st Century BC.
- [8] Image from <http://en.wikipedia.org/wiki/File:Magnetite.Lodestone.jpg>, licenced under the Creative Commons Attribution ShareAlike 2.0 License.
- [9] Image from http://en.wikipedia.org/wiki/File:Model_Si_Nan_of_Han_Dynasty.jpg, licenced under the GNU Free Documentation License.
- [10] P. Wasilewski and G. Kletetscha, Geophys. Res. Lett. **26**, 2275 (1999).
- [11] W. Gilbert, De Magnete, 1600, trans., Gilbert Club, London, 1900, rev. ed., Basic Books, New York, 1958.
- [12] N. Bohr, Ph.D. thesis, 1911.
- [13] H. J. van Leeuwen, Journal de Physique et le Radium **2**, 361 (1921).
- [14] A. K. Compton, Jour. Frankl. Inst. 145 (1921).

-
- [15] S. A. Goudsmit and G. E. Uhlenbeck, *Naturwissenschaften* **13**, 953 (1925).
- [16] P. A. M. Dirac, *Proc. R. Soc.* **A117**, 610 (1928).
- [17] J. Kondo, *Progress of Theoretical Physics* **32**, (1964).
- [18] L. Néel, *Ann. Phys. (Paris)* **5**, 232 (1936).
- [19] C. G. Shull and J. S. Smart, *Phys. Rev.* **76**, 1256 (1949).
- [20] L. Néel, *Ann. Phys. (Paris)* **3**, 137 (1948).
- [21] I. Dzyaloshinsky, *Journal of Physics and Chemistry of Solids* **4**, 241 (1958).
- [22] J. Hubbard, *Proceedings of the Royal Society of London. Series A. Mathematical and Physical Sciences* **276**, 238 (1963).
- [23] S. A. Kivelson, E. Fradkin, and V. J. Emery, *Nature* **393**, 550 (1998).
- [24] V. Hinkov, D. Haug, B. Fauqué, P. Bourges, Y. Sidis, A. Ivanov, C. Bernhard, C. T. Lin, and B. Keimer, *Science* **319**, 597 (2008).
- [25] K. B. Cooper, M. P. Lilly, J. P. Eisenstein, L. N. Pfeiffer, and K. W. West, *Phys. Rev. B* **65**, 241313 (2002).
- [26] R. A. Borzi, S. A. Grigera, J. Farrell, R. S. Perry, S. J. S. Lister, S. L. Lee, D. A. Tennant, Y. Maeno, and A. P. Mackenzie, *Science* **315**, 214 (2007).
- [27] P. Fulde and R. A. Ferrell, *Physical Review* **135**, A550 (1964).
- [28] A. I. Larkin and Y. N. Ovchinnikov, *Sov. Phys. JETP* **20**, 762 (1965).
- [29] C. Pfleiderer, A. Neubauer, S. Mühlbauer, F. Jonietz, M. Janoschek, S. Legl, R. Ritz, W. Münzer, C. Franz, P. G. Niklowitz, T. Keller, R. Georgii, P. Böni, B. Binz, and A. A Rosch, *Journal of Physics: Condensed Matter* **21**, 164215 (2009).
- [30] N. Doiron-Leyraud, I. R. Walker, L. Taillefer, M. J. Steiner, S. R. Julian, and G. G. Lonzarich, *Nature* **425**, 595 (2003).
- [31] D. J. W. Geldart and M. Rasolt, *Phys. Rev. B* **15**, 1523 (1977).
- [32] G. Conduit, B. D. Simons, and A. G. Green, , arXiv:0906.1347v1 [cond-mat.str-el].

-
- [33] A. Abrikosov and I. Khalatnikov, *Sov. Phys. JETP* **6**, 888 (1958).
- [34] T. D. Lee and C. N. Yang, *Phys. Rev.* **117**, 897 (1960).
- [35] F. Mohling, *Phys. Rev.* **122**, 1062 (1961).
- [36] R. A. Duine and A. H. MacDonald, *Phys. Rev. Lett.* **95**, 230403 (2005).
- [37] J. A. Hertz, *Phys. Rev. B* **14**, 1165 (1976).
- [38] A. J. Millis, *Phys. Rev. B* **48**, 7183 (1993).
- [39] D. Belitz, T. R. Kirkpatrick, and T. Vojta, *Physical Review Letters* **82**, 4707 (1999).
- [40] J. Rech, C. Pepin, and A. V. Chubukov, *Physical Review B (Condensed Matter and Materials Physics)* **74**, 195126 (2006).
- [41] P. W. Atkins, *Physical Chemistry* (Oxford University Press, Walton Street, Oxford OX2 6DP, 1990).
- [42] H.-Y. Kee and Y. B. Kim, *Physical Review B (Condensed Matter and Materials Physics)* **71**, 184402 (2005).
- [43] H. Yamase, V. Oganesyan, and W. Metzner, *Phys. Rev. B* **72**, 035114 (2005).
- [44] I. I. Pomeranchuk, *JETP* **35**, 524 (1958).
- [45] S.-I. Ikeda, Y. Maeno, S. Nakatsuji, M. Kosaka, and Y. Uwatoko, *Phys. Rev. B* **62**, R6089 (2000).
- [46] V. L. Ginzburg and L. Landau, *Zh. Eksp. Teor. Fiz.* **20**, 1064 (1950).
- [47] M. Uhlarz, C. Pfleiderer, and S. M. Hayden, *Physical Review Letters* **93**, 256404 (2004).
- [48] M. Brando, D. Moroni-Klementowicz, C. Albrecht, W. Duncan, D. Grüner, R. Ballou, B. Fåk, and F. Grosche, *Journal of Magnetism and Magnetic Materials* **310**, 852 (2007).
- [49] A. Huxley, I. Sheikin, and D. Braithwaite, *Physica B: Condensed Matter* **284-288**, 1277 (2000).

-
- [50] T. Goto, Y. Shindo, H. Takahashi, and S. Ogawa, *Phys. Rev. B* **56**, 14019 (1997).
- [51] S. A. Grigera, R. S. Perry, A. J. Schofield, M. Chiao, S. R. Julian, G. G. Lonzarich, S. I. Ikeda, Y. Maeno, A. J. Millis, and A. P. Mackenzie, *Science* **294**, 329 (2001).
- [52] S. A. Grigera, P. Gegenwart, R. A. Borzi, F. Weickert, A. J. Schofield, R. S. Perry, T. Tayama, T. Sakakibara, Y. Maeno, A. G. Green, and A. P. Mackenzie, *Science* **306**, 1154 (2004).
- [53] K. G. Wilson, *Rev. Mod. Phys.* **47**, 773 (1975).
- [54] T. Moriya, *Spin Fluctuations in Itinerant Electron Magnetism* (Springer, Berlin, 1985).
- [55] H. v. Löhneysen, A. Rosch, M. Vojta, and P. Wölfle, *Reviews of Modern Physics* **79**, 1015 (2007).
- [56] L. Van Hove, *Phys. Rev.* **89**, 1189 (1953).
- [57] E. P. Wohlfarth and P. Rhodes, *Philosophical Magazine* **7**, 1817 (1962).
- [58] A. W. Overhauser, *Phys. Rev.* **128**, 1437 (1962).
- [59] W. M. Lomer, *Proc. Phys. Soc.* **80**, (1962).
- [60] R. Casalbuoni and G. Nardulli, *Rev. Mod. Phys.* **76**, 263 (2004).
- [61] H. A. Radovan, N. A. Fortune, T. P. Murphy, S. T. Hannahs, E. C. Palm, S. W. Tozer, and D. Hall, *Nature* **425**, 51 (2003).
- [62] D. E. Sheehy and L. Radzihovsky, *Physical Review Letters* **96**, 060401 (2006).
- [63] A. Bianchi, R. Movshovich, C. Capan, P. G. Pagliuso, and J. L. Sarrao, *Physical Review Letters* **91**, 187004 (2003).
- [64] Q. Huang, J. W. Lynn, R. W. Erwin, J. Jarupatrakorn, and R. J. Cava, *Phys. Rev. B* **58**, 8515 (1998).
- [65] R. S. Perry, L. M. Galvin, S. A. Grigera, L. Capogna, A. J. Schofield, A. P. Mackenzie, M. Chiao, S. R. Julian, S. I. Ikeda, S. Nakatsuji, Y. Maeno, and C. Pfleiderer, *Phys. Rev. Lett.* **86**, 2661 (2001).

-
- [66] S. A. Grigera, R. A. Borzi, A. P. Mackenzie, S. R. Julian, R. S. Perry, and Y. Maeno, *Physical Review B* **67**, 214427 (2003).
- [67] A. Tamai, M. P. Allan, J. F. Mercure, W. Meevasana, R. Dunkel, D. H. Lu, R. S. Perry, A. P. Mackenzie, D. J. Singh, Z.-X. Shen, and F. Baumberger, *Physical Review Letters* **101**, 026407 (2008).
- [68] J.-F. Mercure, arXiv:0902.3937v1 [cond-mat.str-el] .
- [69] B. Binz and M. Sigrist, *EPL (Europhysics Letters)* **65**, 816 (2004).
- [70] A. G. Green, S. A. Grigera, R. A. Borzi, A. P. Mackenzie, R. S. Perry, and B. D. Simons, *Physical Review Letters* **95**, 086402 (2005).
- [71] C. Puetter, H. Doh, and H.-Y. Kee, *Physical Review B (Condensed Matter and Materials Physics)* **76**, 235112 (2007).
- [72] A. M. Berridge, A. G. Green, S. A. Grigera, and B. D. Simons, *Physical Review Letters* **102**, 136404 (2009).
- [73] S. Raghu, A. Paramakanti, E. A. Kim, R. A. Borzi, S. A. Grigera, A. P. Mackenzie, and S. A. Kivelson, *Physical Review B (Condensed Matter and Materials Physics)* **79**, 214402 (2009).
- [74] A. Rost, Ph.D. thesis, 2009.
- [75] J.-F. Mercure, Ph.D. thesis, 2008.
- [76] C. Bergemann, S. R. Julian, A. P. Mackenzie, S. NishiZaki, and Y. Maeno, *Phys. Rev. Lett.* **84**, 2662 (2000).
- [77] R. Kiyonagi, K. Tsuda, N. Aso, H. Kimura, Y. Noda, Y. Yoshida, S.-I. Ikeda, and Y. Uwatoko, *Journal of the Physical Society of Japan* **73**, 639 (2004).
- [78] H. Yaguchi, R. S. Perry, and Y. Maeno, cond-mat/05103831, Proc of 24th Int. Conf. on Low Temperature Physics (LT24). .
- [79] N. Nagaosa, *Quantum Field Theory in Strongly Correlated Electronic Systems* (Springer-Verlag, Heidelberg, 1999).
- [80] C. Honerkamp, *Phys. Rev. B* **72**, 115103 (2005).

-
- [81] P. Monthoux and G. G. Lonzarich, *Physical Review B (Condensed Matter and Materials Physics)* **71**, 054504 (2005).
- [82] T. Moriya, *Physical Review* **120**, 91 (1960).
- [83] P. Bak and M. H. Jensen, *Journal of Physics C: Solid State Physics* **13**, L881 (1980).
- [84] C. Mora and R. Combescot, *Europhys. Lett.* **66**, 833 (2004).
- [85] T. M. Rice, *Physical Review B* **2**, 3619 (1970).
- [86] S. Hayden and S. Ramos, , private communication.
- [87] S. Ramos, E. Forgan, C. Bowell, S. Hayden, A. Schofield, A. Wildes, E. Yelland, S. Brown, M. Laver, R. Perry, and Y. Maeno, *Physica B: Condensed Matter* **403**, 1270 (2008), proceedings of the International Conference on Strongly Correlated Electron Systems.
- [88] H. Yamase, *Physical Review B (Condensed Matter and Materials Physics)* **76**, 155117 (2007).
- [89] E. Wigner, *Phys. Rev.* **46**, 1002 (1934).
- [90] B. Spivak and S. A. Kivelson, *Phys. Rev. B* **70**, 155114 (2004).
- [91] V. J. Emery, S. A. Kivelson, and J. M. Tranquada, *Proceedings of the National Academy of Sciences of the United States of America* **96**, (1999).
- [92] L. Radzihovsky and A. T. Dorsey, *Phys. Rev. Lett.* **88**, 216802 (2002).
- [93] J. Quintanilla and A. J. Schofield, *Physical Review B (Condensed Matter and Materials Physics)* **74**, 115126 (2006).
- [94] C. J. Halboth and W. Metzner, *Phys. Rev. Lett.* **85**, 5162 (2000).
- [95] H. Yamase and H. Kohno, *Journal of the Physical Society of Japan* **69**, 2151 (2000).
- [96] H. Doh and H.-Y. Kee, *Physical Review B (Condensed Matter and Materials Physics)* **75**, 233102 (2007).
- [97] W. Lee and C. Wu, , arXiv:0902.1337v2 [cond-mat.str-el].

-
- [98] R. Moessner and J. T. Chalker, *Phys. Rev. B* **54**, 5006 (1996).
- [99] A. A. Koulakov, M. M. Fogler, and B. I. Shklovskii, *Phys. Rev. Lett.* **76**, 499 (1996).
- [100] L. Balents and C. M. Varma, *Physical Review Letters* **84**, 1264 (2000).
- [101] J. Hubbard, *Phys. Rev. Lett.* **3**, 77 (1959).
- [102] R. L. Stratonovich, *Doklady Akad. Nauk S.S.S.R.* **115**, 1097 (1957).